Multi-Property Internal Flow Field Quantification using Molecular Filtered Rayleigh Scattering

Matthew Thomas Boyda

Dissertation submitted to the Faculty of the
Virginia Polytechnic Institute and State University
in partial fulfillment of the requirements for the degree of

Doctor of Philosophy
in
Aerospace Engineering

K. Todd Lowe, Chair
Wing Ng
Olivier Coutier-Delgosha
Colin Adams

Dec 18, 2024
Blacksburg, Virginia

Keywords: Molecular Filtered Rayleigh Scattering, non-intrusive optical diagnostics, uncertainty quantification, flow quantification, measurement validation, CFD Validation

Multi-Property Internal Flow Field Quantification using Molecular Filtered Rayleigh Scattering

Matthew Thomas Boyda

(ABSTRACT)

Foundational approaches for realizing practical, non-intrusive measurements using filtered Rayleigh scattering (FRS) are presented and analyzed for the multi-property quantification of internal flow fields. Validation is challenging in applying computational fluid dynamics (CFD) solutions to real-world scenarios, necessitating benchmark measurements with well-defined uncertainties. The ideal instrument for achieving the required measurements should be non-intrusive and require no particulate or gas seeding. One approach that satisfies these requirements is filtered Rayleigh scattering. FRS is a laser-based optical diagnostic technique that allows for the simultaneous, non-intrusive measurement of three-component velocity, static temperature, and static density everywhere within a two-dimensional plane illuminated by laser light without using any form of flow seeding. The major disadvantage of FRS is that it is very susceptible to signal contamination from particles and surfaces illuminated by the probing laser source. The effects of these contamination sources of the FRS signal are quantified as a function of their intensity relative to the Rayleigh scattered light. As the most significant contributor to Rayleigh scattering contamination, methods for reducing geometric or background contributions were investigated. Structured illumination was applied in cross-correlation Doppler global velocimetry to reduce geometric scattering contributions in image acquisition, demonstrating the removal of background scattering biases in an FRS-similar technique. For multi-property measurements, it is shown that with only an order of magnitude estimate of Mie and geometric scattering, a range of wavenumbers termed the

rejection region can be pre-defined such that molecular iodine absorbs the contamination. At the same time, Rayleigh scattered light can pass through. Mie and geometric scattering contributions are reduced to negligible levels within the rejection region, allowing for unbiased temperature and density measurement. Additionally, a method for determining only Doppler shift, desirable due to its increased processing speed and spatial resolution, was developed and shown to be robust to at least one order of magnitude greater Mie and geometric scattering than other methods. The biases associated with sampling a statistical average of the flow using time-averaged FRS were also investigated. The result is that measuring flow properties with the "constant in time" assumption is valid up to a turbulent intensity of 20%, resulting in biases in velocity and temperature greater than 10% of the measurement uncertainties predicted without these contributions. These advancements allow researchers to optimize measurement parameters and predict uncertainties before integrating them into a facility. These methods were implemented in a turbulent, highly distorted internal flow environment with Mie and background scattering present. Measurement uncertainties for vector velocity components, static temperature, and static density are predetermined using a 95% confidence interval on the Monte Carlo simulation results. Derived measurement uncertainties are calculated by propagating the results of the Monte-Carlo simulation. Measurements are compared to reference five-hole probe and particle image velocimetry measurements to assess the validity of the predicted uncertainty bounds. The results from this study show good agreement in the measurement of axial velocity and derived circumferential and radial flow angles when compared to reference measurements. These comparisons typically yield measurements that measure the same value as the five-hole probe data within the predefined uncertainty bounds of 9 m/s, 1.0^o, and 3.8^o, with significant deviations occurring at radii greater than 71% for tangential flow angle and radii greater than 55% for radial flow angle. Compared to facility average measurements, static density and static pressure data collected over the entire plane show RMSD values comparable to predicted measurement

uncertainties of 0.043 kg/m^3 and 4.0 kPa, respectively. For the same comparison, temperature measurements show a greater RMSD than the predicted uncertainty of 8.4 K. While additional work remains to identify sources of bias error in some measurements, this work lays the foundation for FRS-based diagnostics to be used as a replacement or supplemental measurement technique in quantifying the state of fluid flow fields.

Multi-Property Internal Flow Field Quantification using Molecular Filtered Rayleigh Scattering

Matthew Thomas Boyda

(GENERAL AUDIENCE ABSTRACT)

Rayleigh scattering is a process that results from the interaction of light with microscopic particles that, whether we know it or not, we experience every day. When sunlight interacts with air molecules, the light scattered to our eyes is blue. The fact that the sky appears blue indicates a key property of Rayleigh scattering in that it is most efficient for the shortest wavelengths. What isn't apparent is that a whole host of other properties can be extracted from observed scattering by imaging it with a camera and a specialized filter when illuminated by a narrow wavelength laser. The problem is that a few dust particles, small enough to pass through a household air filter, can scatter more light than all the air molecules in a shot glass, with laser light scattering off large surfaces even more intense. The primary focus of this dissertation is to define Foundational approaches for realizing practical, non-intrusive filtered Rayleigh scattering techniques and methods necessary so that the light scattered from air molecules can be measured while avoiding the scattering from particles and surfaces. These approaches enable the measurement of the three-component velocity, temperature, and density of the gas being illuminated without the measurement affecting the flow itself. Because all these properties can be measured simultaneously, Rayleigh scattering provides one of the most comprehensive experimental measurement techniques available to researchers, making it highly desirable in quantifying gaseous flows and validating computational fluid dynamics calculations. Measurements collected with the techniques outlined in this work are validated experimentally using reference measurements in a large-scale internal

flow facility, providing the groundwork for future applications of Rayleigh scattering-based diagnostics.

Contents

List of Figures

List of Tables

Chapter 1

Introduction

In today's world of advanced digital aerodynamic design, engineers rely heavily on various computational fluid dynamics (CFD) flow solutions to iteratively evaluate the aerodynamic performance of three-dimensional (3D) geometries. The final geometry is then manufactured so that the performance can be validated in large-scale ground test facilities by comparing high-level aerodynamic performance parameters that can easily be measured in these facilities to the same metrics derived from the CFD solution. Examples of these metrics include lift, drag, their derived coefficients, and a varying number of static pressures on the surface of the vehicle. While these metrics go a long way in validating the CFD flow solution, they are far from perfect due to imperfections in the experimental model and data collected as well as inaccuracies in input flow conditions used in the CFD simulations.

CFD flow solutions depend highly on the inflow and outflow boundary conditions applied to solve the flow. Ideally, time-resolved measurements of three-component velocity, temperature, and pressure would be collected simultaneously across the inflow and outflow planes during the experiment so that the CFD boundary conditions would match the test conditions exactly. Unfortunately, this is extremely difficult to achieve in most large-scale ground test facilities due to the intrusiveness of standard probe-based flow measurement techniques, limited access, and difficulty implementing many optical flow diagnostic techniques. As a result, engineers must use the data that is available to them.

Properties at the inflow and outflow planes are conventionally measured using intrusive

probe-based measurements. Still, they are typically limited to time-averaged measurements of total pressure, static pressure, total temperature, and flow angularity at discrete points in the flow. Due to the intrusiveness of these probe-based measurements and the structure required to hold the probes rigidly in the test section with the flow on, measurements can only be made in a few locations without significantly impacting the flow environment at the measurement location, and the downstream flow environment is always disturbed. Characterizing the entire flow then requires the probe (or probe rake) to be traversed to a series of locations throughout the flow, resulting in the non-simultaneous characterization of the boundary condition over a significant amount of time. Furthermore, the downstream perturbation of upstream probe measurements affects the flow at the model location and the outflow plane, resulting in the need to validate model performance and measure the outflow plane conditions without the upstream instrumentation present.

Optical, laser-based diagnostics have been developed, in part, to combat the intrusiveness of probe-based measurements in ground test facilities. The most popular of these diagnostic techniques measure fluid properties by observing the interaction of the laser light with particles artificially introduced into the flow as tracer particles. Diagnostics such as particle image velocimetry (PIV), Doppler global velocimetry (DGV), and Thermographic phosphor particle imaging enable the measurement of three-component velocity and static temperature of a flow. While seeded laser diagnostics improve significantly on the intrusiveness of probe-based measurements and enable measurements to be made within two-dimensional (2D) and 3D planes simultaneously, they require that foreign particles be injected into the flow, introducing their unique form of intrusiveness and difficulties in implementation.

Unseeded laser-based diagnostic techniques improve further upon seeded techniques by observing the interaction of laser light with gas molecules present in the flow. Techniques included in this regime of optical diagnostics include Laser-induced fluorescence (LIF), molec-

ular tagging velocimetry (MTV), coherent anti-stokes Ramen spectroscopy (CARS), and Laser Rayleigh scattering (LRS), allow for the time-resolved or time-averaged measurement of one or more of vector velocity, temperature, density, and pressure. While these techniques improve measurement intrusiveness, implementing these instruments for flow quantification measurements requires significant effort.

Of these techniques, LRS has been identified as an attractive candidate for flow quantification for CFD validation because of its dependencies on the velocity, temperature, pressure, and density of the scattering medium. Additionally, with recent advancements in laser technology, LRS has been used in various forms to provide flow quantification measurements in two-dimensional planes for both time-averaged and temporally resolved measurements. The primary drawback of LRS, however, is that it is a very low-intensity scattering process that occurs very near the frequency of the incident laser light, making it susceptible to interference from Mie scattering, or scattering from particles present in the flow, and from laser scattering off surfaces and windows visible in the field of view of the measurement, known as geometric or background scattering. Since Mie and geometric scattering occur at the same frequency as the incident light and as Rayleigh scattering, it cannot be filtered using conventional optical filters.

Filtered Rayleigh scattering (FRS) is a measurement technique derived from LRS that utilizes a very narrow bandwidth notch filter positioned between the location of the observed LRS and the imager. The notch filter, typically a molecular absorption filter, can filter out high-intensity Mie and geometric scattering signal contamination to negligible levels while allowing some of the more frequency-broadened LRS signal to pass through to the imager. Additionally, the presence of the molecular filter and the ability to tune the frequency of the incident laser light allows the practitioner to resolve the measurement in the frequency domain, enabling 2D multi-property measurement capability.

The work contained within this dissertation is focused on the development of a molecular filtered Rayleigh scattering instrument and data processing scheme that is broadly applicable for the multi-property measurement of time-averaged vector velocity, temperature, and density for flow quantification and CFD validation. As such, the resulting instrument is robust to Mie and geometric scattering signal contamination and measures desired properties with well-defined uncertainties and bias errors *in-situ*. The techniques described in this dissertation are verified and validated by collecting FRS measurements within a plane downstream of a distortion-generating test article and comparing results to reference five-hole probe and PIV data collected on the same downstream plane. These comparisons, while used to demonstrate the effectiveness of the described techniques, also present areas of future improvement, paving the way for future FRS flow quantification to be used as a supplement or replacement to conventional intrusive flow measurement techniques in validating CFD flow solutions of internal flows.

1.1 Structure and Contents

The dissertation consists of six chapters, as described below:

Chapter 1 introduces the content and structure of the dissertation while also explicitly detailing the motivation for the research and the contributions of the Ph.D. candidate to the scientific community during the development of the publications contained within this work.

Chapter 2 provides a review of relevant literature regarding conventional and state-of-the-art diagnostics used to quantify gaseous flows in internal flow environments and ground test facilities. Previous applications of molecular filtered Rayleigh scattering and the techniques used to measure vector velocity and scalar properties will be introduced and discussed.

Chapter 3 contains studies published in two research articles. The first was published by invitation in *Measurement Science and Technology* (doi: 10.1088/1361-6501/ab0350) which discusses some practical considerations and the theoretical limits of Doppler shift velocity and temperature measurement uncertainty in molecular filtered Rayleigh scattering measurements using the cross-correlation and curve fitting methods respectively. The second can be found in the proceedings of *AIAA Scitech Forum* (doi: 10.2514/6.2020-1516) which expands this uncertainty analysis to density and details the manner in which Mie and geometric or background scattering affect measured molecular FRS signals.

Chapter 4 consists of a research article published by invitation in *Measurement Science and Technology* (doi: 10.1088/1361-6501/ab6b4f). This article discusses the novel application of structured laser illumination planar imaging (SLIPI) for high-power laser sheet imaging to accurately measure Doppler shift-based vector velocity using cross-correlation Doppler global velocimetry (CC-DGV) in the presence of significant background scattering. This article demonstrates the capability of SLIPI to reduce the contributions of background scattering in frequency scanning optical diagnostics and, thus, the bias typically associated with its presence in the CC-DGV signal to negligible levels.

Chapter 5 is a research article that has been submitted to *Measurement Science and Technology*, which details an experiment performed in a full-scale engine inlet test facility operated by the Air Force Research Lab to fully quantify the distorted flow downstream of a distortion-generating test article where novel data collection and processing methods are presented and demonstrated. Velocity, temperature, density, and pressure were quantified in a two-dimensional flow cross-section in a high Mie and geometric scattering environment. Detailed measurement uncertainty quantification is presented in addition to the effects of turbulent fluctuations in this environment.

Chapter 6 concludes the dissertation with a summary of the results established in this work

and a discussion of the additional improvements that need to be established so that the FRS instrument can be robustly applied to a wider variety of flow regimes. Finally, the outlook for future FRS technologies and applications is discussed.

Note that the formatting of each chapter and its contents may differ from one another due to specific publication guidelines of the journal the articles have published in, will be published, or will be submitted.

1.2 Achievements

The primary achievements of this work are as follows:

- The development and validation of data processing algorithms used to measure the Doppler shift of measured FRS convolution spectra in the presence of Mie and geometric scattering contamination.
- The development and validation of a data processing algorithm to fit model convolution spectra to measured FRS spectra to determine Doppler shift, temperature, and density using a least-squares fitting routine.
- Description of the influence of Mie and geometric scattering on multi-property filtered Rayleigh scattering measurements of Doppler shift, temperature, and density, allowing the determination of dependencies between the magnitude of the contaminating light sources and the resulting bias errors and uncertainties.
- The development of the rejection region analysis, a method to collect FRS convolution spectra in the presence of high intensity Mie and geometric scattering contamination without explicit consideration of their respective intensity ratios in fitting modeled

convolution spectra to measured convolution spectra.

- The quantification of measurement uncertainties and bias errors in FRS measured Doppler shift, temperature, and density.
- The quantification of measurement uncertainties and bias errors in measurements derived from FRS measured quantities. These quantities include three-component velocity components, velocity magnitude, static pressure, and total pressure.
- The quantification of the effects of turbulent fluctuations on the measured FRS convolution spectrum, the bias error induced by measuring a turbulent flow with time averaged FRS, and the limits of the "constant in time" property assumption in FRS measurements.
- The novel application of structured illumination to Doppler-based, frequency scanning laser diagnostics to remove geometric scattering, the dominant contributor to bias errors in velocity measurements in filtered Rayleigh scattering.
- Planar multi-property FRS measurements of vector velocity, temperature, density, and pressure of a highly non-uniform flowfield in an internal flow facility, the Annular Cascade Facility located at Wright Patterson Air Force Base.

1.2.1 Claims

The key contributions and main claims of this work are as follows:

- As the main contributors to signal contamination, the effects of varying levels of Mie and geometric scattering on the filtered Rayleigh scattering signal are investigated extensively in scattering environments near atmospheric conditions. This allowed for

the development of a method that explicitly informs the practitioner of the range of wavenumbers that may be used to accurately measure velocity, temperature, and density with only an order-of-magnitude estimate of scattering contributions.

- The downstream effects of signal contamination on the multi-property measurement of velocity, temperature, and density, including added uncertainty and bias error, were also investigated. This research has practical implications, leading to the development of a method that explicitly informs the practitioner about the dependencies between the relative magnitude of the contaminating light sources and the resulting bias errors and uncertainties.

- A novel implementation of structured illumination was developed for Doppler-based, frequency scanning laser diagnostics to remove geometric scattering, the dominant contributor to bias errors in FRS-based velocity measurements, from measured signals.

- The development of an experimentally validated filtered Rayleigh scattering uncertainty quantification methodology to inform knowledge-driven FRS experiment design.

- Investigation into the effects of turbulent fluctuations on the measured FRS signal and the bounds over which the assumption that all properties are constant in time can be applied.

- The experimental validation of a multi-property FRS measurement uncertainty quantification using the filtered Rayleigh scattering technique in an internal flow environment.

1.2.2 List of Publications

Peer reviewed journal publications

- Boyda M.T., Byun G., Lowe K.T. (2019) Investigation of velocity and temperature measurement sensitivities in cross-correlation filtered Rayleigh scattering, Measurement Science and Technology, 30:044004

- Boyda M.T., Byun G., Saltzman A.S., Lowe K.T. (2020) Geometric scattering removal in cross-correlation doppler global velocimetry by structured illumination, Measurement Science and Technology, 31:064004

- Boyda M.T., Byun G., Lowe K.T. (2024) Filtered Rayleigh Scattering for Multi-Property Aerodynamic Measurements in Confined Flows, submitted to Measurement Science and Technology, xx:xxxxxx

Conference proceedings

- Boyda M.T., Lowe K.T. (2018) Cross-correlation doppler global velocimetry using Rayleigh and Mie scattering, AIAA SciTech Forum 2018

- Boyda, M.T., Byun, G. and Lowe, K.T. (2018),Cross correlation filtered Rayleigh scattering (CCFRS), 19th International Symposium on Application of Laser Techniques to Fluid Mechanics, 16-19 July, Lisbon, paper No. 100.

- Boyda M.T., Byun G.B., Lowe K.T. (2019) Cross-Correlation Filtered Rayleigh Scattering (CCFRS), In Proceedings of the 19th International Symposium on the Application of Laser and Imaging Techniques to Fluid Mechanics, 2018

- Saltzman A.J., Boyda M.T., Lowe K.T., Ng W.F. (2019) Filtered Rayleigh scattering for velocity and temperature measurements of a heated supersonic jet with thermal non-uniformity, AIAA Aviation 2019 Forum, AIAA 2019-2677

- Danehy P.M., Wisser B.M., Fahringer T.W., Winski C.S., Falman B.E., Shea S., Boyda M., Lowe K.T. (2019) Laser Light Sheet Flow Visualization of the Space Launch System Booster Separation Test, AIAA Aviation 2019 Forum, AIAA 2019-3507

- Boyda M.T., Byun G.B., Saltzman A., Lowe K.T. (2019) Geometric scattering removal in CC-DGV by structured illumination, 13th International Symposium on Particle Image Velocimetry

- Boyda M.T., Byun G.B., Saltzman A.S., Lowe K.T. (2020) Influence of Mie and Geometric Scattering on Temperature and Density Measurements using Filtered Rayleigh Scattering, AIAA SciTech Forum 2020

Chapter 2

Literature Review

The following sections in this chapter will present the historical and current literature for flow quantification and flow visualization techniques used to understand the performance of aerodynamic models and validate computational fluid dynamics (CFD) flow solutions. Of the measurements discussed, the author has identified filtered Rayleigh scattering (FRS) as a promising candidate for providing non-intrusive measurements that allow for simultaneous quantification measurements. As such, the discussion herein will focus primarily on the various FRS measurement techniques.

2.1 Quantification of Fluid Flows for CFD validation

The primary objective of experimental aerodynamics is quantifying the thermodynamic and aerodynamic state of a fluid flow as the fluid is in motion. Historically, these measurements have been collected to help engineers better understand the performance of an aerodynamic model under test. Still, as more aerodynamic performance-based design iteration takes place in a virtual environment, the role of many ground test facilities has also changed. A more and more common occurrence is that the model's performance is predicted using computational fluid dynamics (CFD), and experimental ground test facilities are then used to validate CFD flow solutions of the final design using experimental measurements.

CFD is a tool that is ever increasing in popularity with the increased affordability of com-

puters powerful enough to run such tools and the availability of commercially available flow solvers that include turbulence models that are questionably universal [21, 40]. The issue with this is that when the question of the accuracy of the results comes up, the answer may not be easy to quantify, and for large-scale or high-impact systems, these answers are critical [40].

CFD validation experiments fundamentally differ from traditional aerodynamic experiments [2, 34, 39]. Usually, experimental measurements are used to improve the understanding of a physical process, improve existing models, or assess system performance. In contrast, validation measurements must consider all sources of bias and uncertainty from the CFD flow solution and the experimental measurements used to validate them for the specific experiment. To do this, explicit consideration of the validation experiments to be conducted must be taken into account and planned for to ensure all of the physics required to model the flow, including boundary conditions and system response quantities (SRQs) of interest, are captured [40]. Favier 2010 [21] goes so far as to indicate that while standard measurements of surface pressures, force, and moment characteristics are still helpful in validating SRQ measurement, these are insufficient to validate CFD flow solutions.

While the advancements of CFD have progressed rapidly, the development and implementation of experimental diagnostics have also progressed. Favier 2010 outlines several non-intrusive techniques that have undergone significant improvement such as Laser Doppler Anemometry (LDA), particle image velocimetry (PIV) and embedded laser Doppler Velocimetry (ELDV) which is capable of measuring two or three components of velocity [4, 20, 49].

Additional examples of comprehensive CFD validation experiment design and execution can be found centered around the Benchmark Validation Experiment for Reynolds-averaged Navier–Stokes (RANS)/large eddy simulation (LES) Investigations (BeVERLI) project tak-

ing place at Virginia Tech. The goal of this project is to generate an "experimental dataset of three-dimensional non-equilibrium turbulent boundary layers with various levels of separation that meets the most exacting requirements of CFD validation" by measuring the flow about the BeVERLI Hill [26, 32].

Intrusive Measurements used for CFD Validation

While many experimental techniques are available for flow quantification measurements, the most straightforward implementation, robustness, and measurement uncertainty quantification are probe-based measurements of static pressure, total pressure, flow angularity, and total temperature. While these probe-based measurements provide accurate measurements when positioned far away from physical geometry [63] and in regions of the flow without large pressure gradients [31, 56], these probe-based measurements rely on the physical interaction of the flow with the probe to measure these properties. These measurements are generally accurate for free or shear flows with no bounding geometry. When the environment becomes bounded by rigid walls, and the researcher wishes to characterize the flow near the wall, physical probes begin to apply influence to the flow field in terms of flow blockage and wall interaction via the probe-wall flow potential [63]. Additionally, downstream flow conditions are significantly perturbed.

In more advanced flow facilities, measurements of wall static pressure, force, and moment characteristics may also be available. These provide less intrusive references for the validation of CFD flow solutions to compare SRQs but do not meet the stringent requirements set forth by Oberkampf and Smith [40] in measuring all of the quantities required to validate the CFD solution and are called out explicitly by Favier [21] as not being sufficient.

Even with the limitations of probe-based measurements near boundaries, regions of high

property gradients remain the standards in internal flow quantification due to the simplicity of implementation, broad application space, and well-defined uncertainties in steady-state, uniform flow fields. With increasing flow complexity and the near-boundary nature of desired regions of interest (ROI), new measurement standards must be developed to collect simultaneous multi-property field measurements, improve near-wall measurement accuracy, and reduce instrument intrusiveness. Most importantly, to replace legacy probes, such techniques must also have low-magnitude, well-defined uncertainties while being robust to the harsh conditions synonymous with large-scale testing facilities.

Non-Intrusive Measurements used for CFD Validation

An attractive alternative to the drawbacks of physical probes embedded in the flow is to use non-intrusive optical diagnostics to interrogate the flow field. Many optical diagnostic techniques have been employed to quantitatively measure various flow properties. These diagnostics can typically be divided into two categories: seeded and unseeded measurements. While there are advantages and disadvantages to both types of diagnostics, they all prove to be useful in one form or another, and they are generally less intrusive than probe-based measurements.

Seeded measurements rely on the interaction of the laser light with particles in the flow environment. While not always the case, these particles are typically introduced into the flow environment specifically for the purpose of measuring them using a seeded technique. Seeded techniques allow for the measurement of temperature by observing the decay rate of the luminosity of thermographic phosphors [1, 29, 41, 65], and in some cases such as [41] simultaneous measurement of velocity is also possible when combined with particle image velocimetry (PIV). Vector velocity, using techniques such as laser Doppler velocimetry (LDV) [4, 20, 32], stereoscopic PIV (S-PIV)[3, 27, 32, 38, 48]. Doppler global velocimetry (DGV)

[11, 12] has also been demonstrated as a valuable technique to quantify the state of a fluid flow with well-defined uncertainties. However, these methods are not entirely non-intrusive and cannot be applied in all facilities due to the need for particles to be introduced into the flow for properties to be measured. In comparison to the physical blockage caused by probe-based measurements, these diagnostic techniques represent a significant improvement.

To address issues associated with introducing foreign particles into the flow, such as installing a seeding system, supplying the appropriate seeding density, achieving uniform seeding density, and navigating potential health and safety concerns, molecular-based optical diagnostic techniques, that rely on the interaction between laser light and fluid being investigated, present themselves as attractive alternatives. Such techniques include coherent anti-Stokes Raman spectroscopy (CARS) [15], molecular tagging velocimetry (MTV) [52], and molecular laser Rayleigh scattering (LRS) [16, 35, 37, 42, 43, 54]. With the increased availability of very high power/energy lasers, their minimal intrusiveness, and broader fundamental application space when compared to seeded measurements, these measurements are becoming more common. As such, molecular-based scattering diagnostics continue to evolve, improving accuracy, uncertainty, and applicability so they may be used as substitutes and/or supplements to their more intrusive counterparts.

When looking for a genuinely non-intrusive internal flow distortion measurement the options are limited, but one method shows promise. Filtered Rayleigh scattering (FRS), first introduced by Miles, Forkey, and Lempert [22, 23, 24, 36], was first demonstrated as a diagnostic for supersonic and hypersonic flows. In 1996, Forkey et al. [22] presented the accuracy of measurements made in a Mach 2 jet where estimated measurement uncertainties of three percent in velocity, two percent in temperature, and five percent in pressure. With these types of uncertainty values in its infancy as an established technique, the measurement showed great promise for accurate future flow quantification measurement.

2.2 Rayleigh Scattering Flow Diagnostics

The following sub-sections are intended to provide the background necessary to understand Rayleigh scattering, how it depends on various flow properties of interest, what considerations need to be taken into account when planning to measure it, and the various diagnostic techniques that can be used to measure flow properties by leveraging the characteristics of Rayleigh scattering. This material is presented to the reader in the presentation and discussion of past and current works.

This is primarily because the behavior of these particles in mass inherently carries highly desirable information about the flow state. Additionally, measuring this interaction directly allows measurements to be made without adding additional particles or seed gasses into the flow, increasing the non-intrusive nature of the measurement.

2.2.1 Rayleigh Scattering

Rayleigh scattering, first described by Lord Rayleigh in the late 19th century [50, 51, 58, 59, 60], is the result of the interaction of an electromagnetic wave with a wavelength λ, with a particle, the diameter of which is much smaller than λ [13, 57]. While Rayleigh scattering theory applies to any particle when the non-dimensional scattering size parameter, $x = \pi a/\lambda$, where a is the radius of the particle, is much smaller than one [13], this section will primarily focus of the interaction of monochromatic, polarized, laser light with molecular gasses, which carry information about the state of the gas, and affect the scattered light.

Molecular light scattering as a result of single-frequency laser illumination is described by Miles et al.[37] for molecular nitrogen near atmospheric conditions. This interaction results in various scattering phenomena. The scattering that occurs the furthest away from the

incident illumination is vibrational Raman scattering, which is observed to occur on the order of hundreds or thousands of wavenumbers away. Closer to the incident illumination are the rotational Raman bands, which consist of a series of lines associated with rotational transitions. The central scattering feature, occurring closest to the incident illumination, is related to elastic scattering and has features indicative of the translational motion of the particles [37]. The features associated with the translational motion are typically referred to as Cabannes lines [68].

The characteristics of this central scattering feature vary depending on the properties of the molecular gas. The gas is at the hydrodynamic limit at high pressures and/or low temperatures, and collisions dominate the particle motion. This results in a central Loentzian peak with two Lorentzian side bands Doppler shifted according to the speed of sound in the gas. Thermal motion dominates at low pressures and/or high temperatures, known as the Knudsen regime, and the lineshape becomes Gaussian in shape [37]. Most applicable to the present work, laser light scattering near 532 nm in air near atmospheric conditions is considered in the intermediate or kinetic regime where neither of the effects mentioned above dominates. In this regime, the scattered line profile displays characteristics of both thermal broadening and acoustic collisional effects. The behavior of the Cabannes lines is modeled using the Tenti S6 lineshape model [62] for conditions that satisfy the conditions for the Knudsen, hydrodynamic, and kinetic regimes in Figure 2.1.

Since the Cabannes lines depend on the translational motion of the particles, resolving these features allows for the measurement of velocity, temperature, density, and pressure. However, when molecularly scattered light is collected by an unfiltered imaging system, the measured signal includes contributions from all of these components. Vibrational Raman scattering only contributes approximately 0.1% of the total intensity, so it is typically neglected [37]. Because rotational Raman scattering occurs so close to the Cabannes lines, it is difficult to

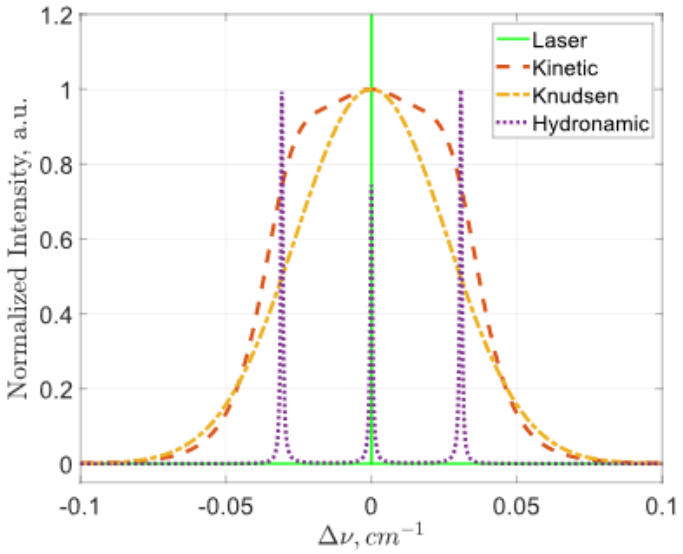

Figure 2.1: Rayleigh scattering lineshapes modeled for conditions that satisfy the kinetic, Knudsen, and hydrodynamic regimes.

filter out without significantly decreasing the intensity of the Cabannes lines, so it is typically included in these measurements.

Since the intensity of Rayleigh scattering is linearly proportional to the number density of the gas, density measurements can be made with a simple imaging system with no advanced filtering. As will be discussed later on, Rayleigh scattering can be dominated by the scattering from small particles such as dust and condensing gasses in the flow, so special care must be taken to ensure these contaminating particles are not present. If not, specialized filters are required. If pressure is known for these measurements, the temperature can also be calculated using the ideal gas law [46]. This method has been used to study the decay rate of subsonic turbulent free jets [53] and to characterize shock structure and shock-vortex interaction in supersonic jets [44].

Measurement of velocity and temperature using Rayleigh scattering requires that the spectral lineshape and its central wavenumber be known with respect to static conditions. Molecules

in motion, whether a result of individual particle motion or bulk fluid motion, impart a Doppler frequency shift of the scattered light according to the Doppler shift equation, shown in Equation 2.1, where $\hat{o}$ is the unit vector that points from the origin of the scattering to the observer, $\hat{\imath}$ is the incident illumination unit vector that points along the direction of illumination propagation, and $\vec{V}$ is the vector velocity of the scattering medium.

$$\Delta\nu = \frac{(\hat{o} - \hat{\imath}) \cdot \vec{V}}{\lambda} \tag{2.1}$$

As discussed above, the Doppler shift imparted by particles in motion, whether an effect of thermal motion or the combination of thermal motion and acoustic effects, is observed as a broadened lineshape centered on the frequency of the monochromatic laser light incident on the volume. Furthermore, this broadened lineshape is shifted away from being centered on the incident laser frequency when the gas is in bulk motion, according to Equation 2.1. Particle-particle interactions rarely occur for gasses in the Knudsen regime, so particle motion is uncorrelated, resulting in a symmetric Gaussian distribution [37]. As pressure increases and/or temperature decreases, particle-particle interactions occur more often, and density fluctuations contribute to the lineshape. Since density fluctuations move at the speed of sound, acoustic side bands, known as Brillouin-Mandel'shtam scattering, located at a frequency shift associated with the speed of sound appear [37].

The characteristics necessary to non-intrusively measure density, temperature, and velocity have been outlined at this point. Summarizing the key attributes of Rayleigh scattering that make it attractive and valuable for measuring gaseous flows are detailed in [47] and [6] are presented as follows:

1. Rayleigh scattering occurs on molecular levels.

2. Rayleigh scattering, resulting from the interaction of light and matter, is elastic and no energy is transferred.

3. The yield of scattered light is proportional to the number density for a gas of constant composition.

4. Light scattered off matter in motion is Doppler shifted in frequency proportional to the velocity of the matter.

5. In a stagnant gas, individual molecules are always in motion, resulting in a Doppler broadened spectrum, centered on the incident laser frequency, and a distribution related to the motion of the particles.

While density may be measured without resolving the RBS lineshape in the frequency domain, temperature and velocity measurement requires it. Three primary methods have been used to resolve the RBS lineshape in the frequency domain. The first of these methods is the utilization of the Fabry-Perot etalon, which allows for the direct observation of the RBS lineshape. The second method requires a very narrow notch filter, typically a molecular absorption cell, and a tuneable laser source. The final method and most recent development is the utilization of a virtually imaged phased array (VIPA) based spectrometer to resolve the RBS lineshape in the frequency domain.

The Fabry-Perot etalon is the conventional tool used to resolve the RBS lineshape and consists of two reflective planar mirrors facing one another that are spaced very precisely. As the separation between the mirrors changes, different frequency intervals can pass through the etalon, allowing the RBS spectrum to be measured directly. This measurement technique is usually referred to as interferometric Rayleigh Scattering (IRS). The downside of this method is that the measurement is typically limited to a point. Previous works have demonstrated its utility in its use to provide snapshot field measurements of temperature and

velocity [55], for temporally resolved velocity measurements in supersonic flow environments [5, 19], temporally resolved multi-property measurements in high-speed flow environments [14].

Similar to the Fabry-Perot interferometer, VIPA-based spectrometers have been recently introduced to determine velocity and temperature along a one-dimensional line [30, 33, 61, 67].

The final method that will be discussed to resolve the RBS lineshape in the frequency domain is the application of narrow linewidth notch filters. For this application, atomic and molecular filters provide an attractive alternative to measuring RBS lineshape characteristics [37]. For laser illumination near 532 nm, a molecular iodine filter with sufficient optical thickness provides sharp transitions between high transmission and absorption regions. By tuning the illumination laser frequency across these transitions, the characteristics of the underlying RBS lineshape can be extracted by comparing the measured signal to the signal predicted using models. The measurement of Rayleigh scattering while employing filters of this type is known as filtered Rayleigh scattering (FRS) [23].

There are several benefits to employing molecular absorption filters to measure the characteristics of Rayleigh scattering. The first, as discussed above, is the ability to resolve RBS lineshape-derived intensity spectra in the frequency domain by tuning the incident laser frequency. The optical configuration for FRS measurements is also more straightforward because it only requires the scattered light to pass through the absorption cell before being imaged by the sensors. Additionally, this allows for the simultaneous measurement of Rayleigh scattered light from a two-dimensional plane instead of a multi-point zero-dimensional or one-dimensional simultaneous measurement available to the conventional and VIPA-based IRS methods discussed above. Finally, one of the most important benefits of implementing the molecular filter is the ability to filter out contaminating light from Mie and geometric

scattering.

2.2.2 Models used in Filtered Rayleigh scattering

While analytical approximations exist for the Knudsen and hydrodynamic regimes, accurate approximations do not exist for the kinetic regime. Currently regarded as the most accurate representation of the Rayleigh scattering lineshape for diatomic gasses in the kinetic regime, the Tenti S6 developed by Tenti et al. [62] may be used to model the Rayleigh-Brillouin scattering (RBS) lineshape. This model has been experimentally validated by [35] over a temperature range of 300 K to 2400 K with a less than 4% difference. The downside of this model is that it requires the solution to a set of six linear equations, which is relatively expensive computationally.

Many researchers have successfully been able to model the behavior of the RBS lineshape in the kinetic regime more efficiently. Still, these are typically associated with limits on where it can be applied or the model sacrifices accuracy. One example is the analytical model in Witschas [66], which has been shown to calculate the RBS lineshape with errors smaller than 0.85% more efficiently but is applicable only when the ratio of the acoustic wavelength to the mean free path is between 0 and 1.027. A machine learning-based approach, developed for the optimization of experiment design, is presented in Hunt et al. 2020 [28] is noted by Powers 2023 [47] to be four orders of magnitude faster than the Tenti S6 model with less than 1% error.

As noted above, molecular iodine is used as the narrow linewidth notch filter in filtered Rayleigh scattering. The model used to predict the iodine transmission as a function of cell length and vapor pressure is described by Forkey et al. [25]. This work describes the corrected and calibrated behavior of the iodine absorption model for wavelengths near 532nm.

2.3 Summary

This chapter was intended to provide a brief overview of the main concepts relevant to the development and advancements presented in the current work. CFD flow validation experiments require that the uncertainty and bias errors in both measurements used to validate the CFD flow solution and the CFD flow solution itself be quantified to truly understand the performance of the models and numerical methods used to evaluate the flow. In addition, conventional measurements of surface static pressure and force and moment characteristics, while helpful in validating the high-level SRQs, are insufficient to validate the CFD solutions as such non-intrusive optical diagnostics are required to provide additional information about the flow. While seeded optical diagnostic techniques offer crucial information about the flow, filtered Rayleigh scattering is the only technique proven to provide non-intrusive, simultaneous measurement of vector velocity, temperature, and density across a two-dimensional plane in internal flow environments, making it a desirable measurement for flow quantification and CFD validation measurements.

Chapter 3

FRS Measurement Uncertainties In the Presence of Signal Contamination

The contents included in Section 3.1 of this chapter were published by invitation in the journal Measurement Science and Technology as "Boyda M.T., Byun G., Lowe K.T. (2019) Investigation of velocity and temperature measurement sensitivities in cross-correlation filtered Rayleigh scattering, *Measurement Science and Technology*, **30** 044004;" and has been reproduced here with the permission of IOP Publishing Ltd.

Significant portions were previously presented as "Boyda M.T., Byun G.B., Lowe K.T. (2019) Cross-Correlation Filtered Rayleigh Scattering (CCFRS), In *Proceedings of the 19th International Symposium on the Application of Laser and Imaging Techniques to Fluid Mechanics*, 2018."

Also included in Section 3.2 of this chapter is a conference proceeding presented as "Boyda M.T., Byun G.B., Saltzman A.S., Lowe K.T. (2020) Effect of Mie and Geometric Scattering on Temperature and Density Measurements using Filtered Rayleigh Scattering, *AIAA SciTech Forum 2020*;" and has been reproduced here with permission of the American Institute of Aeronautics and Astronautics, Inc.

The primary objective of this chapter is to present the uncertainties associated with conventional planar FRS measurements, introduce the effects Mie scattering on the convolution

spectrum and present the uncertainties that result from adapting evaluation methods to overcome the presence of signal contamination.

3.1 Velocity and Temperature Measurement Uncertainty

IOP Publishing Measurement Science and Technology
Meas. Sci. Technol. **30** (2019) 044004 (15pp) https://doi.org/10.1088/1361-6501/ab0350

Investigation of velocity and temperature measurement sensitivities in cross-correlation filtered Rayleigh scattering (CCFRS)

M Boyda, G Byun and K T Lowe[1]

Kevin T. Crofton Department of Aerospace and Ocean Engineering, Virginia Tech, Blacksburg, VA, United States of America

E-mail: kelowe@vt.edu

Received 14 November 2018, revised 4 January 2019
Accepted for publication 30 January 2019
Published 7 March 2019

Abstract

The cross-correlation filtered Rayleigh scattering method is presented for planar measurements of time-averaged velocity, temperature, density, and pressure using laser scanning, Rayleigh scattering, and cross-correlation-based signal processing. Of particular note, the methods and analyses presented show that velocity and temperature measurements are obtainable at acceptable uncertainties for many aerodynamic applications with or without particles present. In the current work, velocity and temperature measurement uncertainties for this method are analysed by Monte Carlo simulations and evaluation of the Cramér–Rao lower bounds for the signals generated in this approach with aerodynamic applications in mind. A key aspect considered is the relative strength of Rayleigh (molecular) scattering and Mie (particle) scattering contributions to the simulated flow signal. Compared to particle-based velocity estimation, the effects due to convolution between the molecular filter and the broadband Rayleigh scattering spectrum are found to increase the estimator variance of the velocity. For given flow conditions, the velocity error associated with the signal processing routine with noise-free signals is found to be less than $\pm 2.5\,\mathrm{m\,s^{-1}}$, and bias error associated with discrete sampling in the laser frequency domain is within $\pm 1.5\,\mathrm{m\,s^{-1}}$. For these same conditions, temperature measurement simulations indicate bias error bounds of $\pm 0.014\%$ with random uncertainty bounds of less than $\pm 1.4\%$ for a signal with no Mie scattering contribution, and bias error bounds of less than $\pm 0.14\%$ with random uncertainty bounds of less than $\pm 3.2\%$ for flows contaminated with Mie scattering sources at a signal-to-noise ratio of 25 dB or greater. This technique is also being further developed to measure density and pressure using the principles of laser Rayleigh scattering in flows containing particles of unknown sizes and concentrations.

Keywords: filtered Rayleigh scattering, velocimetery, flow measurement, temperature measurement, Doppler velocimetry

(Some figures may appear in colour only in the online journal)

[1] Author to whom any correspondence should be addressed.

1. Introduction

Many applications could benefit from robust, minimally intrusive velocimetry and multi-scalar diagnostics, particularly for *in situ* measurements in complex systems. For instance, in propulsion research at Virginia Tech, particle image velocimetry (PIV) has been applied to study propulsion/airframe integration involving complex vortical flows in turbofan engine inlets [1–3]. Frequently, however, the particles required for PIV cannot be reliably or safely introduced, and seedless methods become the only alternative.

The Virginia Tech team has been developing a robust method for applying filtered Rayleigh scattering for mean measurements of vector velocity, temperature and pressure [4, 5]. While impressive results have been reported by other groups, notably Boguszko and Elliott [6] and Doll *et al* [7–9], the central new development reported here is a means of optimally interrogating the cross-correlation function between the incident laser transmission ratio (ratio of light intensity after passing an optical absorption cell to the intensity entering it) and Rayleigh-scattered, Doppler-shifted transmission ratio signal across a laser frequency scan up to 7 GHz in bandwidth. The work exhibits a novel, unified method for estimating velocity for flows with or without particles, while also providing an analysis of estimator bias and variance to the level of detail needed for determining uncertainties in aerodynamics applications. Further, this is the first study known to the authors in which a curve fit method for filtered Rayleigh scattering is systematically considered for the impact of Mie scattering on temperature estimator performance, an important step for improving the robustness of FRS temperature measurements in aerodynamic applications. The so-called cross-correlation Doppler global velocimetry (CCDGV) technique [10] is closely related and has been shown to provide low uncertainties [11] over a nearly unlimited dynamic range of flow velocities [12]. In the current work, the fundamental aspects of extending the CCDGV concept to cross-correlation filtered Rayleigh scattering (CCFRS) are to be discussed.

2. Rayleigh scattering and CCFRS method

Rayleigh scattering is a wave optics phenomenon resulting from the interaction of light and matter on the scale of, or smaller than, the wavelength of the laser light. We here summarize the key attributes of the Rayleigh scattering signal (e.g. [13], see also figure 1).

(1) It is elastic: no net energy transfer between photon and matter.
(2) It occurs down to molecular levels.
(3) The probability of scattering increases with number of molecules per volume.
(4) Even stagnant gas molecules are constantly moving—as described by the kinetic theory of gases—and impart a Doppler shift related to temperature.
(5) Molecules have bulk motion in a flow and impart a directional Doppler frequency shift.

Items 3–5 yield the measurement principles, namely that one may directly measure density (3) and temperature (4) to determine static pressure from a state equation, while the mean Doppler-shifted signal yields flow velocity. These effects are all observed by making use of a molecular absorption filter, in our case iodine vapor in an optical cell, typically in a setup such as shown in figure 2. In this setup we use a continuous wave (CW) laser that is split into two paths, the reference (upper) and measurement (right) paths. The reference path is used to monitor the incident laser frequency and for comparison with the frequency of the light scattered from the flow region (yellow arrow).

The CCDGV method described by Cadel and Lowe [10] provides a framework for processing the data obtained from every pixel of the cameras used to image the flow field (see figure 3). A pair of transmission signals—the variation of transmission with laser frequency through an iodine cell—is depicted in panel A of figure 3, one for the reference signal of the laser before entering the flow and another for the signal received from scattering in the flow. The scattered light absorption spectrum at each point will be Doppler-shifted, resulting in frequency displacement of the absorption features, as depicted in figure 3, panel A. To process these measurements, the signal at a given pixel is mean-subtracted to obtain S_{Signal} which is cross-correlated with the mean-subtracted reference transmission signal, $S_{\text{reference}}$, over the range of the laser frequency scan (figure 3, panel B):

$$R(\nu_i) = \frac{1}{\sigma_{S_{\text{Signal}}}\sigma_{S_{\text{Reference}}}} \times \sum_{i=1}^{N} S_{\text{Signal}}(\nu_i) S_{\text{Reference}}(\eta_i - \nu_i) \quad (1)$$

where $R(\nu_i)$ is the value of the cross-correlation coefficient for a set of discrete frequency values ν_i and frequency shift values, η_i, while $\sigma_{S_{\text{Signal}}}$ and $\sigma_{S_{\text{Reference}}}$ are the standard deviations of the scattered-light signal and reference transmissions, respectively. For Doppler velocity measurements, the correlation values around the peak are curve fit to find the Doppler frequency shift (figure 3, panel C). Three velocity component measurements ($\vec{V}$) are possible using the Doppler equation, $f_{\text{D}} = \frac{(\hat{o}-\hat{\imath})}{\lambda} \cdot \vec{V}$, where $\hat{o}$ is the unit vector pointing from the measurement point in the flow to the detector, $\hat{\imath}$ is the unit vector of the laser propagation direction, and λ is the wavelength of the laser light. Three independent measurement directions are used to obtain a vector velocity measurement (e.g. [14]).

3. Signal simulation of CCFRS method

To extend the technique beyond Doppler velocity measurements, we note that the signal received is a convolution of the molecular filter transmission spectrum and the scattered light spectrum, made up of the summation of particle Mie scattering and molecular Rayleigh scattering spectra (see figure 1, lower panels),

$$S_{\text{Signal}}(\nu) = S_{\text{Mie+Rayleigh}} \otimes T_{\text{iodine}} = \int_{-\infty}^{\infty} S_{\text{Mie+Rayleigh}}(\nu - \eta)\, T_{\text{iodine}}(\eta)\, \mathrm{d}\eta \quad (2)$$

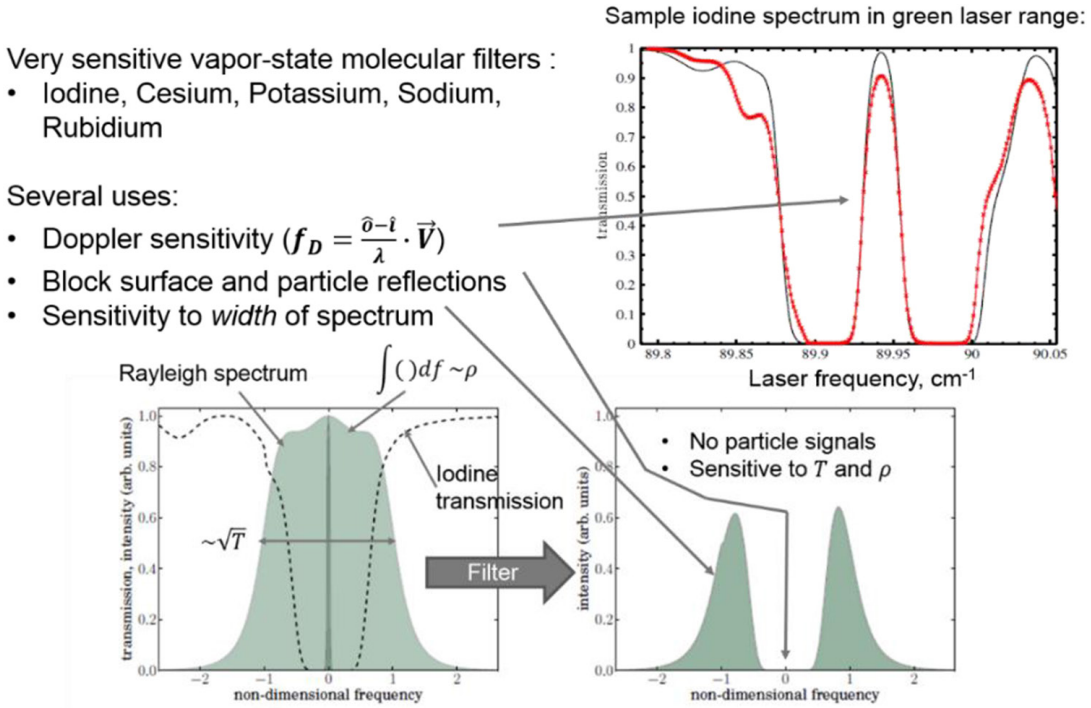

Figure 1. Some attributes of filtered Rayleigh scattering principles. The figure in the top right shows an example of a measured iodine vapor cell transmission profile (red) and the analytical model used for comparison (black).

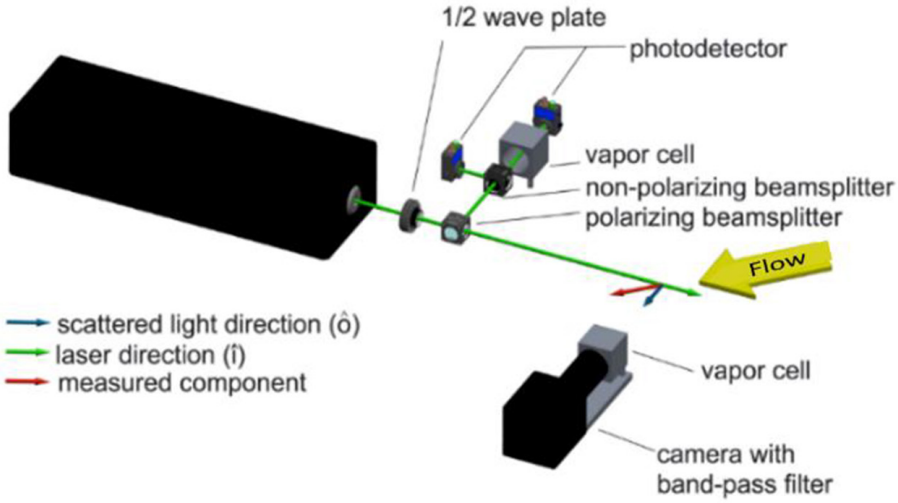

Figure 2. Laser, reference vapor cell, and flow detector vapor cell arrangement for vapor absorption cell-filtered measurements. Reprinted from [10], Copyright (2015), with permission from Elsevier.

where $S_{\text{Mie+Rayleigh}}$ is the summed Mie and Rayleigh spectra centred around the incident laser frequency when observed in a medium with no bulk velocity and T_{iodine} is the transmission spectrum of the iodine cell. Figure 4 shows example images that result from summed Mie and Rayleigh scattering in a free jet viewed through an iodine filter. When the laser frequency is set to correspond to a high transmission region of the iodine transmission spectrum (figure 4(a)), Mie- and Rayleigh-scattered light is observed from both the slow moving air in the ambient region and the high speed jet region. When the laser is tuned to a highly absorptive region of the iodine spectrum (figure 4(b)), the Mie-scattered light from the ambient region is absorbed after passing through the iodine cell. The scattered light signal from the high speed flow within the jet is Doppler shifted such that more light is transmitted through the iodine cell from this region, appearing slightly brighter in the region of the jet. While the particle signals are filtered outside the jet region, the laser beam is still visible due to the broadened Rayleigh scattering signal that is transmitted. Mielke *et al* [15] reported point-wise measurements of time-averaged velocity,

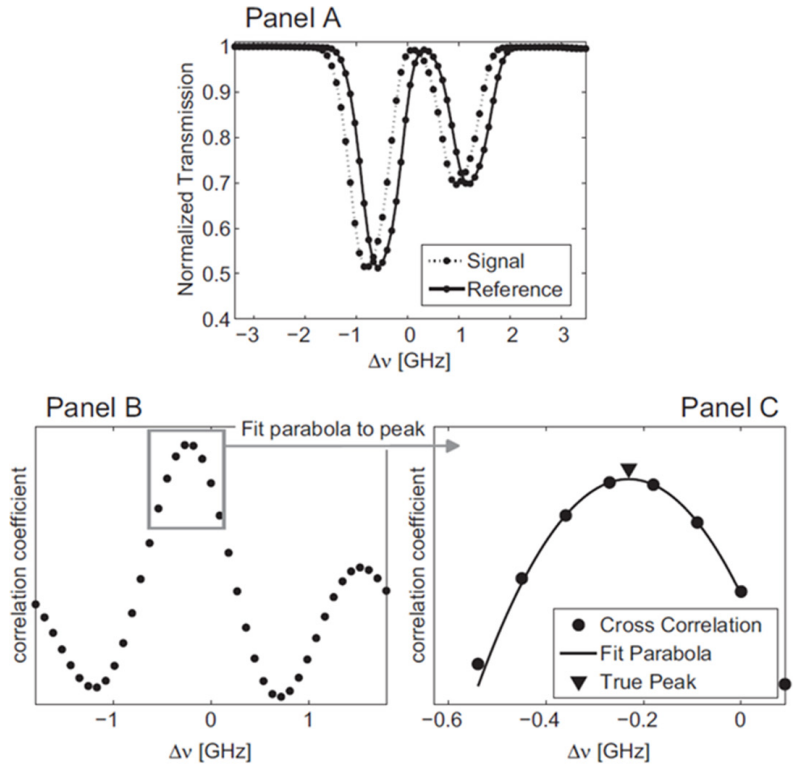

Figure 3. Cross-correlation signal processing for CCDGV. Panel A: Flow signal and reference transmissions are acquired as a function of laser frequency. Panel B: Flow signal and reference transmissions are cross-correlated. Panel C: The peak cross-correlation value is interpolated to find the precise Doppler frequency shift. Reprinted from [10], Copyright (2015), with permission from Elsevier.

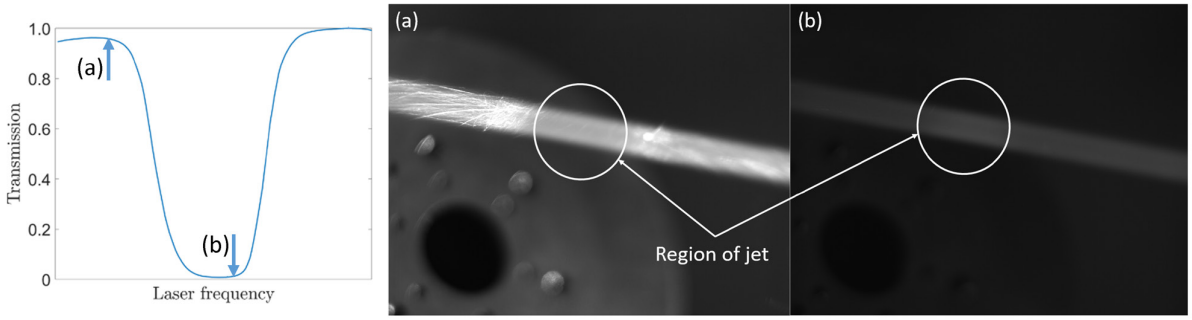

Figure 4. Sample images obtained using filtered Rayleigh and Mie scattering in a free jet. Left: Transmission spectrum showing frequencies and transmissions at which images (a) and (b) are obtained.

temperature and density in sparsely seeded flows using Mie and Rayleigh scattering. It is worth noting, in contrast to the single-point technique of [15], that the presented CCFRS enables planar measurements for flow velocity, temperature and density with high spatial resolution. The flow-scattered Mie and Rayleigh spectrum is shifted via the laser scanning already described to obtain the sufficient range of the convolution from equation (2). Since $S_{\text{Mie+Rayleigh}}$ contains velocity, temperature and density (and, thereby, pressure as well) information, the convolution signal of equation (2), also contains this information. A measurement is obtained by scanning the laser frequency through a deeply absorbing feature of the iodine spectrum (a transmission trough) to obtain the properties of the Rayleigh spectrum.

3.1. Velocity estimation

One of the most attractive features of the CCFRS is to measure velocities of seedless flow. The Cramér–Rao lower bounds (CRLB) was determined by the method presented by Fischer *et al* [16] and Monte Carlo simulations have been performed using the same procedure previously applied to CCDGV technique and described at length in [11]. The signal model $S(f)$,

$$S(f) = \text{QE}\, n_s \tau(f) / \text{AD} \tag{3}$$

is a function of the number of scattered photons (n_s), the quantum efficiency of sensor (QE), the iodine vapor cell transmission function, $\tau(f)$ at the laser frequency, f, and the analog-to-digital conversion factor (AD).

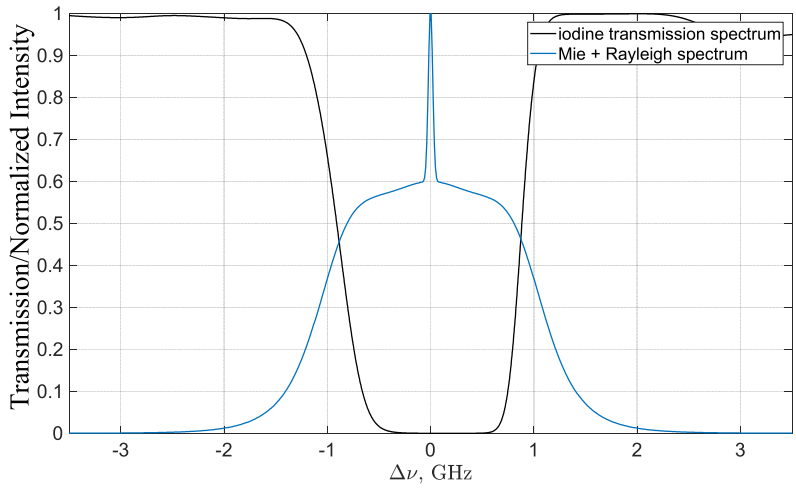

Figure 5. Normalized Mie and Rayleigh scattering intensity spectrum (peak intensity ratio = 0.6) and iodine cell (1 torr and 65 °C) transmission spectrum.

There are two noise sources considered for the CRLB, shot noise with Poisson distribution and electronic detector noise with Gaussian distribution. The number of scattered photons (n_s) needs to be changed as Rayleigh and Mie scattering contributions are combined due to light scattered by small (low sub-μm diameter) particles naturally exist in most practical aerodynamics applications, even those that are not intentionally seeded with particles. Therefore, the range $10^2 \leqslant n_s \leqslant 10^{4.7}$ was considered for the signal simulations. The CRLB analysis, which yields estimator variance, previously presented by Fischer *et al* [16] has been adapted for the current FRS application:

$$\mathrm{CRLB}(U)_{\mathrm{Poisson}} = \frac{\lambda^2}{\mathrm{QE}}\frac{1}{n_s} \times \frac{\sum_{k=0}^{N-1}\tau(f_k)}{\sum_{k=0}^{N-1}\frac{\tau'(f_k)^2}{\tau(f_k)}\sum_{k=0}^{N-1}\tau(f_k)-\left(\sum_{k=0}^{N-1}\tau'(f_k)\right)^2}$$

$$\mathrm{CRLB}(U)_{\mathrm{Gaussian}} = \frac{\lambda^2}{\mathrm{QE}^2}\frac{\sigma_{\mathrm{ne}}^2}{n_s^2} \times \frac{\sum_{k=0}^{N-1}\tau(f_k)}{\left(\sum_{k=0}^{N-1}\tau(f_k)^2\right)\left(\sum_{k=0}^{N-1}\tau'(f_k)^2\right)-\left(\sum_{k=0}^{N-1}\tau(f_k)\tau'(f_k)\right)^2}$$

$$\mathrm{CRLU}(U) = \mathrm{CRLB}(U)_{\mathrm{Poisson}} + \mathrm{CRLB}(U)_{\mathrm{Gaussian}} \quad (4)$$

where $\tau(f)$ is the normalized transmission of the iodine vapour cell as a function of laser frequency at index k and $\tau'(f)$ is its slope. N is the number of frequency scanning samples (101 samples were used for the current simulation). σ_{ne}^2 and λ are the variance of the electrical signal of photodetectors and the laser wavelength, respectively. Note that the CRLB directly depends on the transmission function and for the current simulation, $\tau(f)$ is the convolution of iodine transmission spectrum and combined Mie and Rayleigh scattering spectrum, which is described in the following section. Final velocity calculations were obtained using a sensitivity vector $(\hat{o} - \hat{\imath})$, as depicted in figure 2.

The Monte Carlo simulation was performed with noise-added synthetic signals (Mie + Rayleigh) in the signal-to-noise ratio (SNR) range $8\,\mathrm{dB} \leqslant \mathrm{SNR} \leqslant 41\,\mathrm{dB}$, where $\mathrm{SNR} = 10\log_{10}[\sigma_s^2/(\sigma_P^2 + \sigma_G^2)]$, σ_s^2 is the variance of the noise-free signal, σ_P^2 is the Poisson-distributed shot, and σ_G^2 is the Gaussian-distributed detector noise. σ_G^2 is computed using constant random noise added to signal and σ_P^2 is defined as the mean number of received photons without Gaussian noise [11]. The estimator variance for the signals and signal processing method used was computed using 10 000 Monte Carlo samples, while the laser frequency discretization bias error was computed using 1000 samples.

Table 1. Flow conditions for simulations.

Case	M	U, m s^{-1}	T, K	P, psi
a	0.4	137.1	293.6	19.1
b	0.7	232.6	275.7	15.4
c	1.9	493.3	168.3	2.8

The Mie scattering spectrum may be modelled with the Doppler-shifted laser centre frequency and a width according to the turbulence intensity. For the present simulation, the Mie scattering spectrum has been modelled with 100 MHz width (5% to 18% turbulence intensity for the present flow conditions) and maximum intensity peak ratio (PR) to Rayleigh scattering intensity peak to account the existence of natural particles in facilities. For example, PR = 0.001 denotes the Mie spectrum peak of 1000 × Rayleigh spectrum peak. For the signal simulation of CCFRS, the model due to Forkey *et al* [17] was used for the iodine vapor cell transmission spectrum, while the model due to Tenti *et al* and improved by Pan *et al* [18, 19], commonly referred as the Tenti S6 model, was used for the Rayleigh scattering spectrum for air at the conditions of interest. The resulting normalized signals as modelled for Mie and Rayleigh scattering intensity and iodine cell transmission are presented in figure 5.

As the Rayleigh scattering depends on pressure and temperature, the simulations were performed for three different flow conditions of interest, as presented in table 1. Therefore, the present study will investigate the measurement capability of CCFRS for a wide range of flow conditions, representative of low and high speed wind tunnel conditions, for velocity,

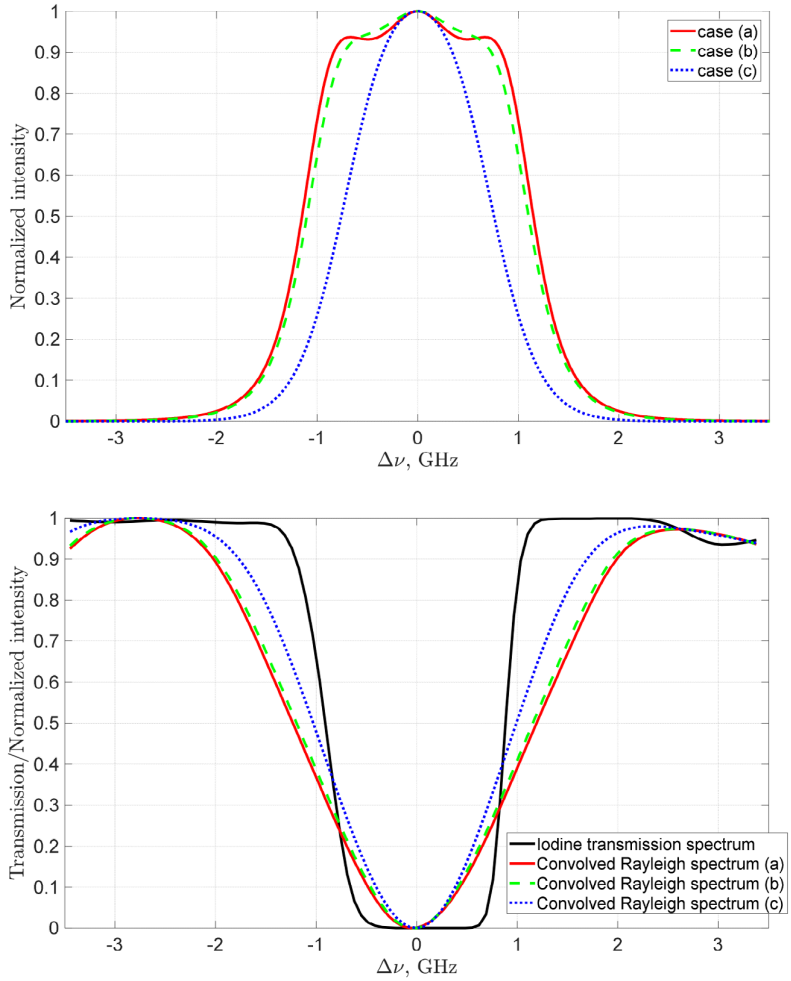

Figure 6. Rayleigh scattering spectrum (top) and its convolution with iodine transmission spectrum (bottom) for simulation conditions but with zero velocity for clarity.

temperature and pressure. Figure 6 shows the Rayleigh scattering spectra and their convolutions with the iodine transmission spectrum for the three simulated thermodynamic conditions but zero velocity. More details of the routine for the simulation are described by Cadel and Lowe [11].

As described earlier, the CCFRS leverages the cross-correlation of $S_{\text{reference}}$ and S_{signal} in order to obtain Doppler-shifted frequency and corresponding velocity (see figure 3). S_{signal} is the convolution of the transmission spectrum and Mie and Rayleigh scattering spectrum defined as equation (2). $S_{\text{reference}}$ is the un-shifted reference transmission spectrum. Figure 7 shows the transmission spectra of reference and convolved filtered signals. Note that there are two reference signals; iodine transmission reference and convolved reference of the iodine transmission and Mie + Rayleigh spectral lineshapes. As the result of convolution, the shape of a measured transmission spectrum is different from that of the iodine transmission reference. This is due to the much wider bandwidth of the Rayleigh lineshape. This difference causes significant bias errors in velocity estimated by the cross-correlation scheme when using the measured spectrum and the iodine transmission reference. Therefore, the identical convolution is applied to iodine transmission reference and the Mie + Rayleigh lineshapes, which is termed the 'convolved reference'. Note that the Tenti S6 model was used for the Rayleigh spectrum in the convolved reference.

For the cross-correlation, various schemes have been considered to minimize bias errors, and the final scheme is optimized by selecting the number of points in the 'convolved reference' around its centre frequency. As mentioned by Cadel and Lowe [11], the number of points in 'convolved reference' need to be enough to present the complete trough region and the resulting characteristics of the transmission spectrum. For the correlation peak finding interpolation, it is observed that the centroid interpolation generates greater error than the parabolic fitting.

3.2. Temperature estimation

The ability to measure temperature and pressure using scanning methods of FRS has been demonstrated from past work (e.g. [6–9]). The current effort, which includes work beyond the scope of this paper, seeks to extend the past findings in these references to allow scalar measurement of temperature,

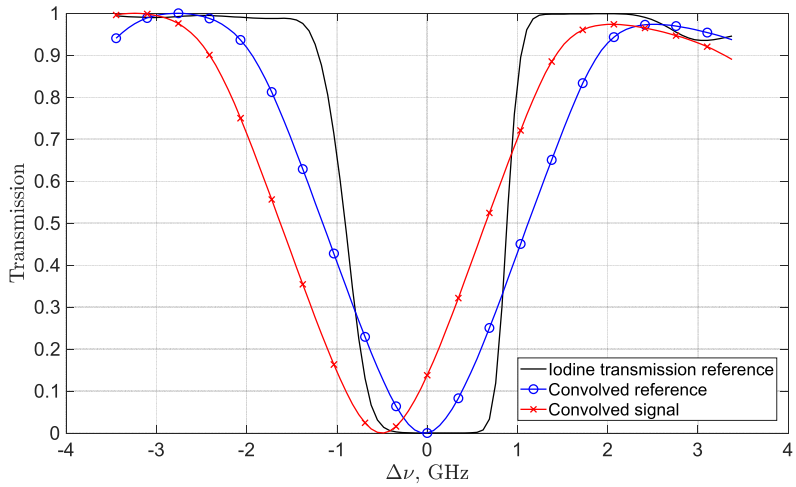

Figure 7. Normalized spectra for cross-correlations; iodine transmission reference (-), convolution of the iodine transmission reference spectrum and unshifted Rayleigh spectrum (o), and convolved signal of iodine transmission reference and Doppler shifted Rayleigh spectrum (×).

density, and pressure even in the presence of particles in the flow of unknown size and concentration levels.

Given the broad bandwidth of the frequency scan used, measurements of the Doppler-shifted trough will be available at all points within the flow, and a local frequency/transmission fit is necessary for each point in order to determine temperature. Clearly, the information content of such an approach is lower than a scan of the full transmission trough bandwidth, but the prospect of applications in harsh environments containing unknown particle sizes and concentrations could enable spatially resolved measurements in situations only accessible to intrusive physical sensors in the past.

Towards achieving these measurement capabilities, signal simulations have been conducted to determine the precision of a least-squares curve fitting algorithm developed to fit measured spectral data for local static temperature values in the flow. These simulations were conducted for two different scattering cases and the three different flow scenarios presented above for velocity determination (table 1).

The first of the two different scattering cases investigated was a signal generated only from Rayleigh scattering, where the convolution spectrum over the entire available bandwidth $(-3.45\,\text{GHz} \leqslant \Delta\nu \leqslant 3.45\,\text{GHz})$ was discretized into 100 scan points and used to fit for temperature. This analysis is used as an ideal case as a benchmark for accuracy and precision for the least-squares fit temperature estimator.

The second scattering case used in this analysis was a Rayleigh scattering signal contaminated with Mie scattering such that the PR was 0.01. This scattering scenario is, thus, presented to model the flow typically observed in experimental measurements where a significant portion of the collected light is a result of Mie scattering from particles present in the facility. For this case, only a small portion of the convolution spectrum, $(\Delta\nu = -0.24\,\text{to}\,0.57\,\text{GHz})$ discretized into 50 points, was used to fit for temperature estimation.

The number of discretization points in both cases were chosen based upon practical experimental concerns with

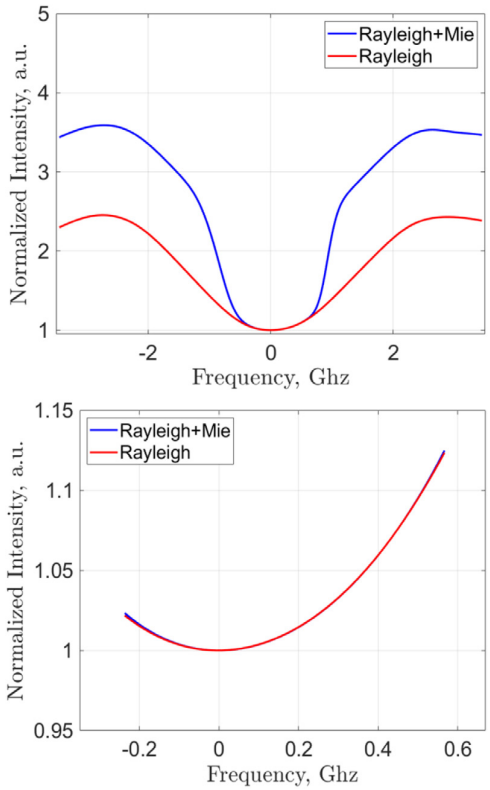

Figure 8. Normalized simulated signal convolution spectrums for the pure Rayleigh (red) and Rayleigh + Mie (blue) scattering cases used in the 100-sample full convolution scan (top) and the 50-sample partial scan signal simulations (bottom). These signal spectra are shown without noise for clarity.

sampling time. The specific frequency range chosen for the partial scan is determined considering the effects of Mie scattering signal contamination of the resulting convolution spectrum. It is shown in figure 8 that the optical density of the one Torr vapor pressure iodine filter over the chosen frequency

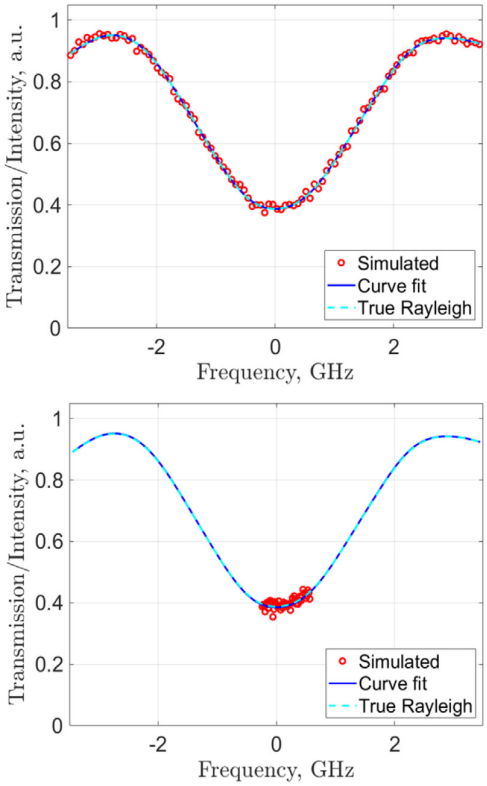

Figure 9. Normalized single shot simulation measurements shown for the 100-sample pure Rayleigh scan (top) and 50-sample Rayleigh + Mie scan (bottom) scattering cases shown at a SNR of 20 dB. For these measurements, the assigned static temperature was 293.6 K and the static temperature determined by the full scan was 293.4 K. Where the static temperature determined by the partial scan was 291.1 K.

range is high enough to provide filtering of Mie scattered light—the resulting convolution values are within 0.001 normalized intensity of the convolution resulting from the pure Rayleigh signal. Failure to properly select the frequency range so that the Mie-scattered light is adequately filtered will lead to bias errors in the measurement, tending toward lower temperatures due to the higher intensity values. To conduct the Monte Carlo simulations for the temperature estimator, a specific physical condition, corresponding to one of the flow cases presented in table 1, is applied to generate the analytical Rayleigh lineshape using the Tenti S6 model [18, 19]. This lineshape model is then convolved with the iodine transmission spectrum at a specified number of discretization points (in this case, 50 or 100) to create a noise-free convolution spectrum, according to equation (2). Noise is then added to the convolution spectrum in the form of random noise resulting from A/D conversion, background interference, and dark current, as well as shot noise resulting from the use of a 16-bit camera sensor, as described in section 3.1. Since the shot noise is a physical parameter based on the number of photons incident on the camera sensor, only the random noise is varied in these simulations. After the noise is applied to the convolution spectrum, the convolution spectrum is then normalized. Once this is complete, the least-squares curve fitting algorithm is applied to the convolution spectrum to estimate the flow temperature that was required to generate the spectrum. Figure 9 shows the results of a single shot measurement simulation for both scattering cases discussed. For these results, we used a SNR of 20 dB and set the static temperature at a constant 293.6 K, corresponding to simulation case (a). In this example, the full scan method was used to estimate a temperature of 293.4 K, while the partial scan method yielded a temperature estimate of 291.1 K. Anecdotally, this is the expected result for the comparison of these two cases, as the full scan has more points and more characteristics to help the algorithm fit the data properly. Statistical characterization of these results are presented in section 4.

The Monte Carlo simulations consisted of 1000 samples for each flow case at each SNR of interest. Convolution spectra were simulated at each of the three flow conditions (a, b, and c) and at SNR values of 10, 15, 20, 25, 30, and 35 dB. This study provides an evaluation of the temperature estimator precision over a range of SNR, for guidance on the SNR requirements for practical applications. In actual experiments, we would expect the signal to noise ratio to be 25 dB or higher. It is important to note that the least-squares search algorithm was not bounded in temperature, and results will show that the method robustly converges to proper values over the range of SNR studied. For the purposes of the temperature estimator study, it was assumed the velocity, pressure, and optical geometry (set at a constant 90° observation angle) were known to isolate the temperature estimator performance, although the algorithm for temperature and pressure estimation is developed and the result of temperature estimate does not change much while quite longer simulation time is required.

4. Results

To follow, analytical results from a theoretical analysis for the CRLB and Monte Carlo signal simulations are used to analyse the random estimator variance and bias errors associated with the CCFRS technique. The results for the velocity estimator are presented first before providing further results and discussions of the temperature estimator performance.

4.1. Velocity estimator results

To begin, consider the comparison of the effect of the reference signal choice, as depicted in figure 6 (bottom). In figure 10, it is shown that bias errors in velocity are smaller when using the iodine transmission spectrum convolved with the estimated Rayleigh scattering spectrum, generating less than 5% bias over the range of velocities and temperature of interest. Therefore, all results presented to follow are estimated using cross-correlation with the convolved reference transmission and five-point parabolic interpolation of the cross correlation function for the final Doppler frequency estimator.

The CRLB and simulation results of the velocity estimator variance (σ^2) are presented in figure 11, while the estimator efficiency results, CRLB/σ^2, are provided in figure 12 versus SNR. The SNR directly depends to the number of scattered

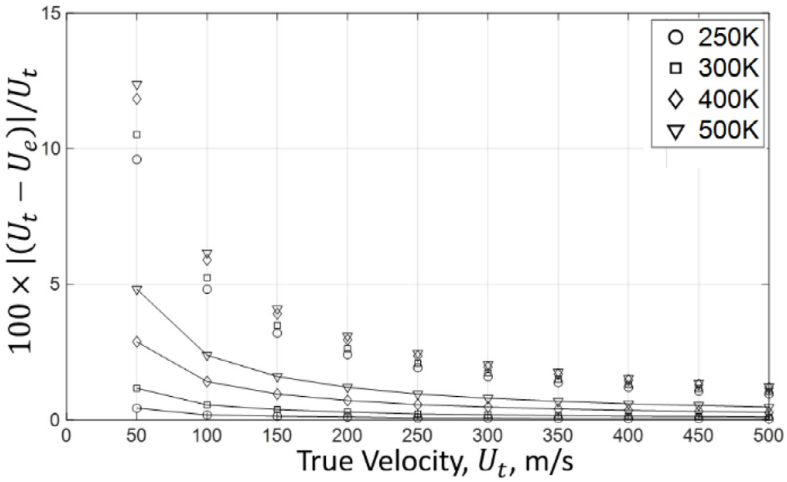

Figure 10. Estimated velocity error (%) using CCFRS noise-free signals at $P = 1$ atm and $250\,\mathrm{K} \leqslant T \leqslant 500\,\mathrm{K}$. Symbols without line: Cross-correlation of convolved signal and iodine reference transmission. Symbols with line: Cross-correlation of convolved signal and convolved reference. U_t and U_e denote 'true velocity' and 'estimated velocity', respectively.

photons. Note that the signals for simulations included Mie and Rayleigh spectra as shown in figure 5 accounting for some portion of the received photons being scattered by small particles. As mentioned earlier, the Mie scattering spectrum has been modelled up to its maximum intensity of 1000× (Rayleigh scattering intensity). For the simulation, the PR is considered in the range of 0.001–0.9. Note that the signal model in figure 5 is for PR = 0.6. Small changes in CRLB for three cases are observed since CRLB is directly dependent on the convolved transmission spectrum and its slope, which are presented in figure 6, and independent of frequency shift due to flow velocity, cross-correlation and peak finding process. The CRLB and variance decrease with increasing SNR and lower PR (higher Mie contribution). The Mie scattering effect on CRLB and variance are observed for PR $\leqslant$ 0.1, which shows that the velocity estimation is more accurate with lower PR The broadened transmission function, resulting from the convolution of Rayleigh dominant spectrum, is also observed to increase the variance of estimated velocity. Intuitively, the lower PR values will produce sharper peaks in the correlation function, improving the frequency estimation. For PR = 0.001, for which Mie scattering is most dominant, the CRLB shows a slightly different slope from other PR cases due to a major shift in the signal structure. This slope difference is primarily due to changes in the signal variance with PR, effectively changing the computed SNR for the same number of scattered photons. It is an artefact of the SNR definition and not thought to be significant.

All estimators are relatively efficient (figure 12) indicating that the processing makes good use of the available information, with realized variance values less than twice that predicted by the CRLB. The exception to this, again, is PR = 0.001 which is less efficient. As observed in CCDGV processing algorithm [11], the higher variance seems to be caused by the zero transmission at the centre frequency. While the minimum 5%–10% transmission has been recommended for CCDGV, note that the zero transmission is required for CCFRS to extract the information of temperature and density as well as velocity from Rayleigh spectrum.

Finally, the bias error associated with the discrete frequency step magnitude required for spectral sampling is estimated as the laser frequency is scanned with a specific frequency step for CCFRS measurements. Given this integral step size, interpolation of the Doppler frequency between samples should be assumed to have a bias dependent upon the Doppler frequency value relative to the sampled frequencies. Therefore, this analysis provides the bias error when the frequency shift caused by flow velocity is within the frequency scanning step size and it is dependent on the frequency scanning step size. The simulation is conducted only for the number of scattered photons of $10^{4.7}$ (i.e. the highest SNR case considered). The normalized bias error is presented in figure 13 for the three cases in table 1. Note that $(\nu - \nu_i)/\Delta\nu$ denotes the relative frequency shift, which is the frequency shift of the interpolated peak relative to the centred scan step size, and $\Delta U = \Delta\nu/\lambda$ is the velocity corresponding to the scan step size, $\Delta\nu$. According to CCDGV analysis [11], this error has a cyclical behaviour across the relative shift and it depends on transmission spectrum and its non-linearity line feature about the minima. For CCFRS, the similar cyclical trend is observed for higher Mie scattering contributions (PR = 0.05–0.001), while the error is nearly constant across the relative shift as higher Rayleigh scattering contribution. The mean bias is different for the three different flow conditions, and it can be misunderstood as an effect due to velocity magnitude. However, it is caused by the change of convolved transmission spectrum and its line shape at the trough for different flow conditions and Rayleigh/Mie contributions, rather than velocity magnitude since the signal spectrum depends upon temperature, pressure and PR. Its dependency seems greater in Rayleigh-dominant scattering as the convolved spectrum shape becomes almost identical to the iodine spectrum at PR = 0.001. The discretization

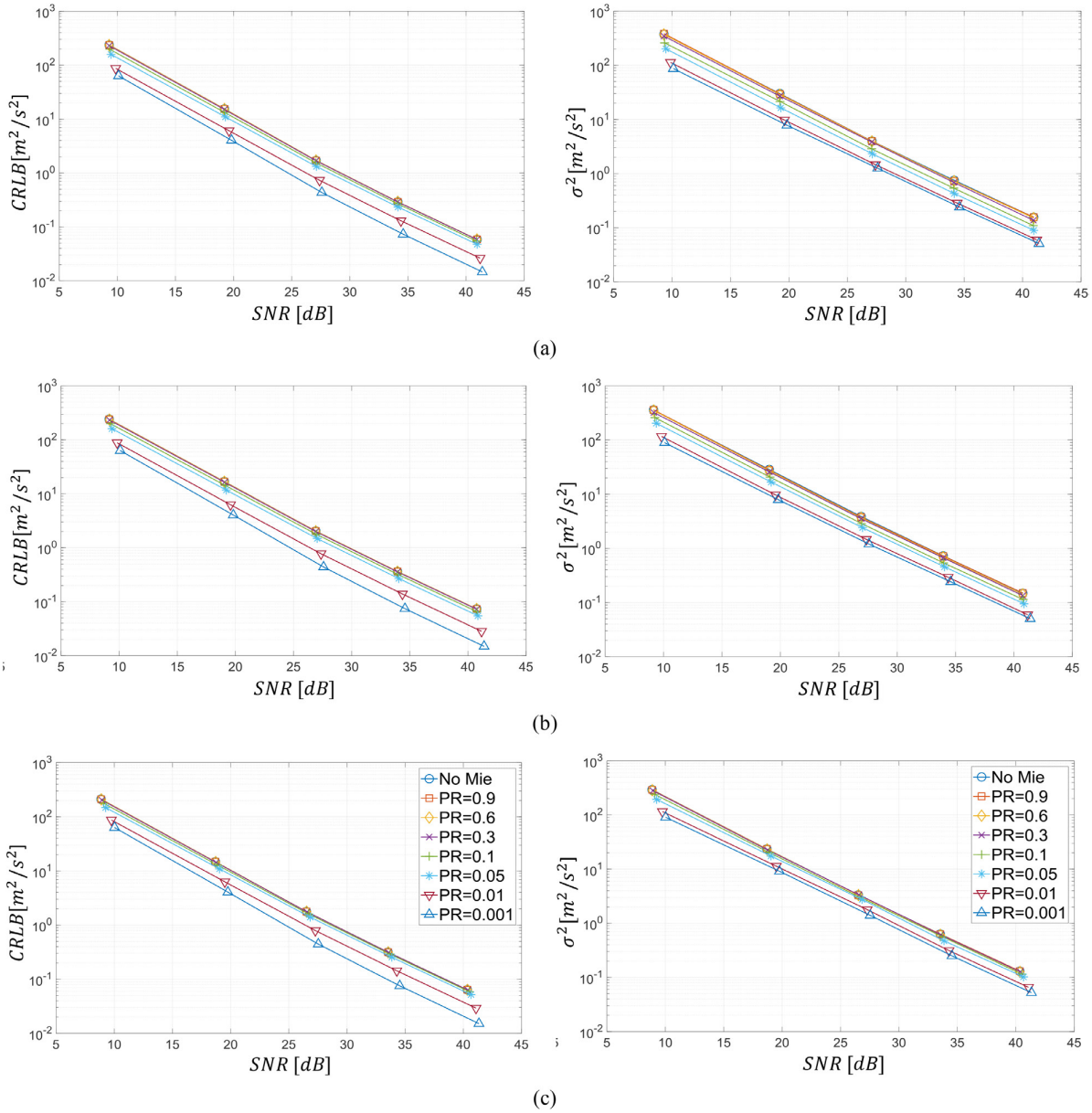

Figure 11. CRLB (left) and variance (σ^2) (right) for simulation cases, (a) $U_t = 137.1$ m s^{-1}, (b) $U_t = 232.6$ m s^{-1} and (c) U_t =493.3 m s^{-1}.

error is within $-4\% \leqslant (U_t - U_e)/\Delta U \leqslant 1\%$ (for our scales, within ± 1.5 m s^{-1}) for all simulated conditions. It is worthwhile to mention that the velocity uncertainties are absolute because the spectral characteristics of iodine transmission are independent of the velocity range.

4.2. Temperature estimator results

For the temperature simulations, bias errors were calculated using the mean estimated temperature value of all 1000 Monte Carlo samples. Estimator random error values, δ_T, were determined from the Monte Carlo simulations by finding the 95% confidence interval of the temperature estimations by evaluating $\delta_T = 1.96\sigma_T$. When using the entire scan spectrum (see figure 9 top, applicable only for PR = 1), the Monte Carlo simulations returned bias errors less than 0.014% for all simulated flow cases, while the bias errors resulting from the partial scan method (PR = 0.01, see figure 9 bottom) were less than 0.32% for all cases with an SNR of 20 dB or greater.

Note that the bias error does not decrease with SNR $\geqslant$ 20 dB in the partial scan. It might be the effect of Mie signal which may contaminate temperature information in Rayleigh signal. From this, it was determined SNR $\geqslant$ 20 dB are recommended for whenever particles are present in the flow. Below 20 dB,

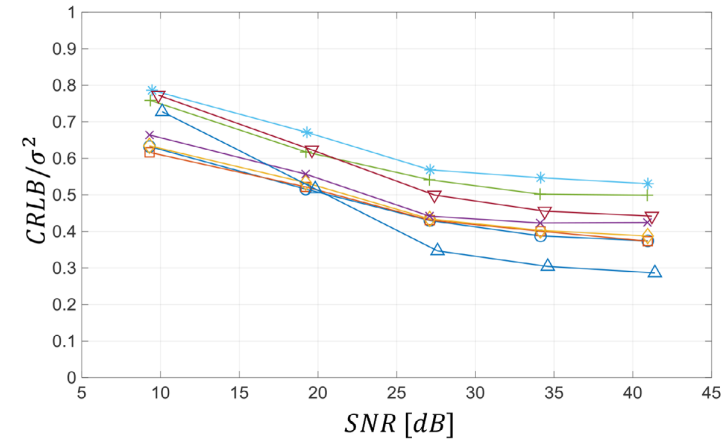

(a)

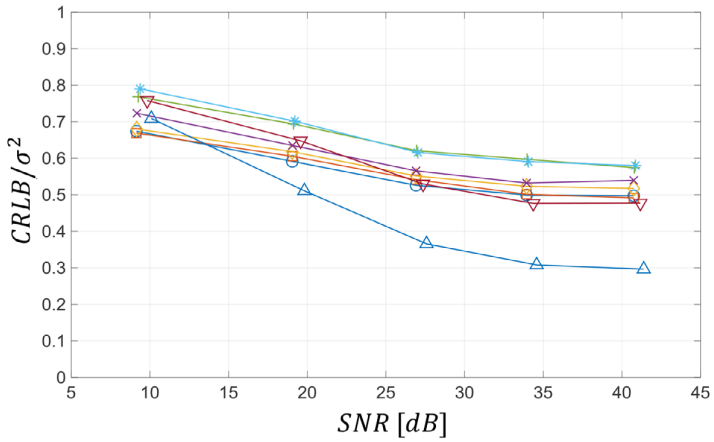

(b)

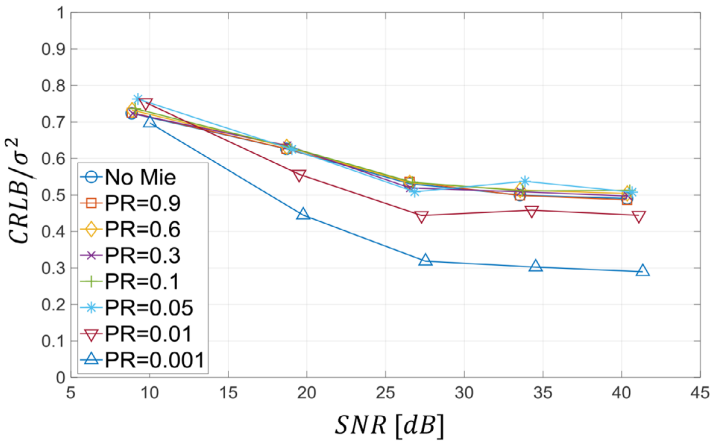

(c)

Figure 12. CRLB$/\sigma^2$ for simulation cases, (a) $U_t = 137.1$ m s^{-1}, (b) $U_t = 232.6$ m s^{-1} and (c) $U_t = 493.3$ m s^{-1}.

the current methods are not recommended due to accuracy limitations. The authors' experience indicates that this signal quality is achievable in many practical applications.

The measurement bias errors and uncertainty values for all simulated cases are shown in figure 14 and provided numerically in tables 2–5 for the range of both the PR = 1 and 0.01 signal simulations. As noted above, both the bias errors and uncertainty values for the full scan method applied to the PR = 1 signal are much lower than that seen when using the partial scanning method in the Mie

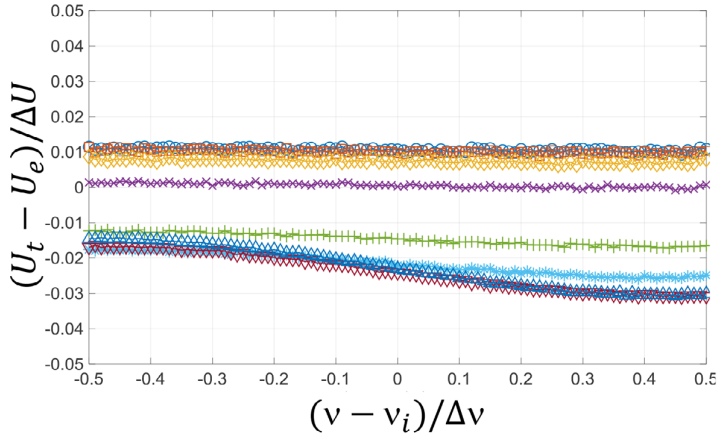

(a)

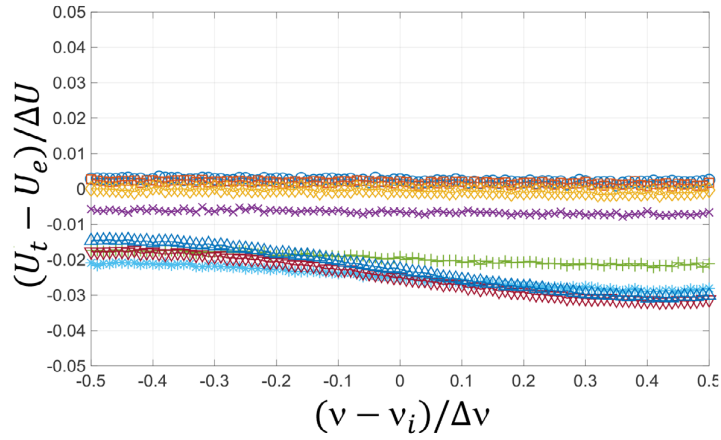

(b)

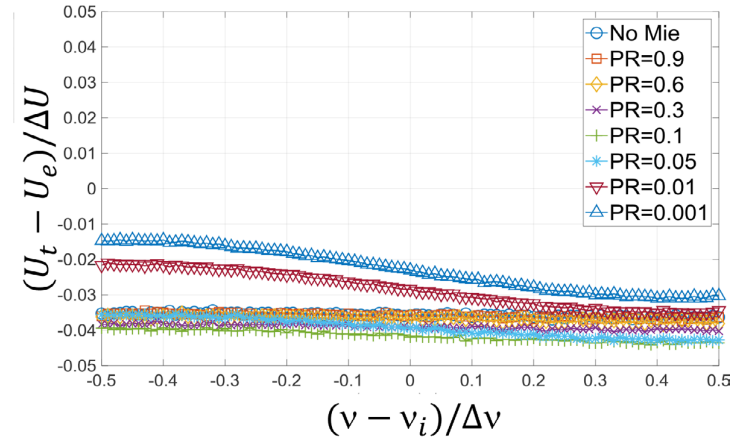

(c)

Figure 13. Normalized bias error associated with discrete frequency step for simulation cases, (a) $U_t = 137.1$ m s^{-1}, (b) $U_t = 232.6$ m s^{-1} and (c) $U_t = 493.3$ m s^{-1}.

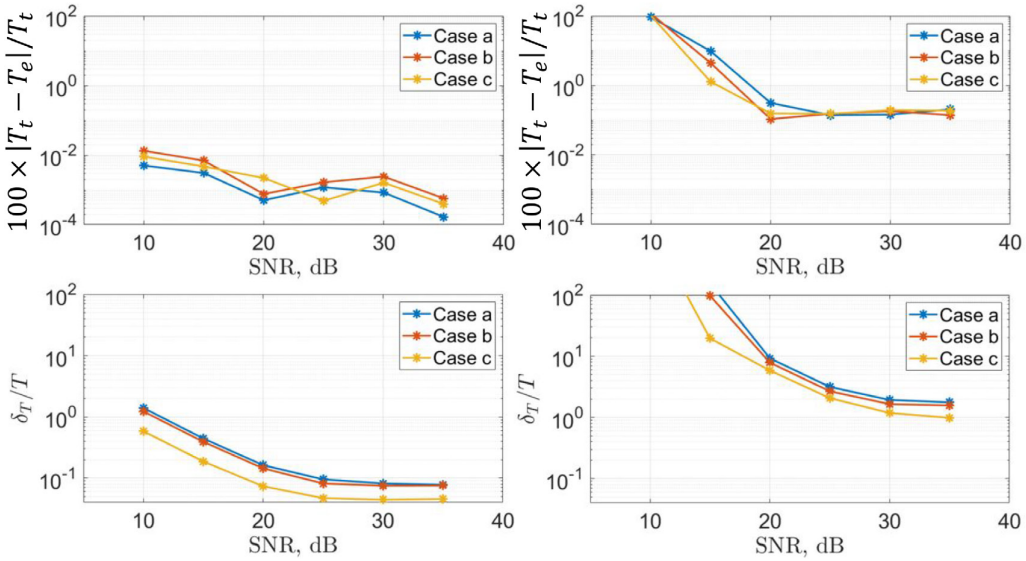

Figure 14. Monte Carlo simulation bias errors and 95% confidence estimator uncertainties, PR = 1 (left); PR = 0.01 (right). As expected, the results for the full scan method (left) show much more precise and accurate results in determining temperature compared to the partial scan method (right).

Table 2. PR = 1 signal, full scan bias errors (values defined by $E_{\text{bias}} = 10 \times (100 \times |T_t - T_e| / T_t)$).

Case	10 dB	15 dB	20 dB	25 dB	30 dB	35 dB
a	0.050	0.031	0.005	0.012	0.008	0.002
b	0.134	0.070	0.008	0.017	0.024	0.006
c	0.091	0.047	0.022	0.005	0.016	0.004

Table 3. PR = 1 Signal, full scan uncertainty (values given in percent).

Case	10 dB	15 dB	20 dB	25 dB	30 dB	35 dB
a	1.39	0.444	0.162	0.096	0.082	0.078
b	1.23	0.392	0.144	0.082	0.075	0.076
c	0.582	0.187	0.074	0.047	0.044	0.046

contaminated case (PR = 0.01). The uncertainty values observed for lower SNR cases further underscore the need to achieve SNR $\geqslant$ 20 dB when applying the partial scan temperature estimator.

Another trend that we notice in the results is how the bias errors and uncertainty values depend upon with the flow case temperature, and to a lesser extent pressure. For these simulations, we set a constant total pressure ($P_0 = P\left(1 + \frac{\gamma-1}{2}M^2\right)^{\frac{\gamma}{\gamma-1}}$, where $\gamma = c_p/c_v$ is the air specific heat ratio) and total temperature ($T_0 = T + U^2/2c_p$) and allow the Mach number of the flow to dictate the resulting static temperature and pressure. Thus, as the Mach number increases both the static temperature and pressure decrease and the temperature determination becomes both more accurate and more precise. This can be attributed to two well-known characteristics of the Rayleigh spectral lineshape, namely that the full width at half maximum (FWHM) of the Rayleigh spectral lineshape is proportional to the square-root of temperature [18],

$$\text{FWHM} \propto \sqrt{T} \tag{5}$$

and that the Rayleigh scattering spectral shape scales on a the pressure dependant y-parameter given [4],

$$y = \frac{P}{\sqrt{2}k\nu_0\eta} \tag{6}$$

where k is the laser wave vector magnitude, ν_0 the mean molecular velocity from kinetic theory, and η the shear viscosity of the gas. When $y \ll 1$, the flow is considered in the Knudsen regime, and the Rayleigh scattering spectral lineshape can accurately modelled as a Gaussian. This combination of decreasing pressure and temperature as we increase the Mach number in turn causes the modulation depth of the convolution spectrum to increase, increasing the sensitivity of the trough signal to temperature.

In experimental applications, SNR can be increased by increasing laser power/energy used, increasing camera exposure time, and/or reducing background light, but shot noise can additionally be mitigated by filling the camera intensity bit depth and binning pixels to effectively increase intensity bit depth, albeit at the expense of spatial resolution. To maximize temperature sensitivity, the camera/laser positioning may be optimized to change the width of the measured spectrum, as the width is also dependant on the angle between the laser propagation direction and the observation direction [18].

Overall, it is possible to obtain a measurement for temperature using a 16-bit camera that has an acceptable level of accuracy and precision in an environment that is highly contaminated with Mie Scattering, given a SNR $\geqslant$ 20 dB. Based upon the authors' experience in practical applications, we expect SNR to be at least 25 dB, yielding temperature uncertainty values of 2%–3%, or less, for the flow conditions considered in this work.

Table 4. PR = 0.01 signal, partial scan bias errors (values defined by $E_{\text{bias}} = 100 \times |T_t - T_e| / T_t$).

Case	10 dB	15 dB	20 dB	25 dB	30 dB	35 dB
a	94.0	9.65	0.312	0.139	0.145	0.204
b	117	4.38	0.107	0.153	0.182	0.140
c	103	1.27	0.156	0.153	0.195	0.188

Table 5. PR = 0.01 signal, partial scan uncertainty (values given in percent).

Case	10 dB	15 dB	20 dB	25 dB	30 dB	35 dB
a	479	154	9.20	3.15	1.93	1.76
b	754	96.6	7.83	2.67	1.65	1.56
c	1250	19.5	5.83	2.06	1.17	0.984

5. Conclusions

In this paper the CCFRS technique has been presented and assessed for flow velocity and temperature measurement using Rayleigh scattering, including influences from Mie scattering. Three different flow conditions of interest to aerodynamics applications are considered to investigate the dependency of velocity and temperature estimators on the absolute velocity magnitude and Rayleigh scattering spectral lineshape. A series Monte Carlo signal simulations were conducted to estimate errors and uncertainties of estimating Doppler shift using a signal model of combined Rayleigh and Mie scattering. The bias errors of velocity estimation are within ± 2.5 m s^{-1} when using a reference signal generated by pre-convolving an estimated Rayleigh scattering spectrum with the known iodine transmission spectrum. The CRLB is independent of Doppler shift estimator using a cross-correlation, but it depends on the transmission function. Therefore, an effect of the convolved transmission function on the CRLB was observed. The CRLB is slightly higher as Rayleigh scattering broadens the signal and reduces the Fischer information. The similar effect of Rayleigh scattering is also observed on the variance of estimated velocity obtained from Monte Carlo simulations. Estimator efficiencies were typically greater than 0.5, with the exception of an extreme case with large amounts of Mie scattering where known performance issues occur due to the wide transmission trough at the centre frequency—a transmission characteristic which is required for CCFRS in order to extract the information of temperature and pressure (density) from the Rayleigh spectrum when particles are present. The bias error related to the peak finding and the discrete frequency scanning step were also investigated. Due to the nature of Rayleigh scattering spectrum dependency on temperature and pressure, the convolved transmission function was different for all cases, except the highest contribution of Mie scattering. Therefore, this error is evaluated within ± 1.5 m s^{-1} for all simulated conditions. Further analysis is required to describe better the effect of the choice of iodine transmission function and its convolution with Rayleigh spectrum on this error.

Monte Carlo simulations were conducted to determine the uncertainties of temperature for both an idealized signal consisting only of Rayleigh scattering contributions and a signal containing contribution from Rayleigh and Mie scattering. In the former case, a broad bandwidth of the spectrum (about 7 GHz) may be used, while only a narrow portion of the spectrum in the trough can be used for the Rayleigh and Mie scattering signal. The broad bandwidth fitting method yielded bias errors of less than $\pm 0.014\%$ and uncertainty values within $\pm 1.4\%$ for all simulated cases, while the partial scan technique varied significantly across the SNRs examined. It was concluded that practical applications of this method will require SNRs of at least 20 dB for the partial scan technique. For SNR $\geqslant$ 20 dB, the temperature bias errors were within $\pm 0.2\%$ and the random uncertainty values were less than $\pm 3.2\%$.

As an expanded application of the proven and robust CCDGV technique, CCFRS has a great deal of value and potential for simultaneous flow velocity and temperature measurements with or without seeding particles. The method is particularly attractive in facilities where seeding is not able to be introduced or is not desirable in the application. The authors continue to expand the method to determine density and pressure with acceptable uncertainties. Towards these objectives, early efforts (not shown) indicate that there is sufficient information contained within the Doppler-shifted low transmission trough to estimate both temperature and density at acceptable uncertainty values. Given the stringent demands for interpreting the reduced amount of information contained in this signal, additional work is needed to improve the presented fitting methods for this relatively narrowband spectral region. In results to be presented in future work, the authors seek to show that this method is viable for planar measurements of not only flow velocity and temperature but also density and pressure at high spatial resolution, with or without the presence of particles, particularly in complex applications that do not enable control for the presence of particles.

ORCID iDs

K T Lowe https://orcid.org/0000-0002-0147-4641

References

[1] Nelson M A, Lowe K T, O'Brien W F, Kirk C and Hoopes K M 2014 Stereoscopic PIV measurements of swirl distortion on a full-scale turbofan engine inlet *Proc. 52nd AIAA Aerospace Sciences Meeting AIAA SciTech 2014 (National Harbor, MD, 13–17 January)* paper 2014-0533

[2] Guimarães T, Lowe K T and O'Brien W F 2016 An overview of recent results using the StreamVane method for generating tailored swirl distortion in jet engine research *AIAA SciTech 2016 (San Diego, CA, 4–8 January)* AIAA-2016-0534

[3] Guimarães T, Frohnapfel D, Lowe K T and O'Brien W F 2017 Complex flow generation and development in a full-scale turbofan inlet *ASME Turbo Expo 2017* GT2017-64756

[4] Yeaton I, Maisto P and Lowe K T 2012 Time resolved filtered Rayleigh scattering for temperature and density measurements *28th AIAA Aerodynamic Measurement*

Technology, Ground Testing, and Flight Testing Conf. (New Orleans, LA, 25–28 June) AIAA-2012-3200
[5] Boyda M and Lowe K T 2018 Cross-correlation Doppler global velocimetry using Rayleigh and Mie scattering *AIAA SciTech 2018 (Kissimmee, Florida, 8–12 January)*
[6] Boguszko M and Elliott G S 2005 On the use of filtered Rayleigh scattering for measurements in compressible flows and thermal fields *Exp. Fluids* **38** 33–49
[7] Doll U, Stockhausen G and Willert C 2014 Endoscopic filtered Rayleigh scattering for the analysis of ducted gas flows *Exp. Fluids* **55** 1690
[8] Doll U, Burow E, Stockhausen G and Willert C 2016 Methods to improve pressure, temperature and velocity accuracies of filtered Rayleigh scattering measurements in gaseous flows *Meas. Sci. Technol.* **27** 125204
[9] Doll U, Stockhausen G and Willert C 2017 Pressure, temperature, and three-component velocity fields by filtered Rayleigh scattering velocimetry *Opt. Lett.* **42** 3773–6
[10] Cadel D R and Lowe K T 2015 Cross-correlation Doppler global velocimetry (CC-DGV) *Opt. Lasers Eng.* **71** 51–61
[11] Cadel D R and Lowe K T 2016 Investigation of measurement sensitivities in cross-correlation Doppler global velocimetry *Opt. Lasers Eng.* **86** 44–55
[12] Fischer A 2017 Model-based review of Doppler global velocimetry techniques with laser frequency modulation *Opt. Lasers Eng.* **93** 19–35
[13] Miles R B, Lempert W R and Forkey J N 2001 Laser Rayleigh scattering *Meas. Sci. Technol.* **12** R33–R51
[14] Ecker T, Brooks D R, Lowe K T and Ng W 2014 Development and application of a point Doppler velocimeter featuring two-beam multiplexing for time-resolved measurements of high speed flow *Exp. Fluids* **55** 1819–33
[15] Meilke A F, Seasholtz R G, Elam K A and Panda J 2005 Time-averaged measurement of velocity, density, temperature and turbulence velocity fluctuations using Rayleigh and Mie scattering *Exp. Fluids* **39** 441–54
[16] Fischer A, Pfister T and Czarske J 2010 Derivation and comparison of fundamental uncertainty limits for laser-two-focus velocimetry, laser Doppler anemometry and Doppler global velocimetry *Measurement* **43** 1556–74
[17] Forkey J N, Lempert W R and Miles R B 1997 Corrected and calibrated I_2 absorption model at frequency-doubled Nd:YAG laser wave lengths *Appl. Opt.* **36** 6729–38
[18] Tenti G, Boley C D and Desai R C 1974 On the kinetic model description of Rayleigh–Brillouin scattering from molecular gases *Can. J. Phys.* **52** 285–90
[19] Pan X, Shneider M N and Miles R B 2004 Coherent Rayleigh-Brillouin scattering in molecular gases *Phys. Rev.* **69** 033814

3.2 Temperature and Density Measurement Uncertainty

AIAA SciTech Forum
6-10 January 2020, Orlando, FL
AIAA Scitech 2020 Forum

10.2514/6.2020-1516

Effect of Mie and Geometric Scattering on Temperature and Density Measurements using Filtered Rayleigh Scattering

Matthew T. Boyda[1], Gwibo Byun[2], Ashley J. Saltzman[3], and K. Todd Lowe[4]
Virginia Tech, Blacksburg, Virginia, 24060, USA

Unwanted signals from particle and surface scattering cause bias errors and substantial uncertainties when using conventional filtered Rayleigh scattering approaches. A means for accounting and removing these effects are investigated by developing a comprehensive scattering model including Rayleigh scattering (via Tenti's S6 Rayleigh lineshape model), Mie scattering, and geometric scattering contributions. The insights gained from this model are then applied for the first time using several cases that vary in flow conditions and spectral bandwidth to reduce the uncertainties of the in situ multi-property measurements of vector velocity, temperature, and density. Both Mie and geometric scattering are individually found to cause significant distortions in the shape and intensity of a measured Rayleigh scattering/iodine transmission convolution spectrum. However, these contributions may be filtered out using the molecular iodine vapor cell when optimal bands in the iodine absorption spectrum are applied. For cases considering only Mie scattering, temperature and density uncertainties are found to be below 3.5% and 4.5%, respectively, while the uncertainties for cases considering only geometric scattering are found to be below 3% and 3.5% for temperature and density estimation, respectively, over a range of subsonic flow Mach numbers, $0.4 \leq M \leq 0.7$. Owing to a large Doppler shift in the Rayleigh spectrum, a supersonic case at M =1.9 is found to yield a greater uncertainty in temperature of 8%. When Mie and geometric scattering contributions are combined, the intersection of the individual rejection regions must be used, resulting in temperature and density uncertainties of 2.0% and 2.6% for the M = 0.4 case and 2.6% and 2.8% for the M = 0.7 case, respectively. An alternative method is proposed and demonstrated qualitatively for applications where the Doppler shift magnitude is too large to rely solely upon the iodine filter rejection region method. In comparison to experimental measurements, the developed composite scattering model captures the majority of the observed scattering physics.

I. Nomenclature

M	=	Mach number
T	=	temperature, [K]
P	=	pressure [psi]
U	=	flow velocity, [m/s]
IR	=	intensity ratio of Mie and geometric scattering to Rayleigh scattering
τ_{iodine}	=	transmission spectrum of iodine cell
S	=	scattering spectrum
η, ν	=	frequency, [GHz]

[1] Graduate Research Assistant, Crofton Department of Aerospace Engineering, AIAA Student Member.
[2] Research Scientist, Crofton Department of Aerospace Engineering, AIAA Senior Member.
[3] Graduate Research Assistant, Crofton Department of Aerospace Engineering, AIAA Student Member.
[4] Associate Professor, Crofton Department of Aerospace Engineering, AIAA Associate Fellow.

QE = quantum efficiency of sensor
AD = analog-to-digital conversion factor
n_s = number of scattered photons
$\hat{o}$ = scattering light direction
$\hat{\imath}$ = laser propagation direction
λ = laser wavelength

II. Introduction

Many flow measurement applications today benefit from robust, minimally intrusive vector velocity and scalar property determination provided by laser-based diagnostic techniques. In particular, Rayleigh scattering is a very attractive wave optics phenomenon, due to its ability to determine Doppler-based velocity, as well as temperature, density, and pressure simultaneously with or without the presence of seeded particles in the measured flow. This capability makes Rayleigh scattering-based diagnostics ideal for in situ multi-property measurements where it is not possible or desirable for seeding to be introduced. Filtered Rayleigh scattering (FRS) is being utilized more and more in flow and combustion relevant gas measurement applications [1-7], but typically suffers from intensity contamination due to the inherently low signal levels of Rayleigh scattering techniques, when compared to other sources of light scattering. Specifically, the scattering off of small particles suspended in the flow (Mie scattering) typically exists and is difficult to avoid due to particles that naturally exist in most facilities and laboratories. Furthermore, the scattering from solid, stationary boundaries in the background of the interrogation region (geometric or background scattering) including aerodynamic models, wind tunnel walls, and reflections from optical windows also cannot be avoided for many in situ applications due to limited optical access and/or in the interest of obtaining measurements near these regions. In the cases where this cannot be avoided, geometric scattering may be minimized to obtain higher signal-to-noise ratios (SNR) by using fluorescent surface coatings [8], or with advanced imaging techniques such as structured illumination [9,10], but are difficult to eliminate entirely when high intensity geometric scattering is present.

Separately, the intensity contamination from these sources present significant risk when estimating flow properties using any Rayleigh scattering diagnostic techniques, but is especially true for in situ measurements with complicated or restrictive optical environments where Mie and geometric scattering cannot be eliminated and typically result in intensity biases that significantly affect measured FRS signals. Acknowledging the significance of these contributions, their effects on Rayleigh scattering measurements need to be well understood and accounted for to improve estimation accuracy and precision, as well as to aid in measurement system design. If these contributions are not accounted for in the measurement, an accurate estimation would be difficult or impossible to obtain due to the biases they introduce.

The Virginia Tech team has been developing a robust method for applying filtered Rayleigh scattering (FRS) for mean measurements of vector velocity, temperature, and pressure [11, 12]. Recently, authors reported that the cross-correlation filtered Rayleigh scattering (CC-FRS) technique is able to provide velocity, temperature, and density using cross-correlation and curve-fitting methods. In addition to this, the impact of Mie scattering on temperature estimator performance has also been investigated [13]. To extend this investigation to the effects of different levels of Mie and geometric scattering as well as their combined effect on filtered Rayleigh scattering measurements, the present work considers a wide range of these contributions to investigate the accuracy of temperature and density determination using CC-FRS under conditions seen in practical engineering applications.

III. Signal Models

To extend the technique beyond solely Doppler velocity measurements, we note that the signal received is a convolution of the transmission spectrum and the Rayleigh, Mie, and geometric spectrum,

$$S_{Signal}(\nu) = S_{Mie+geo+Rayleigh} \otimes \tau_{iodine} = \int_{-\infty}^{\infty} S_{Mie+geo+Rayleigh}(\nu - \eta)\tau_{iodine}(\eta)d\eta \quad (1)$$

where $S_{Mie+geo+Rayleigh}$ is the combined Mie, geometric, and Rayleigh spectrum centered on the incident laser frequency and τ_{iodine} is the transmission spectrum of the iodine vapor cell. For the signal simulations, the model developed by Forkey et al. [14] is employed to generate the iodine vapor cell's transmission spectrum, while the model developed by Tenti et al. and Pan et al. [15, 16] (referred to as the Tenti S6 model) was used to generate the Rayleigh spectral lineshape for air at the conditions of interest. As the Rayleigh spectral lineshape depends on both pressure and temperature, the simulations will be performed for three different flow conditions, considering applications in both low and high speed wind tunnels. Independent simulations will be conducted for the flow velocity, temperature,

and pressure conditions as they are presented in Table 1. Figure 1 shows the Rayleigh spectral lineshape (top) for each case and their respective convolutions with the iodine transmission spectrum for the three simulated thermodynamic conditions at zero velocity (bottom). Note that in Figure 1, only the pure Rayleigh lineshape and their convolutions are shown with no Mie or geometric intensity contributions.

Table 1. Flow conditions for Rayleigh signal simulations

Case	M	U, m/s	T, K	P, psi	$\rho, kg/m^3$
a	0.4	137.1	293.6	19.1	1.56
b	0.7	232.6	275.7	15.4	1.34
c	1.9	493.3	168.3	2.8	0.4

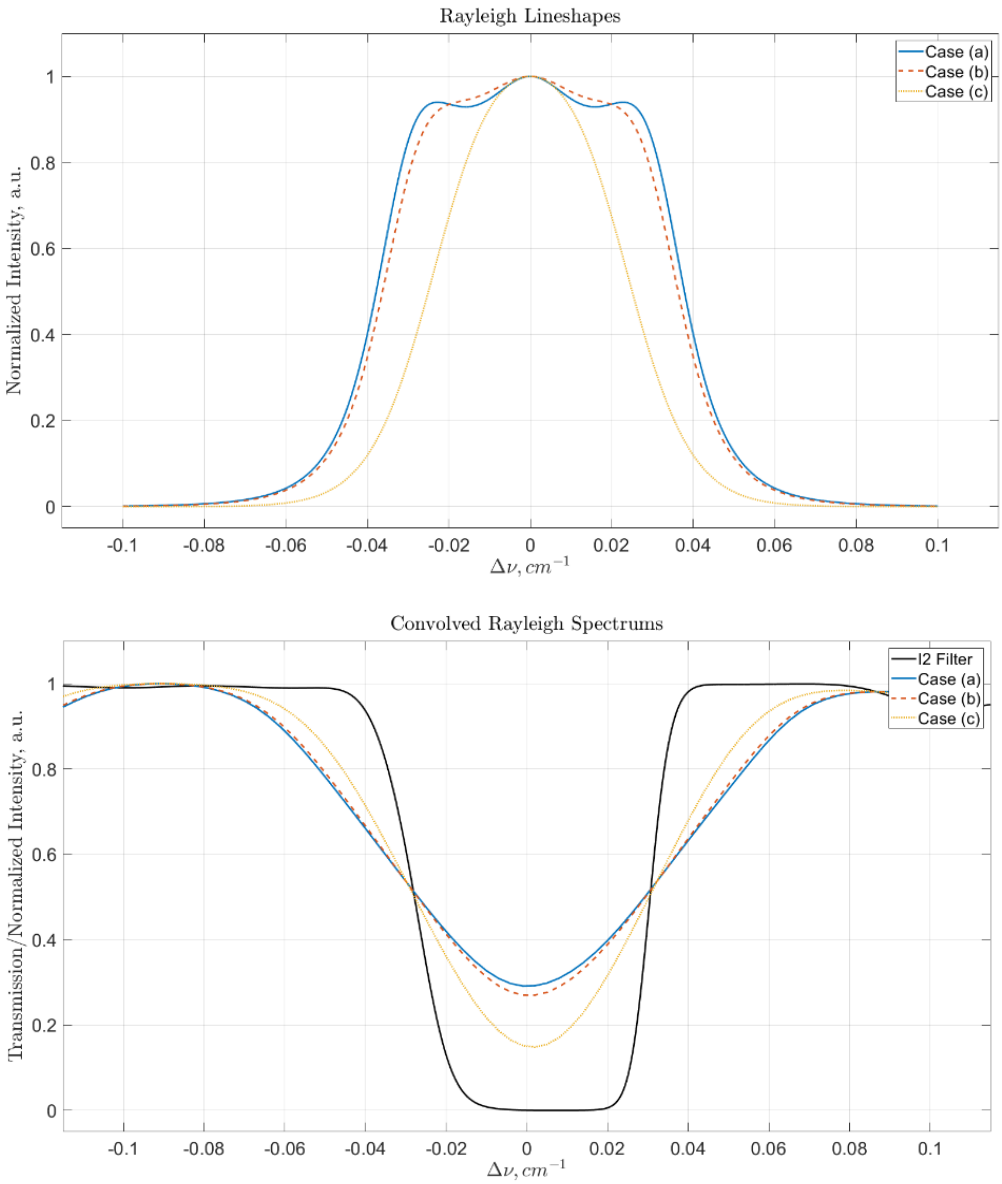

Fig. 1 Rayleigh scattering spectrum (top) and its convolution with iodine transmission spectrum (bottom) for simulation conditions but with zero velocity for clarity.

Mie scattering is the elastic scattering of light off of particles that have a diameter similar to or greater than the wavelength of the incident light. The presence of Mie scattering particles may either be purposefully introduced into

the flow for other laser based measurements (i.e. LDV, PIV, or DGV) or may be particles that have been unintentionally introduced from the environment (i.e. dust, condensed water vapor, or combustion products for engine testing environments). Mie scattering intensity is generally proportional to the square of the particle diameter and therefore is more intense than Rayleigh scattering per unit laser power when present. The Mie scattering spectrum is modelled with the Doppler-shifted laser center frequency and a width according to the turbulence intensity of the flow. For the present simulation, the Mie scattering spectrum has been modelled with a width of 100 MHz (corresponding to 5% to 18% turbulence intensity for the present flow conditions).

Geometric scattering is the scattering of light off particles or objects that are much larger than the wavelength of the incident light (i.e. duct walls, jet nozzles, model geometry, etc.) and typically stationary with respect to the flow being measured thus displaying no Doppler shift. The background scattering has been modelled with a width of 5MHz corresponding to the stability of the Coherent Verdi V18 laser, the laser used in laboratory experiments at Virginia Tech. The intensity ratio (IR) of Rayleigh scattering compared to Mie and geometric scattering is used to estimate their contributions to account for the existence of naturally occurring particles and physical objects in facilities is defined as,

$$IR_{Mie} = \frac{\int (Rayleigh) dv}{\int (Mie) dv} \tag{2.1}$$

$$IR_{geo} = \frac{\int (Rayleigh) dv}{\int (Geometric) dv} \tag{2.2}$$

The resulting combined spectral lineshape is modelled for Mie, geometric, and Rayleigh scattering intensity is presented in Figure 2.

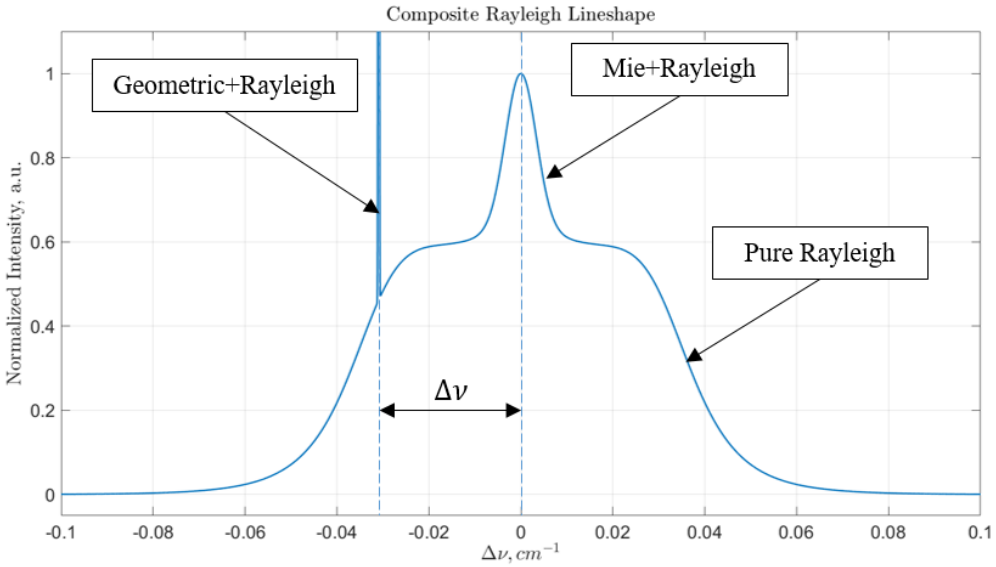

Fig. 2 Composite Rayleigh spectral lineshape resulting from Mie and geometric scattering contributions in the presence of Rayleigh scattering.

IV. Signal Simulations

Monte Carlo simulations have been performed using the same procedure previously applied to CC-DGV technique and described at length in ref. [13]. The signal model $S(v)$ defined as,

$$S(v) = QE\ n_s \tau_{iodine}(v)/AD \tag{3}$$

is a function of the number of scattered photons (n_s), the quantum efficiency of the sensor (QE, photons to electrons), the iodine vapor cell transmission spectrum, $\tau_{iodine}(v)$ at the laser frequency, v, and the analog-to-digital conversion factor (AD, electrons to intensity counts). To conduct the Monte Carlo simulations for the temperature and density

estimators, a specific physical condition corresponding to one of the flow cases presented in Table 1, is applied to generate the analytical Rayleigh lineshape using the Tenti S6 model. This lineshape model is then convolved with the iodine transmission spectrum at a specified number of discretization points (in this case, 10 to 100) to create a noise-free convolution spectrum, according to equation (3). Noise is then added to the convolution spectrum in the form of random noise resulting from A/D conversion, dark current, as well as shot noise based on the use of a 12-bit camera sensor. Since the shot noise is a physical parameter proportional to the square root of the number of photons incident on the camera sensor, shot noise is allowed to vary only with the intensity of the measured spectrum while the random noise is controlled by the user in the simulations. Once this is complete, the least-squares curve-fitting algorithm is applied to the convolution spectrum to estimate the flow temperature and density. The estimator uncertainty for the curve-fitting method was computed using 1,000 Monte Carlo samples for a practically achievable SNR = 26 ~ 27 dB, where $SNR = 10log_{10}[\sigma_s^2/(\sigma_P^2 + \sigma_G^2)]$, σ_S^2 is the variance of the noise-free signal, σ_P^2 is the Poisson-distributed shot, and σ_G^2 is the Gaussian-distributed detector noise.

V. Experimental Setup

In order to validate the proposed model of filtered Rayleigh scattering, correcting for Mie and geometric scattering contributions, an experiment was conducted on the heated supersonic jet rig at Virginia Tech's Advanced Propulsion and Power Laboratory (APPL). An axisymmetric converging-diverging nozzle with diameter of 1.5 inches and design Mach number of 1.5 was used to create a supersonic free jet, operating with a nozzle pressure ratio of 2.59. Compressed air feeds two impinging jets, which are heated to a total temperature ratio of 2 using a 192 kW heater several diameters upstream of the nozzle exit, as depicted in Figure 3. The heated stream mixes and passes through four honeycomb screens for straightening before accelerating through the converging-diverging nozzle to create the free jet.

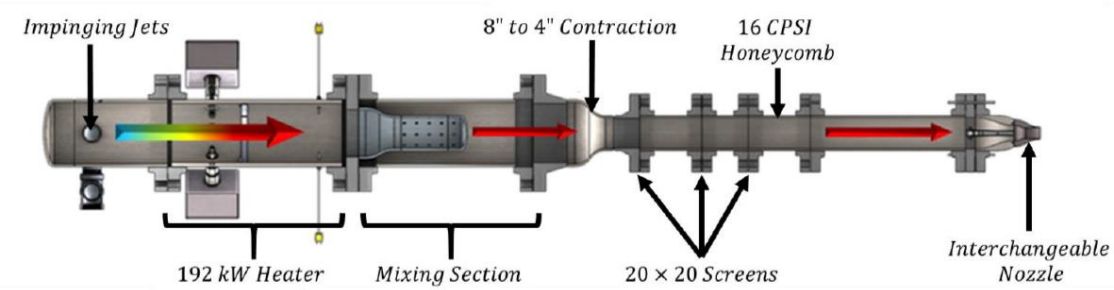

Fig. 3 Diagram of the supersonic jet rig.

A laser conditioning subsystem was used in the experiment to deliver the laser light to the measurement region of interest. The frequency of incident laser light is modulated by applying voltage to a piezoelectric element (PZT) in the laser head. The incident frequency is monitored by measuring the transmission of a small amount of laser light, split from the primary beam path, through an iodine cell using a photodetector pair. This conditioning is conducted in a separate room in order to minimize interference of the jet acoustics with the laser frequency stability. The laser beam is then directed to the jet and expanded through a cylindrical lens to form the measurement plane. For this experiment, the crossflow plane 3 diameters downstream of the nozzle exit was measured. The scattering signal from the jet is recorded by three imaging modules, each containing two 3.2 megapixel CMOS cameras. One camera directly records the scattered light, while the other looks through an iodine cell in order to record the filtered signal. The imaging modules are oriented to look in the downstream flow direction as shown in Figure 4. By recording data for multiple incident laser frequencies, the transmission spectrum scattered by the jet can be obtained with the ratio of the filtered signal to the unfiltered signal. The flow conditions for this experiment are listed in table 2, and further information regarding this FRS measurement application is given in detail by Saltzman et al. [17].

Table 2. Flow conditions for the heated jet experiment

M	U, m/s	T, K	P, psi	$\rho, kg/m^3$
1.25	410	440	13.7	1.54

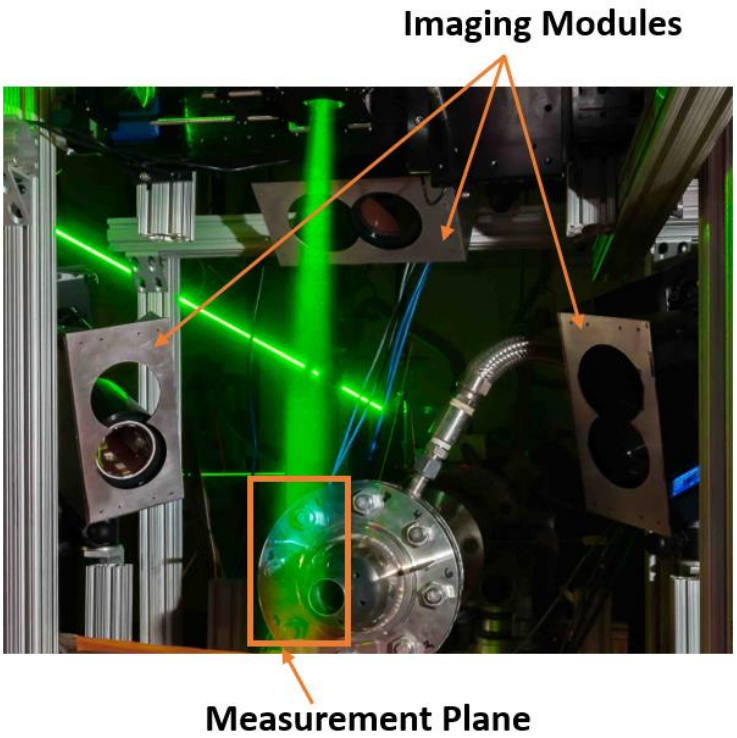

Fig. 4 Experimental setup of laser sheet and imaging modules in jet flow.

VI. Results and Discussion

Analytical results from a theoretical analysis of the Monte Carlo signal simulations are used to analyze the uncertainty and accuracy of the estimator (random variance and bias error) associated with Mie and geometric scattering contributions using the CC-FRS curve-fitting technique. For Mie and geometric contribution rejections, the rejection region for the curve-fitting was determined by the maximum iodine transmission level of 10^{-6}- 10^{-4}, as shown in Figure 5, and 10 points were used for least-squares curve-fitting, chosen as a practical implementation of this measurement.

A. Mie Scattering Contributions

When Mie scattering is present in a flow measured using the FRS technique, it is typically limited to a number of small regions/pixel clusters on a single image due to the size and distribution of naturally-occurring particles suspended in the flow as well as the relatively long exposure times associated with FRS. This Mie scattering influences the intensity of the measured signal but only outside of a region designated as the "Mie scattering rejection region" of the Forkey iodine transmission model. As presented in Figure 6, when the flow velocity is non-zero, a Doppler shift, governed by the Doppler shift equation (Eq. 4) is imposed onto the measured spectrum and is seen as a horizontal shift in both the Rayleigh and Mie scattering spectrums from their zero velocity position, shifting the zero-velocity Mie rejection region as well.

$$\Delta\nu = \frac{(\hat{o} - \hat{\imath}) \cdot \vec{V}}{\lambda} \tag{4}$$

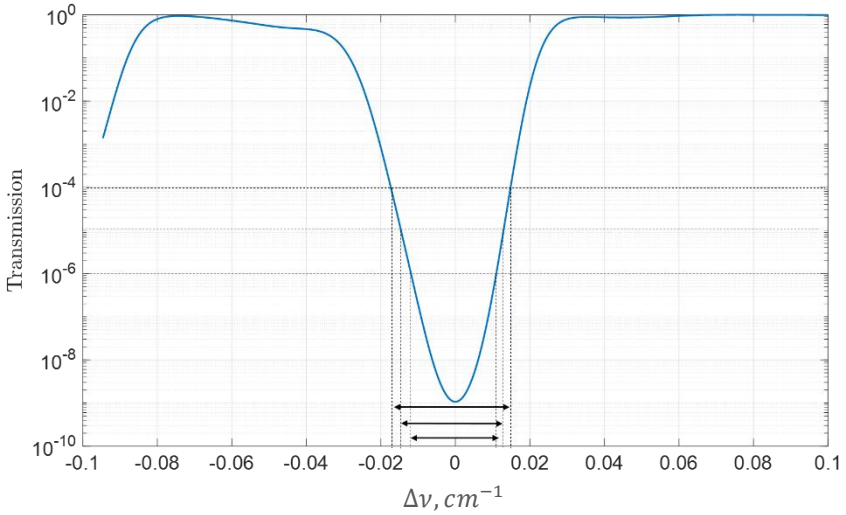

Fig. 5 Iodine cell transmission function and rejection regions for simulations at the center frequency of 18788.4401 cm^{-1}.

The sole presence of Mie scattering allows for the retention of the cross-correlation velocity determination as long as there are no major spectral changes between a no-flow (calibration) scan because all scattering contributions are shifted with velocity. This shift in the rejection region can be determined by either the local flow velocity or by the location of the minimum measured intensity in the scattered spectrum collected by the detector. Once known, the shifted rejection region may be applied, then input into the least-squares curve fitting algorithm and fit for temperature and density.

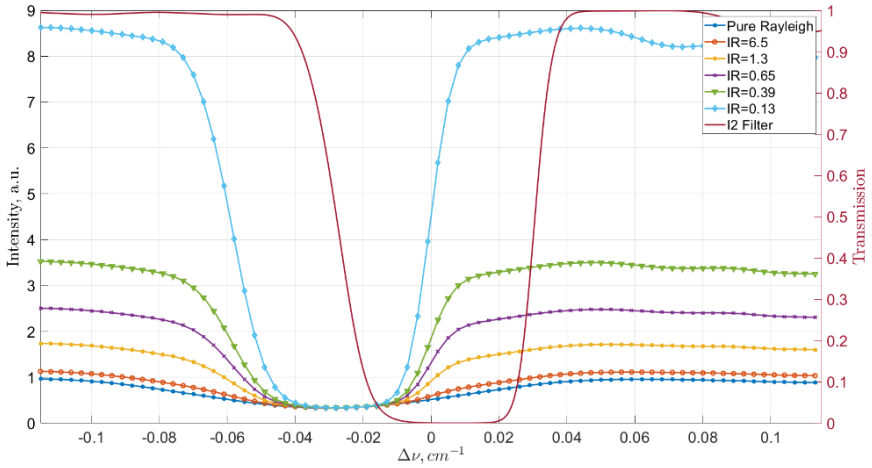

Fig. 6 Rayleigh scattering spectrum with Mie scattering contribution. Note the Mie contribution rejection region of approximately -0.04 to -0.015 cm^{-1}.

The simulation results of Mie scattering contributions for all cases are presented in Figure 7. The uncertainties of the temperature and density estimator are shown for the three maximum transmission level rejection regions. We see that in these figures, the most intense Mie scattering cases, IR = 0.13 and 0.39 corresponding to signals where Mie scattering is approximately 8 and 2.5 times more intense than the measured Rayleigh scattering respectively, are shown to influence the estimation accuracy of temperature and density for the 10^{-4} maximum transmission region with a slight divergence from the uncertainties seen in the other two cases. This demonstrates that for Mie scattering contributions greater than or equal to these values, a lower maximum transmission region must be used. We see that with the exception of temperature determination in case (c), the maximum transmission of 10^{-5} results in property estimations that are similar to or better than the 10^{-6} maximum transmission region. For the cases where they are

similar, this shows that the biases associated with Mie scattering have been efficiently removed from the signal by the 10^{-5} case, and there is no need to reduce the rejection region further. When the maximum transmission reduced further, one removes information from the measurement and risks the estimation becoming less accurate as seen in the results for case (b), where we see that the maximum transmission level of 10^{-5} seems to estimate both density and temperature more efficiently than the 10^{-6} transmission level.

Overall these simulations result in maximum temperature and density estimation uncertainties of below 3.5% and 4.5% with typical bias errors below 0.6% and 1.3% respectively while remaining relatively independent of intensity ratio. Note that a single outlier bias error of 2.5% is recorded for the density estimation in case (c) with a maximum transmission of 10^{-6}, due to the loss of information mentioned previously. The 10^{-6} region contains less information than the 10^{-5} case, and as a result, cannot fully characterize the dependence of Rayleigh scattering on temperature and density, resulting in a less accurate estimation. Although the estimation uncertainties increase at higher Mach number with lower temperature and density, the simulation results support the fact that the proposed method corrects undesired Mie contribution to Rayleigh scattering efficiently for the prescribed range of flow conditions.

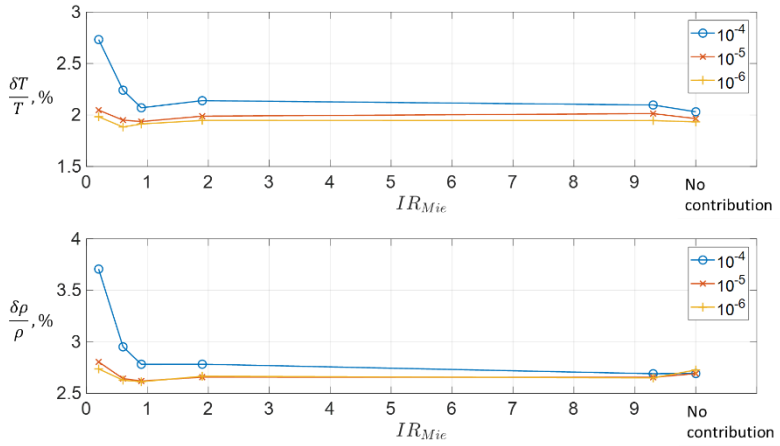

Case (a): M=0.4, T=293.6K and $\rho = 1.56 kg/m^3$

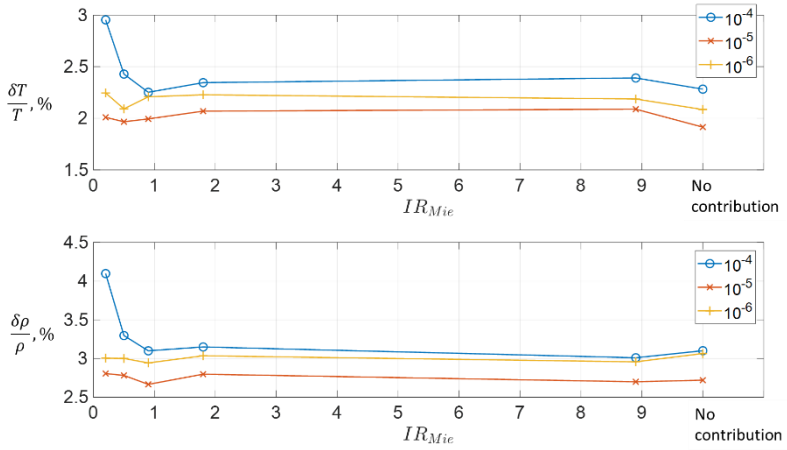

Case (b): M=0.7, T=275.7K and $\rho = 1.34 kg/m^3$

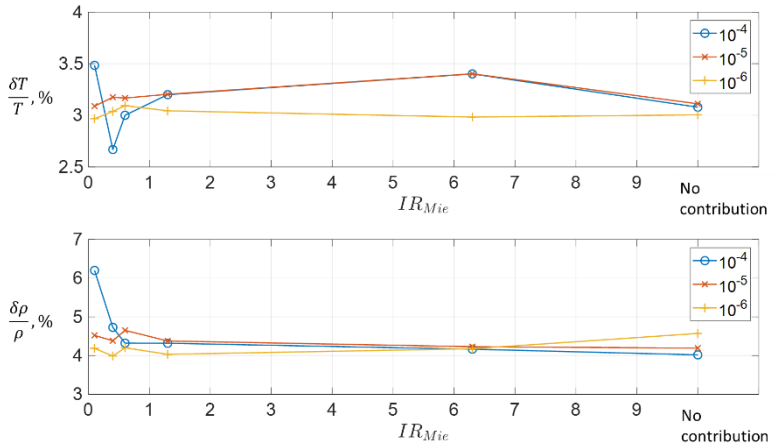

Case (c): M=1.9, T=168.3K and $\rho = 0.4 kg/m^3$

Fig. 7 Uncertainty (95% confidence) of temperature and density estimator with the maximum transmission levels for Mie scattering contribution rejection region.

B. Geometric scattering contributions

Similarly to Mie scattering contributions, when geometric scattering is present in a flow measured with the FRS technique, it influences the measured intensity spectrum outside of the so-called "Geometric scattering rejection region" of the Forkey iodine transmission model. This type of scattering typically produces a significant intensity contribution to the signal when present, introducing biases into the measurements as seen in figure 8. The difference between Mie and geometric scattering is that since geometric scattering is caused by object not moving with the flow, the influence region is uniquely defined by the frequency of the laser at each frequency step and the associated transmission through the iodine vapor cell used. This results in the conclusion that we can no longer retain the use of the cross-correlation algorithm in velocity determination, and the measured intensity spectrum must be curve fit for velocity in addition to the desired scalar parameters. If the use of the cross-correlation method was to be retained, a negative bias in the velocity magnitude would be observed as a result of the increasing intensity bias from purely Doppler shifted signal to purely geometrically scattered signal intensity, and changing the profile to appear more like the transmission spectrum of the vapor cell. Though the presence of background scattering causes significant distortion of the measured spectrum, there is a region of the spectrum where the intensity remains constant with varying geometric scattering contributions referred to above as the geometric scattering rejection region located near $\Delta\nu = 0\ cm^{-1}$ in figure 8. This region allows for an uncontaminated property estimation in the presence of background scattering.

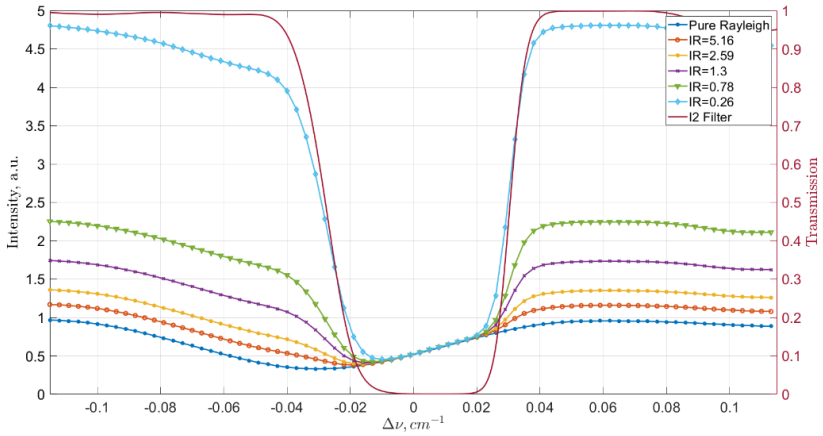

Fig. 8 Rayleigh scattering spectrum with geometric scattering contribution. Note the geometric contribution rejection region of approximately -0.01 to 0.02 cm^{-1}.

The simulation results of geometric scattering contributions for all cases are presented in Figure 9. The uncertainties of the temperature and density estimator are shown for three maximum transmission levels for the prescribed rejection region. Note that the maximum transmission levels seem to have a greater effect on the determined estimation uncertainty as we increase Mach number. For case (a) we see that all three transmission level cases show similar performance to one another. If we then look at case (b) and (c) we see that estimator performance becomes more precise with decreasing maximum transmission level. Unlike the Mie scattering contribution, the geometric scattering effects the temperature estimation more than the density estimation, as the temperature uncertainty is observed to be much higher. For cases (a) and (b) the estimation uncertainties for temperature and density are found to be below 3% and 3.5% and bias errors below 0.2% and 0.3%, while for case (c) it is observed that the temperature uncertainty is approximately 8% with bias errors below 0.9%, yielding the conclusion that this estimation scheme does not perform as effectively in higher velocity cases and is not recommended for cases with similar flow properties. This result is attributed to the fact that the curve-fitting routine has been restricted to fitting only a single side of the Rayleigh spectrum in all of these cases, with case (c) located furthest away from the minimum of the spectrum. Since the Rayleigh lineshape width is proportional to $\sqrt{T}$, causing the convolution spectrum width to have the greatest dependence on temperature. The fact that we cannot sample both the negatively and positively sloped sides causes the curve-fitting routine to estimate temperature with a larger uncertainty.

Overall, the simulation results show that the proposed model corrects geometric scattering contribution to Rayleigh scattering very efficiently for Mach numbers of 0.4 and 0.7, displaying low and consistent estimation uncertainties with varying intensity ratio. For the highest Mach number of 1.9, the proposed curve-fit evaluation scheme does not seem to function as effectively for the temperature estimation due to the high uncertainty observed, although the density uncertainty is only estimated at a max of about 3.5%.

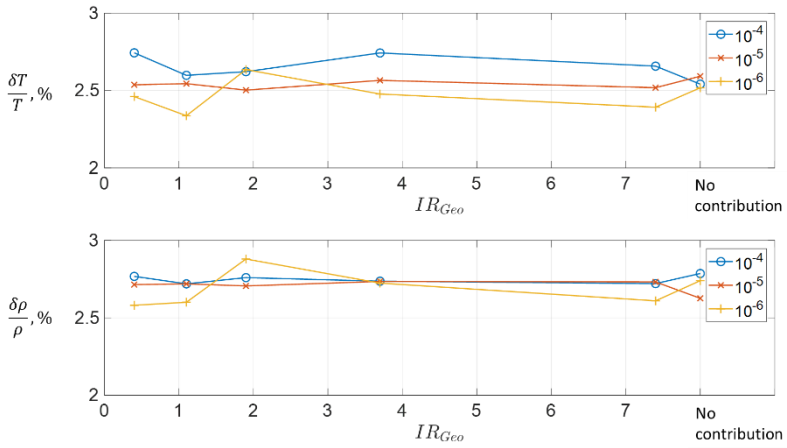

Case (a): M=0.4, T=293.6K and $\rho = 1.56 kg/m^3$

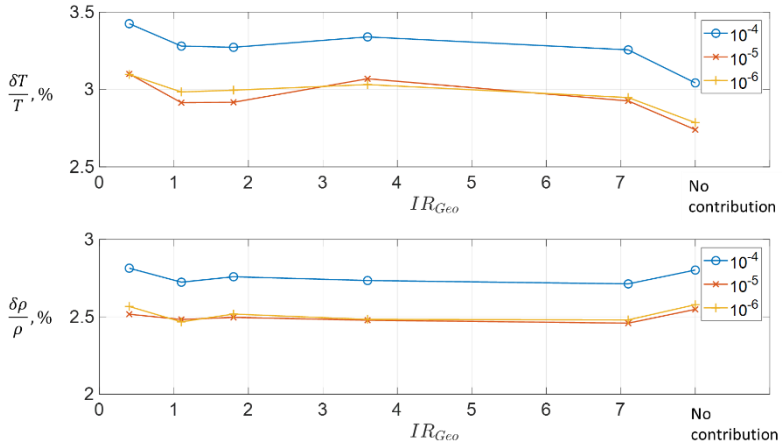

Case (b): M=0.7, T=275.7K and $\rho = 1.34 kg/m^3$

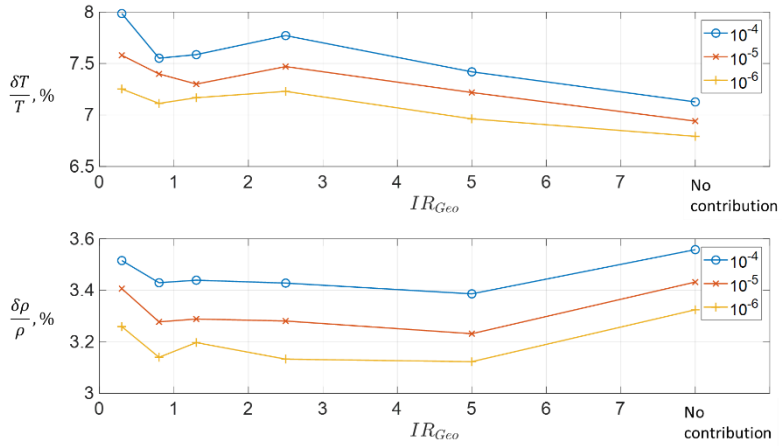

Case (c): M=1.9, T=168.3K and $\rho = 0.4 kg/m^3$

Fig. 9 Uncertainty (95% confidence) of temperature and density estimator with the maximum transmission levels for geometric scattering contribution rejection region.

C. Combined effects of Mie and geometric scattering contributions a measured Rayleigh signal

When the effects of both Mie and geometric scattering are present in a measured Rayleigh signal, the difficulty in collecting uncontaminated measurements increases dramatically. When both of these scattering sources exists in an FRS measurement we now have to consider both the Mie rejection region, which shifts with the local Doppler shift of the flow and the geometric rejection region, which is independent of Doppler shift entirely. What happens when these two are combined is that the measured Rayleigh spectrum is influenced in two different locations, relative to the center of the Rayleigh line in frequency space, as seen in Figure 2, by the Mie and geometric scattering contributions resulting in two separate rejection regions. For the evaluation presented above, only the intersection of the individual rejection regions displayed in Figure 10 may be used to effectively filter out all geometric and Mie scattered intensity contributions. Figure 10 is shown to display the intersection of the Mie and geometric rejection regions at a moderate velocity, where the intersection region still exists but has been restricted.

Figure 11 shows the rejection regions resulting from the three flow cases presented in this work. In the two lower Mach number cases [Fig 11 (a) and (b)], we see that there is a sufficient amount of overlap between the Mie and geometric scattering rejection regions to estimate the temperature and density from the measured spectrum using the existing evaluation technique. In case (c), shown in Figure 11 (c), associated with the highest Doppler shift, we notice

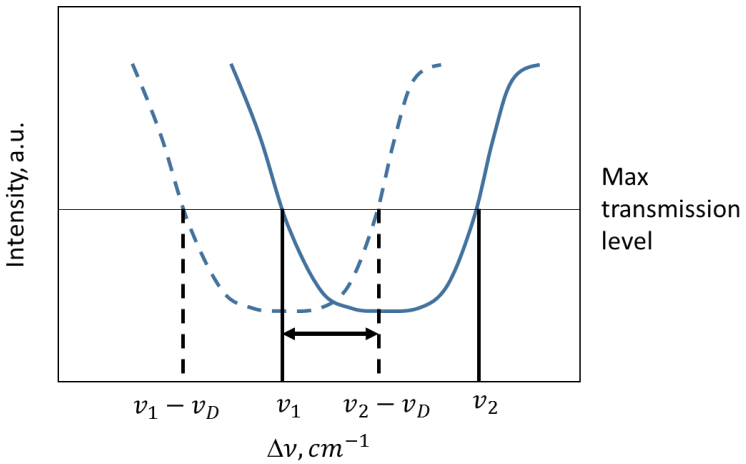

Fig. 10 Possible rejection region $[v_1, v_2 - v_D]$ with $v_1 < v_2 - v_D$ for combined Mie and geometric scattering contributions. Solid line: reference spectrum, dashed line: measured spectrum and v_D: Doppler shift.

that the frequency band $[v_1, v_2]$ is approximately 0.027 cm^{-1} for the transmission level of 10^{-5} as shown in Figure 5. The Doppler shift associated with the M = 1.9 case is found to be approximately 0.031 cm^{-1}, so no possible rejection region for the combined scattering contributions as presented in Figure 10 exists, and the current evaluation technique cannot be used to evaluate the measured spectrum for temperature and density. Thus the M = 1.9 case has been omitted from further quantitative investigation, but is revisited qualitatively for model accuracy.

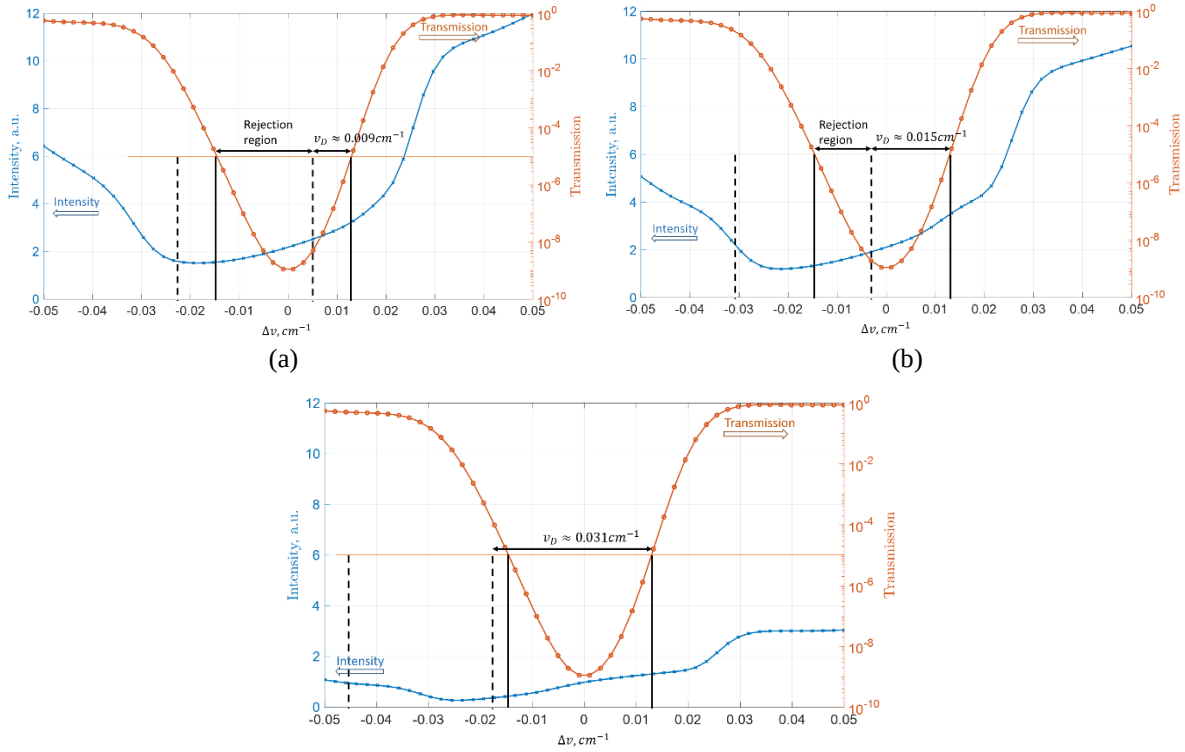

Fig. 11 Rayleigh spectrum with the combined Mie and geometric scattering contributions. Figures (a), (b), and (c) represent the measurement conditions for cases (a) where M = 0.4, (b) where M = 0.7, and (c) where M = 1.9 respectively.

The combined Mie and geometric scattering contribution has been simulated for two flow conditions, cases (a) and (b) (M = 0.4 and 0.7) with the maximum transmission level of 10^{-5}, as this case was found to filter out intensity contamination associated with Mie and geometric scattering most efficiently. For these simulated cases, the intensity ratios for Mie and geometric scattering contribution are selected as 7.2 and 2.1 respectively and are derived from the heated free jet measurement conditions of Saltzman et al. [17] described in section V.

Table 3. Uncertainty (95% confidence) of temperature and density estimator for combined Mie and geometric scattering contributions.

Case	M	$\frac{\delta T}{T}$,%	$\frac{\delta \rho}{\rho}$, %
a	0.4	2.0	2.6
b	0.7	2.6	2.8

The uncertainties for temperature and density estimation are presented in Table 3. For case (a), we see that the listed uncertainties are very close to those presented in the Mie and geometric scattering only cases. This is a result of the relatively low restriction the intersection rejection region displays at a measured Mach number of 0.4. As the Mach number is increased we see an increase in the uncertainty values as well, resulting from further restricting the amount of information available for input into the curve fitting routine. Although the uncertainties are shown to increase with Mach number as the Mie and geometric scattering rejection region becomes narrower, the proposed combined rejection region seems to be effective in correcting the simultaneous presence of Mie and geometric scattering contributions for the temperature and density estimations when compared with the results of the individual Mie/geometric scattering rejection in previous sections. The restriction on this method then becomes that the combined rejection region $[\boldsymbol{v_1}, \boldsymbol{v_2} - \boldsymbol{v_D}]$ must exist and contain enough information to accurately characterize the convolution spectrum. Further analysis is then required to decide the minimum width for required temperature and density estimation uncertainties for high Mach number flows, depending on the specific flow conditions and hardware used to measure these properties.

In applications where the measured Doppler shift magnitude is low, it is shown that there is only a small shift between the center frequencies of the Mie and geometrically scattered light. The combined rejection region is then similar in size to the regions evaluated in sections A and B, and it is expected to have similar uncertainty values. The impact of using only the intersection of the two becomes more prevalent as the measured Doppler shift magnitude increases. In these cases, where the intersection region is small, uncertainty can increase dramatically so special consideration must be taken when determining the applied rejection region, taking into account all factors of the measurement environment.

At a certain point the two rejection regions no longer overlap, resulting in intensity contamination everywhere in the measured spectrum, eliminating the ability to curve fit the spectrum with the evaluation methods presented in this work. For these applications, where there is a very small or non-existent intersection between the Mie and geometric rejection regions a new method must be employed which takes into account the contributions of both Mie and geometric scattering. The proposed method is to determine the Mie and geometric scattering by recording a FRS measurement with all flow information known (i.e. velocity, temperature, density, and pressure), typically at ambient or no-flow conditions. Using this measurement, the Mie and geometric scattering contributions are determined at every pixel by using a least squares fitting routine where the only variables are the intensity ratios of the intensity contaminants. Assuming the contributions do not change from this scan to the desired flow scan, these inputs may then be input as constants to the evaluation technique presented in this work, and the desired flow properties determined considering these contributions. This method provides a more accurate physical description of the collected convolution spectrum, which should allow for the estimation of density and temperature in high Mach number environments containing non-negligible Mie and geometric scattering contributions. Extending this implementation even further, this technique may be applied to lower Mach number flows with these intensity contributions to increase the curve fitting frequency range, adding information to the evaluated region and further driving down estimation uncertainty when compared to the rejection regions presented in the current work.

D. Signal model application

The proposed correction model of Mie and geometric scattering contributions to filtered Rayleigh scattering are applied to process experimental data measured using the cross-correlation filtered Rayleigh scattering technique. In Figure 12, we see that there is a significant amount of both Mie and geometric scattering present in the flow during the measurement. In Figure 12 (a), where Mie and geometric scattering both pass through the cell, the Mie scattering appears in the form of bright streaks or small clusters of pixels as a result of residual seeding particles that were unable to be removed from the plenum of the jet as well as larger dust particles present in the test cell. The background scattering can also be observed in this image most notably as a bright streak near the bottom of this figure but also exists at a lower intensity everywhere in the image, seen by comparing the ambient intensity level in Figure 12 (a) and (b). In this Figure 12 (b), the laser is tuned to a frequency with low transmission through the iodine cell (the transmission trough), the scattering from the particles is filtered out by the iodine cell below the detection threshold of the cameras.

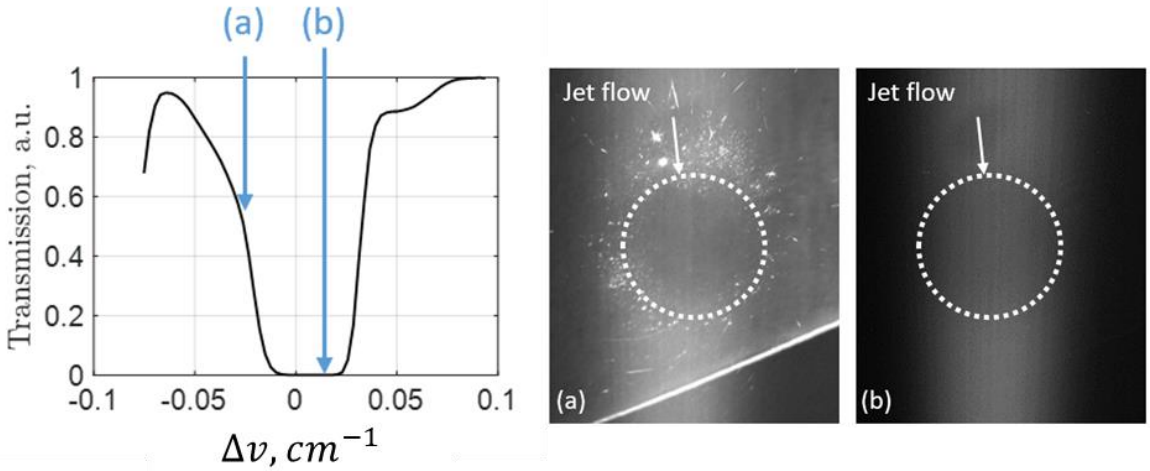

Fig. 12 Left: Transmission spectrum showing the frequency and transmission of the shown images. Right: Raw (warped) images of the uniformly heated jet at x/D = 3, with the flow in the direction out of the page.

The presence of Mie and background scattering sources significantly contribute to the shape of the measured convolution spectrum, as seen in Figure 13. The velocity of the flow, combined with the temperature and optical arrangement, removes the possibility for curve fitting the intersection of the two rejection regions. This causes the resulting spectrum to appear extremely distorted when compared to an uncontaminated Rayleigh scattering spectrum. This situation leaves only the proposed method where Mie and background contributions must be estimated for accurate property determination.

A convolution spectrum was modeled at a specified temperature and velocity knowing that the signal received will be a convolution of the combined Rayleigh, Mie, and geometric scattering lineshape with the iodine transmission spectrum. The contributions of the Mie and background scattering intensity ratios could be varied manually based on the accuracy of the fit to the measured spectra. The generated spectrum, accounting for Mie and geometric scattering, can then be compared to the measured experimental signals. By computing many theoretical transmission spectra, three-dimensional velocity, temperature, and density can be found from the measured camera signals. The fit of the modeled spectrum to the measured signals is evaluated based on minimizing the least-squares error Φ as,

$$\Phi = \sum (S_{model} - S_{measured})^2 \tag{4}$$

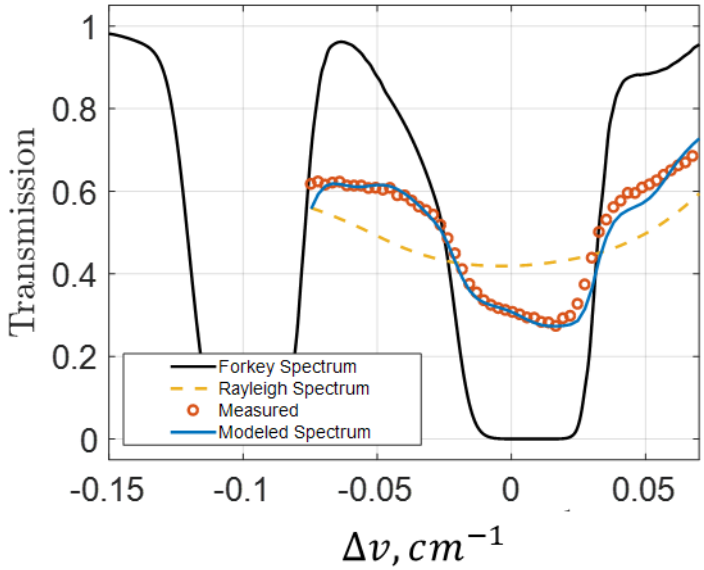

Fig. 13 Measured spectra of the uniform jet at x/D = 3 and z/D = 0.4; modeled at 442K and 410.3 m/s.

Although we cannot expect the measured spectra to perfectly match modelled results, we can vary velocity, temperature, density, IR_{Mie}, and IR_{geo} in order to minimize the least-squares error of the measured signal with the simulated spectrum. Figure 13 shows the experimentally measured transmission spectrum. Note that the spectrum modelled solely with Rayleigh scattering contribution does not compare well to the measured data, however, the spectrum modelled with geometric and Mie scattering shows good agreement. Without the correction of Mie and geometric scattering signal, determining the conditions of the jet would not be possible. To see comparisons between the filtered Rayleigh scattering results temperature probe, and PIV measurements of the heated supersonic jet, the reader is referred to Saltzman et al. [17]

VII. Conclusions

Using the developed models, the separate and combined intensity contributions of Mie and geometric scattering on measured filtered Rayleigh scattering signals have been investigated for the first time using simulated measurement spectra and Monte Carlo simulations to determine the efficiency and adequacy of an evaluation technique commonly used for multi-property measurements of vector velocity, temperature, and density.

It is found that when these intensity contributions exist separately (either Mie or geometric scattering) in a measured signal the iodine filter provides a sufficient optical density to remove the light scattered from these sources in their respective rejection regions, leaving only a purely Rayleigh scattering-dependent intensity spectrum for multi-property estimation over a wide range of Mach numbers (M = 0.4, 0.7, and 1.9). For these cases the maximum temperature and density estimator uncertainties for the Mie only case are found to be below 3.5% and 4.5% with associated bias errors typically below 0.6% and 1.3% respectively. For the geometric scattering only case, and flow cases (a) and (b), the maximum uncertainty for the temperature and density estimators are found to be 3% and 3.5% of with bias errors below 0.2% and 0.3% respectively. The temperature uncertainty results in case (c) are noted to be higher than expected at a value of 8% resulting from only interrogating the positively sloped region of the convolution spectrum while the density estimator uncertainty for this case fell below the bound for cases (a) and (b).

Simultaneous Mie and geometric scattering contributions were also investigated and shown to effectively reject the associated signal contamination at Mach numbers of 0.4 and 0.7 by using a combined or intersection rejection region yielding temperature uncertainties of 2.0% and 2.6% and density uncertainties of 2.6% and 2.8% respectively. During this investigation it was determined that a new evaluation method had to be used for Mach numbers much higher than 0.7 due to the fact that the combined rejection region no longer contained enough information to accurately characterize the measured Rayleigh signal or simply did not exist. A new scheme was proposed, using a measured signal at known flow condition to estimate the Mie and geometric scattering contributions at every pixel and account

for them in the curve fitting routine to allow temperature and density estimation in high Mach number flows and to reduce uncertainty in lower Mach number flows by increasing the region used in the curve fitting algorithm. This method was then compared to experimental data collected from an M = 1.25 turbulent jet flow where the conditions yielded a measurement where the common curve fitting was not possible. In comparison it was shown to qualitatively match the measured spectrum by minimizing the least-squares error enabling measurements of velocity and temperature which were not previously possible with existing evaluation methods in addition to validating the Mie and geometric scattering models to experimental measurements.

Future work for this application of in situ CC-FRS measurements includes implementing the Mie and geometric scattering into the curve fitting routine and using it as a fit parameter for better multi-property estimation followed by application to previous and future measurement campaigns to improve overall estimation uncertainty.

References

[1] [1]Doll U, Stockhausen G and Willert C 2014, "Endoscopic filtered Rayleigh scattering for the analysis of ducted gas flows", Experiments in Fluids, 55, 1690.

[2] Doll U, Burow E, Stockhausen G and Willert C 2016, "Methods to improve pressure, temperature and velocity accuracies of filtered Rayleigh scattering measurements in gaseous flows", Meas. Sci. Technol., 27, 125204.

[3] Doll U, Stockhausen G and Willert C 2017. "Pressure, temperature, and three-component velocity fields by filtered Rayleigh scattering velocimetry", Optics Letters, 42(19), 3773-3776.

[4] Mcmanus, T.A., Monje, I.T. & Sutton, J.A. “Experimental assessment of the Tenti S6 model for combustion-relevant gases and filtered Rayleigh scattering applications”, Appl. Phys. B (2019) 125: 13. https://doi.org/10.1007/s00340-018-7121-8

[5] Miles, R.B., Lempert, W.R., Forkey, J.N. 2001, “Laser Rayleigh Scattering”, Measurement Science and Technology, 12

[6] Meilke AF, Seasholtz, RG, Elam KA, Panda J 2005, "Time-averaged measurement of velocity, density, temperature and turbulence velocity fluctuations using Rayleigh and Mie scattering", Experiments in Fluids, 39, 441-454.

[7] Boguszko M and Elliott GS 2005 "On the use of filtered Rayleigh scattering for measurements in compressible flows and thermal fields", Experiments in Fluids, 38, 33-49.

[8] Cadel DR, Shin D, and Lowe KT (2016) A hybrid technique for laser flare reduction. AIAA SciTech 2016-Proceedings from the 54th AIAA Aerospace Sciences Meeting, San Diego, California, USA January 4-8, paper AIAA-2016-0788

[9] Boyda MB, Byun G, Saltzman AS, Lowe KT, (2019) Geometric scattering removal in CC-DGV by structured illumination, 13th International Symposium on Particle Image Velocimetry

[10] Kristensson E, Ehn A, Bood J, and Aldén M (2014) Advancements in Rayleigh scattering thermometry by means of structured illumination, Proceedings of the Combustion Institute 35: pp3689-3696

[11] Yeaton I, Maisto P and Lowe KT 2012 “Time resolved filtered Rayleigh scattering for temperature and density measurements,” *28th AIAA Aerodynamic Measurement Technology, Ground Testing, and Flight Testing Conference*, New Orleans, LA, 25-28 June, paper AIAA-2012-3200.

[12] Boyda, M. and Lowe, K.T., “Cross-Correlation Doppler Global Velocimetry using Rayleigh and Mie Scattering”, AIAA SciTech Forum, Kissmimmee, FL, AIAA Paper 2018-1766, January 2016.
doi: 10.2514/6.2018-1766

[13] Boyda, M., Byun, G and Lowe, K.T., “Investigation of Velocity and Temperature Measurement Sensitivities in Cross-Correlation Filtered Rayleigh Scattering (CCFRS)”, Meas. Sci. Technol., 30, 2019, 044004.
doi: 10.1088/1361-6501/ab0350

[14] Forkey, J.N, Lempert, W.R., and Miles, R.B., “Corrected and calibrated I_2 absorption model at frequency-doubled Nd:YAG laser wave lengths”, *Appl Opt.* 36(27), 1997, 6729-6738.

[15] Tenti, G, Boley, C.D. and Desai, R. C., “On the kinetic model description of Rayleigh–Brillouin scattering from molecular gases”, Can. J. Phys., 52, 1974, 285–90

[16] Pan, X., Shneider, M.N., and Mile,s R.B., “Coherent Rayleigh-Brillouin scattering in molecular gases”, *Physical Review*, 69, 2004, 033814.

[17] Saltzman, A., Boyda, M., Lowe, K.T., Ng, W.F., “Filtered Rayleigh Scattering for Velocity and Temperature Measurements of a Heated Supersonic Jet with Thermal Non-Uniformity”, 25th AIAA/CEAS Aeroacoustics Conference, Delft, The Netherlands, AIAA Paper 2019-2677, May 2019Vatistas, G. H., Lin, S., and Kwok, C. K., “Reverse Flow Radius in Vortex Chambers,” *AIAA Journal*, Vol. 24, No. 11, 1986, pp. 1872, 1873.
doi: 10.2514/3.13046

Chapter 4

Geometric Scattering Removal using Structured Illumination

The content included in this chapter were published by invitation in the journal Measurement Science and Technology as "Boyda M.T., Byun G., Saltzman A., and Lowe K.T. (2020) Geometric scattering removal in cross-correlation Doppler global velocimetry by structured illumination, *Measurement Science and Technology*, **31** 064004;" and has been reproduced here with the permission of IOP Publishing Ltd.

Significant portions were previously presented as "Boyda M.T., Byun G., Saltzman A., and Lowe K.T. (2020) Geometric scattering removal in CC-DGV by structured illumination, *13th International Symposium on Particle Image Velocimetry – ISPIV 2019* , July 22-24, 2019".

The primary objective of this chapter is to provide the first demonstration of structured illumination-based background removal in Cross-corrolation Doppler global velocimetry as a pre-cursor to the application of structured illumination in FRS-based diagnostic techniques.

IOP Publishing Measurement Science and Technology
Meas. Sci. Technol. **31** (2020) 064004 (13pp) https://doi.org/10.1088/1361-6501/ab6b4f

Geometric scattering removal in cross-correlation Doppler global velocimetry by structured illumination

Matthew Boyda, Gwibo Byun, Ashley Saltzman and K Todd Lowe

Crofton Department of Aerospace and Ocean Engineering, Blacksburg, VA, United States of America

E-mail: boyda13@vt.edu

Received 8 November 2019, revised 19 December 2019
Accepted for publication 14 January 2020
Published 12 March 2020

Abstract

The biases introduced by background light contributions in planar, Doppler-based velocimetry are significantly reduced by the application of structured illumination. The method works by measuring and separating desired flow-scattered signals from unwanted reflections and secondary scattering contributions via a sinusoidal intensity modulation across the laser sheet used to interrogate the flow. In the current work we consider the influence of background light on cross-correlation Doppler global velocimetry (CC-DGV) and present the results for measurements in a turbulent free jet with an exit Mach number of 0.5 in a measurement arrangement with high intensity background contributions. It is shown that if the ratio of the particle-scattering (i.e. Mie scattering) intensity to the background solid surface scattering (i.e. geometric scattering) intensity is greater than 10, then the measured signal displays a significant bias away from the true velocity. With structured illumination, the measured intensity corresponding to geometric scattering is reduced to negligible levels, reminiscent of a measurement arrangement with little or no background light influence. Centreline velocity measurements with this background subtraction method are compared with Kiel-type pressure probe measurements, yielding a root-mean-square (RMS) difference between the two of 1.2 m s^{-1} (less than 1% of the full scale velocity), well within the published uncertainty bound of the CC-DGV technique, underscoring the robustness of this approach. In addition to the centreline validation, the streamwise vorticity and total pressure are also analysed, showing trends indicative of the S-type shape of the duct and aggressive flow entrainment experienced in this environment.

Keywords: Doppler global velocimetry, structured illumination, background removal, optical diagnostics

(Some figures may appear in colour only in the online journal)

1. Introduction

Many applications in aeronautics research currently benefit from the robust and minimally intrusive optical measurements available today due to continuously advancing laser-based technologies. This is particularly true for *in situ* measurements of complex aerodynamic systems. For example, Virginia Tech has previously applied three-component, stereoscopic particle image velocimetry (SPIV) to study complex vortical flows, such as those seen in advanced propulsion/airframe integration concepts [1–3]. In addition to the application of PIV, other optical diagnostics, such as cross-correlation Doppler global velocimetry (CC-DGV) for three-component velocity [4, 5], and filtered Rayleigh scattering (FRS), for multi-property measurements [6–9], are being developed and applied for these types of *in situ* measurements.

Optical measurement techniques are gaining traction for complex environments over conventional probe measurements (e.g. Pitot-static, Kiel, 5-hole probes, and probe rakes) due to their ability to provide critical flow information while

remaining minimally intrusive on the flow being studied. As an added benefit, these measurements typically provide desired flow information at much higher spatial and temporal resolutions.

When any diagnostic technique (probes, optical, etc) is applied for complicated *in situ* measurements, there are added difficulties associated with measuring flow conditions near physical boundaries. Near these boundaries, whether a duct/tunnel wall or an aerodynamic model in a wind tunnel, is often where the most interesting regions of the flow for study are located. For the case of measuring internal flows, such as in the turbomachinary applications discussed previously, measurements near solid boundaries are the most desired region for accurate measurements due to the amount of work done on the flow by fan/compressor blade tips compared to the roots of the blade. Yet, these near-duct regions are often less characterized due the measurement challenges they present.

Using probes to measure conditions near physical boundaries causes increased flow interaction via the probe-wall flow potential, leading to inaccurate measurements [10]. Although the effects are different from the effects experienced by physical probes, applications of optical diagnostics also present challenges when trying to measure near physical boundaries. The laser light used in these applications to measure the desired flow properties typically scatters intensely off the physical surfaces and reduces or eliminates the possibility of accurate flow property measurement. For Doppler-based or spectroscopic measurements, such as in DGV and FRS, this geometrically scattered light carries no flow information and causes biases in the associated mesurements. For methods that track or correlate particle motion, as in PIV, background illumination increases the uncertainty in particle position determination, and thus, the associated velocity measurement precision.

The most common means to avoid the effects of background scattering in laser-based measurement techniques is to position the cameras in such a way that the geometric scattering is not seen or is being viewed at a grazing angle, reducing the imaged geometric scattering intensity, as employed in Bridges and Wernet [11]. The downside to this approach is that it can only be used in facilities that can successfully accommodate the required optical access. In most *in situ* applications, this arrangement is simply not possible: alternative methods must be used. In conventional DGV and PIV applications, background images can be taken without seed in the flow in order to subtract the background intensity from signal images [12, 13]. This method is generally effective but does not remove the additional intensity caused by secondary scattering from particles to geometric surfaces. Frequency scanning DGV methods such as CC-DGV also present another complication in that background images must be taken at every laser frequency used in the scan. This can add measurement time and uncertainty in the measurement if the background images are not taken at the exact same set of laser frequencies as the measurement images.

Other approaches to avoid geometric scattering include changing the wavelength of the light scattered from the background by treating the surface with a fluorescent coating that absorbs the laser light and re-emits it at a different wavelength. This scattered light can then be filtered out using an optical filter [14]. Past efforts, specific to PIV, include both simple and complicated post-processing algorithms that remove background contributions, such as those described by Mejia-Alvarez and Christensen [15] and Honkanen and Nobach [16], or coloring the flow tracer particles with a fluorescent dye and rejecting the laser wavelength, and as a result, the background scattering [17, 18].

Providing an alternative method to those mentioned above, we discuss a means for significantly reducing the effects of background scattering by a novel application of structured illumination. The method of structured illumination, or more precisely termed structured laser illumination planar imaging (SLIPI), was first presented for removing background scattering in CC-DGV measurements by Boyda *et al* [19]. The method removes geometric scattering by applying a well-defined sinusoidal intensity modulation along the width of a laser sheet. This intensity modulation allows for the simultaneous acquisition of the desired Mie scattering intensities necessary for DGV measurements and geometric or background scattered light, including secondary scattering. Since the background scattering does not follow the applied intensity modulation, the background illumination can be determined everywhere in the image and removed. The remaining intensity profile only contains light scattered from the laser sheet, resulting in a pristine measurement with no background contamination.

This method of background removal is then presented as a simple and robust means for removing background scattering in Doppler-based velocity measurements. To validate the approach, a demonstration is conducted in a measurement environment constructed to simulate an *in situ* turbomachinery inlet application. A turbulent jet containing three-dimensional flow is introduced near a curved wall boundary and measurements are made using CC-DGV. The results indicate that velocity bias errors arising from background scattering are reduced to levels expected for pristine measurement situations in which background contributions are negligible.

The paper is organized as follows: the CC-DGV measurement principles are briefly reviewed in section 2 before sections 3 and 4 introduce uncertainties from background scattering and the mitigation of background scattering by SLIPI, respectively. Section 5 contains the description of the demonstration experiment conducted, and the results from this experiment are analyzed and discussed in section 6. Finally, the study is summarized and concluded in section 7.

2. Cross-correlation Doppler global velocimetry

In past works CC-DGV has been presented as a conceptually simple, yet robust, technique for measuring three-component velocities [20]. CC-DGV has also been demonstrated to provide high spatial resolution measurements, with low uncertainty values of $\pm 2\,\mathrm{m\,s^{-1}}$ (absolute) over a nearly unlimited dynamic range [20, 21]. These attributes, along with technique development for a broad range of applications

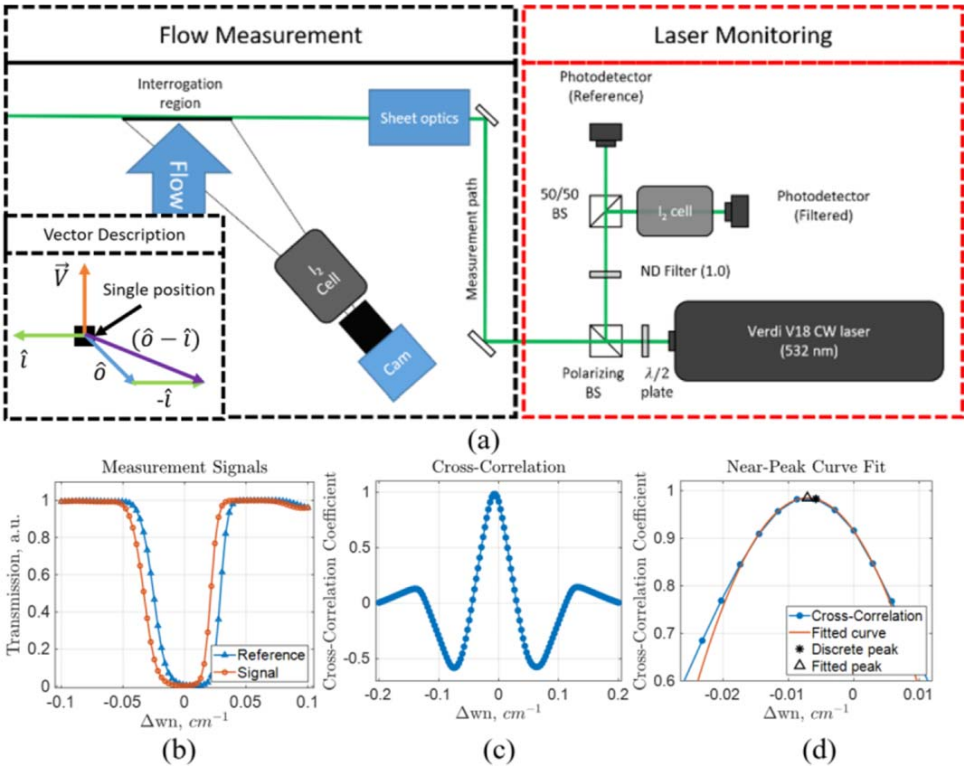

Figure 1. Typical cross-correlation Doppler global velocimetry hardware arrangement and processing for velocity measurement.

[4, 5, 22], provide ample motivation for improving the technique with background removal techniques such as structured illumination.

The basic working principle behind CC-DGV is that a single-frequency laser beam is split into two paths, a low-power reference path and a high-power measurement path (figure 1(a)). Two photodetectors are used in the reference path to measure the amount of laser light which passes through a molecular vapour cell (transmission), a function of the frequency of the laser light, the amount of vapour in the cell, and the length of the cell itself. For this application, we use a 532 nm continuous wave laser and molecular iodine in vapour phase, which has been spectroscopically characterized by Forkey *et al* [23] for wavelengths near 532 nm. The use of the iodine vapour cell acts as a very fine notch filter, allowing the user to resolve an exceptionally high finesse measurement of the laser frequency.

The high power laser path is formed into a sheet and directed into the flow region of interest. Incident laser light is then scattered off small tracer particles in the flow (i.e. flow seeding), through elastic Mie scattering. This scattered light, now carrying flow velocity information in the form of a Doppler frequency shift, is collected on camera pixels immediately after passing through another iodine vapour cell identical to the one present in the reference path.

Measurement spectra are recorded simultaneously from both the reference path and the interrogation region by recording the transmission value through the vapour cell at a discrete set of laser light frequencies. To obtain the presented measurement sensitivity, this frequency range must be chosen to include at least one absorption line associated with characteristics of the vapour in the cell (figure 1(b)). Cross-correlating the transmission spectra recorded from the reference path and that from the camera pixels yields the cross-correlation coefficient as a function of the frequency shift between them (figure 1(c)). A parabola is then fit to a few points near the peak of the cross-correlation spectrum to obtain an analytical expression for the position of the maximum value of the cross-correlation coefficient, reducing errors associated with signal discretization (figure 1(d)). The frequency shift associated with this maximum value then corresponds to the average Doppler frequency shift [4]. This frequency shift is related to the measured velocity using the Doppler shift equation

$$\Delta\nu = \frac{(\hat{o} - \hat{\imath}) \cdot \vec{V}}{\lambda} \tag{1}$$

where $\Delta\nu$ is the measured Doppler frequency shift as a result of the local flow velocity, $\vec{V}$, the wavelength of the incident light, λ, and the optical geometry parameters, $\hat{o}$ and $\hat{\imath}$,which are the unit vectors of the locally scattered light direction and the laser propagation at a single pixel, respectively (lower left of figure 1(a)). The vector given by $\hat{o} - \hat{\imath}$ is referred to as the sensitivity vector and gives the direction of the measured Doppler velocity [4].

To obtain three-component velocity at a single point, one must make three independent measurements of the Doppler shift (i.e. different values of the sensitivity vector) by varying

either the laser direction or camera positions. For an analysis of errors associated with obtaining multi-view measurements, the reader is directed to Charrett *et al* [24].

For the present application, the measurement region was illuminated using a single laser sheet and observed from three different detector angles simultaneously, providing the required variation of the sensitivity vector. The three measured Doppler shift velocities are then rotated to orthogonal components by the rotation matrix defined as

$$\begin{bmatrix} U \\ V \\ W \end{bmatrix} = \begin{bmatrix} (\hat{o}-\hat{i})_{1x} (\hat{o}-\hat{i})_{1y} (\hat{o}-\hat{i})_{1z} \\ (\hat{o}-\hat{i})_{2x} (\hat{o}-\hat{i})_{2y} (\hat{o}-\hat{i})_{2z} \\ (\hat{o}-\hat{i})_{3x} (\hat{o}-\hat{i})_{3y} (\hat{o}-\hat{i})_{3z} \end{bmatrix}^{-1} \begin{bmatrix} U_1 \\ U_2 \\ U_3 \end{bmatrix} \quad (2)$$

where the subscripts of $(\hat{o}-\hat{i})_{n\xi}$ represent the ξ-component of $(\hat{o}-\hat{i})$ for the n^{th} detector, U_n is the measured Doppler velocity from the n^{th} detector (i.e. $(\hat{o}-\hat{i}) \cdot \vec{V} = \lambda \Delta\nu$ in equation (1)), and *U, V*, and *W* are the flow velocities expressed in Cartesian coordinates [4].

3. Effects of geometric illumination in CC-DGV measurements

As the foundational measurement in CC-DGV is an intensity-based spectral distribution, unwanted background contributions directly impact the fidelity of the measurement. The desired signal is a Doppler-shifted transmission spectrum obtained from filtered and unfiltered intensity signals arising from Mie scattering by particles following the flow. In contrast, the geometry of the test apparatus, present in the background (or foreground) of a measurement, does not move relative to the detector; and, therefore, the light scattered from these sources is not Doppler-shifted. Unfortunately, these geometric contributions can be a significant proportion of the overall measured intensity. While conventional background subtraction techniques remove most of the geometric scattering, secondary scattering from the seeded particles remains a serious concern. Measured spectra that contain scattering from both particles seeded into the flow and geometrical structure are observed as being distorted in shape with a Doppler shift of lower magnitude than the pure flow-scattered signal. This effect results in an artificially reduced Doppler shift when using the cross-correlation method, biasing the velocity estimation.

Figure 2 shows the described effect of varying levels of geometric scattering present in a simulated CC-DGV intensity spectrum, presented here as an intensity ratio defined as $IR = I_{Mie}/I_{Bknd}$, where I_{Mie} is intensity of the desired, flow-scattered light and I_{Bknd} is the intensity of the undesired light from geometric and secondary scattering. The black curve is the zero-shift reference spectrum and the other curves represent a Doppler shift of 0.0125 cm^{-1}, corresponding to a measured velocity of 200 m s^{-1}, with increasing levels of background contributions. The case where the intensity ratio is infinite ($IR = \infty$) corresponds to a signal with no geometric scattering present in the signal. The effects of non-negligible geometric scattering contributions can be clearly seen between the pristine signal,

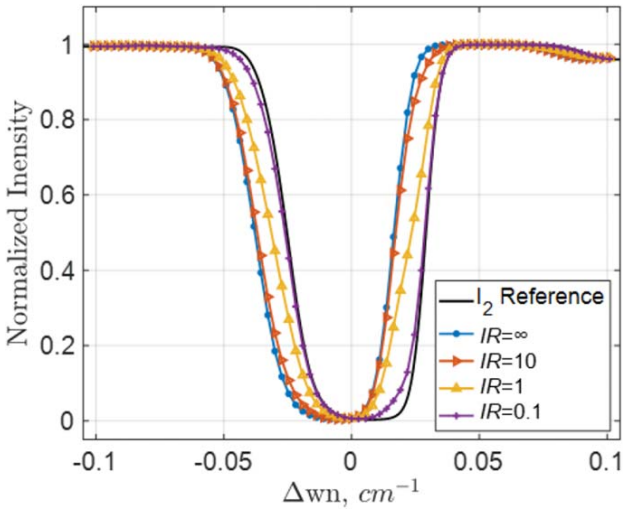

Figure 2. Background contributions on a typical DGV signal. IR is the intensity ratio defined as the ratio of Mie and background scattering intensity ($IR = I_{Mie}/I_{Bknd}$).

$IR = \infty$ (blue dotted), and heavily corrupted signal, $IR = 1$ (yellow vertical triangle), case where the Mie and geometric scattering intensity are the same order of magnitude. When this is the case, a significant shift from the pure Doppler shifted signal is observed. Even in the presence of a background signal an order of magnitude lower in intensity than the recorded Mie signal ($IR = 10$), we observe an influence on the resulting signal. When the signal is dominated by geometric scattering, such as the case where $IR = 0.1$, the accurate measurement of any Doppler shift between the signal and the reference spectrum becomes impossible.

Thus, we conclude that the presence of geometric scattering in CC-DGV signals introduces a negative bias in the Doppler shift magnitude, related to the fractional contribution of the geometric scattering in the measured signal. It is observed that if geometric scattering is recorded at a high enough intensity ($IR \leqslant 10$)), it is detrimental to the estimation of Doppler shift (and thus velocity) using CC-DGV, thus, reliable velocity measurements with this technique demand that this effect be mitigated as much as possible.

Other major forms of measurement uncertainty in CC-DGV are encapsulated in the work presented by Cadel and Lowe [20] which include a random noise contribution due to the AD conversion factor of the camera, as well as the Poisson distributed shot noise associated with the measurement intensity recorded by the technique compared with the dynamic range of the sensor. In combining these two effects, the uncertainty in velocity estimation is well bounded by the 2 m s^{-1} value presented in this work.

Since the bias errors due to background contributions can range from zero (at all negligible background contribution conditions) to the entire dynamic range of the measurement (at extreme background contribution conditions) it is difficult to quantify the errors in velocity due to background contribution in comparison with the errors associated with random and shot

noise. But since the biases have the possibility to be very large, we can say that the geometric scattering errors, when present at significant levels, dwarf the errors associated with random and shot noise. Note that the uncertainty associated with random and shot noise bounds the error at 2 m s^{-1}, which corresponds to a Doppler shift error of 0.000125cm^{-1}, while the maximum error associated with geometric scattering contributions in the simulation presented in figure 2 is 200 m s^{-1}, corresponding to a Doppler shift error of 0.0125 cm^{-1}, 100 times greater than the random error.

4. Structured laser illumination planar imaging

The method of structured laser illumination planar imaging (SLIPI) is the result of combining two separate imaging techniques, structured light and laser light sheet imaging. The structured light technique was developed by Neil *et al* [25] to improve three-dimensional imaging using a conventional wide-field microscope, while laser sheet imaging has been widely used in flow visualization and laser-based diagnostics.

The SLIPI method was developed, and has primarily been used, to suppress multiply-scattered light in sprayed particle visualization experiments. For example, Kristensson *et al* [26] determined that the multiply-scattered light removed in these sprayed particle experiments is identical to stray/background scattering in terms of its imaging characteristics, and were able to successfully apply and evaluate how well the SLIPI method was able to remove stray light in determining the temperature of a CH_4/air flame with varying background complexity using Rayleigh thermometry. The method has also been applied to quantitative imaging of thermographic phosphor particles for gas phase temperature measurements [27, 28], underscoring the versatility of the approach.

SLIPI background removal relies upon the intensity modulation of an illumination laser sheet with a uniform and well-defined frequency. The Mie-scattered photons originating directly from this pattern retain the imposed pattern, and any light that is scattered from other sources are seen as inconsistencies in the applied pattern. Because these inconsistencies can be differentiated from the pattern applied to the laser sheet, they can be accounted for and removed.

The most common way to remove the unwanted stray light in a specific illuminated region of interest is to record a series of images with the sinusoidal intensity pattern imposed on each one. Each one of these images are taken with a different phase shift applied to the sinusoidal pattern. For example, the intensity pattern phase shifts for a SLIPI implementation using three images would be $\phi_1 = 0^o$, $\phi_2 = 120^o$, and $\phi_3 = 240^o$. The corrected signal image with the stray light removed is then calculated from the series of images, given by Kristensson *et al* [26] as

$$I_S = \sqrt{(I_{\phi_1} - I_{\phi_2})^2 + (I_{\phi_1} - I_{\phi_3})^2 + (I_{\phi_2} - I_{\phi_3})^2} \qquad (3)$$

and adapted from a three-image series into a general number of phase shifts as

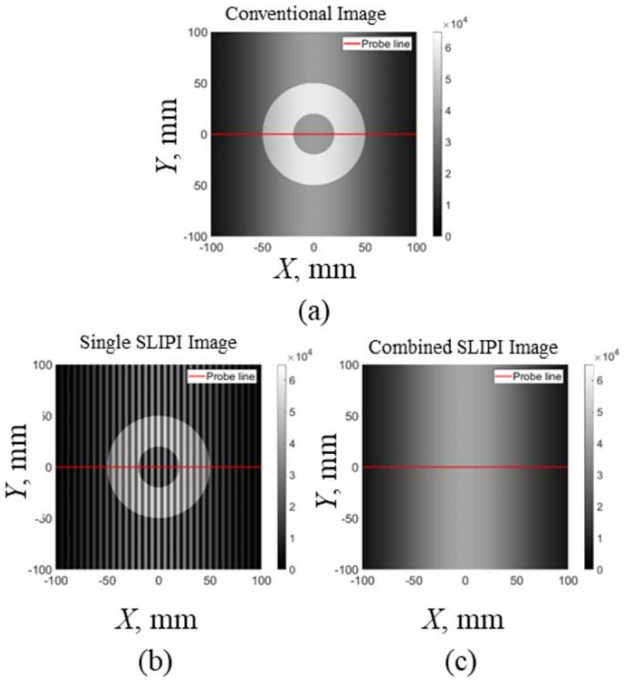

Figure 3. Intensity comparison between conventional planar sheet imaging (a), image collected using the SLIPI method at a single phase shift (b), and the image resulting from SLIPI method application (c).

$$I_s = \left[\sum_{\substack{i,j=1 \\ i \neq j}}^{N} (I_{\phi_i} - I_{\phi_j})^2 \right]^{1/2} \qquad (4)$$

where I_S is the composite laser sheet image, I_{ϕ_k} is the recorded sinusoidal light sheet image of the k^{th} phase shift, and N is the total number of recorded phase shifts. This specific evaluation combines the intensity of all three images by adding together intensities that are different between the set of three images, dominated by the modulated intensity pattern, and removes the intensity signatures that are present in all the phase-shifted images at every pixel. An example of a simulated three-image SLIPI background removal can be seen in figure 3(a). Figure 4 shows the resulting intensity profiles for the 3-image SLIPI application (a) and the conventional sheet image intensity compared to the image processed using the SLIPI method (b). These figures show that the intensity contribution of the disk in the background may theoretically be completely removed with the application of the SLIPI background removal technique.

Although figures 3 and 4 display the effectiveness of the SLIPI method in removing the geometric scattering from an image, there is one main limitation associated with it. Since the camera is only able to measure a limited dynamic range of intensities, the maximum intensity (signal + background) of background that can be effectively removed is then limited to the saturation intensity of the camera. By simple inspection of equation (3), we can see that if a region of the image

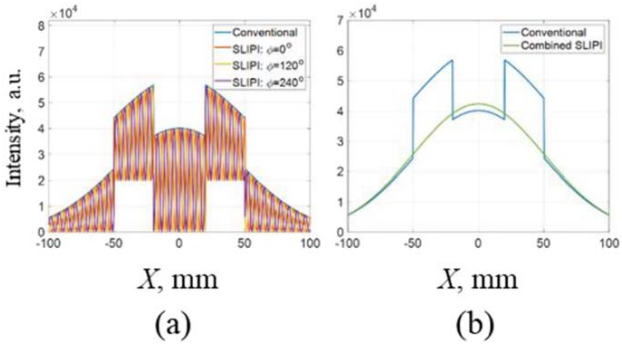

Figure 4. Centreline intensity profiles from the intensity images in figure 3. (a) shows the individual SLIPI image intensity profiles compared to the conventional sheet intensity (blue) and (b) shows the intensity comparison between the SLIPI processed image (green) and the conventional sheet image intensity with the background intensity included.

is saturated in all individual SLIPI images (identical recorded intensity), the intensity of the resultant image in that region will be zero, and no measurement signal is extracted. Therefore, the total intensity recorded must be below the saturation threshold of the camera in each image to extract any measurement information.

The main disadvantage of this technique applies directly to the chosen application of multi-image SLIPI background removal. The applied method requires that a minimum of three images to be taken to obtain a single measurement point with the background removed, effectively tripling the acquisition time of the measurement. Since CC-DGV is a mean velocity measurement in any case, the SLIPI application results in a modest increase in optical complexity and acquisition time when compared to conventional DGV measurement, while dramatically reducing stray and background light contributions. It should be noted that another, less common, post-processing technique for background removal using SLIPI is described in detail by Berrocal *et al* [29] and allows for the removal of the background intensity by the acquisition of a single image using a spatial Fourier transform technique, thus, reducing acquisition time at the expense of spatial resolution. The reader is referred to this work as well as [26] for further details.

5. Flow measurement environment

An experimental demonstration and validation of the SLIPI application for CC-DGV measurements in a representative flow setup was conducted. The flow apparatus and CC-DGV setup are depicted in figure 5, consisting of a blower-driven jet flow, a duct, and the optical components of the CC-DGV system. The primary objective in the current setup was to demonstrate the effectiveness of the SLIPI technique for planar mean velocity measurements in a confined environment with geometric complexity and limited optical access.

The flow was driven by a Busch Panther WA13125DP rotary lobe, positive displacement blower capable of discharging 0.74 $m^3\,s^{-1}$ at ambient conditions of 101 kPa and 21 °C with an outlet diameter of 152 mm. The flow was directed to the measurement region using ducting, contracted down to an exit diameter of 76 mm, and exhausted into the test section at ambient pressure 25.4 mm upstream of the measurement location. This environment created a turbulent jet flow with an approximate exit Mach number of 0.5, and was characterized by traversing a Kiel-type probe, measuring total pressure and temperature, across the centreline of the nozzle exhaust in increments of 3 mm. To simulate some aspects of the confinement for *in situ* measurement applications, the measurement region was positioned inside of a round 533 mm diameter duct, analogous to the walls of a circular cross-section wind tunnel. The laser sheet entered and exited the duct through two anti-reflection-coated acrylic windows above and below the interrogation region, respectively.

5.1. CC-DGV instrument

The CC-DGV instrument setup consisted of a continuous wave laser, laser frequency monitoring subsystem, flow illumination optics, and camera modules, as depicted in figure 5. The coordinate system used in this experiment consists of *Z*, aligned with the primary/axial flow of the jet with the *X* and *Y* axes directed to the right horizontally and vertically upward respectively. The measured velocities corresponding to the *X, Y*, and *Z* directions are *U, V*, and *W* respectively.

A continuous wave Coherent Inc. Verdi V18 model laser is used. This laser is a single-frequency, diode-pumped, solid-state laser with a maximum output power of 18 W at 532 nm and a linewidth of 5 MHz. The emitted beam has a diameter of 2.25 mm with a beam divergence of less than 0.5 mrad. The laser frequency may be coarsely adjusted, on the order of tens of gigahertz, via the internal etalon, while finer-scale frequency tuning may be achieved by changing the internal cavity length in the laser head using a piezoelectric stack (PZT). The frequency scanning required for the CC-DGV measurements is done by applying voltage to the PZT using a BK Precision DC power supply with a voltage range of 0–72 V, resulting in a fine-tuning bandwidth of about 6.4 GHz. Frequency monitoring of the laser is done by collecting the transmission spectrum through a molecular iodine vapour cell. The iodine cell used is an ISSI I2S-5, which is 127 mm long and 76 mm in diameter and is operated in a starved cell configuration with a vapour pressure of 0.675 Torr, maintained during testing by operating at least 20° C above the point where all the iodine in the cell will exist in the vapour state so that the vapour pressure does not fluctuate with minor fluctuations in cell temperature. To collect the reference transmission spectrum, the reference path (upper right of figure 1) is split into two paths using a 50/50 beam splitter, and the intensity of each path is monitored using a ThorLabs PDA100A Si free-space amplified photodetector (PD). One of the paths travels directly to a PD and is used normalize laser output power fluctuations, while the second PD is used to measure the intensity of the beam passing through the reference iodine cell. The ratio between the two PD signals provides the reference iodine transmission spectrum.

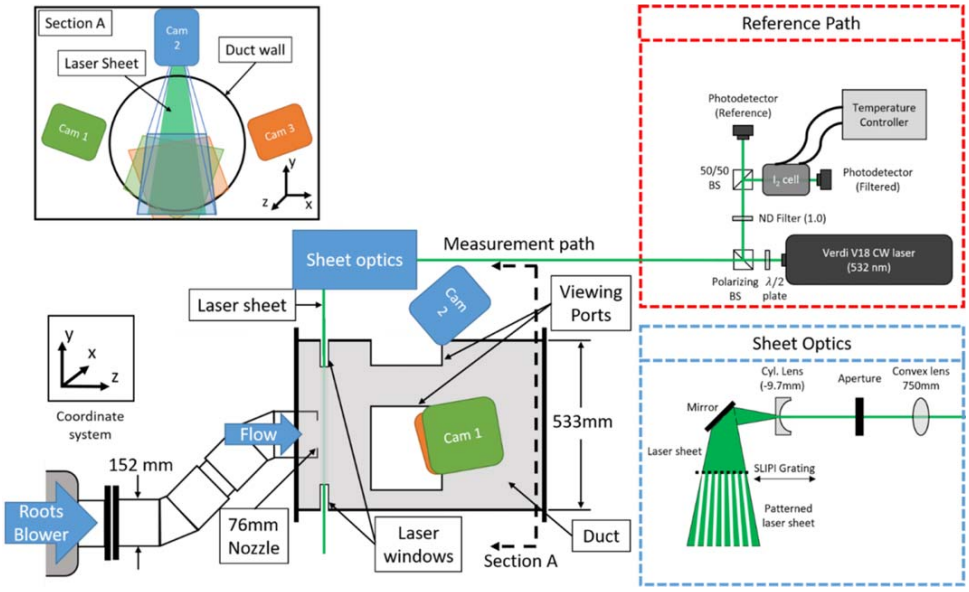

Figure 5. Experimental setup used for the current CC-DGV experiment. The coordinate system used consists of *Z*, aligned with the primary/axial flow with *X* and *Y* axes directed to the right horizontally and vertically upward respectively. The corresponding measured velocities are noted as being *U, V*, and *W* corresponding to the *X, Y*, and *Z* directions respectively. Note the coordinate systems depicted do not reflect the actual origin of the experiment, but the general direction of the axes. The origin is centred on the centre of the jet exhaust.

A theoretical spectral model for iodine absorption developed by Forkey *et al* [23] is then used to map the applied PZT voltage to frequency relative to the centre of the chosen iodine absorption line.

To expand the measurement path beam into a laser sheet and impose the intensity pattern on it, the beam is directed to the sheet-forming optics, expanded using a −9.7 mm focal length cylindrical lens and then passed through a custom-designed metal grating to form the patterned laser sheet, seen in the lower right of figure 5. This sheet is then passed through the test section and imaged using three different camera module assemblies, seen in section A of the imaging environment in the upper left of figure 5. A detailed description of the camera assemblies used can be found in Saltzman *et al* [19].

The camera assemblies were located downstream of the nozzle and were arranged such that there was one assembly positioned around the duct circumference at 3, 9, and 12 o'clock. Basic schematics of the described camera arrangement and flow region are also included in figure 5. The challenge incurred from high background interference was intentionally increased in this study by adding a layer of light-coloured masking tape to both the nozzle and the duct wall to scatter more light into the measurement. This treatment can be seen in the conventional planar image in figure 6(c). The laser power and exposure times were adjusted to avoid camera saturation everywhere except for the laser impact region.

The camera modules consist of two 3.2 megapixel FLIR, 12-bit, Blackfly S model BFS-U3-31S4M-C, machine vision cameras, both with identical 16 mm c-mount lenses and 532 nm band-pass filters, in addition to an ISSI I2S-5 iodine molecular vapour filter identical to the one used in the laser frequency measurement path. The vapour cell was mounted in front of a single camera to record the filtered images, while the other camera was positioned to record images viewing the same interrogation region for an unfiltered intensity reference. In application, the cameras were calibrated using the open-source version of the Matlab camera calibration toolbox of Zhang [30] and the pixels were binned in 20 × 20 pixel regions resulting in a spatial resolution of approximately 4 mm in both the *X*- and *Y*-directions. The sensitivity vector of equations (1) and (2) are then determined by the real space position of the mapped pixels and the sensor as well as the local propagation direction of the laser at each pixel.

5.2. SLIPI implementation

Past applications of SLIPI have often utilized a Ronchi grating to create the intensity modulation in the laser light sheet, but due to the low damage tolerance of commercially available rulings, along with the high laser powers required in imaging large fields of view in DGV, an alternative method had to be devised to impose the pattern. Kristensson *et al* [26] and Kempema and Long [31] found that, in order to accommodate the laser energy required for Rayleigh scattering thermometry, they could induce optical interference patterns in their laser sheets by the implementation of a two-faceted optical component and by a split-beam method, respectively. In our application, we chose to create a custom subtractive grating by machining an aluminium plate with equally-spaced slots for a physical line pair width of 0.762 mm. This provided further optical simplicity with the added benefit of adjustability for the imaged pattern size by changing the relative positions of the grating and the

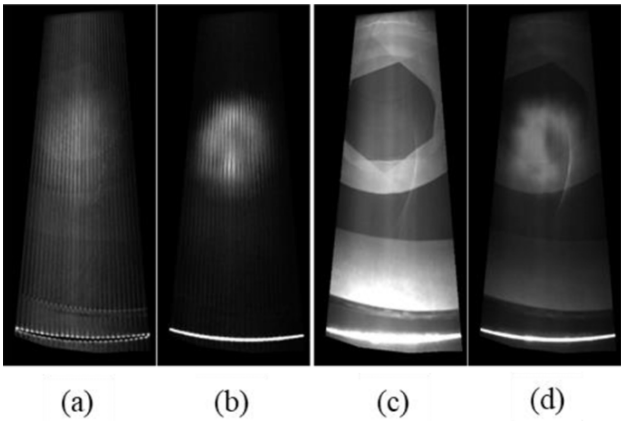

Figure 6. SLIPI processed ((a) and (b)) and conventional sheet images ((c) and (d)) collected for velocity measurement. (a) and (c) show the image in a high transmission region of the iodine spectrum while (b) and (d) are shown in a low transmission region.

sheet-forming cylindrical lens. As a subtractive grating, a major drawback of this choice is the loss of about 50% of the total laser light originally present in the sheet for each individual SLIPI image.

The arrangement used in this study can be seen in the lower right of figure 5, where the SLIPI grating is placed after the cylindrical lens. It should be noted that in this implementation the high intensity sections of the sheet intensity modulation are thinner than the low intensity sections in the individual SLIPI images. This results in combined images with low intensity streaks as seen in figure 6. This artefact seems only to affect our minimum resolvable spatial resolution.

5.3. Reference measurements

For measurement validation, reference total pressure and temperature measurements were taken in the plenum of the jet during all compared measurements. In addition to the conditions measured in the plenum, Kiel-type total pressure and temperature measurements were also collected at the nozzle exit and used as a velocity reference. Quantitative comparisons to flow reference measurements obtained using the Kiel probe allow a more rigorous assessment of the velocity results obtained using CC-DGV. These measurements were collected along the horizontal centreline of the nozzle, near the axial plane where CC-DGV measurements were collected. With the ambient conditions known, one may readily calculate the isentropic exit velocity of the flow via the first law of thermodynamics and isentropic relations using

$$V_{tot} = \sqrt{\frac{2\gamma RT}{\gamma - 1}\left[\left(\frac{p_0}{p}\right)^{\frac{\gamma-1}{\gamma}} - 1\right]} \tag{5}$$

where p_0 is the measured total pressure, p is the ambient static pressure, and T is the static temperature of the flow. The velocity calculated along the centreline is then taken as representative of the jet. For velocity comparisons, we calculate the total velocity of the CC-DGV measurements from all three orthogonal components of velocity measured as

$$V_{tot} = \sqrt{U^2 + V^2 + W^2}. \tag{6}$$

In section 6.3, the reference and CC-DGV velocity measurements are directly compared to provide a quantitative error analysis of the effectiveness of the approach.

6. Results

The results presented in this work are used to demonstrate the capability of SLIPI background removal in Doppler-based velocity measurements, specifically its effectiveness in eliminating background/geometrical scattering contributions in cross-correlation Doppler global velocimetry which lead to biases in measured velocities. In sections 6.1 and 6.2 we look at the effectiveness of the SLIPI technique in removing unwanted background scattering from the recorded images and then compare the measured Doppler shifts from the SLIPI processed images and the conventional sheet imaging respectively. In section 6.3 we look at the three-component velocity results and compare the total velocity with the measured probe results, and in section 6.4 we look at the streamwise vorticity and total pressure results calculated from the CC-DGV measurements.

6.1. Background reduction

Concerning the effectiveness of the SLIPI background removal technique, once applied to the recorded images, a significant qualitative reduction in the background illumination of the images can be noticed immediately as seen in figure 6. The SLIPI-processed images from module 2 (12 o'clock position) seen in figure 6(a), which experiences the most extreme background scattering as a result of its observation angle, shows very little remaining background illumination when qualitatively compared to the conventional sheet image in figure 6(c). We see that the scattering from the nozzle face and wall are nearly eliminated while the only remaining illumination is from the laser impact region and the impacted window. In the laser impact region we also see the saturation limitation of the SLIPI method mentioned in section 4, where the intense laser impact causes a zero-intensity region in the SLIPI processed images.

An unexpected, yet attractive result seen in this basic analysis of these images is the effective removal of a reflection from the lower window, seen as a bright streak near the middle of the conventional sheet images in figures 6(c) and (d). The removal of this reflected light is a very desirable result of SLIPI application because CC-DGV measurements are dependent on the local direction of the laser, and in this region the laser direction is very difficult to determine, and also significantly different from the rest of the laser sheet, resulting in a completely different scattering spectrum, and thus an estimated velocity. Note that this bright streak was also present in the individual SLIPI images, but due to its constant position within the image, it was removed in the SLIPI processing.

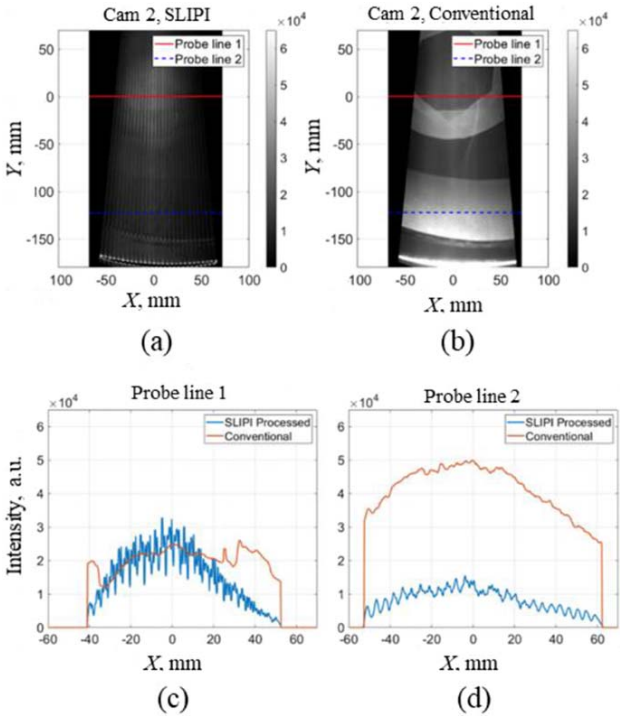

Figure 7. SLIPI background removal inspection at $Y = 0$ mm and $Y = -120$ mm.

Figure 7 shows two sets of profiles from the above images to display how the variation in intensity across the SLIPI-processed and conventional sheet images compare. Figure 7(c) shows an intensity profile across the centre of the measurement region ($Y = 0$ mm) for all values of X. In this image we can clearly see that in the regions of high background scattering on the nozzle (right and left hand sides of the profile) that the SLIPI processing reduces the intensity to display a much more Gaussian-like profile, expected for the laser sheet. More importantly, in the region where there is little-to-no significant background scattering, we see that the SLIPI-processed profile closely matches the profile derived from the conventional sheet image. Also note that the bright steak noted earlier is clearly seen in the middle right ($X = 25$ mm) of the conventional profile with no notable effects seen in the SLIPI profile. These profiles show that the SLIPI processing is extremely capable of removing the unwanted background scattering associated with complex *in situ* optical measurements without compromising the integrity of the combined image where the background intensity is negligible.

Figure 7(d) shows a similar profile but this time taken across the image at $Y = -120$ mm. In this comparison we see that the wall scatters approximately 3–4 times the amount of light to the detector as the recorded Mie-only signal from the SLIPI processed image, and is presented to show the effectiveness of the SLIPI method in removing geometric scattering in extreme cases. Referencing the analysis conducted in section 3, this case would present a signal which would be impossible to obtain an accurate result for Doppler shift with

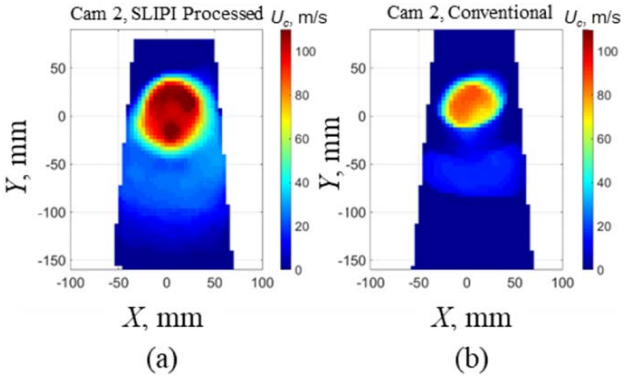

Figure 8. Sensed velocities measured for both the SLIPI processed (a) and the conventional sheet images (b) recorded by module 2 located at the 12 o'clock position in figure 5. Note that in regions with less background scattering result in a measured velocity, while regions dominated by geometric scattering estimate very little to no Doppler shift.

no other geometric scattering mitigation techniques applied. Additionally, due to the level of geometric scattering in this region we would expect to see very little to no Doppler shift determined in this region, and indeed when we look at the results for Doppler shift velocity presented in figure 8, this is exactly the case.

Thus, when the SLIPI method is applied to images with significant background, we can remove the unwanted geometric scattering, leaving only the desired Gaussian distributed laser intensity in the image, resulting from Mie scattering only, underscoring the in application robustness of the method. (Note that the 'noisy' appearance of the intensity profiles seen in figure 7 are due to artifacts in the variation of intensity in the laser sheet resulting in lines of high and low intensity.)

6.2. Measured frequency shifts

As outlined in section 3, the presence of geometric scattering in a CC-DGV signal causes a Doppler-shift bias towards the zero-shift reference spectrum. In figure 8, the sensed velocities from module 2 (12 o'clock) in the region over the nozzle face between $Y = -50$ mm to $Y = -10$ mm display the predicted bias in estimated Doppler shift magnitude. This is a direct result of the geometric scattering dominance in this region. The SLIPI-processed results in figure 8(a) exhibit dramatically different flow features and details consistent with the basic expectations for this setup, including significant entrainment velocities in the lower regions of the measurement field due to the ejector pumping effects of the jet. Further quantitative analysis to establish the validity of these results will be provided to follow by considering the three-component velocity measurements obtained by incorporating the results all three camera modules using equation (2).

6.3. Three-component velocity

The three-component velocity contours of this flow region derived from the SLIPI-processed CC-DGV images are

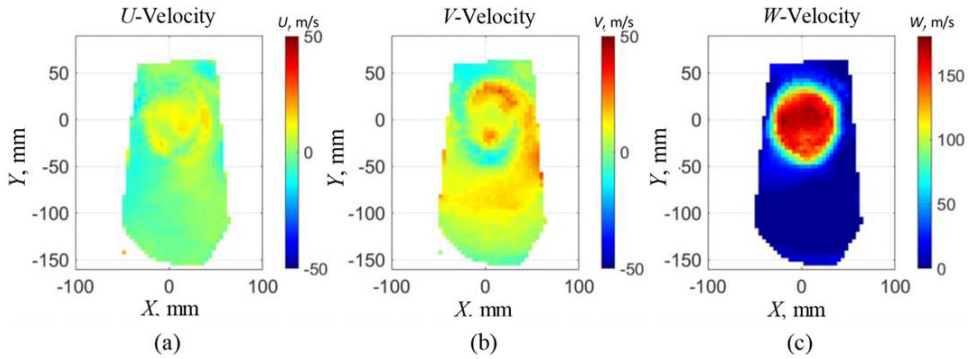

Figure 9. Orthogonal velocity contours derived from the SLIPI processed CC-DGV images representing the *U, V*, and *W*-components of velocity in (a), (b), and (c) respectively.

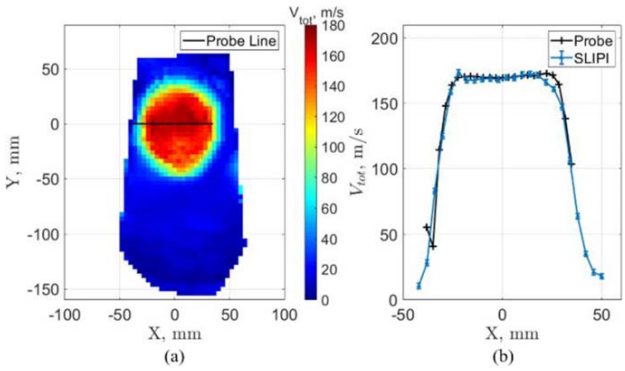

Figure 10. Total velocity contour with probe traverse line designation (a) and total velocity profile comparisons (b) with error bars indicating the uncertainty in the CC-DGV measurements ($\pm 2\,\mathrm{ms}^{-1}$). Note that the errors in the Kiel probe measurements are approximately 0.1%.

provided in figure 9. The application of SLIPI to the CC-DGV technique has not only reduced the geometric scattering contributions to usable levels but has also allowed the recovery of interesting structure in the secondary flow that is realistic given: (i) the double-bend in the 6″ plenum and (ii) setup-specific entrainment that was observed in the lower portion of the rig (the positive V velocity present for $Y < -50\,\mathrm{mm}$ in figure 10(b)). We can also note the smooth contour seen in the W-velocity plot indicative of the nearly constant velocity core of the jet to the gradient outside of the core representing the developing shear layer as a result of this experimental setup.

Figure 10(a) shows the location of the probe-measured profile on the total velocity contour, and as such, the position where the comparison data were taken. Figure 10(b) shows the probe-derived and DGV-derived total velocity profiles, located at the horizontal centreline of the jet, calculated from equations (5) and (6), respectively, and plotted against one another. The velocity magnitude differences seen in the shear layer are likely due to a small difference in the axial position of the CC-DGV plane with respect to where the probe data were acquired. The SLIPI/CC-DGV velocity profile closely matches the probe measurements in the core region of the jet, defined here as $-19\,\mathrm{mm} \leqslant X \leqslant 19\,\mathrm{mm}$, with a root-mean square (RMS) difference of 1.2 m s^{-1}, within the established uncertainty bounds of CC-DGV and the Kiel probe.

In addition to the calculated RMS difference, which displays the similarity in magnitude between the two measurements, the shape of the velocity profile determined using CC-DGV also closely matches the shape observed in the acquired probe measurements. In the jet core region, there is a slight decrease in the total velocity magnitude near the $X = 0$ mm position in figure 10(b). This mild reduction in the total velocity is a result of the double bend in the ducting, causing internal separation and thus a loss in total pressure in the separation region [32]. Thus, the results indicate that the SLIPI background removal technique reduces the geometric scattering contribution to levels expected for pristine measurement situations in CC-DGV applications in which background contributions are negligible.

6.4. Streamwise vorticity

To demonstrate the application of the approach for measuring flow three-dimensionality, the streamwise vorticity was calculated from the secondary velocity vectors estimated using the CC-DGV technique with SLIPI background removal by application of the discrete form of the vorticity equation given as

$$\vec{\Omega} = \left(\frac{\partial V}{\partial X} - \frac{\partial U}{\partial Y}\right)\hat{k}. \tag{7}$$

The streamwise vorticity is presented in figure 11(b), while with the axial velocity contours with the secondary velocity vectors overlaid are provided in figure 11(a). For clarity, the position of the nozzle exit has also been overlaid onto these plots, seen as a black circle, to assist in the association of measured flow characteristics with either the internal flow resulting from the geometry of the duct or the external flow associated with the flow entrainment.

The CC-DGV velocity estimation has captured some very interesting features present in this flow field. In figure 12(b) there are two significant counter-rotating vortex pairs located in a sector between the 4 and 8 o'clock positions relative to the nozzle exit. The pair located entirely inside of the nozzle exit boundary are a direct result of the S-bend in the ducting prior to

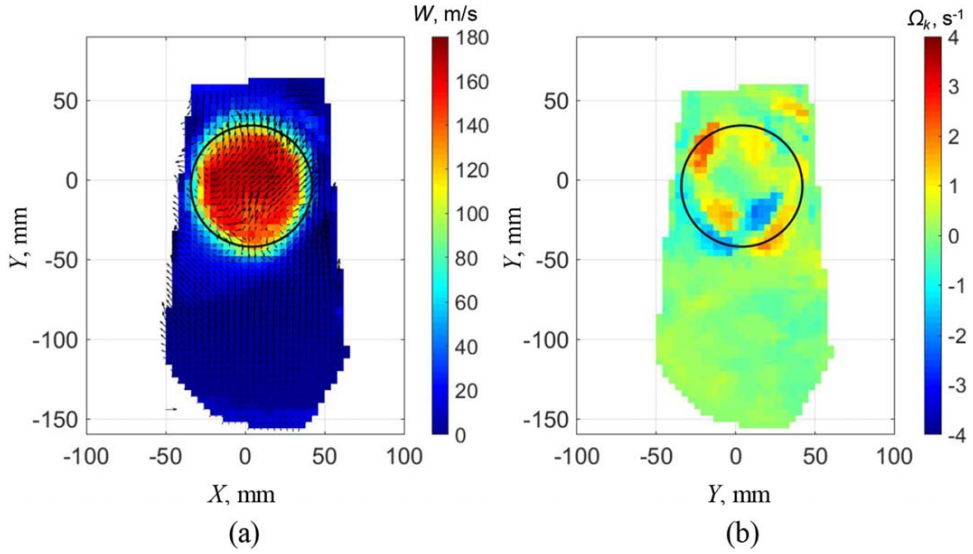

Figure 11. Axial velocity contour with overlaid secondary velocity vectors (a) and streamwise vorticity (b). The black ring in these figures represent the nozzle exit diameter for reference. Note that the vector in the lower left represents a velocity of 20 m s^{-1}.

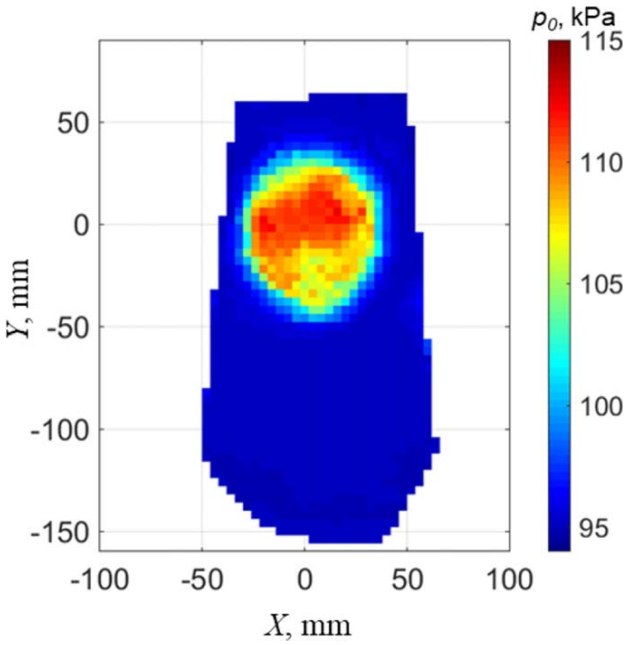

Figure 12. Total pressure calculated from CC-DGV measurements. The region of low total pressure in the lower section of the jet core region is a result of the separation off the second bend in the duct.

the contraction, seen above in figure 5. This bend causes separation to occur at the inside of the turn within the duct, which results in the observed counter-rotating vortex pair within the primary flow [32].

The vortices located approximately on the nozzle exit line in the same region (between 4 and 8 o'clock) are thought to occur as a result of a completely different phenomenon. Due to the geometry of the nozzle exit and the surrounding environment there is a significant amount of non-uniform entrainment. The entrained air, interacting with the external features of the orifice-type nozzle, aggressively mixes with the higher momentum jet exhaust, rolling a pair of vortices.

Near the top of the jet core, these same phenomena are present. Inside the boundary of the nozzle exit, there are (weaker) counter rotating vortex pairs resulting from the first bend in the duct and entrainment vortices similar to the lower sector. In this case the internal vortex presumed to be located in the 10–12 o'clock position is obscured by the strength of the outer vortex near the same position caused by the geometric asymmetry of the surrounding environment.

Returning to the internal flow field, another important characteristic of S-duct flows is the presence of a loss in total pressure due to separation inside of the duct, particularly that from the second turn, as noted by Wellborn *et al* [32], Nessler *et al* [33], and Sanders and List [34], for example. Total pressure was calculated using equation (8), which is identical to equation (5), but solved for total pressure.

$$p_0 = p\left[1 + \frac{\gamma - 1}{2\gamma RT} V_{tot}^2\right]^{\frac{\gamma}{\gamma - 1}}. \tag{8}$$

For this calculation, p was assumed to be atmospheric pressure and T was calculated as

$$T = T_0 - \frac{\gamma - 1}{2\gamma R} V_{tot}^2 \tag{9}$$

with the recorded total temperature, T_0, being that of the plenum inside the core of the jet and the lab ambient temperature outside of it. The resulting total pressure distribution is shown in figure 12, and displays the characteristics expected of the measured flow environment. In this figure we see that in the region where the Kiel-probe measurements were taken ($Y = 0$ mm), there is a slight decrease in the measured total pressure as we approach the centre of the core as a result of

the vortex pair, located in the 4–8 o'clock position of figure 11, convecting the low momentum fluid associated with the internal flow separation toward the middle of the duct. The presence of this separation can be clearly seen in the lower section of the flow region in figure 12, outlining the measured complexity of the measured flow, and displays characteristics of the compared S-duct geometry, outlined in the references listed above.

7. Conclusions

In the present work we discuss the first application, to the authors' knowledge, of the structured laser illumination planar imaging background reduction method in Doppler global velocimetry measurements. It was shown that background scattering significantly modifies the signal used for Doppler shift determination in CC-DGV, resulting in velocity biases. Demonstration of the method for three-component velocity measurements was conducted near the exit of a complex free jet issuing from an S-duct exhaust at a nominal exit Mach number of 0.5.

The results of this study show that the SLIPI method was successful in removing the intense background contributions present in this experimental setup at each of the tuned frequencies, yielding the conclusion that, with this technique, it is not required to collect background images at every frequency prior to, or after, collecting velocity data. In fact, it is presented as a method where measurement and background intensities can be collected simultaneously. Another result seen in this study is that, in addition to removing the background scattering from the recorded images, the light reflected back into the measurement region from the laser exit window was also removed from the images, providing an extended capability of the SLIPI background removal method.

Measured velocities were validated and analysed. The total velocity from the SLIPI-CCDGV method was compared to Kiel-probe measurements taken at the exit of the jet, yielding an RMS difference of 1.2 m s^{-1} in the core of the jet exhaust.

Planar results showed trends consistent with the characteristics of a free jet generated by an S-duct, along with aggressive flow entrainment, resulting in higher secondary velocities inside and outside of the core. The measurements were further analysed to obtain total pressure contours, assuming constant static pressure, showing familiar trends present in S-duct flows that have internal flow separation.

Overall, the SLIPI technique for background removal has been shown to mitigate the biases associated with significant background scattering in CC-DGV measurements by largely removing the source of the negative biases in velocity magnitude. The method offers a major practical benefit for *in situ* quantitative measurement and imaging applications in complex flow systems that often suffer from major obscuration from background light.

ORCID iDs

Matthew Boyda https://orcid.org/0000-0002-6334-4412
K Todd Lowe https://orcid.org/0000-0002-0147-4641

References

[1] Nelson M A, Lowe K T, O'Brien W F, Kirk C and Hoopes K M 2014 Stereoscopic PIV measurements of swirl distortion on a full-scale turbofan engine inlet *AIAA SciTech 2014-Proc. 52nd AIAA Aerospace Sciences Meeting* (*National Harbor, MD, USA*, *13–17 January*) AIAA-2014-0533

[2] Guimarães T, Lowe K T and O'Brien W F 2016 An overview of recent results using the StreamVane method for generating tailored swirl distortion in jet engine research *AIAA SciTech 2016—Proc. 54th AIAA Aerospace Sciences Meeting* (*San Diego, CA, USA*, *4–8 January*) AIAA-2016-0534

[3] Guimarães T, Frohnapfel D, Lowe K T and O'Brien W F 2017 Complex flow generation and development in a full-scale turbofan inlet *Proc. ASME Turbo Expo 2017* (*Charlotte, NC, USA*, *26–30 June*) GT2017-64756

[4] Cadel D R and Lowe K T 2015 Cross-correlation Doppler global velocimetry (CC-DGV) *Opt. Lasers. Eng.* **71** 51–61

[5] Boyda M and Lowe K T 2018 Cross-correlation Doppler global velocimetry using Rayleigh and Mie scattering *AIAA SciTech 2018-Proc. 56th AIAA Aerospace Sciences Meeting* (*Kissimmee, Florida, USA*, *8–12 January*) AIAA-2018-1766

[6] Yeaton I, Maisto P and Lowe K T 2012 Time resolved filtered Rayleigh scattering for temperature and density measurements *Proc. 28th AIAA Aerodynamic Measurement Technology, Ground Testing, and Flight Testing Conf.* (*New Orleans, LA, USA*, *25–28 June*) AIAA-2012-3200

[7] Doll U, Stockhausen G and Willert C 2014 Endoscopic filtered Rayleigh scattering for the analysis of ducted gas flows *Exp. Fluids.* **55** 1690

[8] Doll U, Dues M, Tommaso B, Picchi A, Stockhausen G and Willert C 2018 Aero-thermal flow characterization downstream of an NVG cascade by five-hole probe and filtered Rayleigh scattering measurements *Exp. Fluids.* **59** 150

[9] Boyda M T, Byun G B and Lowe K T 2019 Investigation of velocity and temperature measurement sensitivities in cross-correlation filtered Rayleigh scattering (CCFRS) *Meas. Sci. Technol.* **30** 044004

[10] Treaster A L and Yocum A M 1978 The calibration and application of five-hole probes *Proc. 24th Int. Instrumentation Symp.* (*Albuquerque, New Mexico, USA*, *18 January*) TM 78–10

[11] Bridges J and Wernet M P 2019 PIV measurements of a low-noise top-mounted propulsion installation for a supersonic airliner *AIAA SciTech Forum 2019* 2019-0252

[12] Meyers J F, Lee J W and Schwartz R J 2001 Characterization of measurement error sources in Doppler global velocimetry *Meas. Sci. Technol.* **12** 357–68

[13] Meyers J F, Lee J W and Cavone A A 2010 Boundary layer measurements in a supersonic wind tunnel using Doppler global velocimetry *15th Int. Symp. of Laser Technologies to Fluid Mechanics* 1546

[14] Cadel D R, Shin D and Lowe K T 2016 A hybrid technique for laser flare reduction *AIAA SciTech 2016—Proc. 54th AIAA Aerospace Sciences Meeting* (*San Diego, CA, USA*, *4–8 January*) AIAA-2016-0788

[15] Mejia-Alvarez R and Christensen K T 2013 Robust suppression of background reflections in PIV images *Meas. Sci. Technol.* **24** 027003

[16] Honkanen M and Nobach H 2015 Background extraction from double-frame PIV images *Exp. Fluids.* **38** 348–62

[17] Petroskey J P, Maisto P, Lowe K T, André M A, Bardet P M, Tiemsin P I, Wohl C J and Danehy P M 2015 Particle image velocimetry applications using fluorescent dye-doped

particles *AIAA SciTech 2015- Proc. 53rd AIAA Aerospace Sciences Meeting* (*Kissimmee, FL, USA*, *5–9 January*) AIAA-2015-1223
[18] Danehy P M, Tiemsin P I, Wohl C J, Verkamp M, Lowe K T, Maisto P, Byun G and Simpson R 2012 Fluorescence-doped particles for simultaneous temperature and velocity *NASA Technical Manual* 217768
[19] Boyda M B, Byun G, Saltzman A S and Lowe K T 2019 Geometric scattering removal in CC-DGV by structured illumination *13th Int. Symp. on Particle Image Velocimetry*
[20] Cadel D R and Lowe K T 2016 Investigation of measurement sensitivities in cross-correlation Doppler global velocimetry *Opt. Lasers. Eng.* **86** 44–55
[21] Fischer A, Büttner L, Czarske J, Eggert M and Müller H 2008 Measurement uncertainty and temporal resolution of Doppler global velocimetry using laser frequency modulation *Appl. Opt.* **47** 3941–53
[22] Lowe K T, Byun G, Shea S, Boyda M T and Winski C S 2019 Three-velocity-component cross-correlation Doppler global velocimetry for the space launch system booster separation test in the NASA Langley unitary plan wind tunnel *AIAA Aviation Forum 2019* 2019-3506
[23] Forkey J N, Lempert W R and Miles R B 1997 Corrected and calibrated I2 absorption model at frequency-doubled Nd:YAG laser wavelengths *Appl. Opt.* **36** 6729–38
[24] Charrett T O H, Nobes D S and Tatam R P 2007 Investigation into the selection of viewing configurations for three-component planar Doppler velocimetry measurements *Appl. Opt.* **46** 4102–16
[25] Neil M A A, Juškaitis R and Wilson T 1997 Method of obtaining sectioning by using structured light in a conventional microscope *Opt. Lett.* **22** 1905–7
[26] Kristensson E, Ehn A, Bood J and Aldén M 2014 Advancements in Rayleigh scattering thermometry by means of structured illumination *Proc. Combustion Institute* vol **35** pp 3689–96
[27] Zentgraf F, Stephan M, Berrocal E, Albert B, Böhm B and Dreizler A 2017 Application of structured illumination to gas phase thermometry using thermographic phosphor particles: a study for averaged imaging *Exp. Fluids.* **58**
[28] Stephan M, Zentgraf F, Berrocal E, Albert B, Böhm B and Dreizler A 2019 Multiple scattering reduction in instantaneous gas phase phosphor thermometry: applications with dispersed seeding *Meas. Sci. Technol.* **30** 054003
[29] Berrocal E, Johnsson J, Kristensson E and Aldén M 2012 Single scattering detection in turbin media using single-phase structured illumination filtering *J. Eur. Opt. Soc.-Rapid Publ.* **7** 12015
[30] Zhang Z 1999 Flexible camera calibration by viewing a plane from unknown orientations *Proc. 7th IEEE Int. Conf. on Computer Vision*
[31] Kempema N J and Long M B 2014 Quantitative Rayleigh thermometry for high background scattering applications with structured laser illumination planar imaging *Appl. Opt.* **53** 6688–97
[32] Wellborn S R, Reichert B A and Okiishi T H 1994 Study of the compressible flow in a diffusing S-duct *J. Propul. Power* **10** (66)
[33] Nessler C A, Copenhaver W W and List M G 2013 Serpintine diffuser performance with emphasis on future introduction to a transonic fan *51st AIAA Aerospace Sciences Meeting including the New Horizons Forum and Aerospace Exposition* 2013–0219
[34] Sanders D D and List M G 2013 CFD performance predictions of a serpentine diffuser configuration in an annular cascade facility *51st AIAA Aerospace Sciences Meeting including the New Horizons Forum and Aerospace Exposition* 2013–0220

Chapter 5

Filtered Rayleigh Scattering for Multi-Property Aerodynamic Measurements in Confined Flows

The content of this chapter includes a research article that has been submitted and accepted, pending major revision, to *Measurement science and Technology* as "Boyda M.T., Byun G., and Lowe K.T., Filtered Rayleigh Scattering for Multi-Property Aerodynamic Measurements in Confined Flows." This article details the validation experiment performed in an Air Force Research Laboratory owned full scale inlet distortion facility to fully quantify the flow downstream of a distortion generating test article. The article included in this chapter includes changes to the submitted manuscript made as a result of the first round of the peer review process. IOP Publishing Ltd is not responsible for any errors or omissions in this version of the manuscript or any version derived from it. No significant portions have been discussed outside of this manuscript.

The objective of this chapter is to show the experimental validation of the filtered Rayleigh scattering instrument, novel data collection and processing methods, and the uncertainty quantification methods described within. Velocity, temperature and density in addition to derived measurements of circumferential and radial flow angles, static pressure, and total pressure were quantified in a two-dimensional cross section of the flow in a high Mie and

geometric scattering environment. Detailed measurement uncertainty quantification is presented.

In the manuscript, assumptions surrounding time-averaged multi-property FRS measurements are discussed. This discussion has been expanded upon in Section 5.1, following the manuscript, to include a quantitative analysis of the effects of turbulence.

Filtered Rayleigh Scattering for Multi-Property Aerodynamic Measurements in Confined Flows

Matthew T. Boyda[1,2], Gwibo Byun[1] and K. Todd Lowe[1]

[1] Kevin T. Crofton Department of Aerospace and Ocean Engineering, Virginia Tech, Blacksburg VA, United States of America
[2] D304 – Advanced Measurements and Data Systems Branch, NASA Langley Research Center, 1 Nasa Dr, Hampton, VA 23666

E-mail: matthew.boyda@nasa.gov

Received xxxxxx
Accepted for publication xxxxxx
Published xxxxxx

Abstract

Well defined multi-property measurements are crucial for the quantification of flow within all facilities. Conventionally, these measurements are collected using physically intrusive pressure and temperature probes which introduce undesired perturbation to flow and measurement. More recently, optical techniques have been employed to supplement probe measurements, with most applications requiring particles to be seeded into the flow. In this contribution, the advancements required to integrate a molecular filtered Rayleigh scattering (FRS) instrument into a full-scale flow facility are discussed, laying the foundation for accurate and precise measurements in the presence of high intensity particle and background scattering, the primary sources of bias in applied FRS. Measurements are demonstrated in the 432 mm diameter Annular Cascade Facility (ACF) at Wright-Patterson Air Force Base, downstream of a distortion generating test article, resulting in swirl and total pressure distortion. Multi-property FRS measurements of time-averaged three-component velocity, temperature, and density in addition to derived static and total pressure are compared with standard 5-hole probe and PIV measurements. Comparison between the FRS and reference measurements resulted in differences typically falling within pre-determined uncertainty bounds. Root-mean-square difference (RMSD) values are shown to be less than 8.0 m/s, 1.7 deg, and 4.7 deg for axial velocity, tangential flow angle, and radial flow angle respectively. Measurements of static temperature and density are found to show RMSD values of 11.1 K (4.0%) and 0.043 kg/m^3 (4.3%) respectively compared to the expected average. FRS-derived static and total pressures are compared with reference measurements with good agreement near the center of the duct with RMSD values of less than 3.9 kPa (4.8%) and 5.0 kPa (4.9%) respectively.

Keywords: optical diagnostics, filtered Rayleigh scattering, Doppler velocimetry, temperature measurement, density measurement, flow quantification, measurement validation

1. Introduction

The primary objective of experimental aerodynamic measurement is to quantify the state of a fluid flow around, through, or downstream of some physical geometry to improve a researcher's understanding of how they interact with one another. Today, aerodynamic experiments often take place in wind tunnels, typically characterized by a wall-bounded internal flow, and are often used to validate computational fluid dynamics (CFD) simulations of the same configuration. To perform this type of validation, detailed quantification of the state of the fluid flow is necessary (Oberkampf and Smith 2017 and Lowe et al. 2020) with spatially resolved field measurements of the inflow and outflow conditions being some of the most critical due to the

impact of boundary condition definitions on the CFD flow solution (Lowe et al. 2020). Ideally, spatially resolved measurements of vector velocity, temperature, density, and pressure would be collected everywhere within these planes simultaneously, and with well-defined uncertainties so accurate boundary conditions may be used. Unfortunately, ever since the need to quantify the state of these flows was identified in the early 1900s (Hunsaker et al. 1916), improvements to conventional instruments and the development of new instruments/methodologies have yet to yield a practical technique that allows for the simultaneous collection of multi-property measurements within a two-dimensional plane in large scale facilities.

Standard measurements in internal flow environments typically consist of of static pressure, total pressure, and total temperature using various types of probes and probe rakes. While probe-based measurements provide accurate results when positioned away from physical geometry (Treaster and Yocum 1978) and within flows that contain only small gradients in fluid properties (Livesey 1956, Sevill 2002), they measure pressure and temperature at a single point by physically interacting with the fluid, inducing a perturbation, and altering flow conditions downstream and sometimes upstream of the measurement location.

While instrumentation technology has advanced to collect these measurements at higher spatial and temporal resolution, these instruments cannot provide simultaneous, multi-property measurements, even at a single location, due to the various instrumentation required to measure different fluid properties. Additionally, simultaneous planar measurements of the flow cannot be collected at a sufficient density due to the blockage associated with having numerous probes in the flow. Thus, a single or limited number of probes must be traversed within the domain to obtain the required information over a non-negligible amount of time.

Intrusive measurements, with known limitations near boundaries, in regions of high property gradients, and in simultaneous measurement density considered, remain the standard measurements in internal flow quantification today due to the simplicity of implementation, broad application space, and well-defined uncertainties in steady state, uniform flow fields. With ever more increasing flow complexity and near-boundary nature of desired regions of interest (ROI), new measurement standards must be developed to collect simultaneous multi-property field measurements, improve near wall measurement accuracy, and reduce instrument intrusiveness. Most importantly, to replace legacy probes, such techniques must also have low-magnitude well defined uncertainties while being robust to the harsh conditions synonymous with large-scale testing facilities.

Less intrusive laser-based diagnostic techniques have been developed, in part, to overcome the intrusiveness associated with probe measurements. These techniques rely on the interaction of light and matter within the fluid so there is very little intrusion on the behavior of the flow. Though many different techniques exist to measure fluid properties, they can generally be grouped into two categories: those requiring the laser to interact with particles seeded into the flow and those that rely on the interaction between the laser and the fluid itself (unseeded).

Many of the more common laser-based diagnostics fall into the seeded category, which rely on the observation of light scattered or emitted from particles artificially introduced into the flow, greatly improving upon the physical intrusiveness of probe measurements.

For temperature measurements, observing the decay rate in the luminosity of laser illuminated thermographic phosphors can be correlated with fluid temperature (Omrane et al. 2008, Fond et al. 2015, Kopf et al. 2021, and Witkowski et al. 2020).

Spatially resolved field measurements of three-component velocity can be measured by employing various methods including particle image velocimetry (PIV) and Doppler global velocimetry (DGV)/planar Doppler velocimetry (PDV).

PIV is capable of measuring velocities at very high temporal and spatial resolution by tracking the motion of particles between subsequent frames. PIV has been widely used to quantify internal flows (Guimarães et al. 2018, Beresh et al. 2020, Nelson et al. 2014) and make accurate near wall measurements (Willert et al. 2021, Martins et al. 2019), but challenges associated with performing PIV on a large scale (Leber 2020) and the difficulty in quantifying uncertainty (Wieneke 2015 and Rajendran et al. 2021) leads to costly and challenging applications.

DGV may also be used to obtain high spatial and temporal resolution velocity measurements by determining the Doppler shift between narrow linewidth laser light incident on a seeded flow and the light scattered from the particles to the imager. Since DGV involves algebraically relating the measurement of Mie scattering intensity to Doppler shift generally making the uncertainty quantification more straightforward (Fischer 2017, Cadel and Lowe 2015 & 2016) in comparison with PIV. Additionally, DGV has less stringent requirements on particle size and camera focus with the only difficulties in uncertainty quantification arising from local turbulence when the frequency of Doppler shifted light corresponds with a highly non-linear region of the iodine absorption spectrum. DGV is therefore an increasingly used technique to quantify the velocity of various flows (Burns et al. 2021, Boyda et al. 2020, Lowe et al. 2019, and Meyers et al. 2010).

To address issues associated with introducing foreign particles into the flow, such as installing a seeding system, supplying the appropriate seeding density, achieving uniform seeding density, and navigating potential health and safety concerns, molecular-based optical diagnostic techniques, that rely on the interaction between laser light and molecular gases,

present themselves as attractive alternatives. Such techniques include coherent anti-Stokes Raman spectroscopy (CARS) (Dedic et al. 2017), molecular tagging velocimetry (MTV) (Reese et al. 2020), and molecular laser Rayleigh scattering (LRS) (Panda 2020, Saltzman et al. 2019, Mcmanus et al. 2019, Doll et al. 2018, and Miles et al. 2001, Panda and Seasholtz 1998). With the increased availability of very high power/energy lasers, their minimal intrusiveness, and broader fundamental application space when compared to seeded measurements, these measurements are becoming more common. As such, molecular-based scattering diagnostics are continuing to evolve, improving accuracy, uncertainty, and applicability so they may be used as substitutes and/or supplements to their more intrusive counterparts.

Of these techniques, LRS has been identified as one of the most promising candidates for internal flow quantification and CFD validation due to its capability for simultaneous field measurement of vector velocity, static temperature, static density, and static pressure with negligible energy exchange between the laser and fluid (Doll et al. 2022, Boyda et al. 2020, Boyda et al. 2019, Saltzman et al. 2019, Doll et al. 2018, and Doll et al. 2017, Miles et al. 2001). From these measurements, the aerodynamic and thermodynamic state of the fluid flow may be fully characterized over large ranges of velocities, temperatures, and densities. Additionally, since measurements are based on the Doppler shift and lineshape characteristics of the Rayleigh Brillouin spectrum, the uncertainty of these measurements may be calculated using well-defined spectral models, known contributors to signal noise, and general assumptions of the flow. Specific assumptions used in this work are summarized in Section 3.4.

The downside of molecular Rayleigh scattering is that it is a low intensity scattering process, especially when compared to Mie scattering, and the scattering off static surfaces (geometric or background scattering). With Mie and geometric scattering commonplace in most flow facility applications of laser diagnostics, they have the potential to overwhelm an LRS scattered signal.

The present work focuses on the development of processing methodologies and simple but effective light control solutions necessary to realize reasonable levels of accuracy and precision in filtered Rayleigh scattering (FRS)-based internal flow measurements. FRS measurement uncertainties, derived from the geometry and lighting conditions of the measurement configuration are determined using a Monte-Carlo simulation. These uncertainties are then experimentally validated in a risk reduction experiment and then in-situ using both probe-based and optical reference measurements, demonstrating the applicability of FRS in full-scale internal flow facilities to obtain precise and accurate measurements.

In the following section, the fundamentals of Filtered Rayleigh scattering and how FRS is used to measure the properties of a gas are discussed. FRS signal contamination, to include Mie scattering, geometric scattering, and turbulent fluctuations are also discussed. In Section 3, the specific methods used to determine three-component velocity, temperature, density, and pressure are presented. In Section 4, the FRS measurement validation environment is presented, including the integration of the FRS instrument, the issues encountered in integration, the resulting FRS measurement uncertainties, and the reference measurements used for validation. In Section 5, the results from the FRS measurement campaign are presented, with discussion consisting of the accuracy and uncertainty performance of FRS-derived measurements relative to the reference measurements. The conclusions and outlook are then discussed in Section 6.

2. Filtered Rayleigh scattering

Rayleigh scattering is a wave optics phenomenon that results from the interaction of light and matter on a scale much smaller than the wavelength of the incident light. This includes the interactions between light and gas molecules present in air. The spectral characteristics of molecular Rayleigh scattering directly relate to the aerodynamic and thermophysical properties of the gas, generating substantial interest within the experimental aerodynamics community. Miles et al. 2001 discusses the characteristics of Rayleigh scattering in detail, but highlighting the pertinent characteristics of LRS in air near atmospheric conditions and observed away from the forward scattering direction, the following are observed:

(1) Rayleigh scattering occurs down to molecular levels.
(2) Rayleigh scattering resulting from the interaction between light and matter is elastic and no energy is transferred.
(3) The yield of scattered light is proportional to the number density of the gas for constant composition.
(4) Light scattered off matter in motion is Doppler shifted in frequency proportional to its velocity.
(5) In a stagnant gas, individual molecules are always in motion, resulting in a Doppler broadened spectrum, centered on the incident laser frequency, and a distribution related to the motion of the particles.

Since Rayleigh scattering occurs on molecular levels and the interaction between the laser illumination and the gas results in a negligible amount of energy transfer into the measured flow, non-intrusive measurement of the flow via molecular Rayleigh scattering is possible. When the gas composition is known, properties 3, 4, and 5 provide the necessary mechanisms to determine gas density, velocity, and temperature, respectively.

The spectral attributes of the Rayleigh scattered light are driven by the value of the Knudsen number, which is the ratio of the mean free path of the molecules in the fluid to a representative length scale. At low pressures and/or high temperatures, known as the Knudsen regime, the Knudsen number is large, and molecules rarely interact with one

another. The broadening in this regime is then dominated by individual particle motion resulting in a Gaussian distributed Rayleigh lineshape (Figure 1, orange dash-dot line). Conversely, in high pressure and/or low temperature conditions, the Knudsen number is small and molecules interact more readily. In this regime, known as the hydrodynamic regime, the scattered lineshape forms a three-peaked spectrum, each displaying a Lorentzian shape (Figure 1, purple fine-dashed line), with the outer peaks representing Brillouin scattering. The locations of the two outer peaks of this spectrum are associated with the speed of sound in the gas, while the width of the central peak is associated with the thermal diffusion rate (Miles et al. 2001).

For the present work we interrogate air, not at one extreme or the other, but at moderate temperatures and pressures referred to as the intermediate or kinetic regime. For this regime neither effect is dominant nor negligible; therefore, both must be considered. Tenti et al. 1974 developed a six-moment model for this regime that depends on four dimensionless parameters (Miles et al. 2001) and accurately predicts the lineshape observed in light scattering experiments. The "Tenti S6" Rayleigh scattering lineshape model has been accepted as the standard in modeling the Rayleigh scattering lineshape for diatomic gases for air near atmospheric temperature and pressure (Figure 1, orange dashed line).

To measure the desired flow properties using Rayleigh scattered light, three characteristics must be evaluated. The most straightforward of these to measure is the integral intensity of the Rayleigh scattered light, which is proportional to the number density of the gas. This may be done with any photodetector as long as its response is properly calibrated, and no contaminating scattering sources exist (Panda and Seasholtz 1998). These contaminating sources are difficult to avoid in real world flow facilities, so this method may only be used in highly controlled environments, with most practical applications requiring significant effort.

The second characteristic that is to be determined is the bulk Doppler frequency shift in the Rayleigh lineshape away from the center frequency of the incident laser light which, according to 4 above, is proportional to the bulk velocity of the gas. Mathematically this is defined as

$$\Delta\nu = \frac{(\hat{o} - \hat{\imath}) \cdot \vec{V}}{\lambda} \quad (1)$$

where $\Delta\nu$ is the Doppler frequency shift, $\hat{o}$ and $\hat{\imath}$ are the unit vectors pointing from the origin of the scattered light toward the detector and in the direction of the laser propagation, respectively, and λ is the wavelength of the incident laser light. The parameter $\hat{o} - \hat{\imath}$ is the sensitivity vector and defines the direction and relative magnitude that the detector is sensitive to Doppler shift. The term "sensed velocity" refers to the dot product of the sensitivity vector with the local three-component velocity

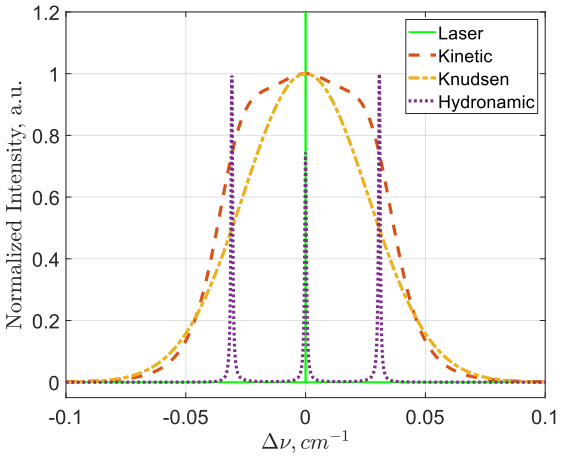

Figure 1. Rayleigh spectral lineshapes generated using the Tenti S6 lineshape model in the Kinetic, Knudsen, and Hydrodynamic regimes.

vector of the flow, $\vec{V}$, and is defined as: $U = (\hat{o} - \hat{\imath}) \cdot \vec{V}$, in units of meters per second.

The third and final characteristic we need to determine is the width of the Rayleigh scattered lineshape which, according to characteristic 5 above and the kinetic theory of gases, is a function of temperature, approximately varying as the square-root of temperature (Boguszko and Elliot 2005). The second two characteristics are more difficult to determine because the measured spectrum must be resolved in the frequency domain. Dependencies on density, velocity, and temperature are shown pictorially in Figure 1 of Mielke et al. 2009 (not reproduced here).

Two commonly utilized methods exist to resolve the Rayleigh scattering lineshape in the frequency domain. The first is by employing a Fabry-Perot interferometer, which provides frequency resolution with a single-shot measurement. The second is to scan the incident laser frequency across a very narrow line-width molecular absorption filter. The reader is encouraged to look at works such as Panda 2020, Cutler et al. 2020, Estevadeordall et al. 2018, and Bivolaru et al. 2011 for information on interferometric Rayleigh scattering. The present work, however, will focus on the use of the molecular filter, pioneered by Forkey, Lempert and Miles in 1990, due to the ability to measure large, and highly spatially resolved flow regions while simultaneously providing a mechanism for filtering Mie and background scattering contamination.

2.1 Ideal FRS signal: model and behaviors

For this work, a molecular iodine filter is used specifically due to its sharp transitions in frequency and high optical density while maintaining an absorption feature width on the same order as the width of the Rayleigh scattering lineshape.

Additionally, molecular iodine filters are commercially available, utilized readily in previous work, and have been very well characterized near a wavelength of 532 nm by Forkey et al. in 1997.

When employing the filtered Rayleigh scattering technique, the Rayleigh lineshape cannot be reconstructed using a single filtered image. The laser itself must be tuned to multiple frequencies near a chosen iodine absorption feature with images collected at each step. The intensity of each pixel at each frequency allows for the construction of an intensity spectrum resolved in the frequency domain. This spectrum is the convolution of the collected Rayleigh spectral lineshape (blue dashed line in figure 2a) and the iodine absorption spectrum (solid black line in figure 2). To evaluate the measured convolution spectrum for the desired quantities, a high fidelity signal model must be used to fit to the collected spectrum.

The theoretical convolution spectrum (blue dot-dashed line in figure 2b) may be calculated with the Tenti S6 Rayleigh-Brillouin scattering (RBS) lineshape model, I_{Ray}, and the iodine transmission spectrum, τ_{I_2}. The convolution of these two spectra at a single laser frequency, ν_i, is defined as

$$S_{Ray}(\nu_i, p, T, \Delta\nu, \Theta) = I_{Ray} \otimes \tau_{I_2}$$
$$= CF \int_{-\infty}^{\infty} I_{Ray}(\eta - \nu_i, p, T, \Delta\nu, \Theta)\tau_{I_2}(\eta)d\eta \qquad (2)$$

where

$$CF = E_{opt} n V_i I_i \frac{d\sigma}{d\Omega}(\Phi) \qquad (3)$$

S_{Ray} is the integral intensity of the point-wise multiplication of the RBS lineshape and the iodine transmission spectra at a single laser frequency, ν_i. η represents the domain of all frequencies and CF is a calibration factor that incorporates optical efficiency (E_{opt}), gas number density (n), the interrogation volume (V_i) laser intensity (I_i), and polarization dependent scattering cross-section ($d\sigma/d\Omega(\Phi)$) where Φ is the angle between the polarization direction and $\hat{o}$. I_{Ray} is shown to dependent on the pressure (p), temperature (T), and Doppler shift ($\Delta\nu$) of the scattering medium in addition to the scattering angle Θ, which is defined as the angle between $\hat{o}$ and $\hat{\imath}$.

The result of Equation 2, shown by the blue asterisk in figure 2 is the fundamental measurand obtained by each photodetector (e.g. camera pixel, photomultiplier, or photodiode) at a single ν_i. During a measurement, a series of S_{Ray} values are collected over a range of laser frequencies, indicated by the blue dash-dot line in figure 2b. The intensity of S_{Ray} is shown to reduce as the overlap between I_{Ray} and τ_{I_2} increases, producing a trough region near the minimum value of τ_{I_2}. For model spectrums in this work, τ_{I_2} represents a molecular iodine vapor cell with a length of 127 mm and a vapor pressure of approximately 1.0 Torr (ISSI inc. model I2S-5 discussed further in Section 4)

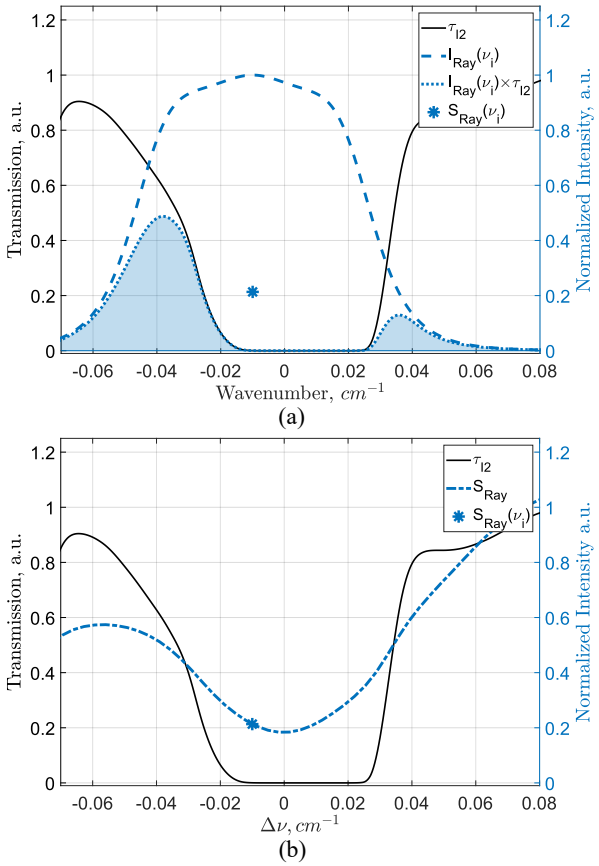

Figure 2. Iodine transmission spectrum τ_{I2} centered on 18788.4321 cm^{-1} (black), Rayleigh lineshape at STP and 90° observation (a, blue dashed line) at a single laser frequency, and the resulting value for S_{Ray} at a single pixel and laser wavenumber (blue asterisk). The convolution spectrum of the Rayleigh lineshape with the τ_{I_2} (b, blue dash-dot line) for multiple laser frequencies. Note that spectra depicted in this figure are generated using noise-free analytical models.

Since both the Tenti S6 RBS lineshape model and the iodine absorption model developed by Forkey et al. accurately predict their behavior, two different methods may be used to fit measured convolution spectra for the desired properties. The first is to generate an RBS lineshape at a candidate condition, convolve it with the iodine absorption spectrum, and then compare that to the measured convolution spectrum to determine the desired parameters using a least-squares fitting algorithm. Another method would be to deconvolve the measured intensity spectrum using the iodine absorption model to obtain the underlying RBS spectrum and fit an RBS lineshape model to the measured lineshape. In either case, the fit yields measurements of Doppler frequency shift (velocity), temperature, density, and pressure averaged over the duration of the frequency scan. The present work, however, utilizes the

former method due to the ease of implementation and to avoid the potential introduction of bias error by deconvolving a convolution spectrum over a limited range of laser frequencies in the highest absorption regions of molecular iodine.

2.2 FRS signal contamination

While multi-property molecular Rayleigh scattering measurements can provide time-averaged velocity, temperature, density, and pressure information within the interrogated volume, challenges associated with collecting a contamination free signal make it a difficult and time-consuming technique to apply. The low intensity nature of Rayleigh scattering makes it highly susceptible to contamination from more intense, Mie and geometric, scattering sources. The mitigation of this contamination in the processed signal is crucial to robust FRS measurements and is the primary motivation for the following discussion. Additionally, since the measurement is time averaged, turbulent fluctuations in the measured properties has the potential to introduce bias into the measurement.

Investigation of the Mie and geometric scattering contamination in the Rayleigh scattering signal requires that their contributions be included in the modeled FRS signal model, resulting in equation 4. Here, S_{scat} is the convolution signal that contains all scattered light sources collected by the imager, I_{Mie} is the Mie scattered light spectrum, and I_{Geo} is the geometrically scattered light spectrum.

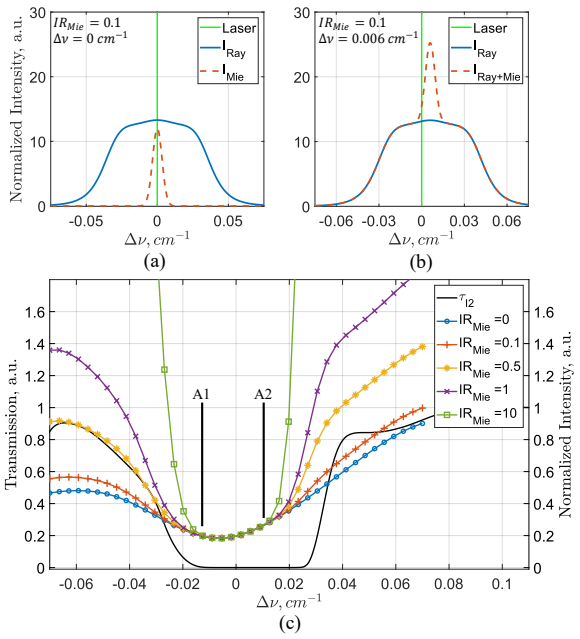

Figure 3. Simulated Rayleigh and Mie scattering lineshapes compared for $IR_{Mie} = 0.1$ (a), The combined, Doppler shifted Rayleigh and Mie scattering lineshapes (b) and convolution spectrums resulting from various Mie intensity ratios, assuming a Doppler shift of $\Delta\nu = 0.006\ cm^{-1}$ (c). The region bounded by A1 and A2 represents the Mie rejection region.

$$S_{scat}(\nu_i) = I_{scat} \otimes \tau_{I_2}$$
$$S_{scat}(\nu_i) = E_{opt} V_i I_i \int_{-\infty}^{\infty} \left[n \frac{d\sigma}{d\Omega}(\Phi) I_{Ray}(\eta - \nu_i, p, T, \Delta\nu, \theta) + I_{Mie}(\eta - \nu_i, \Delta\nu) + I_{Geo}(\eta - \nu_i) \right] \tau_{I_2}(\eta) d\eta \qquad (4)$$

Two parameters are defined to quantify the magnitude of the Mie and geometric scattering relative to the Rayleigh scattering intensity in equations 5a and 5b.

$$IR_{Mie} = \frac{\int_{-\infty}^{\infty} I_{Mie}(\eta) d\eta}{\int_{-\infty}^{\infty} I_{Ray}(\eta) d\eta} \qquad (5a)$$

$$IR_{Geo} = \frac{\int_{-\infty}^{\infty} I_{Geo}(\eta) d\eta}{\int_{-\infty}^{\infty} I_{Ray}(\eta) d\eta} \qquad (5b)$$

IR_{Mie} and IR_{Geo} are the Mie intensity ratio and geometric intensity ratio respectively. These parameters are defined as the ratio of contaminating intensity to observed Rayleigh scattering intensity, allowing the relative changes in each parameter to be investigated.

2.2.1 Mie scattering contamination

When particles are not introduced into the flow artificially, Mie scattering in FRS measurements is a result of particles that occur naturally within the flow, typically dust and condensing gases. When laser light interacts with these particles, the Mie light scattered to the imagers easily dominates the overall signal if it is not filtered out. For example, a single particle with a diameter of 1 μm, would scatter 532 nm laser light with approximately the same intensity as all the air molecules in a volume of 155 mm^3 at standard ambient conditions. Assuming a laser sheet thickness of 0.5 mm, that would represent an area of approximately 18 mm x 18 mm.

Figure 3 shows convolution spectra where both Rayleigh and Mie scattering contributions are considered. When present simultaneously, they are additive in intensity while retaining their unique spectral properties. The Mie scattering spectrum is shown in figure 3a as a Gaussian distributed lineshape, centered on the laser frequency in stagnant flow. The width of the Mie scattered spectrum shown in figure 3 has been arbitrarily broadened for visibility but occurs in application as a result of turbulent velocity fluctuations. When in bulk motion, Mie scattering is Doppler shifted by the velocity of the particles in the flow and is still centered on the RBS lineshape (figure 3b). The simulated convolution spectra in figure 3c demonstrates that Mie scattering has a significant effect on the measured convolution spectrum, but only outside of the region of high iodine absorption. In the regions of highest absorption, the $IR_{Mie} = 10$ case displays the same intensity as the $IR_{Mie} = 0$ case, indicating that a region exists

where Mie scattering can be filtered to negligible levels. But using points outside of this region can lead to biased measurements if not considered.

Since the iodine filter may be used effectively to filter out Mie scattering over a small region near the iodine transmission minimum, Mie scattering may be completely neglected in the curve fitting algorithm with careful selection of wavenumber range, iodine vapor pressure, and iodine absorption feature. This range of frequencies over which Mie scattering is negligible is referred to herein as the Mie scattering rejection region. The Mie scattering rejection region can be pre-determined using signal simulations and in-situ laser frequency scans to determine IR_{Mie}, but bulk flow velocity must also be taken into consideration since the Mie scattered signal is Doppler shifted by particles in motion. When the Doppler shifted rejection region is applied, Mie contamination in FRS temperature and density determination can be removed (Boyda et al. 2020).

Figure 3c shows the effects of various values of IR_{Mie} on the measured convolution spectrum at a sensed velocity of 100 m/s ($\Delta\nu = 0.006\ cm^{-1}$). In this figure, the rejection region is identified as the region bounded by the markers indicated "A1" and "A2," and that within this region, Mie scattering has a negligible effect on the convolution spectrum intensity.

2.2.2 Geometric scattering contamination

Geometric or background scattering is the scattering of light from static surfaces visible in the frame. This results in intensity contributions to the measured signal at the same frequency and linewidth as the incident laser light, as seen in figure 4a and 4b. Here, narrow linewidth background scattering remains fixed in frequency with respect to the incident laser light while the Doppler shifted Rayleigh signal shifts to the right.

To avoid this contamination, the amount of light geometrically scattered toward the sensor must be reduced as much as possible by optimizing *in situ* scattering conditions (discussed in section 2.3). Second, frequencies used in the scan must be chosen to allow for the absorption of narrow linewidth contamination. Multi-property measurements may only be performed within geometric scattering rejection region, or the range of frequencies where background contamination is filtered to a negligible level. Similarly to the Mie scattering example, care must be taken to select the appropriate vapor pressure, absorption feature, and range of wavenumbers to effectively filter background scattering.

Figure 4c shows how the convolution spectrum changes with IR_{Geo} at a sensed velocity of 100 m/s ($\Delta\nu = 0.006\ cm^{-1}$). In this figure, the rejection region is bounded by the markers indicated "B1" and "B2."

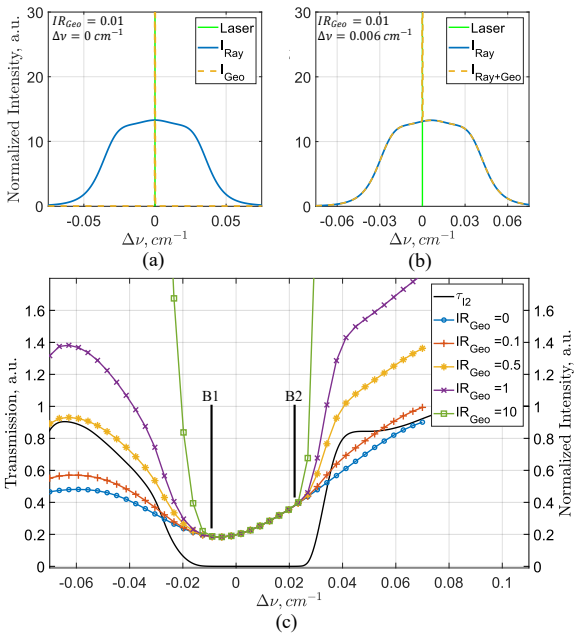

Figure 4. Simulated Rayleigh and geometric scattering lineshapes compared for $IR_{Geo} = 0.01$ (a), The combined Doppler shifted Rayleigh and fixed frequency geometric scattering lineshapes (b) and convolution spectrums resulting from various geometric intensity ratios, assuming a Doppler shift of $\Delta\nu = 0.006\ cm^{-1}$ (c). The region bounded by B1 and B2 represents the geometric rejection region.

2.2.3 Combined Mie and Geometric scattering contamination

It is important to note that both Mie and geometric effects will almost always be present in internal flow facilities simultaneously. When this is the case, both the shifted and unshifted rejection regions must be considered. Once identified, the intersection of the two separate rejection regions must be extracted to define the wavenumber range that must be applied in multi-property measurement to avoid contamination.

Figure 5 shows how the combined effects of Rayleigh, Mie, and geometric scattering signals for intensity ratios of $IR_{Mie} = 0.5$ and $IR_{Geo} = 0.5$ at a sensed velocity of 100 m/s ($\Delta\nu = 0.006\ cm^{-1}$). The region markers "A1" to "A2" indicate the Mie scattering rejection region, "B1 to B2" indicate the geometric scattering rejection region, with the intersection rejection region is bounded by "B1" and "A2." In this region, Mie and geometric contributions to the signal convolution are effectively filtered and do not have to be considered in the curve fitting algorithm.

Considering the conditions of the CARL facility (Discussed in Section #), it is assumed that the FRS instrument would have to be robust to Mie and geometric scattering intensity ratios on the order of 10, necessitating an

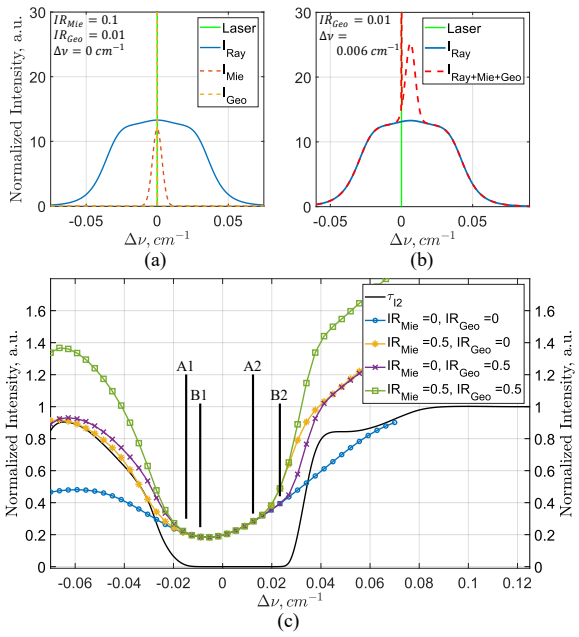

Figure 5. Simulated combined Rayleigh, Mie, and geometric lineshape at $IR_{Mie} = 0.1$ and $IR_{Geo} = 0.01$ (a), the combined, Doppler shifted scattering lineshapes (b) and convolution spectrums resulting from combinations of IR_{Mie} and IR_{Geo} assuming a Doppler shift of $\Delta\nu = 0.006\ cm^{-1}$. For (c) the intensity ratio, when not 0 is held to 0.5. The region B1 to A2 defines the intersection region.

iodine cell transmission of less than 10^{-5} over the span of the rejection region. It was determined that an iodine cell with a vapor pressure near 1 Torr, would result in an absorption line at 18786.4321 cm^{-1} capable of reducing the transmission to less than 10^{-5} over a range of $0.03\ cm^{-1}$ ($\Delta\nu = -0.012 cm^{-1}$ to $0.018\ cm^{-1}$), providing a sufficient range of frequencies over which to conduct curve fitting in the intersection rejection region without significant bias error while keeping scalar uncertainty reasonably low.

Looking at the broader application space of the rejection region analysis, the authors note that when Mie and geometric scattering are present simultaneously at similar scattering intensities, the rejection regions consist of approximately the same range of wavenumbers. The Mie scattered rejection region is then Doppler shifted according to the geometry of the observer and the velocity of the flow. As the Doppler shift increases, the bounds of the intersection rejection region become closer together, reducing the amount of information available to fit a measured convolution spectrum and an increase in measurement uncertainty. At a certain point, the intersection of the two rejection regions no longer provides enough information to accurately fit the convolution spectrum resulting in a drastic increase in measurement uncertainty.

As Doppler shift increases further, the two rejection regions no longer overlap and the intersection of the two rejection regions no longer exists. When this occurs, Mie and geometric scattering contributions must be explicitly accounted for in the multi-parameter curve fit algorithm by fitting Eq. 4 to the measured convolution spectrums as opposed to Eq. 2, drastically increasing computational cost.

2.2.4 Averaging over turbulent fluctuations

In the current measurement campaign, FRS is used to measure the flow properties downstream of a test article that is known to have unstable swirl and total pressure distortions using Eq. 2 which assumes velocity, temperature, density, and pressure are constant. Therefore, the effect of turbulent fluctuations need to be considered.

The first element to consider is whether the FRS measurement samples a statistical average of the flow. For this analysis, we note that the average axial velocity at the measurement plane is approximately 172 m/s and the duct is circular in cross-section with a diameter of 432 mm. To establish a flow time scale in which to compare FRS measurements, the duct diameter flow through time, defined as the amount of time that it takes the bulk axial flow to travel one diameter downstream, can be calculated using $t_D = D/V_z$. This results in a characteristic time scale of 2.5E-3 seconds.

The FRS measurement time scales in this measurement campaign are discussed in section 4.1. Each FRS image is exposed for 4.5 seconds at each laser frequency, resulting in the averaging over approximately 1800 times the duct diameter flow-through time. With a total scan duration of 15 minutes, this results in the averaging over 3.6E5 times the duct diameter flow through time. It is then reasonable to assume that the FRS measurement techniques samples a statistical average of the flow conditions. If this were not the case, it is likely that the FRS measurements would result in higher than predicted uncertainty.

While a detailed analysis of the effect of turbulent fluctuations on the measured convolution signal is beyond the scope of this work, we can infer that at certain turbulent intensity levels, turbulent fluctuations in the various properties would induce bias error into the measurement due to the non-linear relationship between the RBS lineshape and the measured properties, such as velocity fluctuations broadening the RBS lineshape, the non-linear relationship between the width of the RBS and temperature, and the prominence of the three peaks near the maximum intensity region being related to pressure. The only property not expected to have an effect of the accuracy of the curve fit when fluctuating is density, as it does not affect the shape of the RBS.

With these considered it is assumed that the flow is turbulent and that the FRS measurement is representative of a statistical average of the flow properties. It is then assumed that the differences between the measured convolution and the

constant value convolution spectrum are negligible. In future work, the validity of this assumption will be explored.

2.3 Mitigating FRS signal contamination

While Mie scattering is a significant contributor to contamination in FRS signals, there is very little that can be done to eliminate it completely from large scale flow facilities apart from significant flow conditioning. Geometric scattering on the other hand can be mitigated by design with imager positioning and low-impact facility alterations using several simple and robust light control solutions.

The magnitude of laser light that is diffusely scattered toward the measurement region can be mitigated significantly by using high efficiency optics to direct the laser to the test section and expand the beam into a laser sheet. Any remaining diffuse scattering from these optics should be blocked from reaching the measurement region using a containment system. Diffuse light scattered along the beam path from sheet-forming optics can be reduced further by replacing the cylindrical lens with a high reflectivity scanning mirror and by masking of the laser sheet just prior to passing through the optical window in the test section.

In the optical test section, it is impossible to eliminate all reflections, but surface treatments, based off the work of Cadel et al. 2016, can be implemented to effectively reduce the magnitude of the reflected light. This work concludes that the best surface treatments either require application of fluorescent dye-doped paint, a mirrored surface finish, or flat black paint. While fluorescent paint seems to be the best strategy in Cadel et al. 2016, the fluorescent emission of Kiton Red 620 was found to be visible in filtered Rayleigh scattering images due to near-laser wavelength emission and long exposure times. Since mirroring the surfaces are not practical in all full scale flow facilities, a flat black painted surface, finished with medium sandpaper was determined to produce the most favorable results.

The last step in mitigating the amount of geometrically scattered light collected by the imagers is by carefully selecting the imaging positions to minimize such scattering (Bridges and Wernet 2019). Other methods in reducing Geometric scattering contributions in processed data include the application of structured illumination such as seen in the work of Kristensson et al. 2014 and Kempema and Long 2014 but are not demonstrated in this work.

Overall, these mitigation strategies create an exemplary system in reducing the overall intensity of geometrically scattered light and help to expand the bounds of the intersection rejection region discussed in Sections 2.2.1-2.2.3.

3 FRS multi-property flow measurement

3.1 Spectra-based Doppler shift measurement

When only velocity measurements are desired or if velocity determination is to be used as a first step in processing measured Rayleigh spectra, various determination procedures may be applied. The basic principles of these methods are based off the work of Cadel and Lowe 2015, who initially developed the cross-correlation method for use in cross-correlation DGV, and Boyda et al. 2019, where this method was adapted for use with FRS.

For Rayleigh scattering applications, the Doppler shift associated with measured FRS spectra is determined by comparing the measured spectra to a modelled reference convolution spectrum generated at conditions similar to the flow, but with velocity set to 0 m/s. Using this methodology, the Doppler frequency shift between the measured and modeled spectra can be determined using one of three methods: determining the cross-correlation, finding the shift between the two spectra using a least-squares optimization, or by identifying the frequency of the trough minimum in the FRS signal and computing its displacement from the modeled trough minimum. The determined frequency shift is then related to local velocity using the Doppler shift equation defined in Eq. 1. The methods discussed in the following three subsections focus on how the sensed velocity is determined using the measured and modelled reference spectra.

3.1.1 Cross-correlation Doppler shift measurement

The cross-correlation method, discussed in detail in Boyda et al. 2019, determines the Doppler shift by cross-correlating the mean subtracted measured and pre-convolution spectrums over the range of the entire frequency scan, ν, producing the cross-correlation coefficient, R, as a function of shift or lag values, η_i. The cross correlation at the i^{th} pixel is defined as

$$R(\eta_i) = \frac{1}{\sigma_{S_{Meas}}\sigma_{S_{Ref}}} \sum_{j=1}^{N} S_{Meas}(\nu_j) S_{Ref}(\nu_i + \eta_j) \qquad (6)$$

where S_{Meas} and S_{Ref} are the mean-subtracted measured and reference pre-convolution spectra at the i^{th} pixel, respectively, and $\sigma_{S_{Meas}}$ and $\sigma_{S_{Ref}}$ are the standard deviations of their respective signals. The shift or lag value associated with the peak of the cross-correlation spectrum, determined by fitting a parabola to the peak ± 2 points, corresponds to the Doppler frequency shift of the measured spectrum. More information on this method can be found in Cadel and Lowe 2015, Cadel and Lowe 2016, and Boyda et al. 2019.

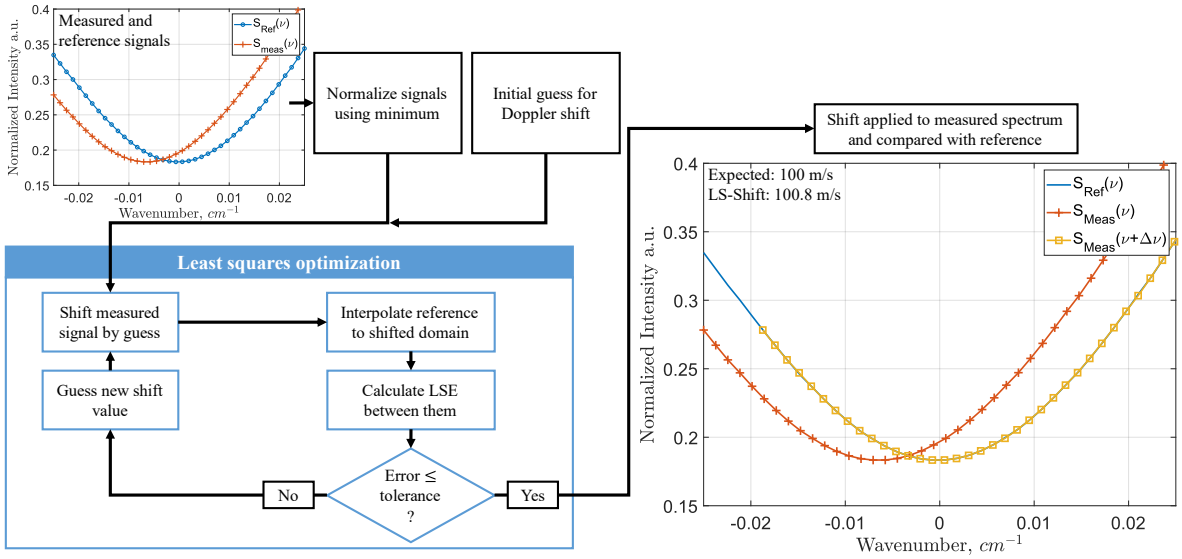

Figure 6. Least-squares Doppler shift determination schematic. Note that all spectra depicted are generated using noise-free analytical models.

3.1.2 Least-squares Doppler shift measurement

To utilize the information in the FRS signal more efficiently, the least-squares Doppler shift (LS-shift) determination was developed. To determine the Doppler shift of a measured spectrum using this method, the measured and modelled signals are first normalized by their minimum intensity. The two normalized signals in addition to an initial guess for sensed velocity (typically 0 m/s) are input into the least-squares optimization algorithm to determine the shift value that results in the lowest least squares error. Inside the LS-shift algorithm, the shift is applied to the reference spectrum and then linearly interpolated to the same wavenumber space as the measured spectrum for point-to-point comparison. Fit error (E_{Fit}) is calculated using the following equation,

$$E_{Fit} = \sum \left(S_{meas}(\eta + \sigma) - S_{Ref}(\eta)\right)^2 \qquad (7)$$

where σ is the shift applied to the measured signal. If this fit quality is minimized sufficiently, the iteration stops, and the final shift value is output as the Doppler shift between the two spectra. The algorithm used to perform this optimization is the derivative free simplex search method of Lagarious et al. 1998, which minimizes the least square error. A flow chart of the LS-shift processing method employed in the current work can be seen in figure 6.

3.1.3 Minimum-displacement Doppler shift measurement

An alternative method to the cross-correlation and the LS-shift methods, developed specifically to provide measurements more robust to signal contamination, is the minimum-displacement Doppler shift (min-shift) determination method. For this method, the Doppler shift is evaluated by fitting a parabola to the logarithm of the normalized measured and pre-convolution spectra using the minimum intensity value ± 2 points. The use of the log function was derived by empirical intuition and the necessity to accentuate the trough region of the spectrum by increasing the magnitude of the gradients outside of the minimum. The difference between the wavenumber associated with the minimum of the measured and reference pre-convolution spectra corresponds to the Doppler frequency shift between them.

This method uses the least amount of information out of any of the discussed Doppler shift determination techniques, and is expected to display higher estimator variance due to the reduction in Fischer information (Fischer 2017) making it more susceptible to signal noise. However, as is only uses information in the highest absorption regions of the iodine transmission, the benefits in robustness to Mie and geometric scattering contamination are expected to outweigh the increased estimator variance. A schematic of the min-shift processing method can be seen in figure 7.

3.1.4 Uncertainty and bias error in Doppler shift measurement

In comparing the Doppler frequency shift determination methods, we note that the bias error and uncertainty associated with the cross-correlation method, though low when broadband spectral information is available, becomes large as the range and total number of collected datapoints within the frequency scan approaches zero (Cadel and Lowe 2016). Since the present work focuses on highly contaminated Rayleigh signals over a small rejection region, our

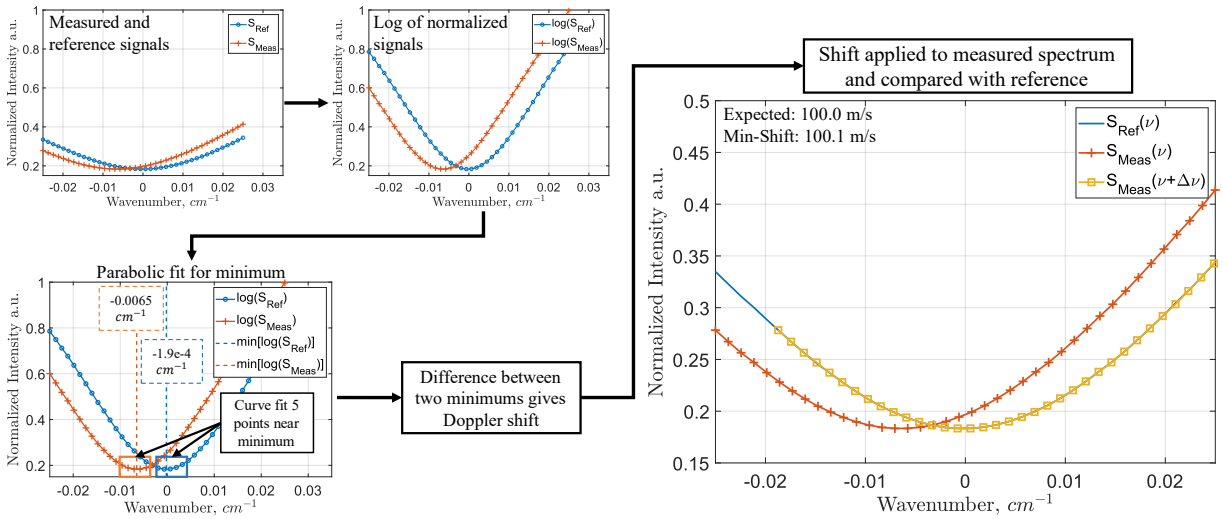

Figure 7. Minimum-displacement Doppler shift determination schematic. Note that all spectra depicted are generated using noise-free analytical models.

experimental spectra only consist of approximately 20 discrete frequencies spanning across 0.03 cm^{-1}. As such, the cross-correlation method would result in large bias errors, while the LS-shift and min-shift methods do not.

Figure 6 and figure 7 show the analysis of a theoretically perfect Rayleigh convolution spectrum with no noise and no signal contamination included. These spectra are generated for a frequency range and resolution similar to experimental measurements at a pressure of 1 atm, a temperature of 290 K, and an observation angle of 90°. In figures 6 and 7, we see that the LS-shift and min-shift methods both estimate the Doppler shift with little bias, as expected with perfect signals. To establish the robustness of these methods we investigate them further by looking at three separate cases. The first case will be a Monte-Carlo (MC) simulation, neglecting the cross-correlation method, including Gaussian distributed random noise to determine the behavior of the bias error and uncertainty at various signal-to-noise ratios (SNR). Cases two and three investigate the biases introduced in velocity measurement with the introduction of Mie and geometric scattering contamination for signals free of random noise.

For the MC simulations we use the same wavenumber range and scan resolution as shown in figure 7, while varying SNR. For each SNR, 100,000 samples are used to ensure proper convergence. The bias error magnitude is shown to be less than 1 m/s for all cases (figure 8a). In figure 8b, the LS-shift method is shown to exhibit a significantly lower variance than the min-shift method when the signal contains no contaminating light sources, as predicted in Section 3.1.3. In general, SNR's of 25 dB or greater are achievable without unreasonable effort in experiment design, and for the present measurements, 25 dB is representative of the total noise measured. This results in a sensed velocity uncertainty of approximately 3.5 m/s. For signals with an SNR near 30 dB, uncertainties of 1.1 m/s are expected.

For the case where Mie scattering intensity is varied, shown in figure 9a, we see that at low levels of Mie scattering, the bias error in all three measurements remain constant up until $IR_{Mie} \approx 10^{-2}$. At this point, the LS-shift and cross-correlation methods (shown for relative changes only) rapidly diverge from the bias error values obtained with no Mie scattering contamination. The surprising result from this investigation is that the min-shift determination method significantly outperforms the other two and is shown to be robust to Mie scattering with a bias error less than 2 m/s when $IR_{Mie} \leq 5$.

For the case where various geometric scattering intensity ratios are applied to the noise-free signal, shown in figure 9b, we see a similar trend where the bias errors in the LS-shift and cross-correlation methods remain constant for $IR_{Geo} \leq 10^{-2}$ but quickly diverge for larger values. Once again, the min-shift method is shown to be more robust to geometric scattering contamination when compared to the other two methods, displaying a bias error of less than 2 m/s until the magnitude of background scattering is the same order of magnitude as the Rayleigh scattered light.

For this very specific simulation case, one could assume that the opposing effects presented in the ls-shift bias error results, when comparing the results from Mie and geometric scattering presented in figure 9, would be additive and may reduce the overall bias. This assumption, however, cannot be applied in general without explicit determination of Mie and geometric scattering contributions for a specific optical arrangement and scan range.

Even though measurement variance is increased by employing the min-shift method, the benefits in contamination

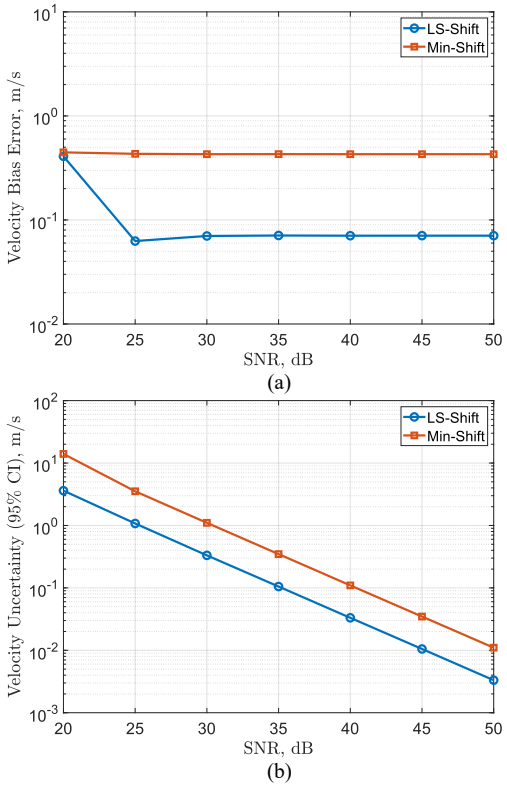

Figure 8. Monte-Carlo simulation results for bias error (a) and uncertainty prediction (b) varying random noise contributions. Note that all spectra depicted are generated using analytical models with simulated noise.

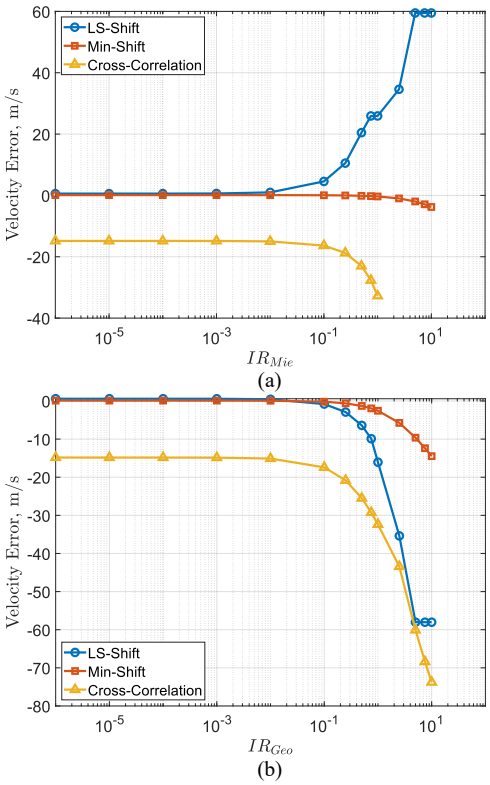

Figure 9. Bias error estimation with increasing signal contamination from Mie scattering (a) and geometric scattering (b). Note that all spectra depicted are generated using noise-free analytical models.

sensitivity is expected to outweigh the loss in measurement precision in high intensity Mie and geometric scattering environments. For the current work, the min-shift velocity is utilized exclusively for high spatial resolution velocity measurements as a result of the robustness to contamination.

3.2 Vector velocity measurements

To evaluate the orthogonal velocity within the measurement plane, a minimum of three independent measurements of Doppler frequency shift is required. The orthogonal velocities (V_x, V_y, and V_z) are determined by transforming the sensed velocity at a single point measured by the three cameras defined by Cadel and Lowe 2015 as,

$$\begin{bmatrix} V_x \\ V_y \\ V_z \end{bmatrix} = \begin{bmatrix} (\hat{o}-\hat{\imath})_{1x} & (\hat{o}-\hat{\imath})_{1y} & (\hat{o}-\hat{\imath})_{1z} \\ (\hat{o}-\hat{\imath})_{2x} & (\hat{o}-\hat{\imath})_{2y} & (\hat{o}-\hat{\imath})_{2z} \\ (\hat{o}-\hat{\imath})_{3x} & (\hat{o}-\hat{\imath})_{3y} & (\hat{o}-\hat{\imath})_{3z} \end{bmatrix}^{-1} \begin{bmatrix} U_1 \\ U_2 \\ U_3 \end{bmatrix} \quad (8)$$

where $(\hat{o}-\hat{\imath})_{ix}$ is the x-component of the sensitivity vector corresponding to the i^{th} imager, and U_i is the sensed velocity measured by the i^{th} imager.

For the present work, the sensed velocity was determined for only two imagers, conventionally yielding only two components of velocity with the state of the third component assumed. In highly non-uniform flows, such as the one interrogated in the current work, significant bias error in the two calculated velocity components is induced anywhere the assumed condition is inaccurate.

Extracting the three-component velocity from this two-camera system required a novel solution. Overlapping FRS measurements in adjacent illuminated regions on the same measurement plane had been designed into the experiment to ensure continuous data over the cross-section of the flow (explained in Section 4). Data collected in the intersection of two adjacent regions was then measured twice by each camera module. This resulted in four independent measurements of Doppler shift, more than sufficient for three-component velocity determination.

In post processing, the sensed velocity for every imager and every plane was first determined using the min-shift method. Then, data from two adjacent planes is imported in the instrument coordinate system (shown in figure 10) and then rotated to the flow centered coordinate system, making sure to rotate the $\hat{o}-\hat{\imath}$ vector by the proper amount as shown in figure

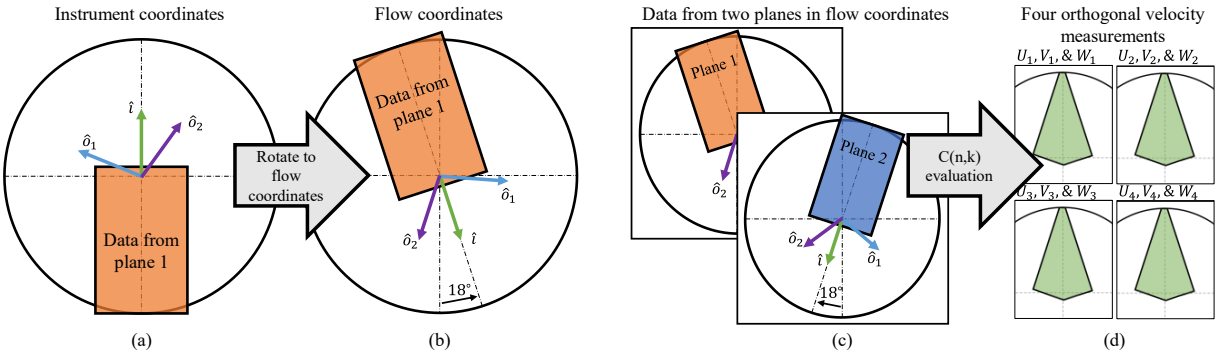

Figure 10. Two-imager, three-component velocity determination schematic

10a and 10b. Three-component velocity is then determined in the overlap region using at least three of the four measurements using equation (8).

To reduce uncertainty in the final measurement, all four of the planes may be used to determine velocity by using mathematical combination. Noting that we must choose a *minimum* of three out of the four options (Charrett et al. 2007), the mathematical formulation for this combination is,

$$\sum_{k\geq 3}^{n} C(n,k) = \sum_{k\geq 3}^{n} \binom{n}{k} = \sum_{k\geq 3}^{n} \frac{n!}{k!\,(n-k)!} \qquad (9)$$

where n is the number of choices, k is the number of chosen elements, and $C(n,k)$ is the syntax for number of possible combinations where k elements are chosen out of n possible choices. Using this formula, five different orthogonal velocity measurements may be extracted using the cases where $k = 3$ and where $k = 4$. For the current work, only the $k = 3$ case was considered, resulting in four independent orthogonal velocity measurements. This procedure can be seen for two planes centered on $-18°$ and $18°$ in the flow centered coordinate system in figure 10c. The four orthogonal velocity results determined are then averaged together, theoretically reducing the resulting orthogonal velocity uncertainty by a factor of approximately 2. In practice, it is possible that this may be less than 2.

3.3 Temperature, density, and pressure measurement

For the measurement of scalar properties, the least-squares curve fit algorithm for simultaneous measurement of velocity, temperature, and density is conducted by performing a three-parameter fit of a modelled Rayleigh convolution spectrum to measured data for every pixel bin. In this fit, sensed velocity (U_{sens_i}), static temperature (T_i), and a static density-dependent intensity scaling (IS_i) parameter, are determined by fitting the model response to the measured intensity spectrum collected within the intersection rejection region. IS_i, is used to scale the normalized convolution spectrum to match the measured spectrum intensity in counts. The methodologies used in this evaluation are similar to those presented in Boyda et al. 2020, Saltzman et al 2019, Boyda et al 2019, and Doll et al. 2017 but are expanded to improve measurement performance in the presence of high intensity Mie and geometric scattering. These additions include an initial guess for velocity (using the min-shift method) in the curve fitting algorithm, a reduced wavenumber range over which to conduct the curve fit due to the filtering of Mie and background scattering using the rejection region analysis, and the requirement to conduct scans at a higher wavenumber resolution so that sufficient information is gathered for low uncertainty measurements while utilizing the reduced wavenumber range.

3.3.1 Temperature and density measurement using the least-squares curve fitting routine

The first step in the curve fit procedure is to determine the sensed velocity for the pixel bins using the min-shift method. This is done so the rejection region analysis, discussed in Sections 2.1.1 through 2.1.3 can be applied to reject Mie and geometric scattering contributions.

As discussed in section 2.2.3, an iodine cell vapor pressure near 1 Torr was sufficient in reducing both Mie and geometric scattering to negligible levels while providing sufficient information for fitting scalar properties. This provided the wavenumber range for the unshifted rejection region used to filter geometric scattering. The shifted region for filtering Mie scattering is then determined by applying the "min-shift" determined sensed velocity to the unshifted rejection region at every pixel bin. The intersection of the two rejection regions is then applied to the pixel bin signals, keeping only the points within this region for the curve fit.

To obtain a density measurement from the intensity, IS_i must be mapped to density by performing a single parameter optimization for the intensity scaling. This is completed by collecting a calibration scan, which is an FRS measurement collected at known temperature and density with no bulk velocity. Figure 11a and 11b show the density calibration procedure for a model spectrum arbitrarily scaled to image intensity. Due to the linear relationship between the density of the gas and the number of photons scattered from the gas

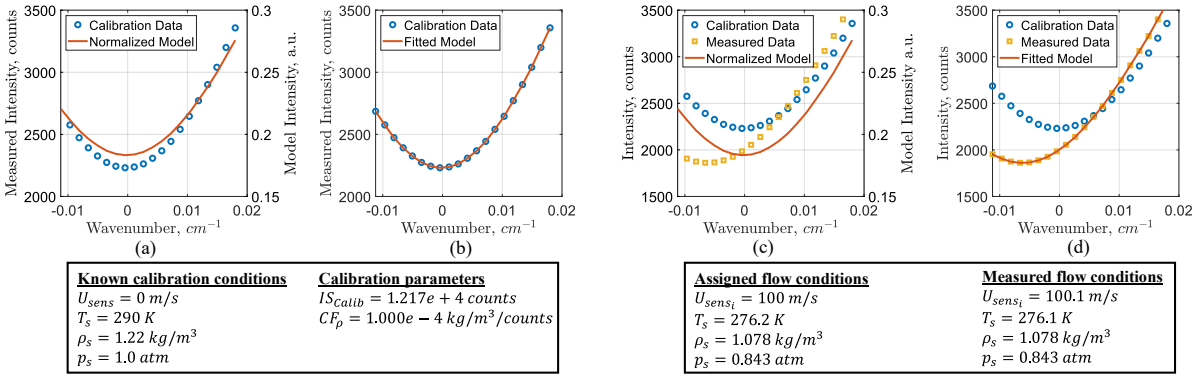

Known calibration conditions	**Calibration parameters**
$U_{sens} = 0\ m/s$	$IS_{Calib} = 1.217e+4\ counts$
$T_s = 290\ K$	$CF_\rho = 1.000e-4\ kg/m^3/counts$
$\rho_s = 1.22\ kg/m^3$	
$p_s = 1.0\ atm$	

Assigned flow conditions	**Measured flow conditions**
$U_{sens_i} = 100\ m/s$	$U_{sens_i} = 100.1\ m/s$
$T_s = 276.2\ K$	$T_s = 276.1\ K$
$\rho_s = 1.078\ kg/m^3$	$\rho_s = 1.078\ kg/m^3$
$p_s = 0.843\ atm$	$p_s = 0.843\ atm$

Figure 11. Simulated FRS density calibration ((a) and (b)) and multi-property determination example ((c) and (d)) using noise free signals.

molecules, it can be assumed that the relationship between IS_i and the known density can be defined using the density calibration factor (CF_{ρ_i}), and is expressed as,

$$CF_{\rho_i} = \frac{\rho_{calib}}{IS_{calib_i}} \tag{10}$$

where ρ_{calib} is the density of the interrogation region during the calibration scan and IS_{calib_i} is the calibration intensity scaling parameter at the i[th] pixel bin. when Mie and geometric scattering are filtered to negligible levels, CF_{ρ_i} is strictly a function of the efficiency of the imaging system and the system geometry. It is important to note that CF_{ρ_i} is susceptible to the random noise present in image data, so, multiple calibration scans may be used to improve results. Note that the density calibration should be performed using the exact same measurement and evaluation settings (rejection region, camera exposure, laser power, etc.) as the multi-property determination to obtain the most accurate value for CF_{ρ_i}.

Once the density calibration factor has been determined, the density at every pixel bin (ρ_i) is determined in flow-on measurements using the following equation.

$$\rho_i = CF_{\rho_i} IS_i \tag{11}$$

With density determined, we now have explicit results for U and T from direct curve fitting and ρ from IS_i and CF_{ρ_i} at every pixel. For three-component velocity results, the values for U (determined from the curve fit or min-shift determination) can be rotated to orthogonal velocity components using equation 8. For this application, the min-shift velocity determination was selected due to higher spatial resolution and better accuracy.

3.3.2 Pressure measurement

Using the known static temperature and static density, the static pressure may then be calculated using the state equation, $p = \rho RT$, where $R = 287.05\ J/kg\ K$ is the specific gas constant for air. Total pressure may then be calculated using static pressure, total velocity, and static temperature using

$$p_0 = p\left(\frac{{V_{tot}}^2}{2c_pT} + 1\right)^{\frac{\gamma}{\gamma-1}} \tag{12}$$

where V_{tot} is the total velocity, determined using the min-shift method, $c_p = 1.005\ kJ/kg\ K$ is the specific heat of air, and $\gamma = 1.4$ is the ratio of specific heats for air. Figures 11c and 11d show an example multi-property measurement for theoretically perfect, density dependent simulated signals.

3.4 Assumptions in FRS multi-property measurements

To summarize the assumptions made in the current work, the authors note that Eq. 2 is used to fit the measured convolution spectrum for U, T, and CF, using the Tenti S6 lineshape model and the iodine transmission model presented in Forkey 1997. It is then first assumed that these two models accurately represent the physical behavior of Rayleigh scattering in this environment and the iodine cells utilized in this environment.

Fundamentally, the use of Eq. 2 to fit the measured convolution assumes that the measured properties are constant at across that FRS scan. In Section 2.2.4, the presence of turbulent fluctuations was discussed but it was also assumed that the FRS instrument samples a statistical average of the flow properties. The assumption then becomes that the differences between the convolution that results from sampling a statistical average of the turbulent flow and the convolution spectrum that would result from a flow at constant conditions, indicative of the average flow values are negligible.

Additionally, it is assumed that when employing the rejection region analysis in these measurements, that Mie and geometric scattering contamination is negligible. It is therefore assumed that the Mie and geometric scattering induce no bias error on the flow measurements.

Since all measurements are dependent on the accurate measurement of camera position with respect to the measurement plane and the laser propagation directions, it is assumed that these positions are know exactly.

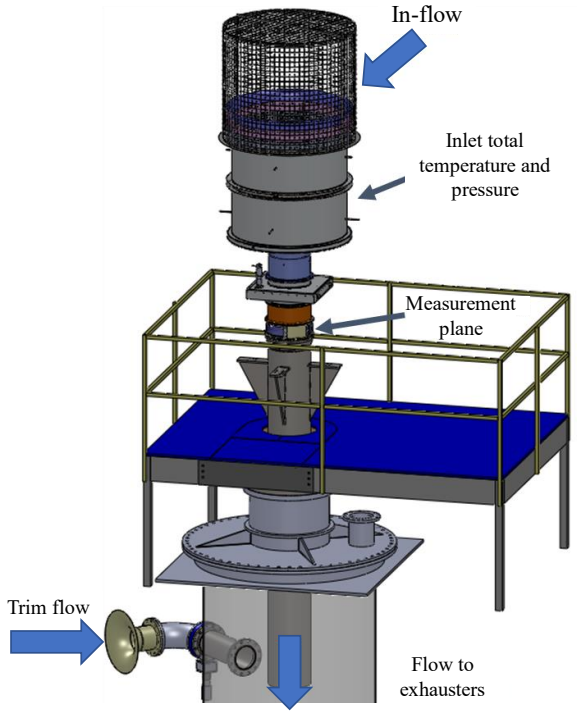

Figure 12. ACF Facility overview, showing the flow conditioning barrel, the measurement plane, and the trim flow setup.

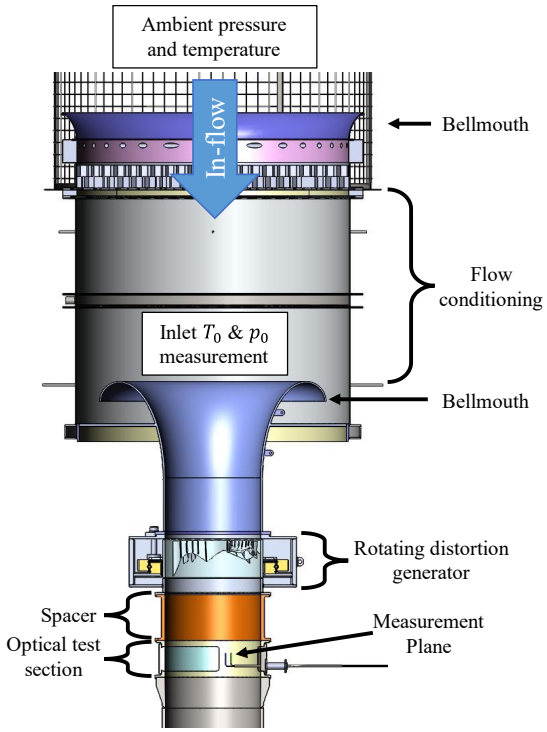

Figure 13. ACF Flow line assembly showing a section view of the measured flow line including the total condition measurement location, the rotating distortion generator, and the optical test section.

4. Experimental setup and FRS instrument integration

The experimental facility used for this FRS demonstration is the Compressor Aero Research Laboratory (CARL) which contains a 1.83 m diameter pipe connection to the Component Research Air Facility (CRAF) exhausters with an exhaust capability of 100,000 CFM at a minimum pressure of 11 inHg (Air Force Research Laboratory 2013). Utilizing this exhauster resource, the static test facility known as the Annular Cascade Facility, shown in figure 12, was constructed using a configurable 432 mm diameter, 10-diameter-long flow line mated to the 1.83 m diameter exhauster section to minimize the influence of the exit on the measurement plane. To allow for closed loop control, a trim valve was installed so that the overall Mach number in the test section could be held at M = 0.5 $\pm$0.5% (nominal cross-sectional average). For the current work, measurements were made in a completely enclosed flow environment less than one diameter downstream of a distortion generating test article such as the one shown in figure 13.

The specific test article was chosen to produce a highly non-uniform flow, characterized by large variations in both vector velocity and total pressure, with a static temperature and density difference greater than the FRS uncertainty when compared to flow-off calibration. Additionally, the test article had been previously characterized using a 5-hole probe survey and two component PIV measurements at the same downstream location. These reference measurements are used in the results section to validate the FRS measurements and their respective uncertainties to the current standard, as well as to compare FRS measurements to a widely used laser-based diagnostic technique.

To capture the entire flow field, the distortion generating test article was mounted in a rotating assembly so that it, and thus the flow at the measurement plane, could be rotated with respect to the integrated FRS measurement system.

4.1 FRS instrument integration

The present measurement system, shown in figure 14, consists of a single frequency, continuous wave (CW) laser, a laser monitoring subsystem, measurement region illumination optics, and two camera modules used to observe the flow. While the facility was operating on condition, the entire system including safety systems were operated remotely from a control room adjacent to the test cell.

The laser used in this measurement campaign was a Coherent Verdi V18 laser, a single-frequency, diode-pumped, solid state laser with a maximum output power of 18 Watts at a wavelength of 532 nm and linewidth of approximately 5 MHz. The emitted beam has a diameter of approximately 2 mm with a beam divergence of less than 0.5 mrad. Within the laser, the temperature of the internal etalon may be adjusted

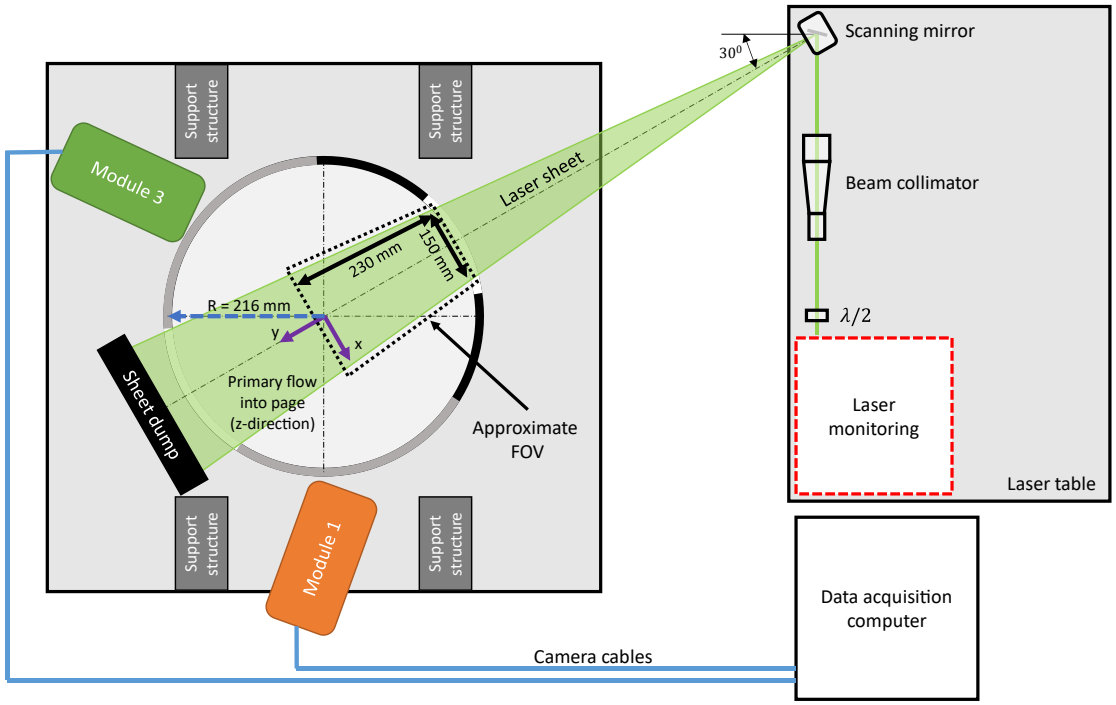

Figure 14. Top-down view of the integrated FRS instrument. The coordinate system shown is the instrument coordinate system. The flow coordinate system rotates with the distortion generating test article.

for coarse frequency tuning, while fine frequency adjustment and scanning is achieved by changing the internal cavity length via voltage applied to a piezoelectric stack (PZT). The laser system was placed within an enclosure (red dashed line in figure 14) which housed the laser head, heat sink, an external shutter, and all the reference optics for recording the frequency of the laser during a scan shown in Boyda et al. 2020.

As the beam exits the enclosure, it is directed through a $\lambda/2$ plate, optimizing the polarization state of the beam for signal intensity, and then through a collimator that results in a sheet width of approximately 0.5 mm at the measurement plane. The beam was then steered to a scanning mirror which directed the beam to the measurement region while scanning rapidly back and forth to create a flat sheet.

The scanning mirror used is a Thorlabs single-axis large beam diameter scanning galvanometer system, model number GVS311(\M) with a high-power fundamental and second harmonic Nd:YAG anti-reflective coating. The scanning mirror was driven using a triangle waveform, providing uniform illumination across the laser sheet. In addition to the more desirable intensity distribution and a noticeable reduction in diffusely scattered light, compared to a cylindrical lens arrangement, the controllability of the scanning mirror in sheet width and pointing direction allowed for significantly easier alignment of the laser sheet within the test section, even allowing adjustments while the facility was running. Once aligned, the laser sheet width was maximized to the size of the exit window slot, resulting in an FRS measurement plane that measured approximately 150 mm x 230 mm. For this configuration, an exposure time of 4.5 seconds per laser frequency was used. With a total of 65 frequencies, the total scan time for each measurement was approximately 15 minutes, representing the period over which the measurements were averaged.

In this measurement campaign two separate camera modules were utilized to obtain two linearly independent Doppler shift measurements. Each camera module consists of two FLIR Blackfly S USB 3.0 machine vision cameras, model number BFS-U3-31S4M-C. These cameras were set up to collect 12-bit images at a resolution of 3.1 MP and are fitted with Edmund Optics 16 mm focal length c-mount lenses to achieve the desired field of view. 25 mm diameter, 532 nm band-pass filters were fitted to the lenses to reject off-wavelength light.

Light scattered to the camera modules, shown in figure 15, is split and directed to the two cameras using a 100 mm x 75 mm plate beam splitter with a reflectivity to transmission (R/T) ratio of 30/70 and a 100 mm x 75 mm plate mirror. The R/T ratio of the beamsplitter was chosen to improve the use of the camaras' dynamic range by increasing the light used by the filtered camera while reducing the intensity on the unfiltered camera. Reduced unfiltered camera intensity is desired because this imager is routinely saturated by the presence of Mie and background scattering (which still occurred in this experiment). The light incident on the filtered

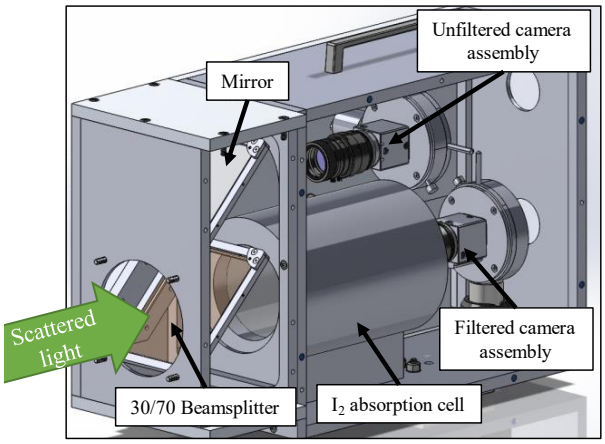

Figure 15. FRS Imaging module assembly

camera passes through an ISSI I2S-5 starved molecular iodine cell with a design vapor pressure of approximately 1 Torr. The cell was then operated at 65°C, greater than 20°C above the dew point of the cell, ensuring a stable transmission profile when imaging through the vapor cell. Minimum achievable transmission values within this range are typically less than 10^{-11} for a starved ISSI iodine cell at a vapor pressure near 1 Torr (Forkey et al. 1997).

4.2 FRS full cross-section measurement

In this measurement campaign, a cross-sectional plane of an internal flow was measured using the FRS instrument. The instrument itself remained static, so the entire flow field was captured by rotating the approaching non-uniform flow, requiring 10 different rotator positions to obtain full coverage while maintaining sufficient overlap. Rotator scans began at an initial angle of $-18°$ and as measurements were collected, the flow was rotated $36°$ from one position to the next. This scheme yielded approximately 20% overlap in adjacent illuminated regions on the same plane. A complete characterization of the cross-section could be measured in approximately 150 minutes. During data collection, however, some scans were repeated yielding a measurement time of approximately 3 hours.

Data from the 10 rotator positions were combined into a single plane using the data meshing procedure of Guimaraes et al. 2017 employing a cartesian mesh instead of a polar mesh. This 10-plane combination provided measurements of three-component vector velocity, static temperature, and static density using only FRS-derived intensity information and allowed for the calculation of static and total pressure.

4.3 Complications in FRS data collection and the uncertainty impacts

During the measurement campaign at the CARL, a few issues were discovered in the system that reduced the quality of the measured data, making desired quantities more challenging to measure. The first issue was that the center wavenumber of the laser was not consistent from scan to scan but oscillated at random low temporal frequencies and amplitudes. To resolve this issue, a combination of least-squares iteration and transmission dependent offsets provided the best result for mapping applied PZT voltage to laser wavenumber, usually a trivial task. Unfortunately, this was not enough, and as a result, significant temperature bias errors were observed that had not been observed in any previous experiments. In future work, a laser frequency feedback control loop, in addition to monitoring with a wavelength meter may be used to reduce or eliminate this issue.

Based on inlet total conditions and wall static pressure measurements collected at the measurement plane, the average temperature at the measurement plane was expected to be approximately $279\ K$. Upon application of the methods described in Section 3.3.1, the FRS measured static temperature was found to have a significant positive bias, measuring a static temperature of $367\ K$. To determine the source of the bias, the density calibration scan was processed using the same three-parameter curve fit and rejection region. In this evaluation over the same region, the determined temperature was found to be $375\ K$, once again much higher than the flow-off temperature of $295\ K$.

With all possible sources of bias error considered, it was determined that the most likely cause of this bias was the instability in the etalon temperature controller, leading to inaccurate mapping from applied PZT voltage to wavenumber space. Because of the nature of the inaccurate mapping, the measured spectrum occupied a larger range of wavenumbers than expected, causing a positive bias in the temperature determination. This was unable to be confirmed due to a lack of independent wavelength monitoring necessary to perform such an analysis.

Over limited ranges, changes in the temperature of the gas and the angle at which Rayleigh-Brillouin scattering is observed have a similar effect on the modeled convolution spectrum. This relationship is shown in figure 16, where a convolution spectrum modelled at $T = 295\ K$ and $\theta = 90°$ is very similar visually to a spectrum modelled at $T = 375\ K$ and $\theta = 77.5°$. Quantitatively, the RMSD of these two spectrums is 0.23% of the mean intensity.

By adding a calibrated offset to either temperature or observation angle, we were able to offset the other while still maintaining sensitivity to changes in the fitted value. Since temperature was one of the primary measurands, it was determined that this calibrated offset would be applied to the observation angle using the calibration scan, where the state of the gas is known by fitting the calibration scan data for angle while assuming temperature is set to ambient conditions. This calibration enabled the measurement of static

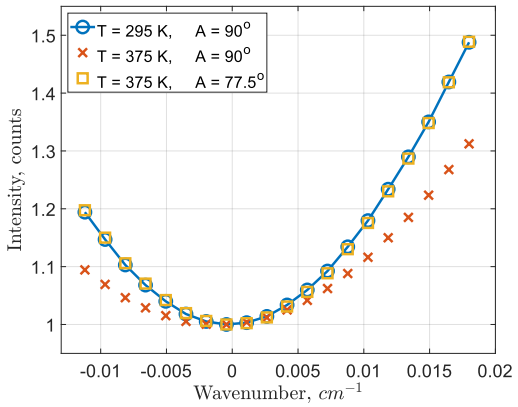

Figure 16. Similarity in the effect of changing temperature and observation angle in the FRS convolution spectrum.

temperature in the flow on condition more accurately than would have otherwise been possible.

In application, this calibration was conducted by fitting the calibration scan for observation angle and the intensity scaling parameter at every pixel bin while holding the sensed velocity, temperature, and pressure constant at the known values in the iteration. The density correction factor is then determined for each bin as outlined in Section 3.3.1. These results are then applied to the flow on measurement scans by substituting the calibrated angle for the angle determined using the spatial calibration. Multi-property determination for sensed velocity, temperature, and intensity scaling was otherwise determined as described in Section 3.3.

The laser also experienced a low amplitude, high frequency laser instability derived from the noise emitted from the flow production facility. While this type of instability has the potential to impact the measurement by artificially broadening the Rayleigh lineshape, similar to the effect of turbulence on the Mie scattered spectrum, an investigation into the magnitude determined that the laser linewidth was increased from 5 MHz to approximately 16 MHz, yielding a negligible change in determined temperature in simulated signals.

The final issue we ran into in this measurement was the application of the open source CalTech calibration toolbox (Zhang 1999). In final processing, only two imaging modules were used resulting in a reduction in the number of independent views of the calibration plate. As a result, error was induced in extrinsic parameter determination in the spatial calibration. It was determined that a simpler image calibration scheme (Tsai 1987) outperformed contemporary tools developed for multi-view configurations (e.g., Zhang 1999). With only two views of significantly different viewing angles, the Tsai method provided more accurate and consistent extrinsic calibration parameters and thus was utilized exclusively. The reader is encouraged to review the works referenced above for details on the benefits and deficiencies of these methods under different conditions.

4.4 Measurand Uncertainties

The properties of observed Rayleigh scattering and thus the measurements obtained from the FRS instrument are highly dependent on the optical arrangement employed to measure both vector velocity and scalar measurements. Therefore, a high-level overview of the integrated FRS instrument uncertainties is presented. In some situations where the magnitude of uncertainty cannot be expressed as a constant value or as a percent of the measured value, assumptions are used to simplify equations and nominal flow properties are introduced to provide an estimate for uncertainty.

A benchtop experiment and signal simulations were conducted to estimate the measurement uncertainties prior to entry at the CARL facility. The experiments were conducted using the same optical hardware and similar camera positions shown in figure 14. The flow to be measured was generated using a 19 mm diameter turbulent jet, probed 25 mm downstream of the nozzle exit using the FRS instrument. This jet flow was supplied using a small centrifugal compressor, generating a Mach 0.4 exhaust flow with a total temperature of 310 K at an exit static pressure of 0.93 atm. Plenum total temperature and pressure were measured using a Kiel-type combination total pressure and temperature probe, with measurement uncertainties of 0.1% (ZOC17 pressure transducer) and 0.75% (K-type thermocouple). Exit total pressure and temperature were measured using a similar combination probe, allowing for the calculation of velocity. The jet measurement was not used to determine uncertainty in density or temperature due to the similarity between ambient conditions in the lab and the conditions of the jet core flow.

Velocity uncertainties determined from these experiments were calculated by applying a 95% confidence interval on the root-mean-square difference between pressure-derived velocity of the jet core flow and FRS measurements in the same region. Results are presented in table 1, and while the velocities vary locally in the jet experiment, the axial velocity uncertainty (δ_{v_z}) represents a value of about 7% of the average axial velocity in the jet core.

Signal simulations were then used to determine pre-measurement temperature and density uncertainties. This consisted of a Monte-Carlo simulation of the FRS measurement of a Mach 0.5 expanded from the average atmospheric conditions of the flow facility. The secondary components of velocity were varied with magnitudes producing a maximum flow angle of 30 deg. This signal simulation assumes a signal noise of 25 dB. The uncertainties in vector velocity, temperature, and density were calculated using the 95% CI between the determined values and the assigned values. Results are presented in table 1.

As a result of the mathematical combination of planes, discussed in Section 3.2, the velocity uncertainties should theoretically be reduced by a factor of approximately two. In application however, it was observed that the variation in separately determined orthogonal velocity values had a standard deviation that was similar in magnitude when compared to the 2σ uncertainty. As a result of this observation, the factor of two reduction in uncertainty is not applied, and the uncertainty bars displayed in the results section represent the uncertainties presented in table 1.

Table 1. FRS measurement uncertainty results

	δ_{V_x}	δ_{V_y}	δ_{V_z}	δ_T	δ_ρ
Sim.	$\pm$3 m/s	$\pm$11 m/s	$\pm$9 m/s	$\pm$3 %	$\pm$4 %
Exp.	$\pm$3	$\pm$11	$\pm$10	N/A	N/A

While the uncertainties in table 1 are calculated for the measurements made directly using the FRS spectral information, the excess of simultaneously measured flow properties allows for the calculation of additional flow properties, the uncertainty quantification of which must also be quantified.

Static pressure is calculated as discussed in Section 3.3.2. As a result, the uncertainty in pressure can be expressed as shown in equation 13, resulting in an uncertainty of 5% as presented in table 2.

$$\frac{\delta p}{p} = \left[\left(\frac{\delta\rho}{\rho}\right)^2 + \left(\frac{\delta T}{T}\right)^2\right]^{1/2} \tag{13}$$

Total pressure is then calculated using equation 12, defined as being a function of pressure, velocity, and temperature. As such, the error is represented as the norm of the partial derivatives of the original equation with respect to the independent variables. The expression for this is then shown in equation (14) below.

$$\delta p_0 = \left[\left(\frac{\partial p_0}{\partial p}\delta p\right)^2 + \left(\frac{\partial p_0}{\partial V_{tot}}\delta V_{tot}\right)^2 + \left(\frac{\partial p_0}{\partial T}\delta T\right)^2\right]^{1/2} \tag{14}$$

Plugging in for the partial derivatives we get the expression shown in equation 15. Note that each term in this equation has local dependencies on one or more of the independent variables, leading to the conclusion that the uncertainty will vary spatially and must be determined locally.

$$\delta p_0 = \left[\left\{\left(\frac{V_{tot}^2}{2c_pT}+1\right)^{\frac{\gamma}{\gamma-1}}\delta p\right\}^2 + \left\{-\frac{\rho V_{tot}^2}{2T}\left(\frac{V_{tot}^2}{2c_pT}+1\right)^{\frac{1}{\gamma-1}}\delta T\right\}^2 + \left\{\rho V_{tot}\left(\frac{V_{tot}^2}{2c_pT}+1\right)^{\frac{1}{\gamma-1}}\delta V_{tot}\right\}^2\right]^{1/2} \tag{15}$$

The only uncertainty in equation 15 that has yet to be defined is the uncertainty in total velocity. Using the same method applied above, the uncertainty in total velocity can be expressed as shown in equation 16.

$$\delta V_{tot} = \left[\left(\frac{v_x}{V_{tot}}\delta v_x\right)^2 + \left(\frac{v_y}{V_{tot}}\delta v_y\right)^2 + \left(\frac{v_z}{V_{tot}}\delta v_z\right)^2\right]^{1/2} \tag{16}$$

Once again, this process results in an uncertainty expression that will vary locally. However, to get a general idea about the magnitude of the total velocity uncertainty, we assume that the axial velocity dominates, which is true for most of the flow. Removing the δv_x and the δv_y terms from equation 16, yields an uncertainty of $\delta V_{tot} \approx \delta v_z = 9\ m/s$.

Plugging this uncertainty back into equation 15, in addition to nominal values for the other flow properties ($V_{tot} \approx 173 m/s, T \approx 279\ K,\ \rho \approx 1.0\ kg/m^3,$ and $p \approx 80.2\ kPa$) yields a total pressure uncertainty of $\delta p_0 \approx 5.15\ kPa$ (5.5%), as shown in table 2.

Finally, to obtain the expression for uncertainty in measured flow angle, the procedure used to derive equations 15 and 16 are applied to the definitions for tangential flow angle (α) and radial flow angle (β) in equations 17a and 17b respectively.

$$\alpha = \tan^{-1}\left(\frac{v_\theta}{v_z}\right) \tag{17a}$$

$$\beta = \tan^{-1}\left(\frac{v_r}{v_z}\right) \tag{17b}$$

Due to the orientation of the measurement plane, shown in figure 14, the tangential flow velocity (v_θ) is approximately equal to v_x, and the radial flow velocity (v_r) is approximately equal to v_y over most of the measurement plane. To simplify the uncertainty expression, these are substituted, noting that the uncertainty in α will be slightly underestimated in portions of the flow while the uncertainty in β will be slightly overestimated. The uncertainty expressions are then shown in equations 18a and 18b.

$$\delta\alpha = \frac{1}{v_x^2+v_z^2}\left[v_z^2\delta v_x^2 + v_x^2\delta v_z^2\right]^{1/2} \tag{18a}$$

$$\delta\beta = \frac{1}{v_y^2+v_z^2}\left[v_z^2\delta v_y^2 + v_y^2\delta v_z^2\right]^{1/2} \tag{18b}$$

The expression for flow angle uncertainty is once defined using local velocity values. For an estimate of the uncertainty in the flow angles, it can be assumed that $v_z \gg v_x$, and that $v_z \gg v_y$, yielding uncertainties of $\delta\alpha \approx \delta v_x/v_y = 0.018\ rad$ (1.0°) and $\delta\beta \approx \delta v_y/v_z = 0.066\ rad$ (3.8°). Results are shown in table 2. Note that this approximation results in a minimum in the 95% confidence interval uncertainty, and as α and β increase, so too will their uncertainties.

Table 2. FRS uncertainty prediction results (continued)

	δ_p	δp_0	$\delta\alpha$	$\delta\beta$
Sim. Derived	±5 %	±5.5 %	1.0°	3.8°

4.5 Reference measurements

For the purposes of validating the FRS instrument, individual measurements determined using the techniques described in this this work are compared to reference data collected for the same distortion generating test article in previous measurement campaigns. FRS velocity measurements are compared directly to 5-hole probe and PIV measurements using circumferential profiles at four different radii shown in the flow-centered coordinate system in figure 17. Due to that lack of comparable measurements, time-averaged FRS temperature and density measurements are compared with the expected average static temperature and static density at the measurement plane. These are calculated by relating total conditions measured at the facility inlet to the average of several wall static pressures at the measurement plane using isentropic relations.

5-hole probe measurements were collected using a two-element rake, separated by approximately 24 mm, that was developed in-house by AFRL and calibrated individually by AeroProbe Inc. The individual elements were assembled using a single stem that was 9.5 mm in diameter and 483 mm long. The assembly was traversed radially at the measurement plane using a Rotodata radial traverse system, while circumferential travel was achieved by rotating the distortion generating test article.

The repeatability and accuracy of the 5-hole probe measurements were evaluated experimentally using 38 common probe locations yielding a repeatability to within ± 1.5 deg for tangential and radial flow angles. Velocity could be measured most accurately for axial velocity, tangential flow angle, and radial flow angle with 95% confidence interval uncertainties of ±2.7 m/s for axial velocity and 1.5 deg for tangential and radial flow angle (Sanders et al. 2016). In comparison with PIV and FRS data, radial and tangential flow angle will be used in lieu of orthogonal velocity components. Static pressure could be measured within 0.32 kPa and total pressure could be measured within ±0.11 kPa (Nessler et al. 2017 and Sanders et al. 2016). Static temperature and density used to compare FRS scalar measurements to are calculated using isentropic relations, total temperature ($\delta T_0 = 0.75\%$) and total pressure measured at the inlet, and static pressure measured using the 5-hole probe. Uncertainties are estimated as $\delta T_s = 0.75\%$, and $\delta\rho = 0.8\%$.

Reference PIV measurements are collected as two-dimensional, planar PIV with the laser sheet oriented in the x, z-plane shown in figure 17 (tangent to the circumferential direction and aligned with the axial flow respectively). In this application the velocity component V_y, aligned perpendicular to the laser sheet during these measurements, are not resolved.

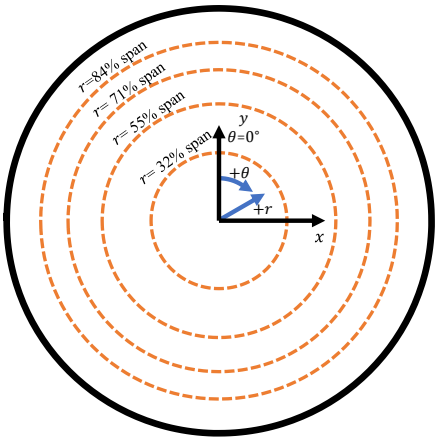

Figure 17. Circumferential profile locations where FRS measurements are compared to 5-hole probe and PIV data. Coordinates are relative to the distortion generator and the z-direction follows the right hand rule and is along the primary flow direction.

The laser optics and camera for the PIV measurement system were mounted on a stage so that the measurement system could be traversed parallel to the y-axis the need for optical adjustment. Coupling this motion with the capability to rotate the flow allowed for most of the flow path to be visible to the PIV measurement system. PIV measurements were recorded at 2 kHz and 2000 image pairs were recorded and averaged at each measurement location with a 73 mm x 50 mm inspection region. The maximum bias error of tangential flow angle measured by the PIV was found to be ±0.6 deg of the maximum angle based on repeated measurements. Uncertainties of additional PIV-derived measurements were not explicitly determined but are estimated herein based upon past work in a similar application (Guimaraes et al. 2018). PIV uncertainties were found to be $\delta V_Z = 3.8\, m/s$ of measured axial velocity and $\delta V_\theta = 1.1\ deg$ of measured swirl angle. For comparison of PIV data with 5-hole probe and FRS data, these uncertainty bounds will be used.

5. Results and discussion

FRS-based vector velocity measurements are determined for the entire cross section of the ACF at a spatial resolution of 3 mm x 3 mm (3 pixel x 3 pixel bin) using the min-shift method while multi-property measurements of temperature, density, and pressure were collected at a spatial resolution of 12 mm x 12 mm (12 pixel x 12 pixel bin). This disparity in spatial resolution is due to the greater SNR required for acceptable precision in temperature and density measurements. Three-component velocity and scalar

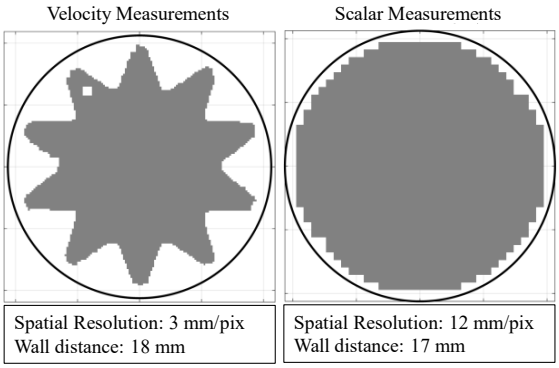

Figure 18. Measurement coverage in comparison with the entire circular cross-section of the ACF.

measurement (temperature, density, and pressure) coverage are shown in comparison with the full cross-sectional area of the ACF in figure 18.

Comparisons between 5-hole probe, PIV and FRS measurements are displayed as the difference between the PIV or FRS measurement and the 5-hole probe data on the y-axis, while the x-axis is the rank of the measurement, ordered from smallest to largest value according to the 5-hole probe value.

5.1 Three-component velocity

FRS results for time-averaged axial velocity, tangential flow angle, and radial flow angle are compared to reference 5-hole probe and PIV measurements in figure 19. The axial velocity comparisons in figure 19(a) and (b) show good agreement, indicated as overlap in uncertainty bounds for a majority of the data, in accuracy in comparison with the 5-hole probe measurements with all the 32% span data and much of the 71% span data measuring the same value as the 5-hole probe within the uncertainty bounds. However, in figure 19 (a), the FRS results are more similar in value to the 5-hole probe data when compared to the PIV data when $rank < 40$ but display values less similar to the 5-hole probe. FRS axial velocity results at the 71% span position (figure 19b) seem to show similar agreement with the 5-hole probe data when compared to the PIV data everywhere but are characterized as having larger variation in value. This effect is most likely due to the increased proximity to the wall, resulting in less overlap-based averaging and greater noise magnitude. A further increase in variance is seen at 84% span in comparison to the results at 71% while results at 55% span perform similarly in comparison to the results at 32%. Looking at the quantitative results in table 3, similar performance is seen between FRS and PIV measurements in mean difference (MD) and root-mean square difference (RMSD). Most of the FRS measured values are observed to agree with the 5-hole probe data within the pre-determined uncertainty bounds (table 1 and table 3).

Table 3. Axial velocity comparison results in m/s

Span	MD_{PIV}	$RMSD_{PIV}$	MD_{FRS}	$RMSD_{FRS}$
32%	5.9	9.1	5.9	6.3
55%	1.9	5.6	-1.5	6.5
71%	2.4	5.9	-5.5	8.0
84%	3.3	6.2	-3.7	6.7

Table 4. Three-component tangential flow angle comparison results in deg

Span	MD_{PIV}	$RMSD_{PIV}$	MD_{FRS}	$RMSD_{FRS}$
32%	-0.10	1.87	-0.35	0.96
55%	0.11	1.49	-0.16	1.04
71%	-0.04	1.04	-0.02	1.07
84%	-0.14	1.92	-0.94	1.67

Table 5. Three-component radial flow angle results in deg

Span	MD_{FRS}	$RMSD_{FRS}$
32%	1.43	1.91
55%	1.60	3.26
71%	2.52	4.32
84%	2.85	4.73

The tangential flow angle comparisons shown in figure 19 (c) and (d) once again show good agreement between all three measurement techniques. In this comparison, most of the FRS measurements are accurate, within uncertainty bounds, to the reference 5-hole probe measurements. We also see a similar trend in the error of the measured FRS values in comparison to the PIV measurements. Table 4 shows the quantitative comparison between the FRS and PIV measurements, indicating that these two techniques perform very similarly, mimicking the axial velocity results.

Noting that the uncertainty of the 5-hole probe measurement is 1.5 deg, the RMSD of the FRS measurement is bounded by this uncertainty except for the outermost span. When looking at the 84% span location, we see the FRS data produces a much larger RMSD, thus indicating higher levels of noise than the measurements at 71%.

The radial flow angle comparison shown in figure 19e and (f) shows that the FRS results once again measure β accurately within uncertainty bounds for the 32% span position while a few of the data points collected at the 71% span position close to $rank = 0$ fall outside of these bounds. We can see in figure 19f that most of the FRS-measured values slightly underestimate the magnitude of the radial flow angle compared to the 5-hole probe, while values of lower rank overestimate the magnitude. Looking at the quantitative comparison in table 5, and noting that the uncertainty of the 5-hole measurements, the MD in the FRS measurements compared to the 5-hole probe measurements is either close to,

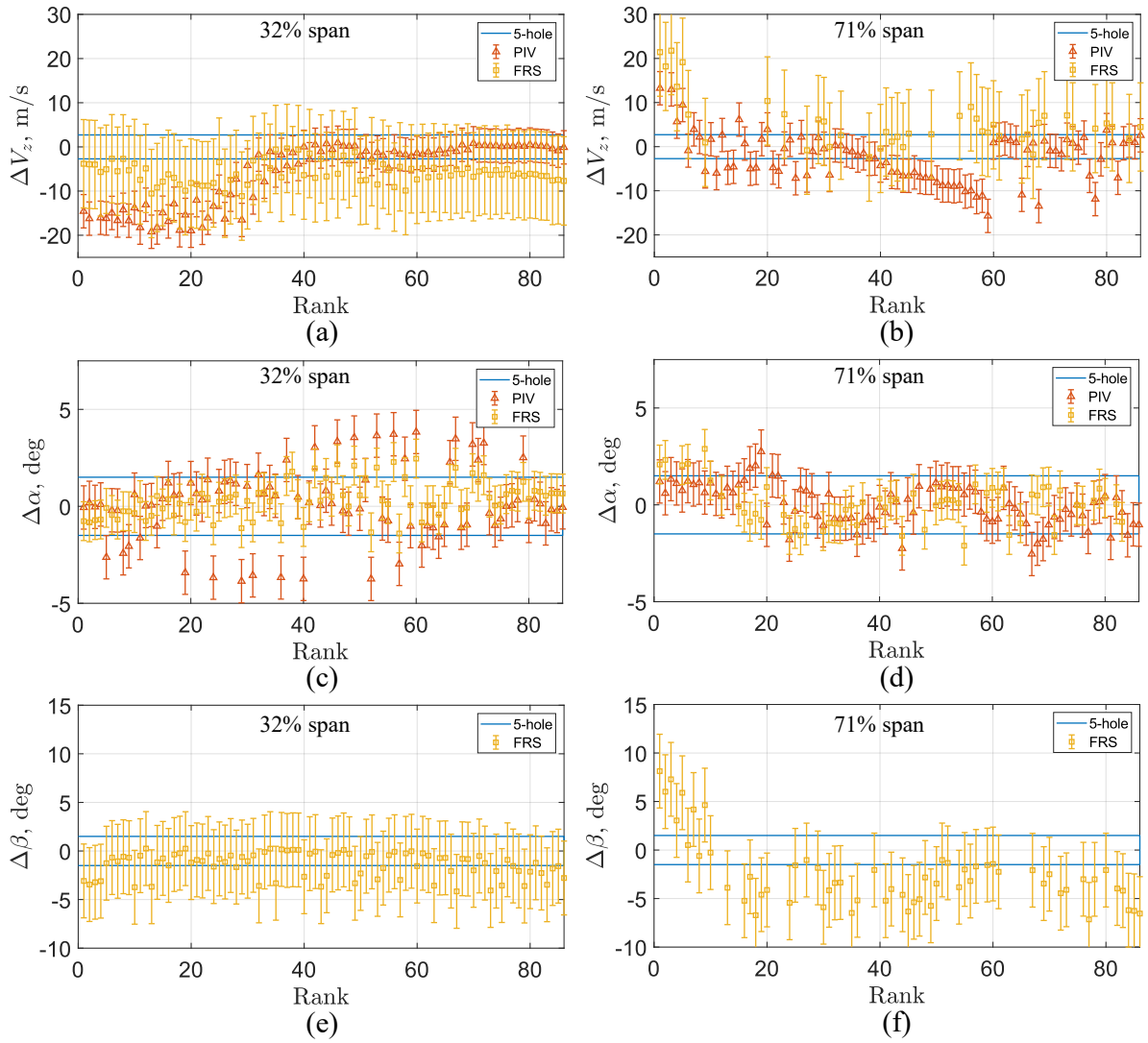

Figure 19. Orthogonal velocity determination results using the minimum-shift method and adjacent plane combination for axial velocity (a and b), tangential flow angle (c and d), and radial flow angle (e and f) at the 32% span position (a, c, and e) as well as the 71% span position (b, d, and f).

or larger in magnitude in all cases, indicating bias in the measurement. The $RMSD$ is larger for the measurement of β in comparison to α as expected from pre-measurement uncertainty prediction for v_y, however, a significant portion of the RMSD results from the bias in the measurement, accounting for more than half of the RMSD.

Overall, the FRS velocity measurements performed similarly to the reference PIV measurements with measured values typically accurate within the determined uncertainty bounds. The increase in variation at greater span positions is attributed to an increase in noise near the wall, resulting from less overlap averaging and possibly the presence of high intensity contamination from the window. A small bias exists in the measurement of β as we get closer to the wall as well.

Overall, FRS values in comparison with 5-hole probe and PIV reference data yields the conclusion that for this complex application, accurate FRS measurements of three-component velocity can be made using the collection and processing techniques introduced and applied in this measurement campaign.

5.2 Temperature and density

Full plane results for time-averaged temperature and density are determined using the least squares curve fitting algorithm described in Section 3.3. Time-averaged static pressure is then determined using temperature, density, and the state equation (ideal gas). Statistics for measurements

collected within the entire cross-section of the ACF are summarized in table 6.

Results in table 6 show that when the entire plane is considered, the mean difference in temperature and density compared to the measured average temperature and over the entire domain has a small positive average difference of 0.6 K and 0.003 kg/m^3 respectively or less than 0.3% for both measurements. However, the RMSD values seen for temperature, are observed to be significantly greater than the expected uncertainty bounds discussed in Section 4.4 in table 1 of 3% (8 K). The static temperature comparison shown here yields an 11.1 K RMSD in temperature, indicating the presence of unaccounted for bias error. For density measurements, the 4% (0.04 kg/m^3) predicted uncertainty is nearly identical to the 0.043 kg/m^3 RMSD seen in the density measurements when compared to the measured flow average.

Table 6. FRS full plane statistics for static temperature, density, and pressure determination.

Measurement	Expected	FRS Average	*MD*	*RMSD*
$T_s\ (K)$	279.2 ($\pm 2K$)	279.8	0.6	11.1
$\rho_s\ (kg/m^3)$	1.001 ($\pm 1\%$)	1.004	0.003	0.043
$p\ (kPa)$	80.26 ($\pm 1\%$)	80.57	0.31	4.29

Radial scatter plots as well as a histogram representing all the data collected within the cross-section shown in figure 18 (b) are presented in figure 20 and figure 21 for temperature and density respectively.

The static temperature comparison in figure 20a shows the FRS determined static temperature as a function of radius compared with the average static temperature calculated using the total temperature and total pressure measured at the inlet and the average static pressure measured at the measurement plane. The uncertainty in this measurement is approximately 0.75% or 2.1 K but the red dashed lines shown in figure 20 are indicative of the minimum and maximum static temperature calculated using the local static pressure measured using the 5-hole probe.

In this comparison, we see the cause of the high RMSD value presented in table 6 is related to bulk variation in temperature from the center outward. The measured static temperature is generally less than the expected value near the center of the duct with a small variance. As the radial position increases, we see an increase in the local average temperature value as well as the variance in the data until a radius of about 175 mm, at which point the local average temperature decreases while the variance continues to increase. This trend is also observed in the uncalibrated temperature determination, so the root cause of this variation is unclear.

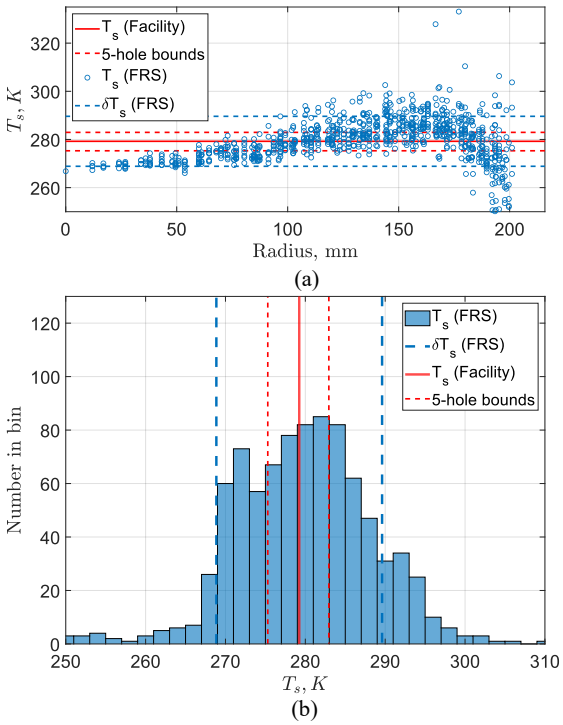

Figure 20. Static temperature results compared to the expected full plane average compared with the radial position of the measurement (a) with the distribution shown in (b). Both (a) and (b) represent measurements collected within the entire cross-section of the flow.

The increase in variance shown here, at radii greater than 125 mm is similar to the trend seen in the velocity measurements where the signal noise increases near the wall, leading to less precise measurements. Additionally, it can be inferred that mild signal contamination via geometric scattering is present because of the sharp reduction in measured temperature when radius > 180 mm. Most likely, this is due to the intense scattering of light of the laser entrance window as the light passes through. When processing the data, a smaller rejection region was attempted but produced much larger RMSD values throughout the entire cross-section.

Interrogating the measured temperature further, we look at the histogram of all the determined temperature values within the plane in figure 20b. Here we see that average temperature of the plane falls close to the average value, and the distribution of the data displays a somewhat Gaussian shape, except for the secondary peak near 270 K. This secondary peak may be associated with the negative bias at radii less than 100 mm and greater than 180 mm. It is difficult to comment precisely on the performance of this measurement due to the lack of comparable, spatially resolved data, but overall the cross-sectional average of the flow is represented accurately

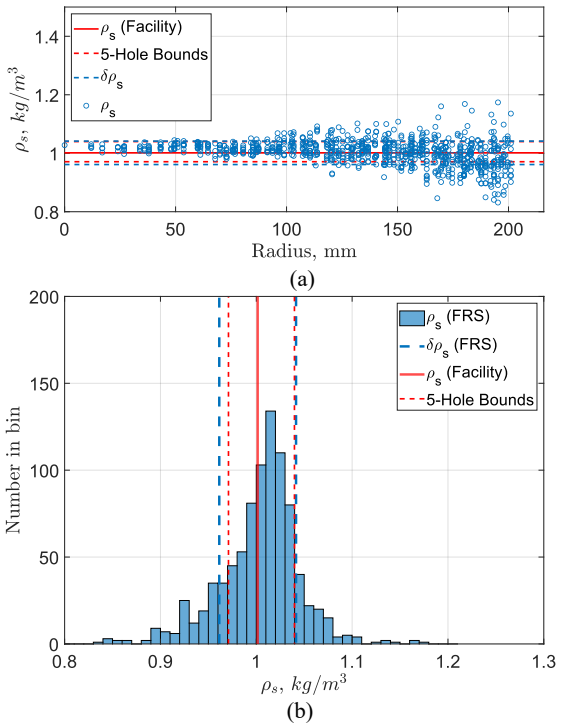

Figure 21. Static density results compared to the expected full plane average compared with the radial position of the measurement (a) with the distribution shown in (b). Both (a) and (b) represent measurements collected within the entire cross-section of the flow.

but the FRS data displays an unexpected radial variance that is not seen in reference measurements.

The static density comparison in figure 21(a) and (b) shows the FRS determined static density compared with the average static density calculated using the total conditions at the inlet, the 5-hole probe measured static pressure, and the calculated static temperature used in figure 20. The bounds on static density calculated using the 5-hole probe measurements are shown using the red dashed lines. Overall, the density measurements show very good agreement with both the measured average static density except for a small positive bias. Mirroring the velocity and temperature measurement behavior, an increase in the variance of the data is observed as radius increases.

The histogram shown in figure 21(b) shows confirmation of the successful density measurement with a mean within <0.3% of the measured average and a distribution that is roughly normally distributed shape.

5.3 Static and total pressure

Time-averaged static pressure, in this measurement, is calculated using the measured static temperature, static density, and the state equation as shown in equation 13. Figure 22a and (b) shows the FRS-derived static pressure measurements compared with the 5-hole probe static pressure. In the 32% span position (a) we see very good agreement between the 5-hole probe measurements and the FRS measured static pressure values, with all measurements falling within uncertainty bounds. At the 71% span, we see a positive bias associated with the measured static pressure when compared to the 5-hole probe data and better agreement near higher rank values. Since the FRS derived static pressure is calculated using the measured temperature and density values, this bias can be attributed to the elevated temperature values near 150 mm in figure 20 (a).

Combining all the measured values, the time-averaged total pressure is calculated using equation 12. Total pressure is then compared back to the 5-hole probe measured total pressure in figure 22c and (d). In the 32% span comparison (figure 22c) we see good agreement between the FRS and the 5-hole probe data, with most measurements matching magnitude within measurement uncertainty bounds. For the 71% span, we once again see a positive bias, relating back to the biased static temperature measurement. A larger variation in the measured values is also observed due to a larger than expected variation observed in the measurements from which pressure is derived. Quantitative results comparing FRS derived static and total pressure ratio to 5-hole probe data can be found in table 7.

Table 7. Static pressure and total pressure comparison in kPa

Span	MD_{p_s}	$RMSD_{p_s}$	MD_{p_0}	$RMSD_{p_0}$
32%	-0.09	1.01	1.04	1.49
55%	-2.88	3.53	-3.04	3.81
71%	-2.91	3.88	-4.22	5.01
84%	0.28	3.67	1.24	3.59

5.4 Discussion

It is shown in this section that the FRS instrument has the capability of directly measuring time-averaged vector velocity, static temperature, and static density of a complex internal flow, in a large-scale flow facility with minimal alterations to the facility itself. These measurements, determined directly from FRS spectra are typically observed to measure the flow within pre-determined uncertainty bounds when compared to reference measurements. The region in which this breaks down for nearly all measurements is when radius > 153 mm (71%). At radii > 71% we see that the variance in the measurements increases drastically as a result of higher signal noise, typically exceeding pre-determined uncertainty bounds. In scalar temperature measurements it is also observed that bias error increases significantly, most likely due to the presence of unfiltered geometric scattering from the window.

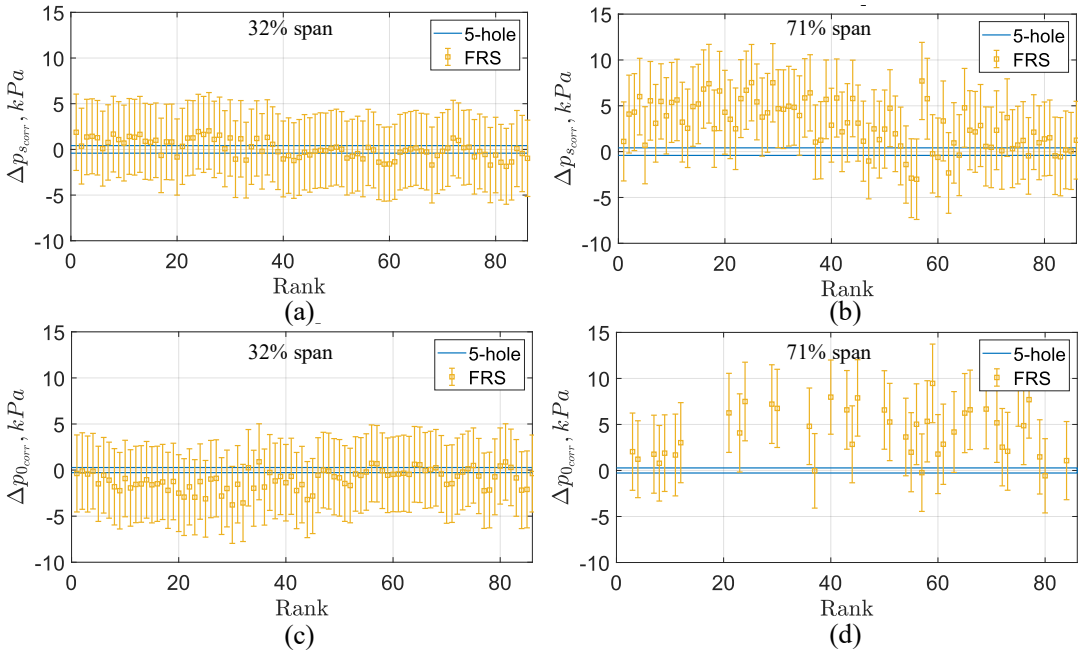

Figure 22. Static pressure results compared to 5-hole probe measurements (a & b). Total pressure results calculated using equation (12) are compared to the 5-hole measurements (c & d).

Due to the nature of the directly measured values, the FRS instrument also allows for the calculation of flow angles, static pressure, and total pressure. For this measurement campaign, these values are typically measured within pre-determined uncertainty bounds near the center of the duct but bias errors in temperature near the wall of the test section cause these measurements to diverge from predicted values. Additionally, as measurement locations approach the wall, a reduction in measurement precision is observed across all measurements.

Above all, these measurements demonstrate the capability of the FRS instrument to accurately measure multi-property flow measurements and shows promise for future improvement with improved laser frequency control, improved processing algorithms, and by better understanding the interactions between light and matter that are typically neglected in empirical applications. As this technique matures over time, time-averaged molecular FRS is poised to be a non-intrusive candidate for supplementing or replacing intrusive probes and PIV measurements for internal flow quantification.

6. Conclusions and outlook

The CARL ACF provides a rigorous proving ground in the development of a robust FRS instrument because it draws in atmospheric air with no advanced flow conditioning, minimal wall surface treatment, small test section size, and limited optical access. This facility is therefore analogous to many industrial and government research wind tunnels and flow rigs containing high intensity Mie and geometric scattering contamination.

Several practical aspects of implementing time averaged FRS for internal flow facilities are presented, including choice of surface treatment, choice of optical elements, and how to select molecular iodine lines and frequency scanning regions to optimize measurement information while avoiding signal contamination from Mie and geometric scattering.

Multiple methods for processing FRS spectra are also presented for the first time to the authors' knowledge. In this application, these methods were required to measure the flow properties accurately using FRS in the presence of undesired scattering sources. Among others, a novel FRS spectral processing method, termed minimum displacement Doppler shift determination, was shown to be applied robustly in applications with high intensity Mie and geometric scattering contamination with no explicit consideration. When paired with an order of magnitude estimate of contaminating intensity, the min-shift method may be used to determine the Doppler shifted rejection region for optimal multi-property determination.

FRS measurements obtained were quantitatively compared with reference 5-hole probe and PIV measurements where applicable, providing a validation with both the modern standard for internal flow quantification and a widely used optical diagnostic technique.

FRS velocity measurements are generally characterized as having good accuracy in magnitude, while performing quantitatively similar to PIV measurements in comparison with the 5-hole probe. With the exception of the outer-most span position, FRS measurements typically measured the

same as the 5-hole probe measurements within predicted uncertainties with RMSD values less than 8.0 m/s in axial velocity, 1.7 deg in tangential flow angle, and 4.7 deg in radial flow angle.

For multi-property measurements of temperature, density, and pressure, only reference static and total pressure measurements were available for calculating comparison values. For the entire plane, the average static temperature was found to be accurate compared to the measured value with a mean difference of 0.6 K, but local, radially dependent bias and variance in the measured temperature resulted in RMSD values of 11.1 K, greater than the predicted uncertainty of 3% or 8 K. Density measurement comparisons performed very well with a mean difference of 0.003 and an RMSD of 0.043 when compared to the calculated static density values, very similar to the predicted uncertainty of 4% or 0.04 kg/m^3.

Calculated static and total pressure measurements near the center of the duct typically measured the same as the 5-hole probe within the uncertainty bounds, but measurements at larger radii presented RMSD values typically greater than predicted uncertainty due to the bias and variance observed in FRS measured static temperature and density. MD and RMSD values are typically less than 2.9 kPa and 3.9 kPa for static pressure respectively. MD and RMSD values for total pressure are typically less than 4.2 kPa and 5.0 kPa respectively.

This work demonstrates that the present FRS instrument is capable of non-intrusively quantifying the aerodynamic and thermophysical state of a highly distorted gaseous flow using simultaneous measurement of time-averaged vector velocity, static temperature, and static density without the use of seed. From these measurements, flow angles, static pressure and total pressure are calculated to fully quantify the state of the fluid flow.

Work remains to further improve the robustness of the FRS instrument, especially for measurements near wall boundaries in internal flows and for applications requiring temporally resolved measurements. The primary improvement needed to drive down the FRS measurement uncertainty is to install a feedback control system onto the laser so that low temporal frequency oscillations in the laser center frequency can be removed, greatly improving the accuracy of both vector and scalar measurements while reducing the labor to post-process data. Similar systems using high finesse wavelength meters (Doll et al. 2016), which provide an absolute measure of emitted light wavenumber, has been shown to be the most robust method on past work, though is a substantial investment to implement.

Another improvement to be made is the ability to accurately predict camera signals in a simulated measurement environment to further reduce risk in application. For example, three cameras were simulated and set up in this measurement campaign but only two cameras were simulated accurately, leading to the third being unusable in processing due to the magnitude of diffuse light captured by the camera in addition to a large amount of random noise seen in the resulting signal.

While work remains to further mature the FRS instrument and accompanying processing techniques, future implementations of these instruments will be a valuable tool for well-defined quantification of complex internal flows and provide a non-intrusive supplement or replacement for legacy measurement techniques.

Acknowledgements

Distribution Statement A: Approved for Public Release; Distribution is Unlimited. PA# XXXXX

References

[1] Oberkampf W L and Smith, B L 2017 Assessment Criteria for Computational Fluid Dynamics Model Validation Experiments, *Journal of Verification, Validation and Uncertainty Quantification* **2(3)** 031002.

[2] Lowe K T, Beardsley C, Borgoltz, A, Devenport WJ, Duetsch-Patel J E, Fritsch D J, Gargiulo A, Roy C J, Szőke M, Vishwanathan V 2020 Status of the NASA/Virginia Tech Benchmark Experiments for CFD Validation *AIAA SciTech 2020* (Jan. 2020, Orlando FL, USA) AIAA 2020-1584

[3] Hunsaker, J C, Buckingham E, Rossell H E, Douglas D W, Brand C L and Wilson E B 1916 *Reports on Wind Tunnel Experiments in Aerodynamics* (Baltimore: Smithsonian Institution)

[4] Treaster A L, and Yocum A M, 1978 The Calibration and Application of Five-Hole Probes *Proceedings from the 24th International Instrumentation Symposium* (January 1978, Albuquerque, New Mexico, USA) pp. 255-266

[5] Livesey J L 1956 The Behavior of Transverse Cylindrical and Forward Facing Total Pressure Probes in Transverse Total Pressure Gradients *Journal of the Aeronautical Sciences* pp. 949-955.

[6] Sevill E 2002 Experimental Investigation of the Systematic Errors of Pneumatic Pressure Probes Induced by Velocity Gradients *PhD Thesis* Institute of Thermal Turbomachines and Powerplants, Vienna University of Technology

[7] Omrane A, Petersson P, Aldén M and Linne M A 2008 Simultaneous 2D flow velocity and gas temperature measurements using thermographic phosphors. *Applied Physics B*, **92** pp.99-102

[8] Fond B, Abram C and Beyrau F 2015 On the characterisation of tracer particles for thermographic particle image velocimetry *Applied Physics B*, **118** pp.393-399.

[9] Kopf A, Bardi M, Kohler E, Endres T, Bruneaux G, and Schulz 2021 Survivability of the thermographic phosphors YAG:Pr and SMP:Sn in a premixed flame, *Measurement Science and Technology* **32** 074001

[10] Witkowski D, Herzog J M, and Rothamer D A 2020 Combustion-relevant temperature imaging with scattering referenced aerosol phosphor thermometry applied to Eu:BAM, *Combustion and Flame* **224** pp.233-238

[11] Guimaraes T, Lowe K T, and O'Brien W F 2018 StreamVane Turbofan Inlet Swirl Distortion Generator: Mean Flow and

Turbulence Structure *AIAA journal of Propulsion and Power* **34** 2 pp.340-353
[12] Beresh S J, Spillers R, Soehnel M, and Spitzer S 2020 Extending the Frequency Limits of "Postage-Stamp PIV" to MHz Rates *AIAA SciTech Forum 2020* (Jan. 2020, Orlando FL, USA) AIAA 2020-1018
[13] Nelson M A, Lowe K T, O'Brien W F, Kirk C, and Hoopes K M 2014 Stereoscopic PIV measurements of swirl distortion on a full-scale turbofan engine inlet *AIAA SciTech 2014* (Jan. 2014 National Harbor, MD, USA) AIAA-2014-0533
[14] Willert C, Schanz D, Novara M, Geisler R, Schroll M Ribergard S, and Schroder A 2021 Multi-Resolution, Time-Resolved PIV Measurements of a Decelerating Turbulent Boundary Layer nearSeparation, *14th International Symposium on Particle Image Velocimetry – ISPIV 2021*
[15] Martins F J W A, Foucaut J M, Stanislas M, and Azevedo L F A 2019 Characterization of near-wall structures in the log-region of a turbulent boundary layer by means of conditional statistics of tomographic PIV data, *Experimental Thermal and Fluid Science* **105** pp.191-205
[16] Leber E J 2020 Development and Implementation of PIV Systems with Selective Particle Seeding For Production Wind Tunnel Testing *MSc Thesis*, Texas A&M University
[17] Wieneke B 2015 PIV uncertainty quantification from correlation statistics *Measurement Science and Technology* **26** 074002
[18] Rajendran L K, Bhattacharya S, Bane1 S P M , Vlachos P P 2021 Meta-Uncertainty for Particle Image Velocimetry *Measurement Science and Technology* **32** 104002
[19] Burns R A, Fahringer T W, and Danehy P M 2021 Velocity measurements across an oblique shock using pulse-burst cross-correlation DGV *AIAA SciTech Forum 2021* AIAA 2021-0120
[20] Boyda M T, Byun G, Saltzman A, and Lowe K T 2020 Geometric scattering removal in cross-correlation Doppler global velocimetry by structured illumination, *Measurement Science and Technology*, **31** 064004
[21] Lowe K T, Byun G, Shea S, Boyda M T, and Winski C S 2019 Three-Velocity-Component Cross-Correlation Doppler Global Velocimetry for the Space Launch System Booster Separation Test in the NASA Langley Unitary Plan Wind Tunnel, *AIAA Aviation 2019*, AIAA 2019-3506
[22] Meyers J F, Lee J W, and Cavone A A 2010 Boundary layer measurements in a supersonic wind tunnel using Doppler global velocimetry *Proceedings of the 15th international symposium on applications of laser techniques to fluid mechanics* (July 2010, Lisbon Portugal) 1546
[23] Fischer A 2017 Model-based review of Doppler global velocimetry techniques with laser frequency modulation, *Optics and Lasers in Engineering* **93** pp.19-35
[24] Cadel D R and Lowe K T 2015 Cross-correlation Doppler global velocimetry (CC-DGV), *Optics and Lasers in Engineering* **71** pp.51-61
[25] Cadel D R and Lowe K T 2016 Investigation of measurement sensitivities in CC-DGV, *Optics and lasers in engineering*, **86** pp.44-52
[26] Dedic C E, Meyer T R, and Michael J B 2017 Single-shot ultrafast coherent anti-Stokes Raman scattering of vibrational/rotational nonequilibrium, *Optica*, **4** 5 pp.563 – 570
[27] Reese D T, Jiang N, and Danehy P 2020 Unseeded velocimetry in nitrogen for high-pressure, cryogenic wind tunnels: part III. Resonant femtosecond-laser tagging, *Measurement Science and Technology* **31** 075203
[28] Panda J, 2020 Spectrally-resolved Rayleigh scattering to measure velocity, temperature, density, and density fuctuations in high-speed fows, *Experiments in Fluids **61** 74*
[29] Saltzman A, Boyda M, Lowe K T, and Ng W F, 2019 Filtered Rayleigh Scattering for Velocity and Temperature Measurements of a Heated Supersonic Jet with Thermal Non-Uniformity *25th AIAA/CEAS Aeroacoustics Conference* (May 2019 Delft, The Netherlands) AIAA 2019-2677
[30] Mcmanus T A, Monje I T, and Sutton J A 2019 Experimental assessment of the Tenti S6 model for combustion relevant gases and filtered Rayleigh scattering applications *Applied Physics B* **125** 13
[31] Doll U, Dues M, Tommaso B, Picchi A, Stockhausen G, and Willert C 2018 Aero-thermal flow characterization downstream of an NVG cascade by five-hole probe and filtered Rayleigh scattering measurements, *Experiments in Fluids* **59** 150
[32] Miles R B, Lempert W R, and Forkey J N 2001 Laser Rayleigh Scattering *Measurement Science and Technology* **12** R33
[33] Panda J, Seasholtz R 1998 Density measurement in underexpanded supersonic jets using Rayleigh scattering, *36th AIAA Aerospace Sciences Meeting and Exhibit* AIAA 98-0281
[34] Doll U, Migliorini M, Baikie J, Zachos P K, Rohle I, Melnikov S, Steinbock J, Dues M, Kapulla R, MacManus D G, and Lawson N J 2022 Non-intrusive flow diagnostics for unsteady inlet flow distortion measurements in novel aircraft architectures *Progress in Aerospace Sciences* **130** 100810
[35] Boyda M T, Byun G, Saltzman A, and Lowe K T 2020 Influence of Mie and geometric scattering on temperature and density measurements using filtered Rayleigh scattering *AIAA SciTech Forum 2020* AIAA 2020-1516
[36] Boyda M T, Byun G B, and Lowe K T 2019 Investigation of velocity and temperature measurement sensitivities in cross-correlation filtered Rayleigh scattering (CCFRS), *Measurement Science and Technology* **30** 044004
[37] Doll U, Stockhausen G, and Willert C 2017 Pressure, temperature, and three-component-velocity fields by filtered Rayleigh scattering velocimetry *Optics Letters* **42** 19 pp.3773-3776
[38] Tenti G, Boley C D, and Desai R C 1974 On the kinetic model description of Rayleigh–Brillouin scattering from molecular gases *Can. J. Phys.* **52** 4 pp.285-290
[39] Boguszko M, Elliot G S 2005 Property measurement utilizing atomic/molecular filter-based diagnostics, *Progress in Aerospace Sciences* **41** 2.
[40] Mielke A F, Elam K A, Sung C J 2009 Multiproperty Measurements at High Sampling Rates Using Rayleigh scattering *AIAA Journal* **47** 4
[41] Panda J. 2020 Spectrally resolved Rayleigh scattering to measure velocity, temperature, density, and density fluctuations in high speed flows, *Experiments in fluids* **61** 74
[42] Cutler A D, Rein K, Roy S, Danehy P M and Jiang, N 2020 100-kHz Interferometric Rayleigh Scattering for multi-parameter flow measurements. *Optics express* **28** 3 pp.3025-3040.

[43] Estevadeordall J, Jiang N, Cutler A D, Felver J J, Slipchenko M N, Danehy P M, Gord J R, and Roy S 2018 High-repetition rate interferometric Rayleigh scattering for flow-velocity measurements, *Applied Physics B* **124** 41
[44] Bivolaru D, Cutler A D, and Danehy P M 2011 Spatially- and Temporally-resolved Multi-parameter Interferometric Rayleigh Scattering *49th AIAA Aerospace Sciences Meeting* (January 2011, Orlando Fl)
[45] Forkey J N, Lempert W R, and Miles R B 1990 Flow field diagnostics by spectrally filtered Rayleigh scattering, *International Laser Safety Conference*
[46] Forkey J N, Lempert W R, and Miles R B 1997 Corrected and calibrated I2 absorption model at frequency-doubled Nd:YAG laser wavelengths *Applied Optics* **36** 27 pp.6729-6738
[47] Cadel D R, Shin D, and Lowe K T 2016 A Hybrid Technique for Laser Flare Reduction, in *Proceedings of the 54th Aerospace Sciences Meeting* AIAA 2016-0788
[48] Bridges J and Wernet M P 2019 PIV measurements of a low-noise top-mounted propulsion installation for a supersonic airliner *AIAA SciTech Forum* AIAA 2019-0252
[49] Kristensson E, Ehn A, Bood J, and Aldén M 2014 Advancements in Rayleigh scattering thermometry by means of structured illumination, *Proceedings of the Combustion Institute **35*** 3 pp.3689-3696
[50] Kempema N J and Long M B 2014 Quantitative Rayleigh thermometry for high background scattering applications with structured laser illumination planar imaging, *Applied Optics* **53** 29 pp.6688-6697
[51] Lagarias, J C, Reeds J A, Wright M H, and Wright P E 1998 Convergence Properties of the Nelder-Mead Simplex Method in Low Dimensions *SIAM Journal of Optimization* **9** 1 pp.112–147.
[52] Charrett T O H, Nobes D S, and Tatam R P 2007 Investigation into the selection of viewing configurations for three-component planar Doppler velocimetry measurements. *Applied Optics* **46** 19 pp.4102-4116
[53] Air Force Research Laboratory 2013 Facility Factsheet: Component Research Air Facility, https://www.afrl.af.mil/Portals/90/Documents/RQ/rq-component-research-air-CRAF.pdf?ver=2020-08-28-132029-847
[54] Sanders D D, Nessler C A, Copenhaver W W, List M G, and Janczewski T J 2016 Computational and Experimental Evaluation of a Complex Inlet Swirl Pattern Generation System, *52nd AIAA/SAE/ASEE Joint Propulsion Conference* AIAA 2016-5008
[55] Zhang Z 1999 Flexible Camera Calibration by Viewing a Plane from Unknown Orientations, *Proceedings of the Seventh IEEE International Conference on Computer Vision* (Kerkyra, Greece)
[56] Tsai R Y 1987 A Versatile Camera Calibration Technique for High-Accuracy 3D Machine Vision Metrology Using Off-the-shelf TV Cameras and Lenses, *IEEE Journal of Robotics Automation* **3** 4 pp.323-344
[57] Nessler C A, Sanders D D, List M G, Janczewski T J, and Copenhaver W W 2017 Axial Extent of Flowfield Variation from the StreamVane™ Swirl Pattern Generation System *Proceedings of the 55th Aerospace Sciences Meeting* AIAA 2017-1621
[58] Guimaraes T, Lowe K T, and O'Brien W F 2017 StreamVane Turbofan Inlet Swirl Distortion Generator: Mean Flow and Turbulence Structure *J Prop Power*. **34** 2 pp.340-353

5.1 Effects of measuring a Turbulent flow Using Time-Averaged FRS

While many wall-bounded flow facilities aim to create a flow mostly free from turbulent fluctuations, a flow utterly free of turbulence is difficult to achieve. In addition, many measurements within wall-bounded flows aim to characterize the flow near or downstream of a test article, as is the case for the work in this chapter.

For the measurement campaign discussed in the present work, FRS measures the time-averaged flow properties downstream of a test article known to have unstable swirl and total pressure distortions. Therefore, it is essential to understand how fluctuations in velocity and scalar properties affect temporally averaged FRS measurements in terms of bias error and uncertainty. To investigate these effects, a series of Monte-Carlo simulations were performed at various turbulent intensity levels based on the flow conditions at the CARL ACF.

The equations used in this work to determine three-component velocity, temperature, and density using FRS spectra assume that the flow is constant in time throughout the scan of laser frequencies. For the case where the flow is known to be turbulent, this assumption becomes that a measurement over a scan of laser frequencies represents a statistical average of the flow properties to be measured and that this averaging results in a convolution spectrum that is the same as if there were no turbulent fluctuations at all.

This investigation aims to establish the validity of this assumption, establish the bounds of its applicability in this environment, and demonstrate how averaging over turbulent fluctuations affects bias error and uncertainty in FRS measurements.

5.1.1 Turbulent Flow Conditions

This investigation was carried out by performing a series of Monte-Carlo simulations of the FRS measurement in the ACF using analogous flow conditions in air. Stagnation pressure, temperature, and density conditions are set to 1 atm, 290 K, and 1.217 kg/m^3, respectively. Average flow conditions were then calculated by expanding the stagnation conditions to a Mach number of 0.5 using isentropic relations. A summary of the stagnation conditions and the static (flow-on) conditions can be found in Table 5.1.

Table 5.1: Baseline flow conditions for the FRS turbulent flow simulation.

Property	Total Conditions	Static Conditions	Unit
M	0	0.5	n.d.
$\vec{V}$	[0,0,0]	[0,0,167]	m/s
U_{sens}	0	104	m/s
p	1.00	0.843	atm
T	290	276	K
ρ	1.22	1.08	kg/m^3

For this simulation, it was assumed that the flow only propagates in the z-direction, and any turbulent fluctuations introduced into this flow affect only the z-component of velocity with x and y-components of velocity held constant at 0 m/s. This was a necessary simplification because the turbulent intensity of the flow directly relates to the turbulent intensity of sensed velocity, which can be applied more generally to multiple, single-perspective measurements of Doppler shift. Bias errors in velocity were only investigated in sensed velocity space.

5.1.2 Optical Configuration

Figure 5.1 shows the optical configuration used for the Mote-Carlo simulations. The laser used to probe the flow was assumed to be 532 nm laser light polarized in the z-direction

and propagating along the negative y-direction. with a unit vector of $\hat{\imath} = [0, -1, 0]$. The simulated FRS imager observes the probed volume from a position directly above the x-axis with an observation unit vector of $\hat{o} = [0.781, 0, 0.625]$ resulting in an observation angle of $\theta = 90^o$ from the laser propagation direction, measured in the xy-plane. The baseline sensed velocity, defined as $U_{sens} = (\hat{o} - \hat{\imath}) \cdot \vec{V}$ that results from this FRS configuration is determined to be 104 m/s.

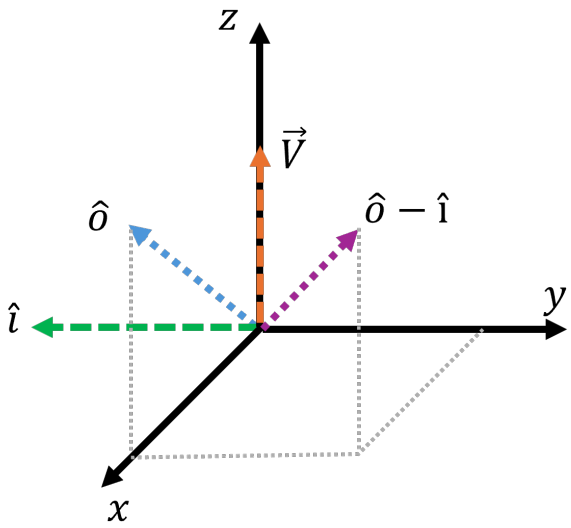

Figure 5.1: Geometric configuration of the FRS instrument used in the turbulent flow Monte-Carlo simulations.

5.1.3 Sampling Turbulent Fluctuations

Turbulent fluctuations are simulated by choosing a turbulent intensity, $I = V_z'/\overline{V_z}$, where V_z' is the root-mean-square (RMS) of the velocity fluctuations and ($\overline{V_z}$) is the average velocity in the z-direction, which is held constant for all cases. The turbulent intensity and the mean flow velocity were then used to calculate $V_z' = I * \overline{V_z}$ which, since the flow was chosen to be unidirectional, was used to define the standard deviation of the random data set.

The random set of turbulent samples was generated using the MATLAB random number

generator in the equation $V_z = \overline{V_z} + \overline{V_z} * I * randn(1, N_{turb})$, where V_z is the resulting set of turbulent velocities consisting of N_turb number of samples. V_z was then validated to represent a statistical average by ensuring the average and standard deviation fall within $0.05m/s$ of the baseline flow conditions and the RMS of the velocity fluctuations, respectively.

For every sample in each turbulent set, V_{z_i} was used to determine M_i using isentropic relations while assuming $T_i = \overline{T}$. Isentropic relations were then used to expand the stagnation conditions to M_i to obtain p_i, T_i, ρ_i, and V_i. Subsequent iterations were conducted by calculating M_i using V_{z_i} and T_{i-1} from the previous iteration until $|V_{z_i} - V_i| < 10^{-6}$, at which point the static flow conditions were considered sufficiently converged. The average flow conditions of each turbulent set are included in Table 5.2, and the standard deviation of each turbulent set is included in Table 5.3.

Table 5.2: Average turbulent flow property values for each turbulent intensity case. Note that variation in velocity is used to define the magnitude of the turbulent fluctuations and average scalar properties vary with turbulent intensity as a result.

		$I = 10\%$	15%	20%	25%	30%	40%	50%	60%
$\overline{U_{sens}}$	m/s	104	104	104	104	104	104	104	104
$\overline{p}$	atm	0.842	0.841	0.838	0.836	0.833	0.826	0.816	0.806
$\overline{T}$	K	276	276	276	275	275	274	273	271
$\overline{\rho}$	kg/m^3	1.08	1.08	1.07	1.07	1.07	1.06	1.05	1.04

5.1.4 Monte-Carlo Simulation

Convergence of the Monte-Carlo simulation was established using the turbulent intensity of I=60% and N_{turb}=20,000 samples. This investigation determined that N_{turb}=5,000 samples were sufficient to converge the 60% turbulent intensity case, with turbulent intensities of less than 60% generally demonstrating better convergence behavior.

Table 5.3: Standard deviation of the turbulent flow property values for each turbulent intensity case. Standard deviations are presented as an absolute magnitude and as percent values relative to the corresponding average value in Table 5.2.

		$I = 10\%$	15%	20%	25%	30%	40%	50%	60%
$\sigma_{U_{sens}}$	m/s	10.4	15.6	20.8	26.0	31.3	41.6	52.1	62.4
	(%)	(10%)	(15%)	(20%)	(25%)	(30%)	(40%)	(50%)	(60%)
σ_p	atm	0.029	0.044	0.059	0.073	0.087	0.114	0.140	0.165
	(%)	(3.4%)	(5.2%)	(7.0%)	(8.7%)	(10%)	(14%)	(17%)	(20%)
σ_T	K	2.86	4.16	5.57	6.98	8.51	11.4	14.7	18.0
	(%)	(1.0%)	(1.5%)	(2.0%)	(2.5%)	(3.1%)	(4.2%)	(5.4%)	(6.6%)
σ_ρ	kg/m^3	0.027	0.040	0.054	0.067	0.081	0.107	0.133	0.159
	(%)	(2.5%)	(3.7%)	(5.0%)	(6.3%)	(7.6%)	(10%)	(13%)	(15%)

The FRS measurement configuration and the turbulent flow properties were used to generate a set of 5,000 RBS lineshapes and convolution spectra. RBS lineshapes were simulated using each sample of each turbulent set using the Tenti S6 lineshape model. At the same time, convolution spectra were generated by discretizing the convolution of the RBS lineshape and the iodine transmission model into 20 evenly spaced central laser frequencies between -0.0112 cm^{-1} and 0.018 cm^{-1}. The convolution spectra and RBS lineshapes calculated for each turbulent sample were averaged together to create the RBS lineshape and the convolution spectrum that would be representative of a statistical average of the measured turbulent flow. These spectra were then compared to the convolution spectrum and RBS lineshapes simulated using the average flow conditions.

5.1.5 Turbulent Spectra Comparisons

The turbulent RBS lineshape for the I=60% case, shown in Figure 5.2(c), is characterized as being similar in comparison to the non-turbulent lineshape, but with the most significant differences seen near the regions of highest curvature. It was also observed that an asymmetry was present, resulting in more substantial differences in the positive wavenumber region near

0.01 cm^{-1} and the negative wavenumber regions near -0.025 cm^{-1} and -0.041 cm^{-1} when compared to the regions of the same magnitude and opposite sign. This asymmetry is also observed in the 30% (Figure 5.2(b)) and the 15% (Figure 5.2(c)) turbulent intensity cases as well. This asymmetry is due to the non-linear relationship between the change in velocity magnitude and scalar property magnitude.

When looking at the 30% and 15% turbulent intensity cases, we see that the average RBS lineshape spectra agree much better with the non-turbulent RBS lineshapes. In Figure 5.2, percent differences are normalized by the maximum intensity of the average RBS lineshape spectrum.

The resulting average convolution spectra shown in Figure 5.2(d-f) display an overall lower magnitude when compared to the non-turbulent convolution spectra. The average convolution spectra also appear to have a lower curvature, leading to the assumption that curve fitting these spectra will result in a positive temperature bias. This is much more evident in the 60% case than in the 30% and the 15% cases, which have much smaller percent differences than the non-turbulent convolution spectrum. In Figure 5.2, percent differences are normalized by the average convolution spectrum's average intensity.

5.1.6 FRS Measurement Results

To determine the effects of sampling a turbulent flow on FRS measurements, the average convolution spectra were fitted for scalar properties using the FRS curve fitting algorithm, and the Doppler shift was determined using the min-shift method. Results from fitting the average convolution spectra are then compared to the properties determined by evaluating a convolution spectrum simulated at the mean flow conditions presented in Table 5.2 to determine the bias error induced by the turbulent flow. For the following discussion, a

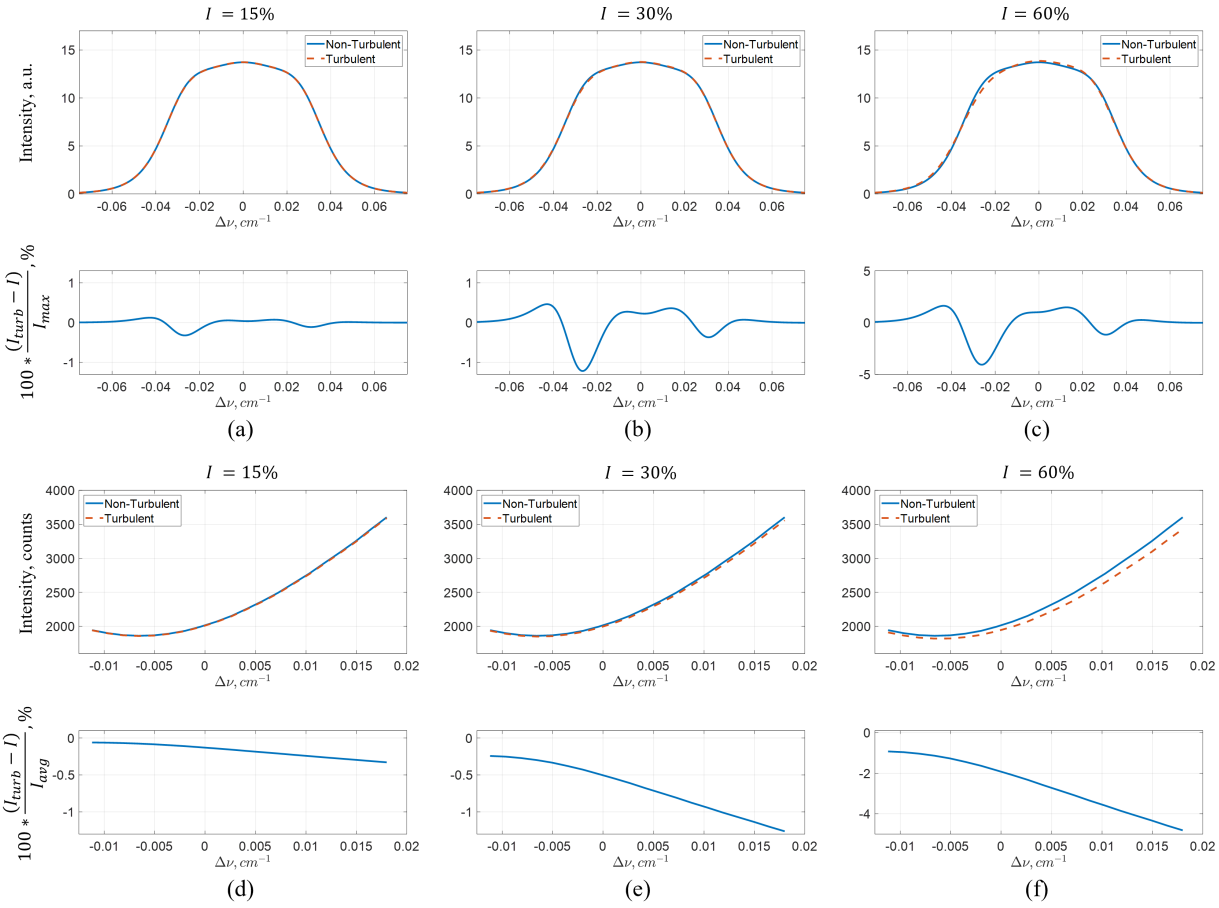

Figure 5.2: (a, b, and c) RBS lineshape spectra resulting from averaging over the I=60%, 30%, and 15% turbulent flow conditions respectively compared to an RBS lineshape spectrum modeled at the average flow conditions. (d, e, and f) convolution spectra resulting from averaging over the I=60%, 30%, and 15% turbulent flow conditions respectively compared to a convolution spectrum modeled at the average flow conditions.

significant bias error is defined as a bias error greater than or equal to 10% of the uncertainty in the measured property. FRS measurement results are summarized in Table 5.4 for all turbulent flow cases investigated.

Table 5.4: Summary of bias errors introduced into FRS measurement by measuring a turbulent flow, assuming measured variables are constant. Bias errors of greater that 10% of the measurement uncertainty are shown in bold font.

		10%	15%	20%	25%	30%	40%	50%	60%
$\varepsilon_{U_{sens}}$	m/s	-0.1	-0.3	**-0.6**	**-1.0**	**-1.5**	**-2.7**	**-4.4**	**-6.4**
	(%)	(-0.1%)	(-0.3%)	**(-0.6%)**	**(-1.0%)**	**(-1.5%)**	**(-2.6%)**	**(-4.2%)**	**(-6.1%)**
ε_p	atm	-1E-4	5E-4	1.4E-3	2.6E-3	3.9E-3	**7.3E-3**	**0.0114**	**0.0160**
	(%)	(-0.01%)	(0.1%)	(0.2%)	(0.3%)	(0.5%)	**(0.9%)**	**(1.4%)**	**(2.0%)**
ε_T	K	-0.2	-0.5	**0.9**	**1.4**	**2.1**	**3.7**	**5.9**	**8.4**
	(%)	(0.1%)	(0.2%)	**(0.3%)**	**(0.5%)**	**(0.8%)**	**(1.4%)**	**(2.2%)**	**(3.1%)**
ε_ρ	kg/m^3	-5E-4	-5E-4	-5E-4	-5E-4	-5E-4	-6E-4	-6E-4	-7E-4
	(%)	(-0.05%)	(-0.05%)	(-0.05%)	(-0.05%)	(-0.05%)	(-0.06%)	(-0.06%)	(-0.06%)

The FRS multi-property measurement techniques described within this work are observed to have no significant bias errors in any measurement when I is less than or equal to 15%, limited by the bias error in min-shift velocity determination and curve fit temperature measurements. For density and pressure measurements specifically, the present FRS technique is observed to be robust to turbulence when I is greater than 60% and when I less than or equal to 40% respectively.

Looking at the bias errors in specific property measurements and how they relate to fluctuations in the measured property, it was observed that sensed velocity determination is robust to fluctuations up to 15% of the mean value of $\overline{U_sens}$; temperature is robust to fluctuations up to 1.5% of the mean value, $\overline{T}$, density is robust to fluctuations greater than 15% of the mean flow value, $\overline{\rho}$, and pressure is robust to fluctuations up to 14% of the mean flow value, $\overline{p}$.

As the magnitude of turbulent fluctuations increased, sensed velocity and density measurements tended to bias toward under-predicting the average flow values. In contrast, temperature and pressure tend toward over-predicting the average flow values, with temperature measurement being the most sensitive to fluctuations in temperature.

While the impact on measurement uncertainty was not explicitly investigated in this study, it is reasonable to assume that if the FRS instrument samples a statistical average of the flow properties, the impacts on uncertainty will be negligible and bias error effects will dominate. Suppose the FRS instrument does not sample a statistical average. In that case, properties are likely to vary from point to point in the collection of the measured convolution spectrum, behaving similarly to random noise.

5.1.7 Summary

Turbulent intensities of 10% to 60% were investigated in this simulation to establish over what range of turbulent fluctuations an FRS instrument that samples a statistical average of a turbulent flow would yield the measurement of the average flow conditions, and outside of this range, what level of additional bias error and/or uncertainty is introduced into the measurement.

All FRS measurements simulated under these flow conditions were robust to turbulent velocity fluctuations when I is less than or equal to 15%, resulting in negligible bias errors of less than 10% of the measurement uncertainty in all measured properties. Therefore, it is valid to assume that in this environment, flow properties can be considered constant in time when I is less than or equal to 15% *and* it is known that the measured convolution represents a statistical average of the flow.

Looking at individual property measurements, min-shift sensed velocity determination is robust to fluctuations up to 15%, temperature is robust to fluctuations of up to 1.5%, density is robust to fluctuations greater than 15%, and pressure is robust to fluctuations up to 8.7% of their respective mean flow values. Furthermore, as the magnitude of turbulent fluctuations increases, sensed velocity and density measurements tend to be biased toward under-prediction of average flow values. In contrast, temperature and pressure tend toward over-prediction, with the temperature being the most sensitive to turbulent fluctuations.

Impacts on measurement uncertainty due to turbulence were not explicitly investigated in these signal simulations, but it is assumed that if the measured convolution represents a statistical average of the turbulent flow, the change in uncertainty would be negligible, and bias error would dominate. Supposing the average flow conditions vary at each of the laser central wavelengths and the scan represents a statistical average, this interaction is expected

to be similar to increasing signal noise and would introduce additional uncertainty into the FRS measurement.

Supposing the average flow conditions vary at each laser central wavelength, the scan does not represent a statistical average of the flow properties. In that case, it is expected that there would be additional uncertainty, as discussed above. Bias errors greater than the values presented in Table 5.4 are expected to be introduced into the FRS measurement.

Chapter 6

Conclusions and Outlook

6.1 Conclusions

The work in this dissertation describes advancements in the application of filtered Rayleigh scattering necessary to harden the measurement and broaden the applicable environments of FRS to environments that would otherwise be impossible to measure due to signal contamination from Mie and background scattering.

In the in-depth investigation into the effects of Mie and background scattering, presented in Chapter 3, the need to reduce those contributions as much as possible was highlighted. Between these two, geometric scattering was identified as a contribution that could be reduced during data collection, leading to the novel application of structured illumination-based background reduction for frequency scanning measurement of three-component velocity in Chapter 4. In post-processing, the combination of the minimum-shift Doppler shift measurement technique and the rejection region analysis is then discussed in 5, allowing for the multi-property measurement of three-component velocity, static temperature, and static density in the presence of Mie and geometric scattering without specific consideration in the signal model. Derived flow angle measurements, static pressure, total pressure, temperature, and density may be calculated using the ideal gas law and isentropic relations. The quantification of bias and uncertainty in these measurements, including the bias associated with time-averaged FRS measurements in turbulent flow environments, are validated and

discussed in 5.

While crucial in applying FRS in these environments, these methods also define the processes necessary to predict the FRS signal in a specified flow environment given a rough order of magnitude of flow conditions, Mie scattering, and geometric scattering. This allows for iteration on instrument and measurement conditions to optimize the measurement system's performance, define the range and density of wavenumbers required to obtain the best possible dataset, and predict measurement uncertainties prior to ever integrating the FRS instrument into the facility.

In working toward these advancements, previous literature was analyzed, highlighting the deficiencies and areas for improvement by applying the techniques described herein. The advancements of the works presented herein are outlined explicitly as follows:

- The development and validation of data processing algorithms used to measure the Doppler shift of measured FRS convolution spectra in the presence of Mie and geometric scattering contamination.

- The development and validation of a data processing algorithm to fit model convolution spectra to measured FRS spectra to determine Doppler shift, temperature, and density using a least-squares fitting routine.

- Description of the influence of Mie and geometric scattering on multi-property filtered Rayleigh scattering measurements of Doppler shift, temperature, and density, allowing the determination of dependencies between the magnitude of the contaminating light sources and the resulting bias errors and uncertainties.

- The development of the rejection region analysis, a method to collect FRS convolution spectra in the presence of high intensity Mie and geometric scattering contamination

without explicit consideration of their respective intensity ratios in fitting modeled convolution spectra to measured convolution spectra.

- The quantification of measurement uncertainties and bias errors in FRS measured Doppler shift, temperature, and density.
- The quantification of measurement uncertainties and bias errors in measurements derived from FRS measured quantities. These quantities include three-component velocity components, velocity magnitude, static pressure, and total pressure.
- The quantification of the effects of turbulent fluctuations on the measured FRS convolution spectrum, the bias error induced by measuring a turbulent flow with time averaged FRS, and the limits of the "constant in time" property assumption in FRS measurements.
- The novel application of structured illumination to Doppler-based, frequency scanning laser diagnostics to remove geometric scattering, the dominant contributor to bias errors in velocity measurements in filtered Rayleigh scattering.
- Validation of planar multi-property FRS measurements of vector velocity, temperature, density, and pressure of a highly non-uniform flowfield in an internal flow facility, the Annular Cascade Facility located at Wright Patterson Air Force Base.

With the FRS measurement techniques described herein providing time-average measurements of three-component velocity, temperature, density, and a host of derived measurements simultaneously with bias and uncertainty definition prior to integration, This work lays the foundation for the use of Filtered Rayleigh scattering as a measurement technique capable of fully quantifying the state of a fluid flow in large scale ground test facilities for CFD solution validation.

6.2 Outlook

The work presented in this dissertation has dramatically improved our understanding of how to harden time-averaged filtered Rayleigh scattering-based diagnostics to environments where signal contamination is unavoidable. This is done by detailing methods to reduce baseline geometric scattering intensity and how to predict the effects of Mie and geometric scattering on resulting signals to predict resultant bias and uncertainties, accounting for turbulent fluctuations in measured properties. Additionally, how these methods can be applied to post-process FRS data most effectively is discussed, laying the foundation for applying FRS in large-scale ground test facilities for multi-property flow quantification and CFD solution validation. However, several drawbacks and challenges remain:

- Because Rayleigh scattering is a low-intensity process, the $1/\lambda^5$ relationship between LRS scattering intensity and wavelength, in addition to the work of Pitt et al. in 2023, [45] indicates that the use of ultraviolet laser radiation has the potential to increase SNR and decrease uncertainty.

- The time it takes to process FRS data for multi-property measurements has long been a concern due to the complexity of the most accurate models to fit these parameters. The work of Powers in 2023 [47] outlines several of the methods that can be used to accelerate the curve fitting algorithm while reducing potential bias in resulting measurements, and the work of Warner et al. in 2023 [64] indicates that there is a significant benefit in the time it takes to evaluate measured FRS convolution spectra by replacing the conventional least-squares curve fitting routine with machine learning based algorithms.

- The design and development of new interferometric Rayleigh scattering measurement techniques that enable one-dimensional, single-frequency, multi-property flow measure-

ments using VIPA dispersion elements for LRS or FRS measurements as demonstrated in Yan et al. in 2023 [67] and Luo et al. 2024 [33] are exciting new developments that once established may prove helpful in "physical rake replacement applications, such as those discussed in [47].

- The main drawback of the FRS implementation presented in this work is the time-averaged nature of the measurements. Recent work in single-frequency FRS measurements developed by Doll et al. [17, 18] indicate significant improvement in the temporal resolution of FRS measurements. Additionally, work by Braun et al. [7, 8, 9, 10] to improve spectral purity of pulse-burst laser emission is enabling the capability to obtain temporally resolved frequency scanning FRS measurements at to address potential biases introduced with time averaging.

- While FRS has been applied and validated in several different environments to measure three-component velocity, temperature, and density, validation in additional environments is required to further expand its applicability and improve researcher and industry confidence in the measurement technique.

The conclusions of this work provide significant knowledge on how to improve the accuracy of FRS-based diagnostics in the presence of high-intensity signal contamination from Mie and geometric scattering. This knowledge can be applied to make the technique more generally applicable to large-scale ground test facilities for flow quantification and CFD solution validation. The potential impact of this research is substantial, as it can significantly enhance the accuracy and applicability of FRS. However, there is still room for improvement in the application of FRS, particularly in the realm of data processing speed and temporal resolution of the multi-property measurements. These improvements will further expand the measurement possibilities to more complicated and more complex environments, increasing

the potential impact of our work.

Bibliography

[1] Christopher Abram, Benoit Fond, and Frank Beyrau. High-precision flow temperature imaging using zno thermographic phosphor tracer particles. *Optics Express*, 23(15): 19453, July 2015. ISSN 1094-4087. doi: 10.1364/oe.23.019453.

[2] Daniel P. Aeschliman and William L. Oberkampf. Experimental methodology for computational fluid dynamics code validation. *AIAA Journal*, 36(5):733–741, May 1998. ISSN 1533-385X. doi: 10.2514/2.461.

[3] Steven J. Beresh, Russell Spillers, Melissa Soehnel, and Seth Spitzer. Extending the frequency limits of "postage-stamp piv" to mhz rates. In *AIAA Scitech 2020 Forum*. American Institute of Aeronautics and Astronautics, January 2020. doi: 10.2514/6.2020-1018.

[4] Eric Berton, D Favier, M Nsi Mba, C Maresca, and C Allain. Embedded ldv measurement methods applied to unsteady flow investigation. *Experiments in fluids*, 30(1): 102–110, 2001.

[5] D. Bivolaru, A. Tzes, G. Papadopoulos, and M. V. Otugen. Image processing for interferometric mie and rayleigh scattering velocity measurements. *AIAA Journal*, 37(6): 688–694, June 1999. ISSN 1533-385X. doi: 10.2514/2.796.

[6] Matthew Thomas Boyda, Gwibo Byun, and K. Todd Lowe. Filtered Rayleigh Scattering for Multi-Property Aerodynamic Measurements in Confined Flows. *Measurement Science and Technology*, 2025.

[7] Amanda M. Braun, Mikhail N. Slipchenko, Terrence R. Meyer, Paul M. Danehy, and

Sukesh Roy. Improved spectral purity of burst-mode laser for filtered rayleigh scattering applications. In *Optical Sensors and Sensing Congress 2022 (AIS, LACSEA, Sensors, ES)*, LACSEA, page LM1B.4. Optica Publishing Group, 2022. doi: 10.1364/lacsea.2022.lm1b.4.

[8] Amanda M. Braun, Mikhail N. Slipchenko, Jason Leicht, Terrence R. Meyer, Paul M. Danehy, and Sukesh Roy. Methods to improve burst-mode laser spectral purity for high-speed gas-phase filtered rayleigh scattering. *Optics Letters*, 48(15):4005, July 2023. ISSN 1539-4794. doi: 10.1364/ol.487369.

[9] Amanda M. Braun, Neil S. Rodrigues, Paul M. Danehy, Alexander Suppiah, James Braun, Mikhail N. Slipchenko, and Terrence R. Meyer. Demonstration of frequency-scanning burst-mode filtered rayleigh scattering for multi-parameter gas-phase measurements. In *AIAA SCITECH 2024 Forum*. American Institute of Aeronautics and Astronautics, January 2024. doi: 10.2514/6.2024-1095.

[10] Amanda Marie Braun. Burst-mode molecular filtered rayleigh scattering for gas-dynamic measurements. 2023. doi: 10.25394/PGS.24712899.V1.

[11] Daniel R. Cadel and K. Todd Lowe. Cross-correlation Doppler global velocimetry (CC-DGV). *Optics and Lasers in Engineering*, 71:51–61, August 2015. doi: 10.1016/j.optlaseng.2015.03.012.

[12] Daniel R. Cadel and K. Todd Lowe. Investigation of measurement sensitivities in cross-correlation Doppler global velocimetry. *Optics and Lasers in Engineering*, 86:44–52, November 2016. doi: 10.1016/j.optlaseng.2016.05.003.

[13] Andrew D. Cutler and K. Todd Lowe. Laser Rayleigh Scattering, Filtered Rayleigh Scattering, and Interferometric Rayleigh Scattering. In *Optical Diagnostics for Reacting*

and Non-Reacting Flows: Theory and Practice, number 0 in Progress in Astronautics and Aeronautics, pages 75–136. American Institute of Aeronautics and Astronautics, Inc., December 2022. doi: 10.2514/5.9781624106330.0075.0136. URL https://doi.org/10.2514/5.9781624106330.0075.0136.

[14] Andrew D. Cutler, Keith Rein, Sukesh Roy, Paul M. Danehy, and Naibo Jiang. 100-khz interferometric rayleigh scattering for multi-parameter flow measurements. *Optics Express*, 28(3):3025, January 2020. ISSN 1094-4087. doi: 10.1364/oe.380934.

[15] Chloe E. Dedic, Terrence R. Meyer, and James B. Michael. Single-shot ultrafast coherent anti-stokes raman scattering of vibrational/rotational nonequilibrium. *Optica*, 4(5):563, May 2017. ISSN 2334-2536. doi: 10.1364/optica.4.000563.

[16] Ulrich Doll, Michael Dues, Tommaso Bacci, Alessio Picchi, Guido Stockhausen, and Christian Willert. Aero-thermal flow characterization downstream of an NGV cascade by five-hole probe and filtered Rayleigh scattering measurements. *Experiments in Fluids*, 59(10), September 2018. doi: 10.1007/s00348-018-2607-z.

[17] Ulrich Doll, Ingo Röhle, Michael Dues, and Ralf Kapulla. Time-resolved multi-parameter flow diagnostics by filtered rayleigh scattering: system design through multi-objective optimisation. *Measurement Science and Technology*, 33(10):105204, July 2022. ISSN 1361-6501. doi: 10.1088/1361-6501/ac7cca.

[18] Ulrich Doll, Ralf Kapulla, Michael Dues, Jonas Steinbock, Sergey Melnikov, Ingo Röhle, Matteo Migliorini, and Pavlos K. Zachos. Towards time-resolved multi-property measurements by filtered rayleigh scattering: diagnostic approach and verification. *Experiments in Fluids*, 65(1), December 2023. ISSN 1432-1114. doi: 10.1007/s00348-023-03740-6.

[19] Jordi Estevadeordal, Naibo Jiang, Andrew D. Cutler, Josef J. Felver, Mikhail N. Slipchenko, Paul M. Danehy, James R. Gord, and Sukesh Roy. High-repetition-rate interferometric rayleigh scattering for flow-velocity measurements. *Applied Physics B*, 124(3), February 2018. ISSN 1432-0649. doi: 10.1007/s00340-018-6908-y.

[20] D Favier, C Maresca, M Nsi Mba, Eric Berton, and A Agnes. New type of embedded laser doppler velocimeter for measurement of rotary wings boundary layer. *Review of scientific instruments*, 68(6):2447–2455, 1997.

[21] Daniel Favier. The role of wind tunnel experiments in<scp>cfd</scp>validation, September 2010.

[22] J. N. Forkey, N. D. Finkelstein, W. R. Lempert, and R. B. Miles. Demonstration and characterization of filtered rayleigh scattering for planar velocity measurements. *AIAA Journal*, 34(3):442–448, March 1996. ISSN 1533-385X. doi: 10.2514/3.13087.

[23] Joseph Forkey, Walter R Lempert, and Richard B Miles. Flow field diagnostics by spectrally filtered rayleigh scattering. In *International Congress on Applications of Lasers & Electro-Optics*, pages 111–120. Laser Institute of America, 1990.

[24] Joseph Forkey, Walter R. Lempert, and Richard B. Miles. Filtered rayleigh scattering measurements of velocity, temperature, and density in supersonic flow. In *Conference on Lasers and Electro-Optics*, page CMG5. Optica Publishing Group, 1993. URL https://opg.optica.org/abstract.cfm?URI=CLEO-1993-CMG5.

[25] Joseph N. Forkey, Walter R. Lempert, and Richard B. Miles. Corrected and calibrated i2 absorption model at frequency-doubled nd:yag laser wavelengths. *Applied Optics*, 36 (27):6729, September 1997. ISSN 1539-4522. doi: 10.1364/ao.36.006729.

[26] Aldo Gargiulo, Julie E. Duetsch-Patel, Aurelien Borgoltz, William J. Devenport,

Christopher J. Roy, and K. Todd Lowe. Strategies for computational fluid dynamics validation experiments. *Journal of Verification, Validation and Uncertainty Quantification*, 8(3), September 2023. ISSN 2377-2166. doi: 10.1115/1.4063639.

[27] Tamara Guimarães, K. Todd Lowe, and Walter F. O'Brien. Complex Flow Generation and Development in a Full-Scale Turbofan Inlet. *Journal of Engineering for Gas Turbines and Power*, 140(8), May 2018. doi: 10.1115/1.4039179.

[28] Gregory J Hunt, Cody R Ground, and Robin L Hunt. Fast approximations of spectral lineshapes to enable optimization of a filtered rayleigh scattering experiment. *Measurement Science and Technology*, 31(9):095203, June 2020. ISSN 1361-6501. doi: 10.1088/1361-6501/ab8a7e.

[29] A Kopf, M Bardi, E Kohler, T Endres, G Bruneaux, and C Schulz. Survivability of the thermographic phosphors yag:pr and smp:sn in a premixed flame. *Measurement Science and Technology*, 32(7):074001, April 2021. ISSN 1361-6501. doi: 10.1088/1361-6501/abf57b.

[30] Yedhu Krishna, Xinguang Luo, and Gaetano Magnotti. One-dimensional interferometric rayleigh scattering velocimetry using a virtually imaged phased array. *Optics Letters*, 46(20):5252, October 2021. ISSN 1539-4794. doi: 10.1364/ol.441913.

[31] J. L. LIVESEY. The behavior of transverse cylindrical and forward facing total pressure probes in transverse total pressure gradients. *Journal of the Aeronautical Sciences*, 23 (10):949–955, October 1956. ISSN 1936-9956. doi: 10.2514/8.3695.

[32] Todd Lowe, Christopher J. Roy, William J. Devenport, Aurelien Borgoltz, Agata Grzyb, Monica Shanmugam, Advait Borole, and Aldo Gargiulo. Experimental results for the vt-nasa cfd turbulence model blind validation challenge. In *AIAA AVIATION FORUM*

AND ASCEND 2024. American Institute of Aeronautics and Astronautics, July 2024. doi: 10.2514/6.2024-4438.

[33] Xinguang Luo, Zeinab Al Hadi, Yedhu Krishna, and Gaetano Magnotti. 1d interferometric rayleigh scattering velocimetry and thermometry using vipa. *Optics Express*, 32 (11):20291, May 2024. ISSN 1094-4087. doi: 10.1364/oe.524049.

[34] Joseph G. Marvin. Perspective on computational fluid dynamics validation. *AIAA Journal*, 33(10):1778–1787, October 1995. ISSN 1533-385X. doi: 10.2514/3.12727.

[35] Thomas A. Mcmanus, Ignacio Trueba Monje, and Jeffrey A. Sutton. Experimental assessment of the Tenti S6 model for combustion-relevant gases and filtered Rayleigh scattering applications. *Applied Physics B*, 125(1), jan 2019. doi: 10.1007/s00340-018-7121-8.

[36] Richard Miles, Walter Lempert, and Joseph Forkey. Instantaneous velocity fields and background suppression by filtered Rayleigh scattering. In *29th Aerospace Sciences Meeting*. American Institute of Aeronautics and Astronautics, January 1991. doi: 10.2514/6.1991-357.

[37] Richard B Miles, Walter R Lempert, and Joseph N Forkey. Laser rayleigh scattering. *Measurement Science and Technology*, 12(5):R33–R51, April 2001. doi: 10.1088/0957-0233/12/5/201.

[38] Michael Nelson, Kevin T. Lowe, Walter F. O'Brien, and Kevin M. Hoopes. Stereoscopic PIV Measurements of Swirl Distortion on a Full-Scale Turbofan Engine Inlet. In *52nd Aerospace Sciences Meeting*. American Institute of Aeronautics and Astronautics, January 2014. doi: 10.2514/6.2014-0533.

[39] W. L. Oberkampf, D. P. Aeschliman, R. E. Tate, and J. F. Henfling. Experimental

aerodynamics research on a hypersonic vehicle. Technical report, U.S. Department of Energy Office of Scientific and Technical Information, United States, 1993. URL https://www.osti.gov/biblio/6532053.

[40] William L. Oberkampf and Barton L. Smith. Assessment criteria for computational fluid dynamics model validation experiments. *Journal of Verification, Validation and Uncertainty Quantification*, 2(3), September 2017. ISSN 2377-2166. doi: 10.1115/1.4037887.

[41] A. Omrane, P. Petersson, M. Aldén, and M.A. Linne. Simultaneous 2d flow velocity and gas temperature measurements using thermographic phosphors. *Applied Physics B*, 92(1):99–102, May 2008. ISSN 1432-0649. doi: 10.1007/s00340-008-3051-1.

[42] J. Panda. Spectrally-resolved rayleigh scattering to measure velocity, temperature, density, and density fluctuations in high-speed flows. *Experiments in Fluids*, 61(3), February 2020. ISSN 1432-1114. doi: 10.1007/s00348-020-2903-2.

[43] J. Panda and R. Seasholtz. Density measurement in underexpanded supersonic jets using rayleigh scattering. In *36th AIAA Aerospace Sciences Meeting and Exhibit*. American Institute of Aeronautics and Astronautics, January 1998. doi: 10.2514/6.1998-281.

[44] J. Panda and R. G. Seasholtz. Measurement of shock structure and shock–vortex interaction in underexpanded jets using rayleigh scattering. *Physics of Fluids*, 11(12): 3761–3777, December 1999. ISSN 1089-7666. doi: 10.1063/1.870247.

[45] Garrett Pitt and Todd Lowe. Ultraviolet (uv) laser implementation and measurement sensitivities in filtered rayleigh scattering for aerodynamic flows. In *AIAA AVIATION 2023 Forum*. American Institute of Aeronautics and Astronautics, June 2023. doi: 10.2514/6.2023-4381.

[46] R.W. Pitz, R. Cattolica, F. Robben, and L. Talbot. Temperature and density in a hydrogen air flame from Rayleigh scattering. *Combustion and Flame*, 27:313–320, August 1976. ISSN 0010-2180. doi: 10.1016/0010-2180(76)90036-5.

[47] Sean William Powers. *Filtered Rayleigh Scattering with an Application to Force Component Decomposition*. PhD thesis, Virginia Polytechnic Institute and State University, 2023.

[48] Markus Raffel, Christian E. Willert, Steven T. Wereley, and Jürgen Kompenhans. *Particle Image Velocimetry : a Practical Guide*. Springer-Verlag Berlin Heidelberg, 2007. ISBN 9783540723080.

[49] Markus Raffel, Christian E Willert, Fulvio Scarano, Christian J Kähler, Steve T Wereley, and Jürgen Kompenhans. *Particle image velocimetry: a practical guide*. springer, 2018.

[50] Lord Rayleigh. X. On the Electromagnetic Theory of Light. *The London, Edinburgh, and Dublin Philosophical Magazine and Journal of Science*, 12(73):81–101, August 1881. ISSN 1941-5982. doi: 10.1080/14786448108627074. URL https://doi.org/10.1080/14786448108627074.

[51] Lord Rayleigh. XXXIV. On the Transmission of Light Through an Atmosphere Containing Small Particles in Suspension, and on the Origin of the Blue of the Sky. *The London, Edinburgh, and Dublin Philosophical Magazine and Journal of Science*, 47(287): 375–384, April 1899. ISSN 1941-5990. doi: 10.1080/14786449908621276.

[52] Daniel T Reese, Naibo Jiang, and Paul Danehy. Unseeded velocimetry in nitrogen for high-pressure, cryogenic wind tunnels: part iii. resonant femtosecond-laser tagging. *Measurement Science and Technology*, 31(7):075203, April 2020. ISSN 1361-6501. doi: 10.1088/1361-6501/ab7bbc.

[53] C. D. Richards and W. M. Pitts. Global density effects on the self-preservation behaviour of turbulent free jets. *Journal of Fluid Mechanics*, 254:417–435, September 1993. ISSN 1469-7645. doi: 10.1017/s0022112093002204.

[54] Ashley J. Saltzman, Matthew T. Boyda, Kevin T. Lowe, and Wing Ng. Filtered rayleigh scattering for velocity and temperature measurements of a heated supersonic jet with thermal non-uniformity. In *25th AIAA/CEAS Aeroacoustics Conference*. American Institute of Aeronautics and Astronautics, May 2019. doi: 10.2514/6.2019-2677.

[55] Richard G. Seasholtz, Alvin E. Buggele, and Mark F. Reeder. Flow measurements based on rayleigh scattering and fabry-perot interferometer. *Optics and Lasers in Engineering*, 27(6):543–570, August 1997. ISSN 0143-8166. doi: 10.1016/s0143-8166(96)00063-2.

[56] Eduardo Sevilla. *Experimental investigation of the systematic errors of pneumatic pressure probes induced by velocity gradients*. PhD thesis, Vienna University of Technology, 2002.

[57] Adam Steinberg and Sukesh Roy, editors. *Optical Diagnostics for Reacting and Non-Reacting Flows: Theory and Practice*. American Institute of Aeronautics and Astronautics, Inc., 2022.

[58] J.W. Strutt. LVIII. On the Scattering of Light by Small Particles. *The London, Edinburgh, and Dublin Philosophical Magazine and Journal of Science*, 41(275):447–454, June 1871. ISSN 1941-5990. doi: 10.1080/14786447108640507.

[59] J.W. Strutt. XV. On the Light from the Sky, its Polarization and Colour. *The London, Edinburgh, and Dublin Philosophical Magazine and Journal of Science*, 41(271):107–120, February 1871. ISSN 1941-5990. doi: 10.1080/14786447108640452.

[60] J.W. Strutt. XXXVI. On the Light from the Sky, its Polarization and Colour. *The*

London, Edinburgh, and Dublin Philosophical Magazine and Journal of Science, 41 (273):274–279, April 1871. ISSN 1941-5990. doi: 10.1080/14786447108640479.

[61] Ketana Teav and Adam M. Steinberg. Measurements of rayleigh–brillouin scattering spectra of ar, n2, and ch4 at pressures up to 20 atm. *Proceedings of the Combustion Institute*, 39(1):1425–1434, 2023. ISSN 1540-7489. doi: 10.1016/j.proci.2022.09.037.

[62] G. Tenti, C. D. Boley, and Rashmi C. Desai. On the Kinetic Model Description of Rayleigh–Brillouin Scattering from Molecular Gases. *Canadian Journal of Physics*, 52 (4):285–290, February 1974. ISSN 1208-6045. doi: 10.1139/p74-041.

[63] Allen L. Treaster and Adam Yocum. The calibration and application of five-hole probes. Technical Report TM 78-10, International Instrumentation Symposium, 24th, Albuquerque, N. Mex., May 1-5, 1978, January 1978.

[64] Evan P. Warner and Todd Lowe. Machine-learned background quantification for filtered rayleigh scattering measurement processing. In *AIAA SCITECH 2023 Forum*. American Institute of Aeronautics and Astronautics, January 2023. doi: 10.2514/6.2023-1373.

[65] Dustin Witkowski, Joshua M. Herzog, and David A. Rothamer. Combustion-relevant temperature imaging with scattering referenced aerosol phosphor thermometry applied to eu:bam. *Combustion and Flame*, 224:233–238, February 2021. ISSN 0010-2180. doi: 10.1016/j.combustflame.2020.11.002.

[66] B. Witschas. Analytical model for rayleigh–brillouin line shapes in air. *Applied Optics*, 50(3):267, January 2011. ISSN 1539-4522. doi: 10.1364/ao.50.000267.

[67] Hongda Yan, Tao Wu, Sihao Pi, Qiang Wu, Chenwen Ye, and Xingdao He. Demonstration of a rayleigh–brillouin scattering spectrometer with a high spectral resolution

for rapid gas temperature detection. *Optics Letters*, 48(22):5931, November 2023. ISSN 1539-4794. doi: 10.1364/ol.506847.

[68] Andrew T. Young. Rayleigh scattering. *Applied Optics*, 20(4):533, February 1981. ISSN 1539-4522. doi: 10.1364/ao.20.000533.